



**HAL**  
open science

# Influence of the casting microstructure on damage mechanisms in Al-Si alloys by using 2D and 3D in-situ analysis

Long Wang

► **To cite this version:**

Long Wang. Influence of the casting microstructure on damage mechanisms in Al-Si alloys by using 2D and 3D in-situ analysis. Mechanics [physics.med-ph]. Ecole Centrale de Lille, 2015. English. NNT : 2015ECLI0004 . tel-01272159

**HAL Id: tel-01272159**

**<https://theses.hal.science/tel-01272159>**

Submitted on 10 Feb 2016

**HAL** is a multi-disciplinary open access archive for the deposit and dissemination of scientific research documents, whether they are published or not. The documents may come from teaching and research institutions in France or abroad, or from public or private research centers.

L'archive ouverte pluridisciplinaire **HAL**, est destinée au dépôt et à la diffusion de documents scientifiques de niveau recherche, publiés ou non, émanant des établissements d'enseignement et de recherche français ou étrangers, des laboratoires publics ou privés.

N° d'ordre : 263

ECOLE CENTRALE DE LILLE

## THESE

présentée en vue  
d'obtenir le grade de

## DOCTEUR

en

Spécialité : Mécanique

par

**Long WANG**

DOCTORAT DELIVRE PAR L'ECOLE CENTRALE DE LILLE

Titre de la thèse :

### **Influence of the casting microstructure on damage mechanisms in Al-Si alloys by using 2D and 3D in-situ analysis**

Étude de l'influence de la microstructure sur les mécanismes d'endommagement  
dans des alliages Al-Si de fonderie par des analyses in-situ 2D et 3D

Soutenue le 23 janvier 2015 devant le jury d'examen :

<b>Rapporteur</b>	<i>Karl-Heinz Lang, Docteur Ingénieur, IAM, Karlsruhe Institutes of Technology (KIT), Allemagne</i>
<b>Rapporteur</b>	<i>Yves Nadot, Professeur, Pprime, ENSMA, Poitiers</i>
<b>Président du jury</b>	<i>Jean-Yves Buffière, Professeur, MATEIS, INSA Lyon, Villeurbanne</i>
<b>Examineur</b>	<i>Tilman Beck, Professeur, Institute of Materials Science and Engineering, Technische Universität Kaiserslautern, Allemagne</i>
<b>Examineur</b>	<i>Julien Réthoré, Chargé de Recherche CNRS, LaMCoS, INSA Lyon, Villeurbanne</i>
<b>Invité</b>	<i>Fabien Szymka, Docteur Ingénieur, PSA Peugeot Citroën, Vélizy</i>
<b>Co-encadrante</b>	<i>Nathalie Limodin, Chargée de recherche CNRS, LML, École Centrale de Lille, Villeneuve d'Ascq</i>
<b>Co-encadrant</b>	<i>Ahmed El Bartali, Maître de Conférences, LML, École Centrale de Lille, Villeneuve d'Ascq</i>
<b>Directeur de thèse</b>	<i>Eric Charkaluk, Directeur de Recherche CNRS, LML, École Centrale de Lille, Villeneuve d'Ascq</i>

Thèse préparée au Laboratoire de Mécanique de Lille (UMR CNRS 8107)

Ecole Doctorale SPI 072 (Lille I, Lille III, Artois, ULCO, UVHC, EC Lille)  
**PRES Université Lille Nord-de-France**



## REMERCIEMENTS

Je tiens tout à bord à remercier tous les membres du jury pour avoir accepté d'examiner ce travail et pour l'intérêt qu'ils lui ont porté.

Je tiens à remercier chaleureusement mon directeur de thèse Eric Charkaluk, Directeur de Recherche au CNRS, mon encadrante Nathalie Limodin, Chargée de recherche au CNRS, et mon encadrant Ahmed El Bartali, Maître de Conférences à l'Ecole Centrale de Lille, pour la confiance qu'ils m'ont accordée en acceptant d'encadrer ce travail doctoral, pour la disponibilité, les précieux conseils et le soutien qu'ils m'ont apportés. Pendant les 40 mois de ma thèse, ils m'ont beaucoup aidé pour mes recherches, mes études et ma vie en France. Je suis très heureux d'avoir eu l'occasion de travailler avec eux pour ma thèse. Je leur exprime toute ma gratitude. Ils sont inoubliables.

J'aimerais par ailleurs souligner la contribution importante d'autres personnes et d'autres établissements à l'aboutissement de ce travail.

Je tiens à remercier le financement de China Scholarship Council (CSC) et le support de PSA Peugeot Citroën pour ma thèse.

Je tiens à remercier particulièrement Jean-Yves Buffière, Professeur à l'INSA-Lyon, et le Laboratoire MATEIS (INSA-Lyon) pour leur aide et leur support technique en caractérisation de matériaux et en essais de traction/fatigue avec observations 3D in-situ.

Je tiens à remercier Julien Réthoré, Chargé de Recherche au CNRS, pour la plateforme MIC3D. Les corrélations pour les essais de traction 3D ont été effectuées avec cette plateforme.

Je tiens également à remercier David Balloy, Professeur à l'Université Lille 1, pour son aide et son assistance avec le Microscope électronique à balayage (MEB).

Je remercie aussi le Swiss Light Source (SLS) du Paul Scherrer Institut (PSI) pour l'essai de fatigue 3D.

Je remercie l'ensemble du personnel du Laboratoire de Mécanique de Lille (LML) et de l'Ecole Centrale de Lille, plus particulièrement : Jean-Francois Witz (corrélations 2D et 3D), Rian Seghir (corrélations 3D), François Lesaffre (usinage des éprouvettes), Alexandre Mege-Revil (MEB), Fabienne Delepaut (secrétariat), Xiaogang WANG (corrélations 2D), Gregory Hauss (Avizo), Nora Dahdah (essais de fatigue 3D) ainsi que tous mes collègues et amis de l'équipe MaSTR et de l'équipe ER5 au LML pour leur gentillesse et l'ambiance amicale qu'ils font régner.

Enfin, ces dernières lignes sont destinées à mes parents, toute ma famille et mes amis que je voudrais remercier pour m'avoir soutenu et encouragé.





# Contents

<b>Contents .....</b>	<b>I</b>
<b>List of Figures.....</b>	<b>IV</b>
<b>List of Tables .....</b>	<b>XIII</b>
<b>Chapter 1 Introduction.....</b>	<b>- 1 -</b>
1.1 Background .....	- 1 -
1.2 Aim and objectives .....	- 3 -
1.3 Thesis structure .....	- 3 -
<b>Chapter 2 Literature review .....</b>	<b>- 5 -</b>
2.1 Introduction.....	- 6 -
2.2 Al-Si Casting Alloys .....	- 6 -
2.2.1 Introduction.....	- 6 -
2.2.2 Microstructure of Al-Si Casting Alloys .....	- 7 -
2.2.3 Lost foam casting .....	- 19 -
2.3 Micromechanisms of fatigue damage in Al-Si casting alloys.....	- 22 -
2.3.1 Influence of casting defects.....	- 22 -
2.3.2 Influence of microstructural constituents/features .....	- 25 -
2.4 Summary of literature review .....	- 32 -
<b>Chapter 3 Material Characterization .....</b>	<b>- 36 -</b>
3.1 Introduction.....	- 37 -
3.2 Characterization methods.....	- 38 -
3.2.1 Optical microscope observation.....	- 38 -
3.2.2 SEM observation.....	- 39 -
3.2.3 X-ray microtomography observation .....	- 39 -
3.2.4 Image analysis process.....	- 45 -
3.3 ‘Phases’ morphologies and sizes.....	- 50 -
3.3.1 Microstructure of A319 alloy.....	- 50 -
3.3.2 Microstructure of A356 alloy.....	- 75 -
3.4 Comparisons .....	- 79 -
3.5 Summary .....	- 82 -
<b>Chapter 4 Experimental methods.....</b>	<b>- 85 -</b>

4.1	Introduction.....	- 85 -
4.2	Extraction of specimens .....	- 86 -
4.3	Preparation and selection of specimens .....	- 89 -
4.4	Experimental protocol.....	- 93 -
4.4.1	In-situ observation methods .....	- 93 -
4.4.2	Mechanical.....	- 95 -
4.4.3	Postmortem analyses.....	- 97 -
4.5	Field measurements .....	- 99 -
4.5.1	Basic principles.....	- 99 -
4.5.2	DIC.....	- 100 -
4.5.3	DVC .....	- 103 -
4.5.4	Measurement uncertainty .....	- 105 -
4.6	Summary .....	- 108 -
<b>Chapter 5 Damage mechanisms in Al-Si alloys.....</b>		<b>- 109 -</b>
5.1	Introduction.....	- 110 -
5.2	Tensile damage mechanisms.....	- 110 -
5.2.1	Tensile tests with 2D in-situ observations .....	- 110 -
5.2.2	Tensile tests with 3D in-situ observations .....	- 120 -
5.2.3	Discussion.....	- 128 -
5.3	Fatigue damage mechanisms .....	- 132 -
5.3.1	Fatigue tests with 2D in-situ observations .....	- 132 -
5.3.2	Fatigue tests with 3D in-situ observations .....	- 152 -
5.3.3	Discussion.....	- 164 -
5.4	Summary .....	- 173 -
5.4.1	Experimental protocol.....	- 173 -
5.4.2	Damage mechanisms.....	- 174 -
<b>Appendix I Digital image processing and analysis.....</b>		<b>- 185 -</b>
I.1	Digital image processing fundamentals.....	- 185 -
I.1.1	Filters .....	- 185 -
I.1.2	Binning .....	- 186 -
I.1.3	Image segmentation.....	- 186 -
I.1.4	Morphological image processing.....	- 191 -
I.2	DAS measurements in 3D rendered image.....	- 193 -
<b>Appendix II FEM simulations .....</b>		<b>- 195 -</b>
II.1	Mesh model .....	- 195 -
II.2	FE calculations .....	- 196 -
II.2.1	Application in tensile test.....	- 196 -

II.2.2 Selection of ROI for fatigue tests with 3D observations .....	- 197 -
II.2.3 Comparisons with DVC results of fatigue tests .....	- 197 -
<b>Appendix III Selections of specimen and ROI .....</b>	<b>- 198 -</b>
III.1 Tensile tests with 2D in-situ observations .....	- 198 -
III.1.1 Specimen T1 .....	- 198 -
III.1.2 Specimen T2 .....	- 199 -
III.2 Tensile tests with 3D in-situ observations: Specimen T3 .....	- 199 -
III.3 Fatigue tests with 2D in-situ observations .....	- 200 -
III.3.1 Specimen F1.....	- 200 -
III.3.2 Specimen F2.....	- 202 -
III.4 Fatigue tests with 3D in-situ observations .....	- 204 -
III.4.1 Specimen F3.....	- 204 -
III.4.2 Specimen F4.....	- 205 -
<b>Appendix IV Field measurements .....</b>	<b>- 207 -</b>
IV.1 Principles of 2D/3D image correlation platform at LML .....	- 207 -
IV.2 Examples of parameters for Elastix software .....	- 208 -
<b>Appendix V Crack length measurements in 2D .....</b>	<b>- 212 -</b>
<b>Appendix VI Fracture analysis using SEM-EDS .....</b>	<b>- 213 -</b>
VI.1 Specimen F1 .....	- 214 -
VI.2 Specimen F2 .....	- 215 -
VI.3 Specimen F3 .....	- 216 -
VI.4 Specimen F4 .....	- 218 -
<b>References.....</b>	<b>- 220 -</b>
<b>Extended Abstract (French).....</b>	<b>- 232 -</b>

## List of Figures

Figure 1-1 Cylinder head and temperature field in the fire deck (PSA data).....	- 2 -
Figure 1-2 LFC and DC casting process (Tabibian, 2011) .....	- 2 -
Figure 1-3 Comparisons between A319-LFC and A319-DC: (a) normalized axial stress cyclic versus number of cycles (Tabibian et al., 2010); (b) stabilized hysteresis loop (Tabibian, 2011). .....	- 2 -
Figure 2-1 Commercial cast Al-Si alloys. (a) Al-Si equilibrium diagram and microstructure of (b) hypoeutectic (1.65-12.6 wt% Si), (c) eutectic (12.6% Si), and (d) hypereutectic (>12.6% Si) alloys. (Warmuzek, 2004) .....	- 8 -
Figure 2-2 Solidification process of Al-Si Alloy (Albonetti, 2000) .....	- 8 -
Figure 2-3 Morphology of the Si crystals in Al-Si alloys observed with Scanning Electron Microscope: (a) in eutectic and (b) in hypereutectic as-cast alloys, and (c) in modified hypoeutectic alloy after heat treatment. (Warmuzek, 2004) .....	- 10 -
Figure 2-4 Optical micrographs of : (a) unmodified AlSi7 alloy showing plate-like Si eutectic structure and (b) modified AlSi7 + 150ppm Sr with coralline-like Si structure. (Barrirero et al., 2013) -	11 -
Figure 2-5 Effects of Sr on the parameters of the eutectic Si particles (Kosa et al., 2012) .....	- 11 -
Figure 2-6 A series of reconstructed images from independently nucleated complex $\beta$ plates, taken at several time steps during their growth by using synchrotron tomography (Terzi et al., 2010). .....	- 12 -
Figure 2-7 Microstructures of Al-Si alloys with (a) 0.3 wt% and (b) 0.7 wt% Fe, respectively (Lu and Dahle, 2005).....	- 13 -
Figure 2-8 Micrographs obtained from : (a) an unmodified base Al alloy; and (b) a Sr-modified Al alloy in as cast condition (E. M. Elgallad, 2010).....	- 14 -
Figure 2-9 Volume fraction of $\beta$ platelets as a function of solidification time (Salvo et al., 2012). -	14 -
Figure 2-10 3-D rendering of pore evolution (blue) in the presence of intermetallics (red) in an A319 alloy at: (a) 565 °C, (b) 561 °C, (c) 555 °C and (d) 550 °C. Examples of pore growth along the solid surface of intermetallics are shown in dashed black and white circles (Puncreobutr et al., 2014).. -	15 -
Figure 2-11 Backscattered electron image of an as-cast AlCuSiFe based alloy (E. M. Elgallad, 2010). -	16 -
Figure 2-12 Focussed Ion Beam cross-section of an Al-Si-Cu alloy (a) without Ce and (b) with 0.02% Ce (Voncina et al., 2014).....	- 16 -
Figure 2-13 (a) Segmented $Mg_2Si$ coral and (b) segmentation of the phase contrast images of $Mg_2Si$ (blue) and the small particles of eutectic Si (including some small $Mg_2Si$ particles) (yellow) from tomography images (Tolnai et al., 2009). .....	- 17 -
Figure 2-14 Four types of pores in aluminum castings (Monroe, 2005).....	- 18 -
Figure 2-15 Illustration of gravity die casting (Niane and Michalet, 2011) .....	- 19 -
Figure 2-16 The basic steps of the LFC process (American Foundry Society, 2004) .....	- 20 -
Figure 2-17 Measurement of SDAS (Charbonnier, 1992).....	- 21 -

Figure 2-18 Microstructure of AlSi7Cu alloy solidified with cooling rate (a) $0.18\text{ }^{\circ}\text{C s}^{-1}$ , and (b) $0.96\text{ }^{\circ}\text{C s}^{-1}$ (Dobrzański et al., 2006).....	- 22 -
Figure 2-19 Evolution of pore size with cooling rate for different hydrogen contents in alloy A356.0. Hydrogen content ( $\text{cm}^3/100\text{ g}$ ): 1, 0.25(no grain refiner); 2, 0.31 (grain refined); 3, 0.25 (grain refined); 4, 0.11 (grain refined); 5, 0.31 (grain refined and modified) (Kaufman and Rooy, 2004). .....	- 22 -
Figure 2-20 Interaction of a fatigue crack with Si particles: (a) at $\Delta K=6\text{ MPa}\sqrt{\text{m}}$ , a fatigue crack along a grain boundary (left) ran into a Si particle (A) and deflected to follow the interface, causing the particle A to fracture; (b) interface and particle fracture at Si particle (B) located ahead of the crack tip; (c) linkage of the main crack with particle cracks at $\Delta K=8\text{ MPa}\sqrt{\text{m}}$ ; and (d) crack coalescence by fatigue crack growth through the matrix ligament at $\Delta K=10\text{ MPa}\sqrt{\text{m}}$ . The loading axis is vertical (Chan et al., 2003). .....	- 26 -
Figure 2-21 SEM micrograph showing fracture of both iron and copper intermetallics in an Al-Si alloy with 0.8%Fe (Ma et al., 2014). .....	- 27 -
Figure 2-22 Typical SEM image and EDAX analysis from a thermal-shock crack propagated through the pores and developed by debonding and cracking of (a) large Cu rich and (b) Cu-Mg rich intermetallics in an A319 alloy (Arami et al., 2008).....	- 29 -
Figure 2-23 Fatigue life for unmodified and Sr-modified A356-T6 alloys as a function of SDAS (Wang et al., 2001b).....	- 30 -
Figure 2-24 Examples of slip bands on the fracture surface indicating the local yielding and dislocation movement (Wang et al., 2001b). .....	- 31 -
Figure 2-25 SEM image showing a PSB crack in A356 alloy (Zeng et al., 2014) .....	- 32 -
Figure 3-1 OM images of an A356 specimen (a) before and (b) after etching.....	- 38 -
Figure 3-2 (a) Principle of tomography; (b) Synchrotron and laboratory tomography. (Salvo et al., 2010).....	- 40 -
Figure 3-3 Absorption contrast and phase contrast.....	- 41 -
Figure 3-4 A CT slice of an A319 alloy from: (a) Lab-CT (only absorption contrast) and (b) SR-CT (absorption and phase contrasts).....	- 41 -
Figure 3-5 (a) Locations of the scans in Specimen 1 (A319) and (b) 3D rendering of the region analyzed in ‘scan4’ .....	- 43 -
Figure 3-6 (a) Location of the scan in Specimen 2 (A319) and (b) 3D rendering of the analyzed region .....	- 43 -
Figure 3-7 (a) Location of the scan in Specimen 3 (A356) and (b) 3D rendering of the analyzed region .....	- 44 -
Figure 3-8 Scheme of image processing and analysis .....	- 45 -
Figure 3-9 Scheme of image processing and analysis for Specimens 1 and 2 in Avizo.....	- 47 -
Figure 3-10 Scheme of image processing and analysis for Specimen 3 in ImageJ .....	- 47 -
Figure 3-11 Illustrations of (a) Feret diameter, (b) minimum bounding box and (c) 3D coordinate system in Avizo software (ZIB et al. 2012).....	- 49 -
Figure 3-12 OM images of A319 alloy: (a) shrinkage and (b) gas pores (after etching).....	- 51 -
Figure 3-13 BSE images of A319: (a) shrinkage and (b) gas pores.....	- 51 -
Figure 3-14 Relation between equivalent and Feret diameters of pores (Specimen 1).....	- 52 -
Figure 3-15 3D renderings of pores having a Feret diameter (a) less than $20\text{ }\mu\text{m}$ , (b) $20\text{-}100\text{ }\mu\text{m}$ , (c) more than $100\text{ }\mu\text{m}$ (Specimen 1).....	- 52 -

Figure 3-16 A close-up view of the largest pore (in yellow) in Figure 3-15 .....	- 53 -
Figure 3-17 Distributions of pores as functions of equivalent and Feret diameters (Specimen 1) ..	- 54 -
Figure 3-18 Granulometry distribution of pores (Specimen 1).....	- 54 -
Figure 3-19 Variability of 3D analysis results of pores between scans (Specimen 1).....	- 55 -
Figure 3-20 Distributions of Feret diameter of pores in Specimens 1 and 2 .....	- 56 -
Figure 3-21 3D renderings of pores having a Feret diameter (a) less than 60 $\mu\text{m}$ , (b) 60-100 $\mu\text{m}$ , (c) 100-1200 $\mu\text{m}$ and (d) more than 1200 $\mu\text{m}$ (Specimen 2).....	- 57 -
Figure 3-22 3D rendering of pores having sphericity factor: (a) $F > 0.4$ and (b) $F < 0.4$ (Specimen 2)-	58
-	
Figure 3-23 Distributions of pores ( $F > 0.4$ and $F < 0.4$ ) as functions of Feret diameter as compared to the fitting curve in (Charkaluk et al., 2014).....	- 59 -
Figure 3-24 Al matrix and eutectic Si (A319, after etching) in (a) BSE and (b) OM images .....	- 60 -
Figure 3-25 3D renderings of Si phase in (a) a volume of $500 \times 500 \times 500 \mu\text{m}^3$ and (b) a subvolume ..	61 -
Figure 3-26 Illustration of the problem of threshold range selection for Si.....	- 61 -
Figure 3-27 Iron intermetallics in OM image (A319, after etching).....	- 62 -
Figure 3-28 BSE image: (a) $\alpha$ phase with "Chinese script" morphology; (b) $\alpha$ phase and needle-like $\beta$ phase (A319). (c) An example of EDS analysis on $\alpha$ phase. ....	- 63 -
Figure 3-29 3D renderings of intermetallics having a Feret diameter (a) less than 20 $\mu\text{m}$ , (b) 20-60 $\mu\text{m}$ , (c) 60-1500 $\mu\text{m}$ , (d) more than 1500 $\mu\text{m}$ .....	- 64 -
Figure 3-30 (a) A slice from the Lab-CT image with (b) 3D rendering of intermetallics .....	- 65 -
Figure 3-31 (a) A 'Chinese script' morphology with (b) 3D rendering.....	- 65 -
Figure 3-32 Distributions of intermetallics as functions of equivalent and Feret diameters .....	- 66 -
Figure 3-33 Granulometry distribution of intermetallics .....	- 66 -
Figure 3-34 Copper containing phases ( $\text{Al}_2\text{Cu}$ and $\text{AlCuMgSi}$ ) in OM image (A319, after etching).....	67 -
Figure 3-35 (a) BSE image: copper containing phases, $\text{Al}_2\text{Cu}$ and $\text{AlCuMgSi}$ (A319), and a small connected microstructure of $\text{Al}_2\text{Cu}$ and $\text{AlCuMgSi}$ phases marked with a circle. Examples of EDS analysis on (b) $\text{AlCuMgSi}$ and (c) $\text{Al}_2\text{Cu}$ . ....	- 68 -
Figure 3-36 BSE images: (a) some small connected microstructure of $\text{Al}_2\text{Cu}$ and $\text{AlCuMgSi}$ phases, and (b) a zoom on one example of this connected microstructure.....	- 68 -
Figure 3-37 BSE images: copper containing phases connected with (a) Al-Si eutectic and $\beta$ intermetallics and (b) with $\alpha$ intermetallics .....	- 69 -
Figure 3-38 3D renderings of $\text{Al}_2\text{Cu}$ having a Feret diameter (a) less than 20 $\mu\text{m}$ , (b) 20-90 $\mu\text{m}$ , (c) 90-750 $\mu\text{m}$ , (d) more than 750 $\mu\text{m}$ .....	- 70 -
Figure 3-39 (a) A slice from the Lab-CT image and (b) a 3D rendering of $\text{Al}_2\text{Cu}$ .....	- 71 -
Figure 3-40 Distributions of $\text{Al}_2\text{Cu}$ as functions of equivalent and Feret diameters .....	- 72 -
Figure 3-41 Granulometry distribution of $\text{Al}_2\text{Cu}$ phase.....	- 72 -
Figure 3-42 BSE images: Pb particles in A319 alloy .....	- 73 -
Figure 3-43 3D renderings of Pb having a Feret diameter (a) less than 30 $\mu\text{m}$ , (b) more than 30 $\mu\text{m}$ , and (c) close-up view of objects in figure (b) .....	- 74 -

Figure 3-44 Distributions of Pb as functions of equivalent and Feret diameters.....	- 75 -
Figure 3-45 Microstructure of A356 alloy (after etching): (a) BSE image, (b) OM image.....	- 75 -
Figure 3-46 Example of one lab-CT slice (Specimen 3, A356 alloy, voxel of 3.4 $\mu\text{m}$ after binning) that presents intermetallics, porosity and Al matrix .....	- 76 -
Figure 3-47 3D view of (a) pores and iron intermetallics at (b) a 3.4 $\mu\text{m}$ voxel size (Specimen 3) and at (c) a 0.9 $\mu\text{m}$ voxel size (courtesy of RX-Solutions); intermetallics are in yellow and pores in black- 77 -	- 77 -
Figure 3-48 Distributions of Feret diameter of pores in A356 and A319.....	- 78 -
Figure 3-49 Granulometry distributions of intermetallics in A319 and A356.....	- 79 -
Figure 3-50 Distributions of pores, intermetallics, $\text{Al}_2\text{Cu}$ , Pb as a function of size (Feret diameter for pores and Pb, granulometry for intermetallics and $\text{Al}_2\text{Cu}$ ).....	- 81 -
Figure 4-1 Extraction of specimens from prototype cylinder heads: (a) small and (b) large size specimens from the fire deck areas and (c) from small pieces. ....	- 86 -
Figure 4-2 Size of extracted specimens (in mm) for (a) tensile tests and fatigue tests with 3D in-situ observations, (b) fatigue tests with 2D in-situ observations (X=10 for Specimen F1, and X=8 for Specimen F2). ....	- 88 -
Figure 4-3 Examples of OM images on the surface of grinded specimens: (a) unselected and (b) selected. (c): One example of a large casting defect in the shoulder area on the 3D rendered surface (left) and in volume with the material set transparent (right) .....	- 90 -
Figure 4-4 Lab-CT at Laboratoire de Mécanique de Lille (LML).....	- 91 -
Figure 4-5 Size distributions of pores in Specimen T3 and in a larger sample (Specimen 2) .....	- 92 -
Figure 4-6 Comparison of granulometry distributions of iron intermetallics and $\text{Al}_2\text{Cu}$ phases in Specimen T3 and in larger Specimen 1 .....	- 93 -
Figure 4-7 2D in-situ observation equipment .....	- 94 -
Figure 4-8 Example of images taken at one step using Questar and stitching of images .....	- 94 -
Figure 4-9 Tensile tests with (a) 2D and (b) 3D in-situ observations.....	- 95 -
Figure 4-10 Tensile tests process.....	- 96 -
Figure 4-11 Fatigue tests with (a) 2D and (b) 3D in-situ observations.....	- 97 -
Figure 4-12 Images taken during fatigue tests .....	- 97 -
Figure 4-13 Schematic diagram illustrating X-ray mapping area for large size specimens.....	- 98 -
Figure 4-14 Example showing decohesion and fracture of eutectic Si in X-ray mapping images of two fracture surfaces of the same specimen.....	- 98 -
Figure 4-15 Schematic illustration of the two images recorded before and after deformation: a “reference” and a target (or deformed) images. ....	- 100 -
Figure 4-16 The basic registration components (Klein and Staring, 2012) .....	- 101 -
Figure 4-17 Examples of a strain field calculated: (a) without and (b) with bending energy penalty term (‘Metric0 Weight = 1.0’ and ‘Metric1 Weight = 100’). ....	- 103 -
Figure 4-18 Measurements uncertainties .....	- 106 -
Figure 4-19 Four types of tests in this thesis .....	- 108 -
Figure 4-20 Basic experimental protocol in this thesis.....	- 108 -



Figure 5-1 (a) Postmortem OM image (bottom) of Specimen T1 compared with radiography (top) and OM (middle) images taken before the tensile test, with (b) a larger magnification in the ROI marked by a rectangle. .... - 111 -

Figure 5-2 Postmortem OM image of Specimen T2 (top) compared with radiography (middle) and OM (bottom) images taken before the tensile test ..... - 112 -

Figure 5-3 Fracture analysis of Specimens (a) T1 and (b) T2 ..... - 112 -

Figure 5-4 Stitched Questar images at the last step before failure: (a) 7<sup>th</sup> step of Specimen 1 at 71MPa (large cracks are marked by arrows); (b) 16<sup>th</sup> step of Specimen 2 at 237MPa ..... - 113 -

Figure 5-5 SEM postmortem analysis in Specimens (a) T1 and (b) T2: microcracks and final fracture at hard inclusions (Si particles, iron intermetallics)..... - 114 -

Figure 5-6 Stress-strain curves deduced from DIC measurements for Specimens T1 and T2 and from a standard test performed on A356 alloy. .... - 115 -

Figure 5-7 Displacement fields (U1, in pixels, 1 pixel = 0.34  $\mu\text{m}$ ) of Specimen T1 in the loading direction at: (a) 3<sup>rd</sup> step, (b) 4<sup>th</sup> step, (c) 5<sup>th</sup> step, (d) 6<sup>th</sup> step, (e) 7<sup>th</sup> step with (f) a close-up view of the region marked with a rectangle in (e). Images obtained with post-mortem SEM are shown in transparency. The stress and mean strain calculated by DIC are specified for each step. .... - 116 -

Figure 5-8 (a) Longitudinal strain field ( $\epsilon_{11}$ ) of Specimen T1 for the 7<sup>th</sup> step and (b) a close-up view of the region marked with a rectangle in (a). Images obtained with post-mortem SEM are shown in transparency. .... - 117 -

Figure 5-9 Displacement fields (U1, in pixels) of Specimen T2 in the loading direction: (a) 15<sup>th</sup> step, (b) 16<sup>th</sup> step. Images obtained with post-mortem SEM are shown in transparency. The stress and mean strain calculated by DIC are specified for each step. .... - 118 -

Figure 5-10 Longitudinal strain field ( $\epsilon_{11}$ ) of Specimen T2: (a) 15<sup>th</sup> step, (b) 16<sup>th</sup> step; Equivalent von Mises strain field at (c) 15th step, (d)16th step; (e) A close-up view of the area marked in (b) and (d) compared with the microcracks (circled in red on the SEM image). Post-mortem SEM images (c) are shown in transparency in (c) and (d)..... - 119 -

Figure 5-11 Comparison of stress-strain curves from DVC and from a standard test on A319 alloy ..... - 120 -

Figure 5-12 Displacement fields (in pixels, 1 pixel = 1.695  $\mu\text{m}$ ) and strain fields of Specimen T3- 121 -

Figure 5-13 Comparison of 3D residual error in yellow and segmented cracks in red color in Specimen T3. Pores are rendered in green..... - 122 -

Figure 5-14 3D renderings of Specimen T3 at the 6<sup>th</sup> step (198MPa): (a) residual error, (b) displacement field (in pixels, 1 pixel = 1.695  $\mu\text{m}$ ) along loading direction (z-axis) and (c)  $\epsilon_{zz}$  strain field with pores shown in black and cracks in purple color; (d) Comparison between the cracks, in purple color, and pores, in green, with (e) the microstructure observed in one slice of tomography image..... - 123 -

Figure 5-15 A partial view of (a) residual error field at 198MPa in one slice near the specimen's flat surface 1 and (b) of tomography image in the corresponding slice; (c) SEM image of surface 1 near the slice shown in (a) and (b) with (d) a higher resolution image on the area where a crack is marked with a red circle in (a)(b)(c) ..... - 124 -

Figure 5-16 A partial view of (a) residual error field at 198MPa in one slice near surface 2 and (b) of tomography image in the corresponding slice; (c) the SEM image of surface 2, near the slice shown in (a) and (b), with (d) a higher resolution image on the area where a crack is marked with a red circle in (a)(b)(c) ..... - 125 -

Figure 5-17 SEM image of Specimen T3 showing cracks at  $\text{Al}_2\text{Cu}$  and  $\text{AlCuMgSi}$  phases ..... - 126 -

Figure 5-18 Cracks growth around pore in Specimen T3 during the tensile test (Pores in translucent grey and cracks in translucent yellow).....	- 127 -
Figure 5-19 (a) Strain field ( $\epsilon_{zz}$ ) from FEM with (b) a focus on the sub volume in the area marked with a red rectangle in (a) that corresponds to the area where the DVC measurements were performed (pores shown in golden, cracks in red) and corresponding strain field from DVC at 198MPa (pores shown in black and cracks in purple).....	- 132 -
Figure 5-20 Maximum applied stress for Specimen F1 and F2 during 2D in-situ fatigue tests ....	- 133 -
Figure 5-21 Stitched Questar image of Specimen F1 before the fatigue test. The crack initiation site after 7 000 cycles is marked by an arrow.....	- 134 -
Figure 5-22 Fracture surface of Specimen F1. The SEM image in Zone B is shown in Figure 5-23.....	- 135 -
Figure 5-23 SEM image of the fracture surface of Specimen F1 in Zone B in Figure 5-22.....	- 135 -
Figure 5-24 Zone C in Figure 5-23 observed using SEM with a higher resolution.....	- 136 -
Figure 5-25(a) Stitched Questar image of Specimen F2 after 20 300 cycles with the 2D projection of 3D pores from Figure III-5 in purple; the final fracture is marked with a blue line. (b) The fracture surface observed by SEM in the corresponding area shown in (a). ....	- 137 -
Figure 5-26 Stitched Questar images of Specimen F2 during the tensile stage at the 1 <sup>st</sup> cycle at about (a) 80 MPa and (b) 98 MPa.....	- 138 -
Figure 5-27 SEM image of Zone A marked in Figure 5-25(b) .....	- 138 -
Figure 5-28 Stitched Questar images of Specimen F2: (a) after 15 500 cycles, (b) after 16 000 cycles .-	- 139 -
Figure 5-29 Fracture analysis performed on Zone B marked in Figure 5-25(b).....	- 140 -
Figure 5-30 OM image in ROI of Specimen F2: the observed crack is marked with lines and arrows indicate locations of crack arrest.....	- 141 -
Figure 5-31 Cracks length evolution with number of cycles in Specimens F1 and F2.....	- 141 -
Figure 5-32 Questar images in Zone 0 of Specimen F1: (a) after 7 000 cycles; (b) after 13 000 cycles; (c) after 90 000 cycles; (d) after failure at about 100 000 cycles.....	- 142 -
Figure 5-33 BSE image in Zone 0 of specimen F1 .....	- 143 -
Figure 5-34 Schematic drawing of the area where crack tip is arrested by barrier .....	- 144 -
Figure 5-35 Examples of crack tip having the shape of ‘Y’ .....	- 145 -
Figure 5-36(a) Plastic zone shapes through specimen thickness obtained by using the theoretical calculations (Botsis and Humbert, 2006); (b) plastic zone in an aluminum sheet (Hutchinson, 1968) ...-	- 145 -
Figure 5-37 BSE images of the surface of Specimen F1 where in-situ observations were done. The selected ROI for in-situ observation is marked with a red rectangle (in left). The area where many microcracks are observed is marked with a yellow rectangle (in right).....	- 147 -
Figure 5-38 BSE images of the surface of Specimen F2 where in-situ observations were done. The selected ROI for in-situ observation is marked with a red rectangle (in left). The area where many microcracks were observed is marked with a yellow rectangle (in right).....	- 147 -
Figure 5-39 Evolution of average longitudinal strain in Specimens F1 and F2, as measured by extensometer and DIC at the maximum load, with the number of cycles .....	- 149 -
Figure 5-40 Schema of DIC measurement and extensometer measurement .....	- 149 -

Figure 5-41 Field measurement in zone 0 of Specimen F1: (a) displacement (in pixels, 1 pixel = 0.38  $\mu\text{m}$ ) and (b) strain field after 13 000 cycles; (c) displacement and (d) strain field after 85 000 cycles..- 150 -

Figure 5-42 Field measurement in the ROI of Specimen F1: (a) displacement ( $V$ , in pixels, 1 pixel = 0.38  $\mu\text{m}$ ) and (b) strain ( $\epsilon_{22}$ ) field after 90 000 cycles (last step before final failure)..... - 151 -

Figure 5-43 Field measurement in the ROI of Specimen F2: (a) displacement ( $V$ , in pixels, 1 pixel = 0.38  $\mu\text{m}$ ) and (b) strain field ( $\epsilon_{22}$ ) after 18 410 cycles ..... - 152 -

Figure 5-44 Evolution of average maximum longitudinal strain in Specimens F3 and F4, as measured by DVC, with the number of cycles..... - 153 -

Figure 5-45 (a) 3D rendering of pores and fracture surface of Specimen F3. (b) Displacement field (in pixels, 1 pixel = 1.625  $\mu\text{m}$ ) and (c) strain field at 10<sup>th</sup> cycle shown in translucent with the tomographic image in below. DVC was performed between the minimum loading of the 1<sup>st</sup> cycle and the maximum loading of the 10<sup>th</sup> cycle. .... - 154 -

Figure 5-46 Two examples showing cracks in Specimen F3 in the same slice at the maximum loading of 1<sup>st</sup> cycle and 10<sup>th</sup> cycle, and the final fracture after 10 cycles. .... - 154 -

Figure 5-47 (a) 3D cracks and 3D rendering of pores in black; (b) figure (a) shown with fracture surface..... - 156 -

Figure 5-48 Comparison of 3D rendering of pores and fracture surface and tomographic image slice revealed the two main cracks initiated around a large pore (in the left image) and at hard inclusions (in the right image) in Specimen F4 ..... - 157 -

Figure 5-49 3D cracks in Specimen F4 around the 3D rendered pores at different cycles. View along the loading direction. .... - 158 -

Figure 5-50(a) Cracks length evolution with the number of cycles in Specimen F4 with (b) the projection plane used for the cracks measurements..... - 159 -

Figure 5-51 One slice (about 65  $\mu\text{m}$  below the flat surface) shown with a 3D rendering of pores and fracture surface of Specimen F4 ..... - 159 -

Figure 5-52 DVC displacement fields (in pixels, 1 pixel = 1.625  $\mu\text{m}$ ) of one slice (about 65  $\mu\text{m}$  below the flat surface) of Specimen F4 at different cycles..... - 160 -

Figure 5-53 DVC strain fields of the same slice (about 65  $\mu\text{m}$  below the flat surface) of Specimen F4 in Figure 5-52 at different cycles..... - 160 -

Figure 5-54 Examples showing residual plastic zones with a shape of ‘Y’ near cracks tips: (a) about 80  $\mu\text{m}$  and (b) about 200  $\mu\text{m}$  below flat surface of Specimen F4. DVC was performed between the minimum loads of the 1<sup>st</sup> cycle and of the 10 500<sup>th</sup> cycle..... - 162 -

Figure 5-55 Residual plastic strain localizations in the same slice at different cycles (Specimen F4)....- 163 -

Figure 5-56 Cracks opening displacement map of Specimens F3. .... - 164 -

Figure 5-57 Cracks opening displacement map of Crack 1 and Crack 2 in Specimen F4. The location of each crack was shown by a circle in the last cycle. .... - 164 -

Figure 5-58 Comparison of same slice (390  $\mu\text{m}$  below the flat surface) between FEM simulation results and the tomographic image at 10 500 cycle (Specimen F4)..... - 167 -

Figure 5-59 Equivalent Von Mises strain field from DVC: correlation between the minimum loading of 1st cycle and the maximum loading of (a) 2<sup>nd</sup> cycle and (b) 20<sup>th</sup> cycle. (c) PEEQ field (after 3 cycles) from FE simulation. (Slice shown is about 680  $\mu\text{m}$  below the flat surface of Specimen F4) .....- 171 -

Figure I-1 Principle of median filtering ..... - 185 -

Figure I-2 Principle of anisotropic diffusion filtering.....	- 186 -
Figure I-3 Procedure of binning.....	- 186 -
Figure I-4 Pre-treatment methods for SR-CT images: (a) original image; (b) a strong filter is performed on image (a); (c) the roughly segmented image from image (b); (d) a closing operation is performed on image (c); (e) an opening operation is performed on image (d) and the segmentation of porosity is finished; (f) invert color of image (e) to obtain a mask; (g) the original image (a) covered by the mask (f) in order to segment Si; (h) erosion/dilation operation performed on the mask (f) to enlarge the pores and cover the bright contrast around the pores; (i) the original image (a) covered by the mask (h) in order to segment iron intermetallics and Al <sub>2</sub> Cu phases.....	- 188 -
Figure I-5 Distributions of intermetallics as functions of equivalent and Feret diameters .....	- 189 -
Figure I-6 Comparison of 3D renderings between standard threshold (104-177) (in the left, purple) and upper bound threshold (102-182) (in the right, green).....	- 190 -
Figure I-7 Comparison of 3D renderings between standard threshold (104 -177) (in the left, purple) and lower bound threshold (106-174) (in the right, yellow).....	- 190 -
Figure I-8 Illustration of the problem of threshold range selection: the original image (a), the threshold range selected (99-150) are shown by red colour .....	- 191 -
Figure I-9 Eroding of an object.....	- 192 -
Figure I-10 Dilation of an object.....	- 192 -
Figure I-11 Example of opening operation.....	- 193 -
Figure I-12 Example of closing operation.....	- 193 -
Figure I-13 Examples of Dendrite Arm Spacing (DAS) measurements performed in 3D rendering of pores.....	- 194 -
Figure II-1 Schematic of FE mesh process .....	- 196 -
Figure III-1 Specimen T1: (a) radiography and (b) OM image with the ROI marked by a rectangle. ....	- 198 -
Figure III-2 Specimen T2: (a) radiography and (b) OM image with the ROI marked by a rectangle. ....	- 199 -
Figure III-3 (a) 3D rendering of pores in Specimen T3; the selected ROI is marked by a red rectangle. (b) A close up-view of the largest pore in (a) marked by an arrow. ....	- 200 -
Figure III-4 Specimen F1: 3D rendering of (a) pores in bulk (b) and surface pore in the notched surface marked with a yellow arrow; the specimen surface was set transparent in the left image and opaque in the right image. (c) OM image of the specimen surface after etching: the pore marked with the yellow arrow was projected on the surface and is shown in purple; the selected ROI for the in-situ observation with Questar microscope is marked with a red rectangle; where crack initiated after 7000 cycles on the surface is marked with a green arrow.....	- 201 -
Figure III-5 3D rendering of a cluster of pores near the flat observed surface: in (a) view intercepted perpendicular to the flat surface, (b) view intercepted parallel to the flat surface. (c) OM image taken after etching with the projection of pores shown in (b). (d) OM image taken after etching, the selected ROI was marked with a blue rectangle. ....	- 203 -
Figure III-6 Specimen F3: (a) distribution of pores and (b) FEM simulation results (E33: longitudinal strain); the selected ROI is marked by a red rectangle.....	- 205 -
Figure III-7 Thickness distribution of hard inclusions in Specimen F3.....	- 205 -
Figure III-8 Specimen F4: (a) distribution of pores and (b) FE simulation results (E33: longitudinal strain) with selected ROI marked by a red rectangle. ....	- 206 -
Figure III-9 Thickness distribution of hard inclusions in Specimen F4.....	- 206 -

Figure IV-1 The basic registration components of image correlation platform at LML .....	- 207 -
Figure V-1 Crack length measurement method. ....	- 212 -
Figure VI-1 X-ray mapping of Si (Specimen F1) .....	- 214 -
Figure VI-2 X-ray mapping of Fe (Specimen F1) .....	- 214 -
Figure VI-3 X-ray mapping of Mn (Specimen F1).....	- 214 -
Figure VI-4 X-ray mapping of Cu (Specimen F1).....	- 215 -
Figure VI-5 X-ray mapping of Si (Specimen F2) .....	- 215 -
Figure VI-6 X-ray mapping of Fe (Specimen F2) .....	- 215 -
Figure VI-7 X-ray mapping of Mn (Specimen F2).....	- 216 -
Figure VI-8 X-ray mapping of Cu (Specimen F2).....	- 216 -
Figure VI-9 X-ray mapping of Si (Specimen F3) .....	- 216 -
Figure VI-10 X-ray mapping of Fe (Specimen F3) .....	- 217 -
Figure VI-11 X-ray mapping of Mn (Specimen F3).....	- 217 -
Figure VI-12 X-ray mapping of Cu (Specimen F3).....	- 217 -
Figure VI-13 X-ray mapping of Si (Specimen F4) .....	- 218 -
Figure VI-14 X-ray mapping of Fe (Specimen F4) .....	- 218 -
Figure VI-15 X-ray mapping of Mn (Specimen F4).....	- 218 -
Figure VI-16 X-ray mapping of Cu (Specimen F4).....	- 219 -

## List of Tables

Table 2-1 Reactions occurring during solidification of two A319 alloys (Mart ínez D. et al., 2005) according to (B äckerud et al., 1990) and (Samuel et al., 1996).....	- 9 -
Table 2-2 Main microstructure constituents and casting defects in Al-Si alloy .....	- 34 -
Table 2-3 Micromechanisms of fatigue damage in Al-Si casting alloys .....	- 35 -
Table 3-1 Chemical composition of Lost Foam Casting A356 and A319 alloys (wt.).....	- 37 -
Table 3-2 Phases or constituents studied in 3D in A356 and A319 alloys .....	- 37 -
Table 3-3 Specimens studied in this chapter.....	- 43 -
Table 3-4 Parameter settings of laboratory X-ray microtomography .....	- 44 -
Table 3-5 Size and volume of analysed volume for each specimen .....	- 46 -
Table 3-6 2D and 3D results of pores in A319 alloy .....	- 53 -
Table 3-7 3D and 2D results of pores in A319 alloy .....	- 56 -
Table 3-8 DAS values measured on 3D images (Specimen 2) .....	- 59 -
Table 3-9 Results of segmentation tests for Si phase.....	- 62 -
Table 3-10 Comparisons between 3D and 2D results of iron intermetallics .....	- 64 -
Table 3-11 Comparison of 3D and 2D results of Al <sub>2</sub> Cu .....	- 69 -
Table 3-12 3D results of Pb (Specimen 1).....	- 73 -
Table 3-13 3D vs. 2D results of pores and intermetallics in A356 .....	- 77 -
Table 3-14 Comparison of the different characterization methods used .....	- 79 -
Table 3-15 Mechanical properties of Al and Pb .....	- 81 -
Table 3-16 Summary of 2D and 3D characterization .....	- 84 -
Table 4-1 Extraction, preparation, selection and in-situ observations of specimens .....	- 87 -
Table 4-2 Parameter settings for 3D in-situ observations.....	- 95 -
Table 4-3 Natural tracers for DIC and DVC.....	- 107 -
Table 4-4 Selected element size for each measurement.....	- 107 -
Table 5-1 Results of 2D tensile tests.....	- 111 -
Table 5-2 Results of 2D fatigue tests .....	- 133 -
Table 5-3 Results of 3D fatigue tests .....	- 153 -
Table 5-4 Parameters of large pores in Figure 5-47.....	- 156 -
Table 5-5 Basic information on fatigue tests .....	- 165 -
Table 5-6 Ratios of elements mass fraction on fracture surface and on flat surface.....	- 172 -
Table I-1 Main parameters of filters selected for Specimen 1 and 2 in chapter 3 .....	- 186 -

Table I-2 Threshold ranges of the different phases in all the specimens ..... - 186 -  
Table I-3 Results of the segmentation tests on intermetallics ..... - 189 -  
Table III-1 Size and location of Pore A, B and C shown in Figure III-5 (b) ..... - 204 -

# Chapter 1 Introduction

## Contents

---

<b>1.1</b>	<b>Background</b> .....	- 1 -
<b>1.2</b>	<b>Aim and objectives</b> .....	- 3 -
<b>1.3</b>	<b>Thesis structure</b> .....	- 3 -

---

## 1.1 Background

The development of automotive industry must meet economic and ecological objectives and at the same time ensure performance, driving quality and safety. Reduction of cars weight not only saves fuel but also reduces emission of CO<sub>2</sub>. A reduction of 100 kg in the mass of a car induces a reduction of about 9 grams of CO<sub>2</sub> per kilometer (Hirsch, 2011). In order to achieve these goals, it is necessary to choose a suitable material for automobile manufacturing.

Aluminum alloys have high strength to weight ratio, good machinability, corrosion resistance, optimum surface finish and high electrical and thermal conductivity (Tabibian et al., 2013) (Gruzleski and Closset, 1990); they can also save the weight of parts up to 50% (Hirsch, 2011). Therefore, they are widely used in automotive industry, such as for chassis, structure, components, seam welded tubes, car body, engine blocks, heat exchanger.

Al-Si alloy is one of the most commonly used Al alloys in automotive industry mainly in engine parts. Cylinder head is one of the key components of the engine, it composes engine with cylinder block, pistons, crankcase, crankshaft and connecting rod. Its main role is to seal the cylinders and to form the combustion chamber with pistons and cylinder block. The compressed combustibles gas burning and swelling in combustion chamber, push the piston and the crankshaft connecting rod mechanism to provide power. Thus cylinder heads (Figure 1-1) are submitted to severe thermomechanical stresses (temperature gradient, high cyclic loadings, and thermal shock) with temperature variation from 20 to 250°C. In particular, the inter-valve zone in fire deck is the most critical area. In order to adapt to these working conditions, there is a high requirement for the material mechanical properties of cylinder head, for example, in fatigue and more particularly in Low Cycle Fatigue (LCF).



# Chapter 1 Introduction

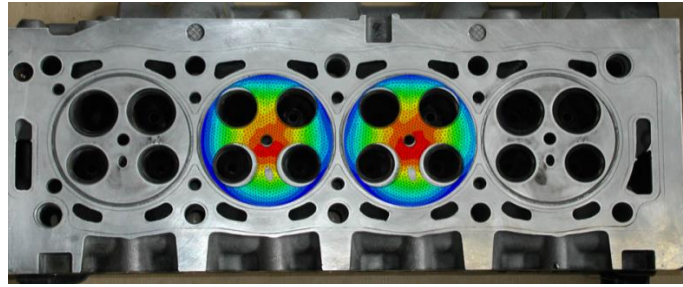


Figure 1-1 Cylinder head and temperature field in the fire deck (PSA data)

The conventional casting process to manufacture cylinder head is gravity Die Casting (DC) process, but it is progressively being replaced by the Lost Foam Casting (LFC) process for the purpose of geometry optimization, cost reduction and consumption control. However, aluminum alloy automotive parts produced by the LFC process have a coarser microstructure and more porosity defects than parts produced with conventional casting processes at faster cooling rates (Figure 1-2) and it is well known that microstructure has a major influence on the fatigue properties. In a previous thesis (Tabibian, 2011) performed in the laboratory, the fatigue life of LFC A319 alloy was drastically reduced compared to DC A319 alloy while the strain-stress hysteresis loop was virtually unchanged (see Figure 1-3).

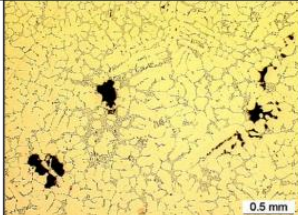

	Lost foam casting (LFC)	Die casting process (DC)
Cooling rates	0,8 °C/s	30 °C/s
DAS	85 μm	35 μm
Microstructure		

Figure 1-2 LFC and DC casting process (Tabibian, 2011)

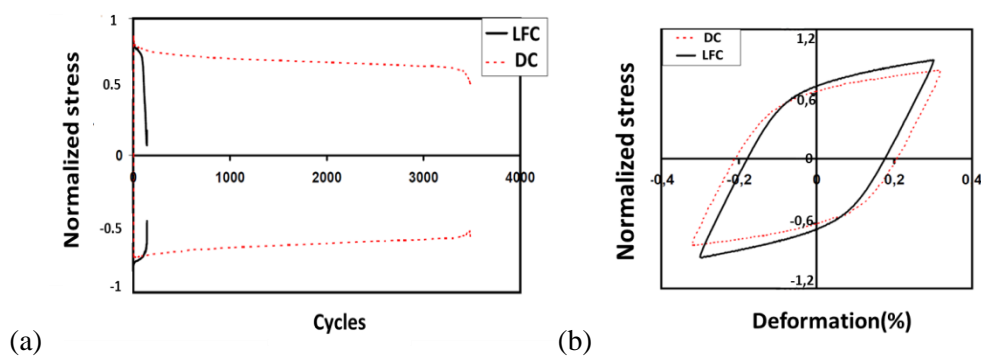


Figure 1-3 Comparisons between A319-LFC and A319-DC: (a) normalized axial stress cyclic versus number of cycles (Tabibian et al., 2010); (b) stabilized hysteresis loop (Tabibian, 2011).

# Chapter 1 Introduction

---

Moreover, in past years, some studies have been performed in order to reveal the damage mechanisms of Al-Si alloys. Above a critical size (Wang et al., 2001) (Zhang et al., 2007) (Mu et al., 2014), pores play a decisive role by providing preferential crack initiation sites (Ammar et al., 2008). An influence of Si phase (Buffière et al., 2001) (Stolarz et al., 2001), iron intermetallics and copper containing phases (Firouzdor et al., 2007) (Tabibian et al., 2013) is also observed. However, most of these studies were performed in High Cycle Fatigue (HCF) regime. Only a few studies focused on the damage mechanisms in Al-Si alloy with large casting defects in Low Cycle Fatigue (LCF) regime. Moreover, even if post-failure analysis makes it possible to track the defect at the initiation site, it does not allow for studying the relationship between microstructure and crack growth kinetic at the surface and in volume. In LCF, this analysis is made even more difficult as failure often results from multicracking (Stolarz et al., 2001) rather than from a single crack. Thus the damage mechanisms in LFC Al-Si alloys in LCF are still unclear and should be further studied.

## 1.2 Aim and objectives

The aim of this thesis is to develop an experimental method to study the damage micromechanisms of LFC Al-Si alloy in LCF at room temperature. This method allows following cracks initiation and their propagations both on surface and in volume and thus allows identifying the relation between damage mechanisms and casting microstructure. In order to achieve this goal, several experimental techniques have been coupled. 2D (Questar long distance microscope) and 3D (X-Ray tomography) in situ tracking of the damage at microstructural scale in real time were used both in monotonic tension and fatigue. 2D/3D displacement and strain fields, which are measured using Digital Image Correlation (DIC) and Digital Volume Correlation (DVC), allow analyzing the relation between the measured fields and damage behavior. In addition, a preliminary characterization of specimens before tests is necessary for the selection of the most suitable and representative specimen and of the ROI for the following analysis. Postmortem analysis using Optical Microscopy (OM), Scanning Electron Microscopy (SEM), and Energy Dispersive Spectrometer (EDS) and FEM simulation give more information to understand the damage mechanisms.

The studied material is from an A319 LFC cylinder head (composition presented in chapter 3). However, due to a lack of A319 material in the early stage of this thesis, specimens extracted from an A356 LFC cylinder head were used to validate the experimental protocol in tensile tests with 2D in-situ observations.

## 1.3 Thesis structure

This thesis contains six chapters, of which this is the first.

## Chapter 1 Introduction

---

The literature review in Chapter 2 is divided into two parts. Firstly, the microstructure of Al-Si alloy is introduced.  $\alpha$ -Aluminum phase, Si phase, iron intermetallics, copper containing phases, addition elements for grain refining and for improving mechanical properties, casting defects including pores and oxides films are presented. At the end of the first part, LFC process that has an important influence on microstructure of casting alloys is detailed. Secondly, the influence of the microstructure on fatigue damage is presented in three aspects: influence of casting defects including pores and oxide films; influence of hard inclusions including eutectic Si, iron intermetallics, copper containing phases and magnesium containing phases; influence of microstructural features such as SDAS, slip bands and grain boundaries.

The microstructure of the studied materials is characterized both in 2D and 3D in Chapter 3. The used characterization methods, i.e. OM, SEM-EDS, X-ray Laboratory Computerized Tomography (Lab-CT) and Synchrotron Radiation Computerized Tomography (SR-CT), are introduced at first. Then, A319 alloy is fully characterized whereas A356 alloy is not characterized in detail.

The experimental protocol is detailed in Chapter 4. The protocol has been first developed in tensile tests for validation before being applied in fatigue tests. The basic steps are similar: extraction, preparation and selection of specimens, tensile/fatigue tests with in-situ observations on surface using Questar microscope and in volume using Lab-CT/SR-CT, postmortem analyses using OM, SEM and EDS, field measurements using DIC in 2D and DVC in 3D.

Chapter 5 presents and discusses experimental results and reveals the damage mechanisms in tensile and cyclic loading. Results of tensile tests on A356 alloy with 2D in-situ observations and on A319 alloy with 3D situ observations are presented separately at first. Then tensile mechanisms and the application of experimental protocol are discussed. Afterwards results of fatigue tests on A319 alloy with 2D and 3D in-situ observations are presented and analyzed respectively. Damage mechanisms in LCF are then discussed by comparison of the above results. Finally, the experimental protocol is evaluated according to its application in this study, and some conclusions are drawn about damage mechanisms in tensile loading and in LCF.

Chapter 6 gives conclusions and outlooks for future works.

# Chapter 2 Literature review

## Contents

---

<b>2.1 Introduction.....</b>	<b>- 6 -</b>
<b>2.2 Al-Si Casting Alloys .....</b>	<b>- 6 -</b>
2.2.1 Introduction.....	- 6 -
2.2.2 Microstructure of Al-Si Casting Alloys .....	- 7 -
2.2.2.1 $\alpha$ -Aluminum phase.....	- 9 -
2.2.2.2 Silicon phase .....	- 9 -
2.2.2.3 Iron intermetallic phases .....	- 11 -
✓ Morphology of intermetallics phases .....	- 12 -
✓ Influence of Fe intermetallics on porosity .....	- 14 -
2.2.2.4 Copper containing phases .....	- 15 -
2.2.2.5 Other phases.....	- 16 -
✓ Grain refining.....	- 16 -
✓ Improving mechanical properties.....	- 17 -
2.2.2.6 Casting defects .....	- 18 -
2.2.3 Lost foam casting.....	- 19 -
<b>2.3 Micromechanisms of fatigue damage in Al-Si casting alloys .....</b>	<b>- 22 -</b>
2.3.1 Influence of casting defects.....	- 22 -
2.3.1.1 Pores.....	- 23 -
2.3.1.2 Oxide films.....	- 24 -
2.3.2 Influence of microstructural constituents/features .....	- 25 -
2.3.2.1 Hard inclusions .....	- 25 -
✓ Eutectic silicon particles .....	- 25 -
✓ Iron intermetallics .....	- 27 -
✓ Copper containing phases and magnesium containing phases.....	- 28 -
2.3.2.2 Microstructural features .....	- 29 -
✓ SDAS .....	- 29 -
✓ Slip bands and grain boundaries .....	- 31 -
<b>2.4 Summary of literature review .....</b>	<b>- 32 -</b>

---

### 2.1 Introduction

Aluminum silicon (Al-Si) casting alloy is a widely used aluminum alloy in the automotive industry. Many alloying elements, such as Cu, Ni, Mg, are added to form various constituents and improve its performances. During the casting process, defects inevitably occur. Therefore the complex microstructure of Al-Si alloys inherited from the casting process affects the fatigue behavior. Many studies were focused on this microstructure and on its influence on fatigue damage in the past years, and some of them are presented in this chapter, which is divided into two parts.

Al-Si alloys, including their microstructure and casting process, are presented in the first part (§ 2.2). After a brief introduction about Al-Si alloys in § 2.2.1, their microstructure, including  $\alpha$ -Aluminum phase, silicon phase, iron intermetallics, copper containing phases, some other phases, e.g. phases containing Mg, Ti, Ni, V, P, and casting defects (porosity and oxides films), is detailed in § 2.2.2. The Lost Foam Casting (LFC) process, i.e. the casting method, its advantages /disadvantages and its influence on the microstructure, is presented at last (§ 2.2.3).

The micromechanisms of fatigue damage in Al-Si alloys are presented in the second part (§ 2.3). The influence of casting defects on fatigue behavior is detailed at first (§ 2.3.1). Then the influence of microstructural constituents/features, including hard inclusions (Si phase, iron intermetallics, Cu containing and Mg containing phases) and microstructure features (slip bands, grain boundaries and SDAS (Secondary Dendrite Arm Spacing)), are presented in § 2.3.2.

### 2.2 Al-Si Casting Alloys

#### 2.2.1 Introduction

Aluminum alloys have many excellent features, such as light weight, high strength-to-weight ratio, corrosion resistance, relatively low cost (aluminum is the most widely distributed of the elements, except for oxygen, nitrogen, and silicon), high electrical and thermal conductivities, ease of manufacturing, and ready availability (Department of defense, U.S.A, 1966). Owing to these properties, they have been widely used in many industrial applications including in the transport industry, e.g. automobiles (Miller et al., 2000), trains (Skillingberg and Green, 2007), ships (Kyle et al., 2012), aviation (Liu et al., 2010), aerospace (Heinz et al., 2000), and in some other fields, such as building structures (Shi et al., 2005).

The growing demand for more fuel-efficient vehicles to reduce energy consumption and air pollution is a challenge for the automotive industry. The characteristic properties of aluminum make it the ideal candidate to replace heavier materials (steel or cast iron) to respond to the weight reduction demand

## Chapter 2 Literature review

---

(Miller et al., 2000). Use of aluminum alloys can make the cars lightweight, environmentally friendly, and energy-saving. For example, they are widely used in the cylinder block and cylinder head of the engine, which are the key components and should withstand high temperatures and cyclic loadings. Therefore, the research and development of automotive aluminum alloys is a key feature.

Commercial cast Al-Si alloys are multiphase materials belonging to the aluminum association classification series 3xx.x for aluminum silicon plus magnesium and/or copper alloys, such as the commonly used alloys in the automotive industry: 319, 356, 357, 380 and 390 aluminum alloys (Albonetti, 2000).

### 2.2.2 Microstructure of Al-Si Casting Alloys

The two principal phases present in Al-Si alloys are primary aluminum based  $\alpha$ -Al and silicon phases. The  $\alpha$ -Al phase, which has the largest volume fraction, acts as a matrix for the alloys. The silicon content in standardized commercial cast Al-Si alloys varies from 5 to 23 wt. %. Depending on this content, the structure of the alloy can be hypoeutectic, eutectic, or hypereutectic, as can be seen on the equilibrium phase diagram (Figure 2-1) (Warmuzek, 2004).

Solidification is the stage when the microstructure is formed. During the solidification of an Al-Si alloy, primary aluminum forms and grows in dendrites if the alloy is hypoeutectic or, silicon phase forms and grows in angular primary particles if the alloy is hypereutectic. Once the eutectic point is reached, the eutectic Al-Si constituent nucleates and grows until the end of solidification.

A319 alloy is a hypoeutectic Al-Si alloy ('a' in Figure 2-1(a)) with two main solidification stages (Figure 2-2): (1) formation of aluminum rich ( $\alpha$ -Al) dendrites, (2) development of two-phase (Al)-Si eutectic. However, the presence of additional alloying elements such as Mg and Cu, as well as of impurities such as Fe, leads to more complex solidification reactions (Dobrzański et al., 2006), which are listed in Table 2-1 (Martínez D. et al., 2005) for two A319 alloys.

## Chapter 2 Literature review

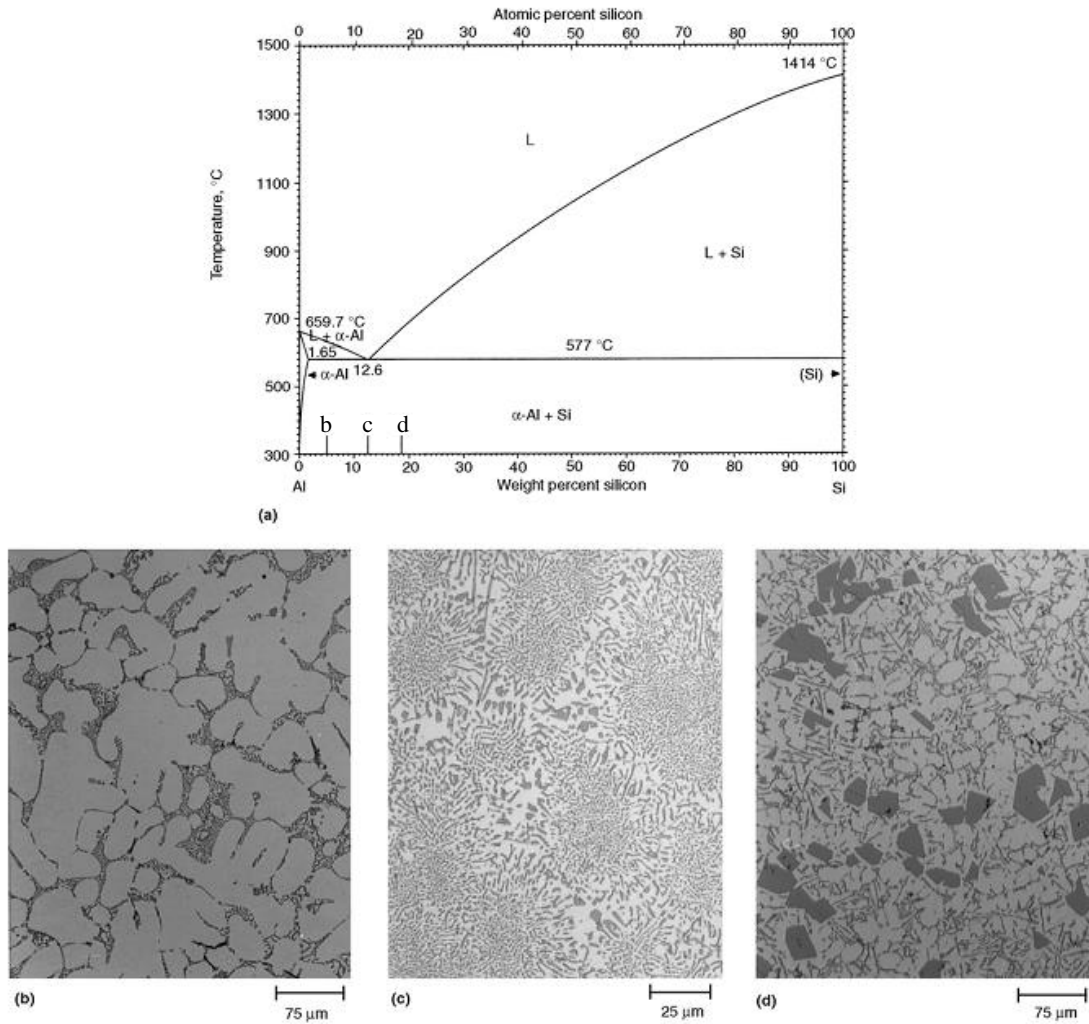


Figure 2-1 Commercial cast Al-Si alloys. (a) Al-Si equilibrium diagram and microstructure of (b) hypoeutectic (1.65-12.6 wt% Si), (c) eutectic (12.6% Si), and (d) hypereutectic (>12.6% Si) alloys. (Warmuzek, 2004)

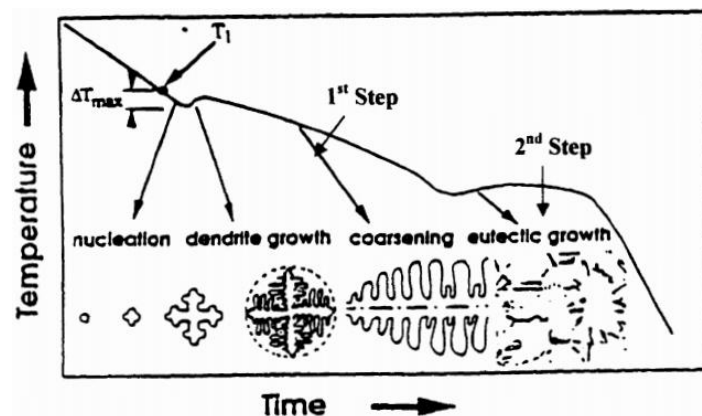


Figure 2-2 Solidification process of Al-Si Alloy (Albonetti, 2000)



## Chapter 2 Literature review

Table 2-1 Reactions occurring during solidification of two A319 alloys (Mart ínez D. et al., 2005) according to (B äckerud et al., 1990) and (Samuel et al., 1996)

Backerud et al.	Temperature (°C)	Samuel et al.	Temperature (°C)
(Al) dendritic network	609	(Al) dendritic network	610
Liq. → (Al) + Al <sub>15</sub> Mn <sub>3</sub> Si <sub>2</sub> + (Al <sub>5</sub> FeSi)	590		
Liq. → (Al) + Si + Al <sub>5</sub> FeSi	575	Precipitation of eutectic Si	562
		Precipitation of Al <sub>6</sub> Mg <sub>3</sub> FeSi <sub>6</sub> + Mg <sub>2</sub> Si	554
Liq. → (Al) + Al <sub>2</sub> Cu + Si + Al <sub>5</sub> FeSi	525	Precipitation of Al <sub>2</sub> Cu	510
Liq. → (Al) + Al <sub>2</sub> Cu + Si + Al <sub>5</sub> Mg <sub>8</sub> Cu <sub>2</sub> Si <sub>6</sub>	507	Precipitation of Al <sub>5</sub> Mg <sub>8</sub> Cu <sub>2</sub> Si <sub>6</sub>	490

### 2.2.2.1 α-Aluminum phase

α-Aluminum phase usually has a dendritic structure, which depends on the solidification conditions (Figure 2-1) (Warmuzek, 2004) (Moffat, 2007). The crystallographic orientation of the aluminum within the eutectic was found to be the same as the surrounding dendrites in both unmodified and Sr-modified alloys (Boulos et al., 2012).

### 2.2.2.2 Silicon phase

Silicon in aluminum alloys improves the casting characteristics. Indeed addition of silicon dramatically enhances fluidity, hot tear resistance and feeding characteristics (Pavlovic-Krstic, 2010). At room temperature, hypoeutectic alloys consist of a hard and brittle eutectic silicon phase and a soft and ductile primary aluminum phase (Ye, 2003).

As shown in Figure 2-1, the silicon content can affect the microstructure of Al-Si alloys. The silicon precipitates, which are almost pure, faceted crystals of Si, can have different morphology: primary, compact or massive precipitates in hypereutectic alloy or branched plates in eutectic alloy (See Figure 2-3) (Warmuzek, 2004). Moffat et al. (Moffat et al., 2006) reported that reducing Si content results in formation of clusters of intermetallics and increases porosity.



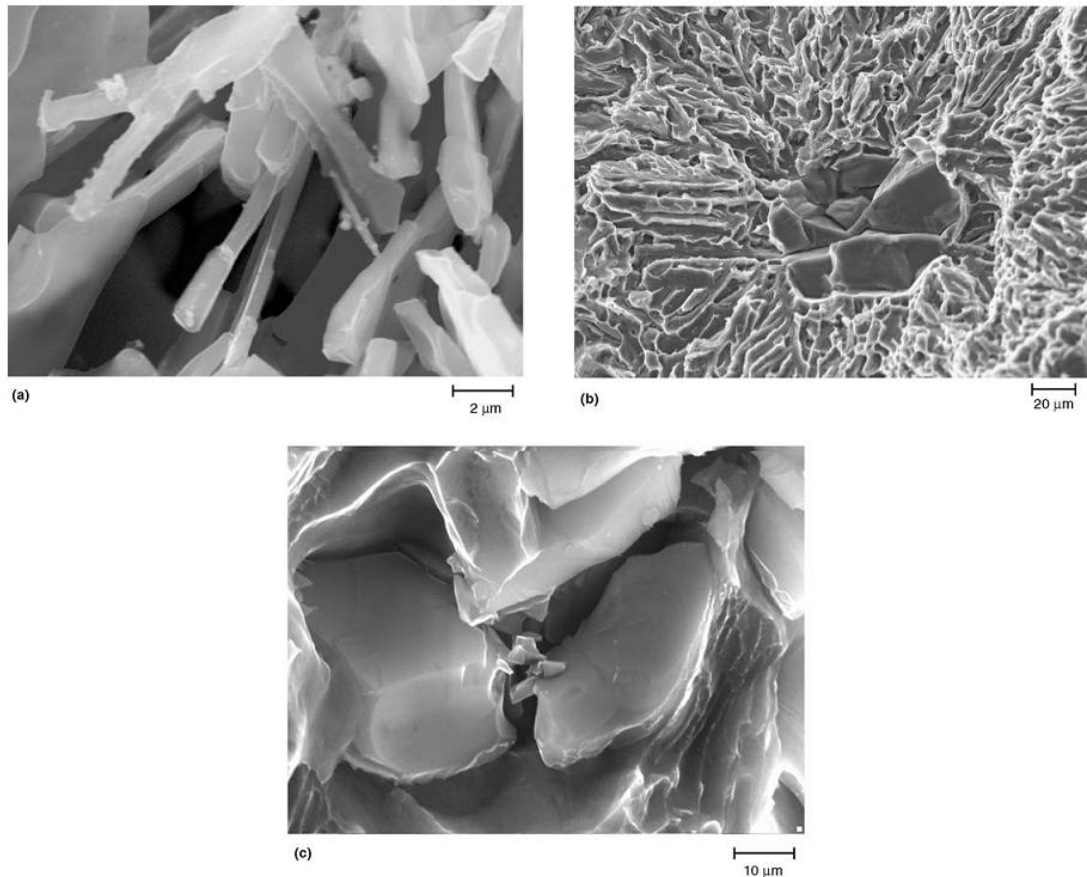


Figure 2-3 Morphology of the Si crystals in Al-Si alloys observed with Scanning Electron Microscope: (a) in eutectic and (b) in hypereutectic as-cast alloys, and (c) in modified hypoeutectic alloy after heat treatment. (Warmuzek, 2004)

The addition of strontium in Al-Si alloy causes Si phase to be more rounded and to present a coralline-like structure (Figure 2-4) (Gruzleski et al., 1990) (Barrirero et al., 2013) (Barrirero et al., 2014). If the content of Sr is below a critical value, the modification effect is insignificant (Ammar et al., 2008a). Then, at increasing content of Sr, the modification effect becomes more and more significant until another critical value is reached, above which the modification effect is stabilized (see Figure 2-5) (Kosa et al., 2012). However these critical values depend on the chemical composition of the alloy and on the cooling rate. A quicker cooling results in a finer eutectic at the same Sr content (Kosa et al., 2012). The content of Sr, above which the modification effect is significant, varies from 50 ppm, to 500 ppm in the literature (Gruzleski et al., 1990) (Kosa et al., 2012) (Ammar et al., 2008b).

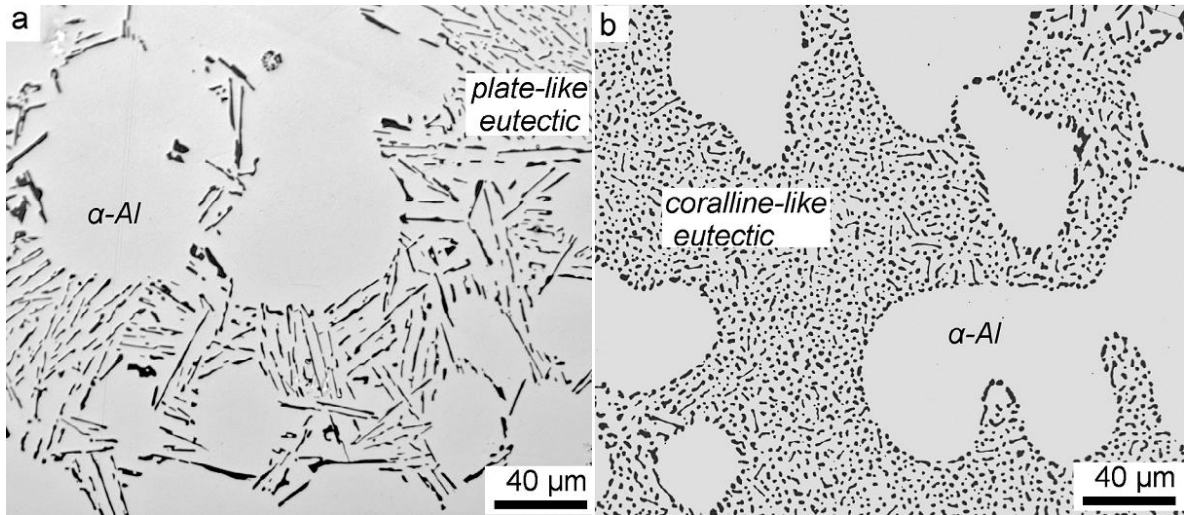


Figure 2-4 Optical micrographs of : (a) unmodified AlSi7 alloy showing plate-like Si eutectic structure and (b) modified AlSi7 + 150ppm Sr with coralline-like Si structure. (Barrirero et al., 2013)

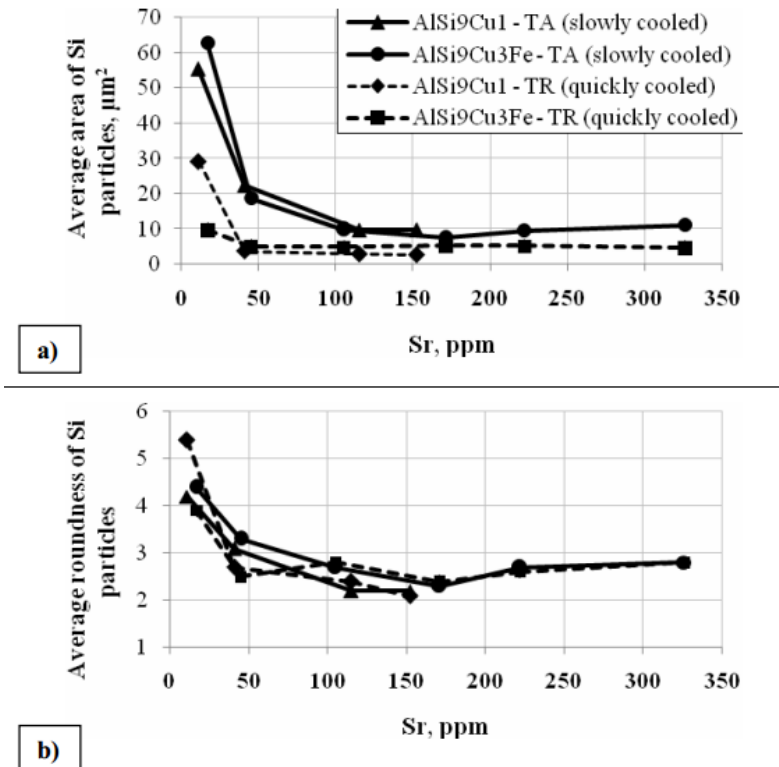


Figure 2-5 Effects of Sr on the parameters of the eutectic Si particles (Kosa et al., 2012)

### 2.2.2.3 Iron intermetallic phases

Due to the use of secondary (recycled) Al-Si alloys and of steel equipment used in the casting processes, Fe can be found as an impurity up to 0.6% in A319 alloy and up to 0.3% in A356 alloy. Therefore, Fe-containing phases are commonly found such as  $\beta(\text{AlFeSi})$ ,  $\text{Al}_9\text{FeNi}$ ,  $\pi(\text{Al}_8\text{FeMg}_3\text{Si}_6)$  and  $\alpha(\text{AlFeMnSi})$  phases (Moffat, 2007). The iron intermetallic phases observed in this study are  $\alpha(\text{AlFeMnSi})$  and  $\beta(\text{AlFeSi})$ .

## Chapter 2 Literature review

### ✓ Morphology of intermetallics phases

$\alpha$  phase has a central polyhedral particle and an external highly convoluted three-dimensional structure (Dinnis et al., 2005). Thus it is often called "Chinese script" or script phase (Tabibian et al., 2010).  $\beta$  phase has a detrimental plate-like morphology (Tabibian et al., 2010), and is considered more harmful than  $\alpha$  phase (Belmares-Perales et al., 2008). By using synchrotron tomography, the solidification process of two independently nucleated  $\beta$  plates in an AlSiFeCu alloy is shown in 3D in Figure 2-6 (Terzi et al., 2010). Herein, the cooling rate was controlled at 1.4 °C/min. These  $\beta$  plates may present a complex branching morphology in 3D. A three-stage mechanism for their formation, i.e. lateral growth, attachment and diffusion-limited growth, final step growth, was proposed in (Wang et al., 2009).

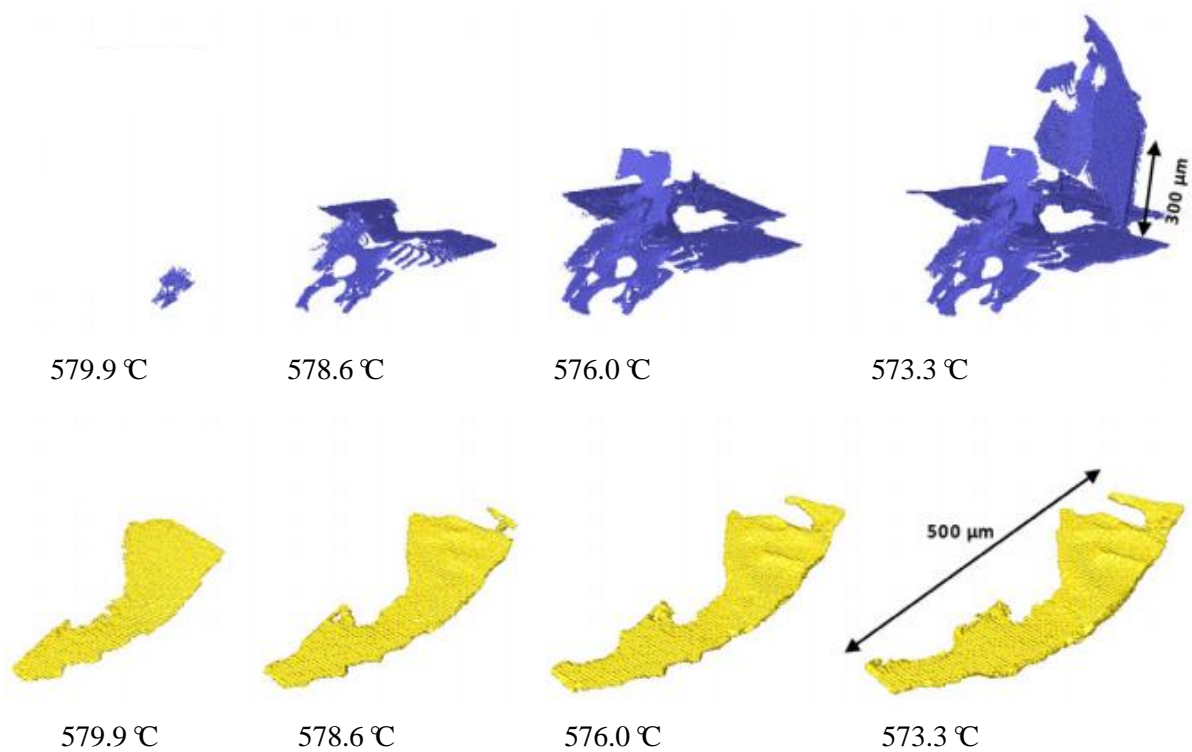


Figure 2-6 A series of reconstructed images from independently nucleated complex  $\beta$  plates, taken at several time steps during their growth by using synchrotron tomography (Terzi et al., 2010).

The cooling rate, casting temperature, iron content and alloying additives control the content and morphology of intermetallics.

The morphology and size of  $\alpha$  phase depend on the **cooling rate**.  $\alpha$  phase solidifies in a fine compact morphology if the cooling rate is high and forms a compact and star-like Chinese script morphology if the cooling rate is low (Ji et al., 2013). Besides, when the **casting temperature** is increased, the  $\alpha$  content increases while the  $\beta$  content decreases (Albonetti, 2000).

## Chapter 2 Literature review

Increasing the **iron content** increases the amount of  $\beta$  phase and results in the precipitation of coarse binary  $\beta$  platelets (see Figure 2-7) at a higher temperature by changing the precipitation sequence of the  $\beta$  phase (Lu and Dahle, 2005). The influence of **alloying additives**, such as strontium (Sr), manganese (Mg), silicon (Si) and copper (Cu), is also reported in the literature:

- ◆ Addition of **Sr** restrains the formation of the coarse binary  $\beta$  platelets (Lu and Dahle, 2005) and refines the morphology of  $\alpha$  phase (see Figure 2-8) (E. M. Elgallad, 2010).
- ◆ **Mn** also refines the morphology of  $\alpha$  phase and increases the ratio between  $\alpha$  phase and  $\beta$  phase, but it also increases the total amount of iron intermetallics (Lu and Dahle, 2005). Besides excess Mn results in hard inclusions and difficulties in machining due to the formation of  $\alpha$  phase although the ductility is improved (Taylor, 2004) (Rana et al., 2012). The commonly used Mn:Fe ratio in the so called 'iron neutralization' process is at least 0.5; however, this treatment does not always work effectively (Taylor, 2004).
- ◆ The coarse binary  $\beta$  platelets could be suppressed by **Si** and **Cu** (Figure 2-9) (Salvo et al., 2012) while the total amount of intermetallics is not increased (Lu and Dahle, 2005).

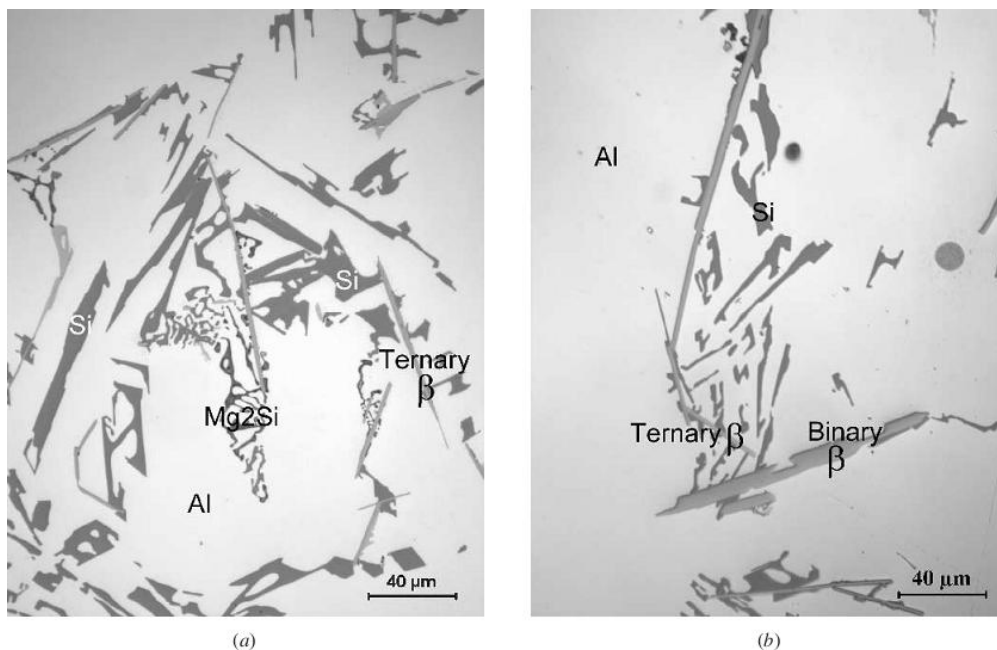


Figure 2-7 Microstructures of Al-Si alloys with (a) 0.3 wt% and (b) 0.7 wt% Fe, respectively (Lu and Dahle, 2005).



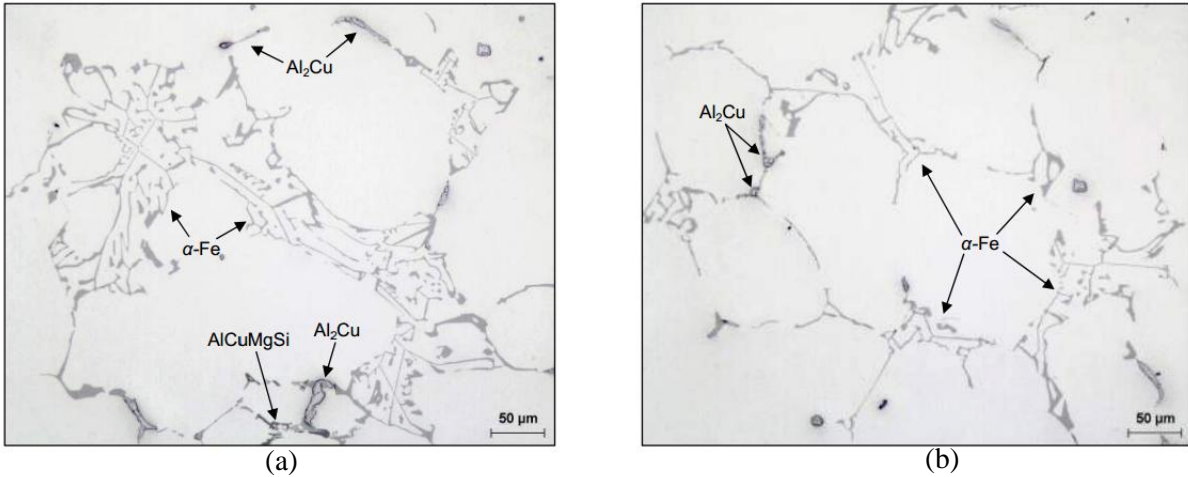


Figure 2-8 Micrographs obtained from : (a) an unmodified base Al alloy; and (b) a Sr-modified Al alloy in as cast condition (E. M. Elgallad, 2010)

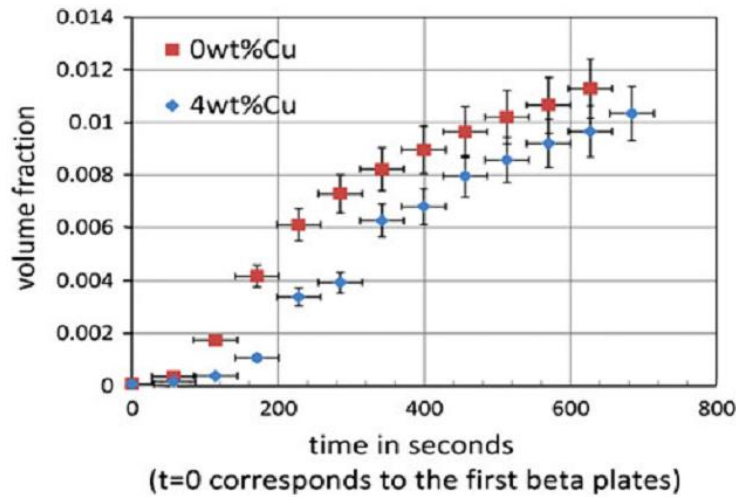


Figure 2-9 Volume fraction of  $\beta$  platelets as a function of solidification time (Salvo et al., 2012).

### ✓ Influence of Fe intermetallics on porosity

The Fe-rich intermetallics affect the formation of porosity because iron forms large flakes that provide good ‘nucleation sites’ for pores due to its restriction of the flow of the cast (Chirita, 2011). A pore was indeed observed to grow preferentially along the solid surfaces of the  $\beta$  plates using synchrotron tomography, as shown in Figure 2-10 (Puncreobutr et al., 2014). Dinnis et al (Dinnis et al., 2006) reported that increasing the iron content increases porosity in all alloys except in the copper-containing Al–5% Si alloy, which displays a minimum porosity at a critical iron content. Besides, Taylor et al (Taylor, 2004) claimed that “ iron levels above the critical level for the silicon content of the alloy should be avoided as this can cause serious loss of ductility in the final cast product and decrease casting productivity through increased rejects due to shrinkage porosity ”. They also proposed a formula to calculate the critical iron content (in wt.%) for a given alloy:  $Fe_{crit} \approx 0.08 \times [\%Si] - 0.05$ .

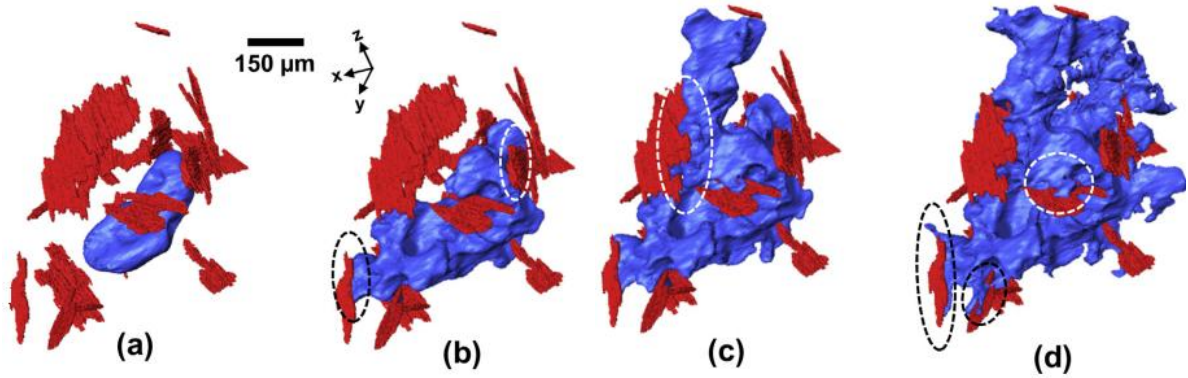


Figure 2-10 3-D rendering of pore evolution (blue) in the presence of intermetallics (red) in an A319 alloy at: (a) 565 °C, (b) 561 °C, (c) 555 °C and (d) 550 °C. Examples of pore growth along the solid surface of intermetallics are shown in dashed black and white circles (Puncreobutr et al., 2014).

### 2.2.2.4 Copper containing phases

The addition of Cu to Al-Si alloys could improve their mechanical properties due to precipitation hardening. The hardness of an Al-Si alloy increases from HB 55 to HB 118 with an increase of Cu content from 3% to 5% (Zeren et al., 2011). Several Cu containing phases have been observed in Al-Si alloys, such as AlCuMgSi, AlCuSiCe (Wu et al., 2009), AlMnFeCuSi (Tanem et al., 2005), and Al<sub>2</sub>Cu (Tabibian, 2011). The Cu containing phases in this study are Al<sub>2</sub>Cu and AlCuMgSi, and their morphologies in a new AlCuSiFe alloy are shown in Figure 2-11 for Scanning Electron Microscope (SEM) images and in Figure 2-8 for Optical Microscope (OM) image (E. M. Elgallad, 2010). The crystallization of all copper based intermetallics in aluminum alloys occurs at the end of solidification in the remaining inter dendritic liquid (Mart ínez D. et al., 2005).

Al<sub>2</sub>Cu phase forms in a limited space, confined within  $\alpha$ (Al) solid solution, plates of eutectic Si phase and plates of intermetallic phase: it is coarser in Ce-containing alloys (See Figure 2-12). They solidify in two forms: the block-like Al<sub>2</sub>Cu and the finer eutectic-like Al+Al<sub>2</sub>Cu (Sj lander and Seifeddine, 2010) (Dobrzański et al., 2007). Besides, the addition of Ce to Al-Si-Cu alloy increases the formation temperature of Al<sub>2</sub>Cu, while the solidification sequence is apparently unaffected (Voncina et al., 2014). In addition, the Al<sub>2</sub>Cu phase is segregated away from the Al-Si eutectic regions by the addition of Sr and its dissolution during solution heat treatment is retarded. Addition of Fe can accelerate the copper phase dissolution as the  $\beta$  phase platelets “act as preferred precipitation sites for the copper phase and hence lessen the degree of segregation” (Li et al., 2003).

The quaternary eutectic AlCuMgSi phase with low melting point of 507 °C forms “when Cu content is more than 2% and its amount increases with increasing Cu content” (Zeren et al., 2011).

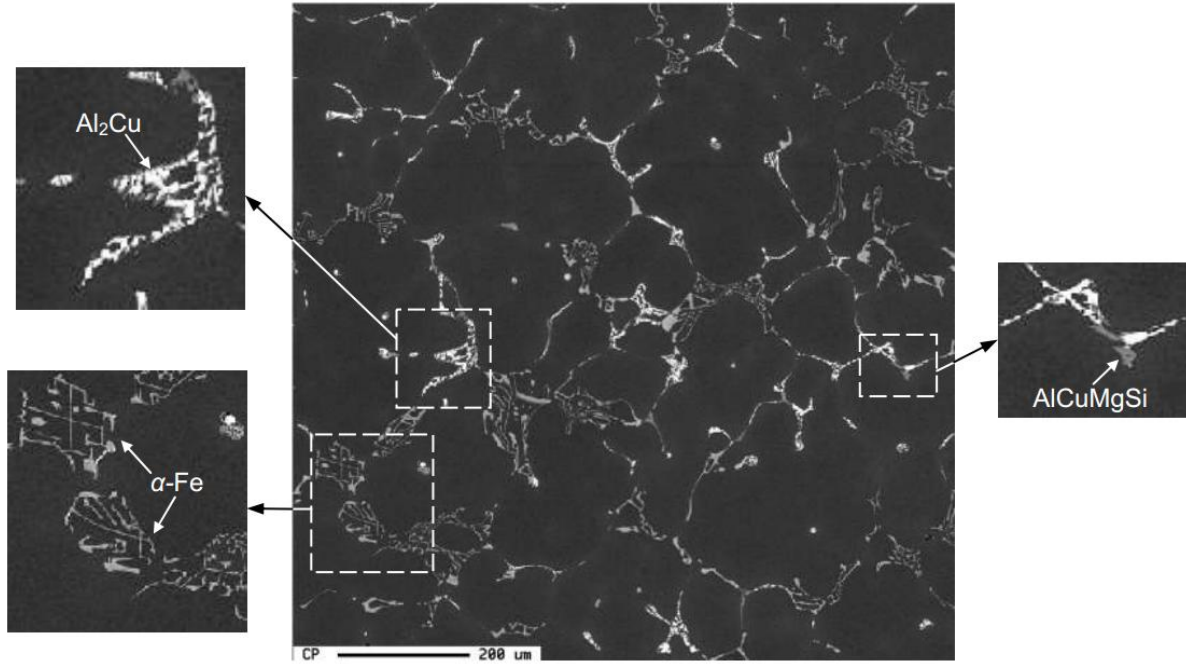


Figure 2-11 Backscattered electron image of an as-cast AlCuSiFe based alloy (E. M. Elgallad, 2010)

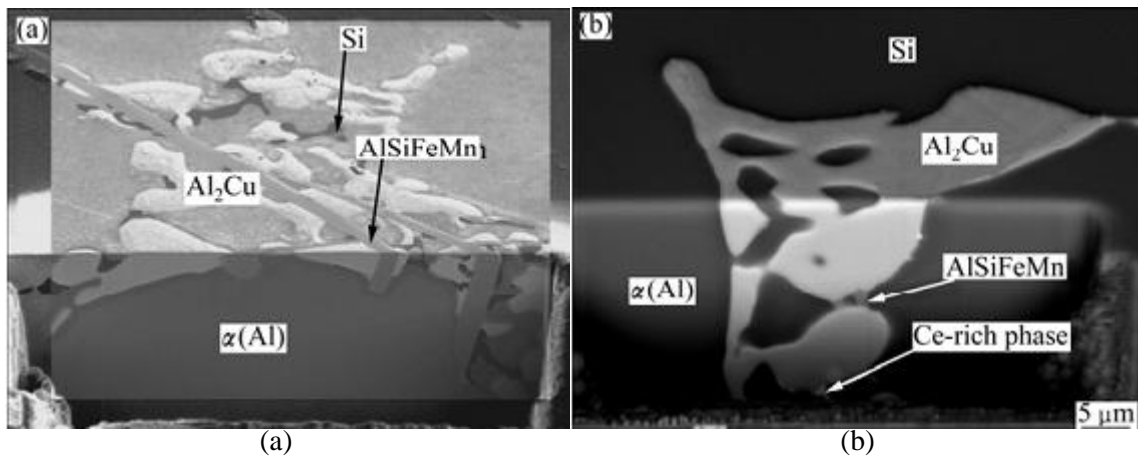


Figure 2-12 Focussed Ion Beam cross-section of an Al-Si-Cu alloy (a) without Ce and (b) with 0.02% Ce (Voncina et al., 2014)

### 2.2.2.5 Other phases

Other elements may be added in Al-Si alloys for the purpose of: (1) grain refining; (2) improving mechanical properties by precipitation of a new phase.

#### ✓ Grain refining

Some elements are usually added for the purpose of grain refinement, which is used to obtain grain boundary strengthening. The most classical refinement, which was used in this thesis at a Ti content of about 0.12%, is performed by adding titanium (Ti) and boron (B) from an Al-Ti-B master alloy.

## Chapter 2 Literature review

The formation of nano-sized particles of  $\text{TiB}_2$  particles (Emamy et al., 2006) (El-Labban, 2013) provides heterogeneous sites for nucleation during solidification and thus it promotes the nucleation of fine grains from  $\alpha$ -Al matrix.

The addition of vanadium (V) enhances grain refining at content above 1% due to the presence of VAl particles (Edwards, 2002). Phosphorus (P) may also be added and forms AlP phase which “acts as a nucleation site for primary ‘blocky’ Si particles inhibiting the formation of large Si plates and thus has an indirect effect on the material properties, by altering the principal microstructural features” (Chirita, 2011).

### ✓ Improving mechanical properties

Mg is often added to Al-Si alloys to improve their mechanical properties. The  $\text{Mg}_2\text{Si}$  phase often present in some commercial alloys, such as A356, has a small black script morphology in SEM observations and develops in the final stages of solidification (Tabibian et al., 2010). The complex shape of  $\text{Mg}_2\text{Si}$  phase was better revealed using synchrotron tomography (Tolnai et al., 2009); 3D reconstruction (Figure 2-13(a)) demonstrates the coral like connectivity of these particles. Besides, the small particles of eutectic Si around the  $\text{Mg}_2\text{Si}$  phase are also revealed (Figure 2-13 (b)).

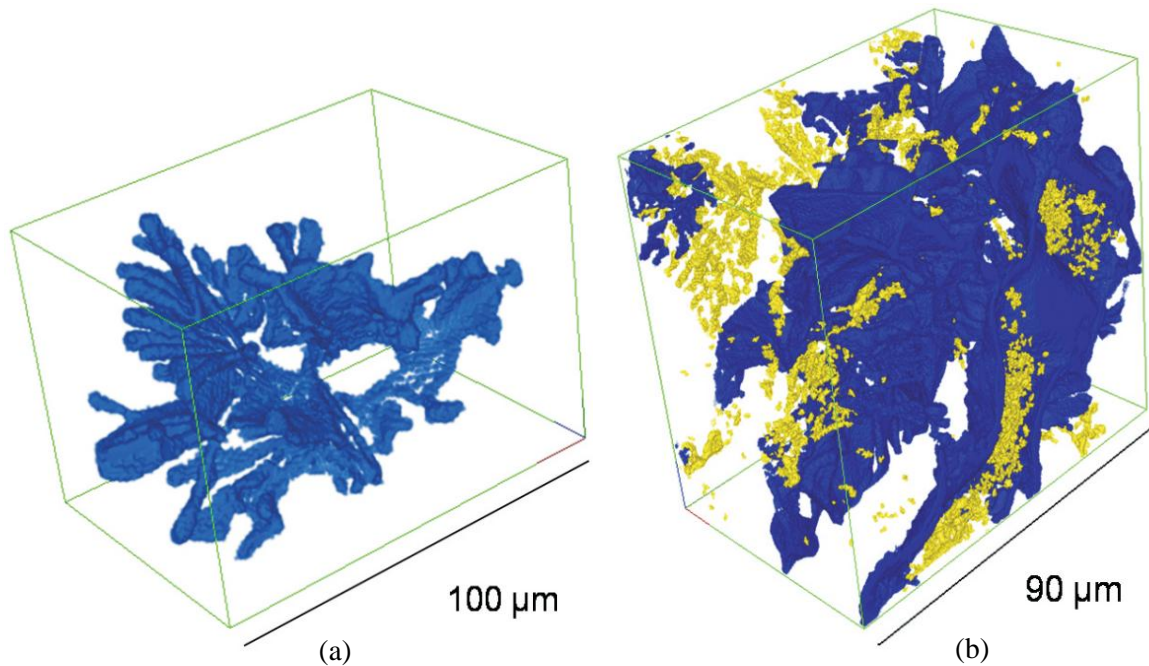


Figure 2-13 (a) Segmented  $\text{Mg}_2\text{Si}$  coral and (b) segmentation of the phase contrast images of  $\text{Mg}_2\text{Si}$  (blue) and the small particles of eutectic Si (including some small  $\text{Mg}_2\text{Si}$  particles) (yellow) from tomography images (Tolnai et al., 2009).

The addition of Ni to Al-Si alloys could increase their high temperature strength. AlNi phase is the binary phase from the Al-Ni system and forms in the case of a high content of Ni. For lower Ni contents ternary phases may form, such as AlCuNi and AlFeNi phases (Edwards, 2002). By using



## Chapter 2 Literature review

tomography, AlSiNi phase is found to present “networks of connected Si lamellae as well as complex 3D shapes of Ni-containing aluminides” in as-cast condition (Asghar et al., 2009).

### 2.2.2.6 Casting defects

Because liquid aluminum is prone to hydrogen adsorption and oxidation, pores are the most common casting defects in Al-Si alloy (Wang, 2013) and they often bring serious harm to the mechanical properties. Their formation may be due to “entrapped air during mold filling, centerline shrinkage that occurs during the final solidification, blowholes from unvented cores, reactions at the mold wall, dissolved gases from melting and dross or slag containing gas porosity” (Monroe, 2005). The various porosity morphologies are shown in Figure 2-14. Generally, pores are divided into two main types : (1) gas porosity resulting from entrapped gases look like smooth bubbles, (2) shrinkage porosity forming during the cooling stage look like rough bubbles (Sobolev and Guilemany, 1996) (Lee and Gokhale, 2006) (Nicoletto et al., 2012). If the casting is not properly fed, shrinkage porosity will form. Compared to gas pores, which are typically spherical, shrinkage pores have an irregular 3D shape, which induces stress concentration, so they will be deleterious to fatigue properties (Wang, 2013).



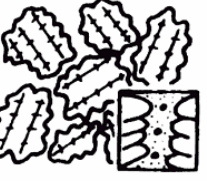
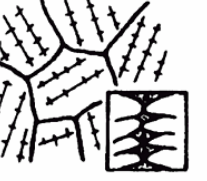



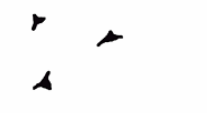
	1) round pores	2) long, broad pores	3) long, fissured pores	4) small, fissured pores
<b>Solidification process and bubble formation</b>	 Bubble formation in liquids			
<b>Pore morphology in the structure</b>				
<b>Characterization</b>	<ul style="list-style-type: none"> <li>- precipitation in the liquid melt or in the beginning of solidification</li> <li>- unrestricted bubble growth</li> <li>- high H<sub>2</sub> concentration required</li> </ul>	<ul style="list-style-type: none"> <li>- bubble formation with still high liquid fraction</li> <li>- arrangement between growing bubbles and dendrites</li> <li>- high to medium H<sub>2</sub> concentration</li> </ul>	<ul style="list-style-type: none"> <li>- bubble formation during formation of the dendrite network</li> <li>- bubble expansion limited by still open melt channels</li> <li>- medium to low H<sub>2</sub> concentration</li> </ul>	<ul style="list-style-type: none"> <li>- precipitation shortly before the end of solidification</li> <li>- shape and size of pores determined by closed interdendritic spaces</li> <li>- low H<sub>2</sub> concentration</li> </ul>

Figure 2-14 Four types of pores in aluminum castings (Monroe, 2005).

The formation of porosity depends on the solidification rate: pores increase in size and decrease in amount with a decrease in solidification rate (Nguyen, 2005) (Lee and Hunt, 1997). It could also be influenced by the content of Si (Zhao et al., 2011). At a high Si content (13%), spherical pores formed

## Chapter 2 Literature review

in the liquid keep their spherical morphology when they encounter the eutectic Solid/Liquid (S/L) interface during their growths. At a medium Si content (7%), pores begin to grow into irregular morphology in the confined inter-dendritic regions and become more irregular when they encounter the eutectic S/L interface. In addition, as previously mentioned, the iron intermetallic phases have an influence on the formation of porosity.

Oxide films, such as  $MgAl_2O_4$ ,  $Al_2O_3$ ,  $MgO$ ,  $SiO_2$ ,  $CaO$ , are also common casting defects in Al-Si alloys. They impact not only on mechanical properties but also on machinability, porosity and corrosion resistance (Bangyikhan, 2005). An oxide film can easily form on the surface of liquid metal when it is exposed to atmosphere as aluminum is a very reactive metal. After melting, it may be entrapped in the melt (Shih and Chen, 2005). Different morphologies are observed depending on the chemical composition, thickness, strength and interaction of oxide films with the melt (Bangyikhan, 2005). However, the oxide films are not the focus of our research as they were not observed in the studied material.

### 2.2.3 Lost foam casting

Some automotive parts such as engine bracket, torque rod, intake pipes, cylinder heads, knuckles, brake calipers, are commonly casted using gravity die casting, which is a traditional casting process in the automotive industry (Saint Jean Industries, 2013). Molten aluminum alloy is poured into a metallic mold in gravity die casting (Figure 2-15) (Niane and Michalet, 2011). The parts so produced have good surface finish, good dimensional accuracy and high mechanical properties owing to the use of a permanent mold, high quality casting tools and a high cooling rate (Mandal, 2008) (Saint Jean Industries, 2013). Very complex components can be casted thanks to the use of sand cores. However, the sand cores should be remade in each mold, and this casting method is expensive.

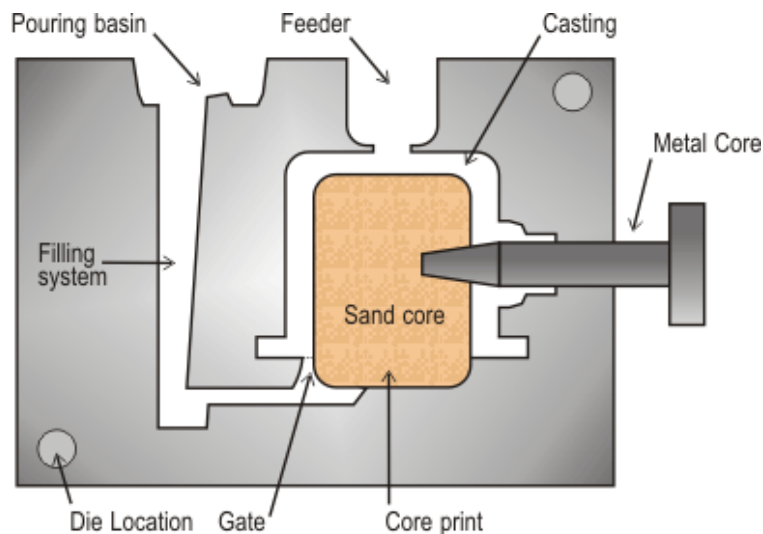


Figure 2-15 Illustration of gravity die casting (Niane and Michalet, 2011)

## Chapter 2 Literature review

Recently this traditional casting process is being replaced by the Lost Foam Casting (LFC) process in order to reduce the cost (by about 15% to 30%) and the weight (by about 1kg per cylinder head) (Niane and Michalet, 2011) (Limodin et al., 2014). The concept of LFC process was introduced by H. F. Shroyer in the United States and was patented in April 15, 1958. This process is also referred as the Evaporative Pattern Casting (EPC) because of the use of expendable polystyrene (EPS) patterns (Geffroy et al., 2006)(Albonetti, 2000). The main steps of the LFC process in automotive industry are summarized in Figure 2-16 (American Foundry Society, 2004):

- 1) Pattern Molding: Bead pre-expansion and conditioning, tool preheat, pattern molding, pattern aging;
- 2) Pattern/cluster assembly;
- 3) Pattern coating and drying;
- 4) Sand fill and compaction;
- 5) Metal casting and cooling;
- 6) Shakeout, clean-up, and finishing.

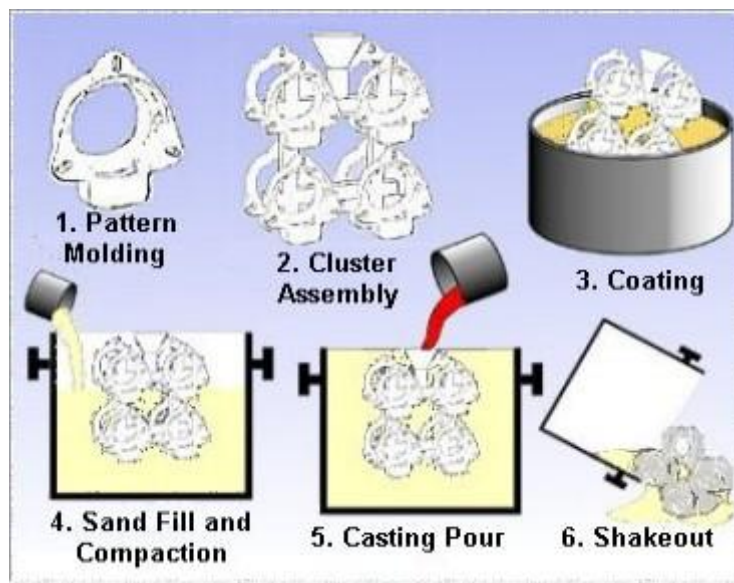


Figure 2-16 The basic steps of the LFC process (American Foundry Society, 2004)

The main benefits brought by this process are the reduction of cost as the pattern does not require to be removed, casting capacity of complex components particularly internal sections, the subsequent decrease in operating costs, etc. (Albonetti, 2000). Thus, the LFC process is nowadays successfully used for metal casting, such as for steel, ductile iron, aluminum, and gray cast iron, in industrial applications such as the automotive cylinder heads (Geffroy et al., 2006).

However, the LFC process has a lower cooling rate, around  $0.8^{\circ}\text{C/s}$ , than the die casting process, around  $30^{\circ}\text{C/s}$ , and this much slower cooling rate has an influence on the microstructure of cast alloy (Tabibian et al., 2010). SDAS is an effective parameter to reflect the coarseness of the microstructure.

## Chapter 2 Literature review

It controls mechanical properties of aluminum alloys as it could affect the size and distribution of porosity, and intermetallic constituents (Charbonnier, 1992). Figure 2-17 shows an example of SDAS measurement done by drawing a straight line perpendicular to the growth direction of the secondary dendrite arms and counting the number of intercepts of eutectic regions along the line. The SDAS value is then determined by the relationship (Charbonnier, 1992) :

$$SDAS(\mu\text{m}) = \frac{\text{Length of the intercept line (mm)}}{\text{Number of intercepts}} \times \frac{1000}{\text{Magnification}}$$

SDAS is not only influenced by the chemical composition of the investigated alloy but also by the solidification rate (González et al., 2011). In an AlSi7Cu alloy, the SDAS decreases from 82.6  $\mu\text{m}$  to 37  $\mu\text{m}$  when the cooling rate increases from 0.18  $^{\circ}\text{C s}^{-1}$  to 0.96  $^{\circ}\text{C s}^{-1}$  (see Figure 2-18) (Dobrzański et al., 2006). An empirical equation about the relation between SDAS and cooling rate in A356/357 alloys was proposed in (Wang and Cáceres, 1997):

$$SDAS = 39.4R^{-0.317}$$

where  $R=dT/dt$  represents the mean cooling rate during solidification. With an increase in solidification time, i.e. a slower cooling rate, the size (Figure 2-19) (Kaufman and Rooy, 2004) and volume fraction (Albonetti, 2000) of pores and the size of the intermetallic particles (Boileau and Allison, 2003) increase, and the size and shape of the eutectic silicon become larger and more acicular (Albonetti, 2000). Thus, the Al-Si alloys casted by the LFC process present coarser microstructure and large pore volume fraction.

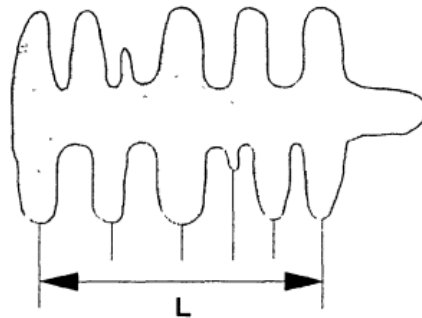


Figure 2-17 Measurement of SDAS (Charbonnier, 1992).

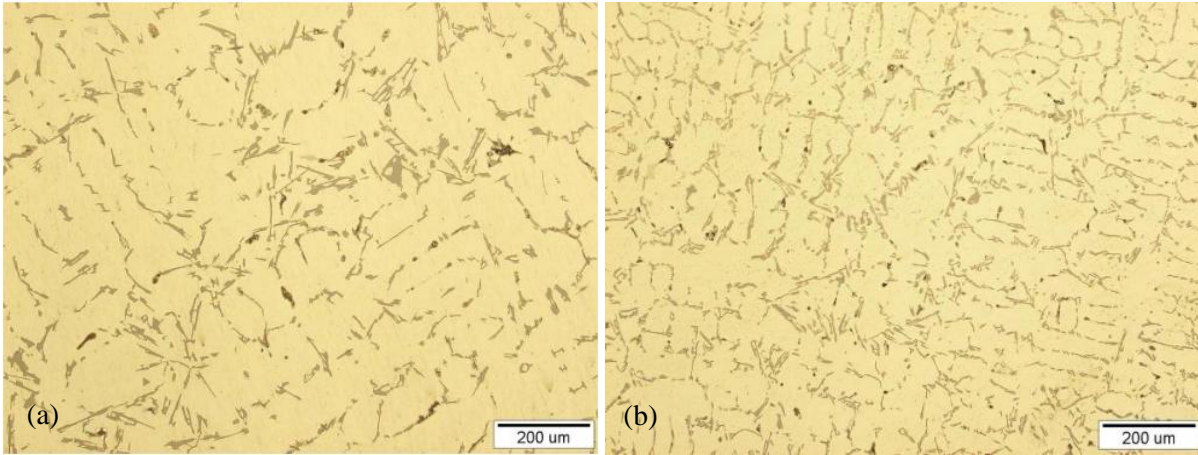


Figure 2-18 Microstructure of AlSi7Cu alloy solidified with cooling rate (a)  $0.18 \text{ }^{\circ}\text{C s}^{-1}$ , and (b)  $0.96 \text{ }^{\circ}\text{C s}^{-1}$  (Dobrzański et al., 2006).

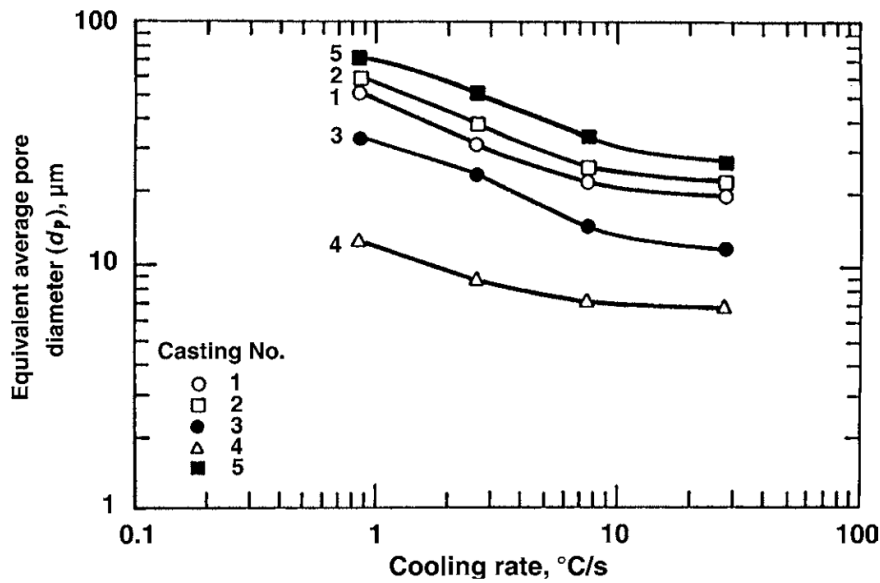


Figure 2-19 Evolution of pore size with cooling rate for different hydrogen contents in alloy A356.0. Hydrogen content (cm<sup>3</sup>/100 g): 1, 0.25 (no grain refiner); 2, 0.31 (grain refined); 3, 0.25 (grain refined); 4, 0.11 (grain refined); 5, 0.31 (grain refined and modified) (Kaufman and Rooy, 2004).

## 2.3 Micromechanisms of fatigue damage in Al-Si casting alloys

### 2.3.1 Influence of casting defects

Fatigue cracks are prone to occur at various microstructural inhomogeneities (Feng, 2013). They may form at grain boundaries, surface extrusions, or inclusions in many wrought alloys, and nucleate at casting pores, silicon inclusions, or oxide inclusions in as-cast materials (Gall et al., 2001). Thus, the fatigue properties of casting alloys largely depend on the sizes of microstructural defects, in particular pores and oxide films. By contrast, the effects of grain size, second-phase particles, and nonmetallic inclusions are less significant (Wang et al., 2006). Therefore the casting defects, which introduce

## Chapter 2 Literature review

---

stress concentrations, play an important role in the fatigue behavior of Al-Si alloys. Defects decrease fatigue life by shortening both the crack initiation and propagation periods (Wang et al., 2001a). The total fatigue life of cast aluminum samples, failing from defects such as porosity and oxide films, is mostly spent in crack propagation. The number of cycles to initiate a fatigue crack from a defect can even be neglected (Wang et al., 2001a).

### 2.3.1.1 Pores

Much research focuses on the influence of pores on fatigue behavior in High Cycle Fatigue (HCF) in the past years. Pores are reported to be highly detrimental to the fatigue behavior of Al-Si alloys (Coty et al., 2011) (Nicoletto et al., 2010) (Boileau and Allison, 2003). A comparison between a porosity-containing (non-HIP: hot isotactic pressing) and pore-free (HIP) alloy in (Boileau and Allison, 2003) shows that the absence of porosity increases the fatigue resistance and strength. The presence of pores dramatically reduces the fatigue damage limit by about 40% in (Gao et al., 2004).

Pores often provide the main **crack initiation site** in HCF (Ammar et al., 2008a). In particular, shrinkage pores, which provide very irregular initial near surface flaws, play a major role in the fatigue behavior of lost foam cast Al-Si alloys (Lee et al., 1992). The nucleation and propagation of fatigue cracks are dominated by the highest local stress-strain concentration caused by the presence of pores adjacent to the free surface and the crack tip, respectively (Li et al., 2009). Using a finite element modelling method (Borbély et al., 2002), the strain localization in the immediate vicinity of a cavity lying just beneath the surface is proved to be severe enough to cause the initiation of subsurface fatigue cracks under cyclic stress. These fatigue cracks can initiate at the pore or at the adjacent outer surface. Although, nearly all surface pores give rise to a crack in (Buffière et al., 2001), most of those cracks remain stopped near the pores.

Pores **shorten the fatigue crack propagation** (Wang et al., 2001a). Once initiated, a fatigue crack steadily surrounds the initiating pore, starting from the intersection between the pore and the specimen surface towards the interior of the sample (Buffière, 2004). With a higher initial porosity level, pore growth and coalescence mechanism become more dominant than void nucleation from the second phase material, although both interact together in the damage process (Horstemeyer et al., 2003).

The location, size, quantity and shape of porosity in casting alloys are considered to be the factors that affect the fatigue behavior of Al-Si alloy in many research works.

**Location :** Pores at the surface (Ammar et al., 2008b) or near the specimen surface (Gao et al., 2004) are reported as the most dangerous defects. They have the greatest propensity for acting as a crack initiation site and for decreasing the fatigue life as they create regions of high stress concentrations.



## Chapter 2 Literature review

---

**Size :** Large pores at or close to the specimen surface were responsible for crack initiation in all fatigue test specimens in (Yi et al., 2003), and the resultant fatigue life could be related to the initiating pore size through a relationship based on the propagation rate of small fatigue cracks. Fatigue life is also observed to decrease as the size of the surface pore increases in (Ammar et al., 2008a) and (Wang et al., 2001a). The study in (Dietrich and Radziejewska, 2011) showed that dispersed small pores do not influence the fatigue behavior. There exists a critical pore size for fatigue crack initiation, below which the fatigue crack initiates from other intrinsic initiators such as eutectic particles and slip bands (Wang et al., 2001a). In Sr modified cast A356 alloy, this critical defect size is 25  $\mu\text{m}$ . The critical defect size that does not lower the fatigue strength is found to be close to the grain size of the material in (Mu et al., 2014), i.e. larger than  $300 \pm 100 \mu\text{m}$ , which is close to the grain size (259–573  $\mu\text{m}$ ), and higher than the SDAS (38  $\mu\text{m}$ ). However, the relation between the grain size and the critical defect size is not clear yet. According to (Zhang et al., 2007), crack initiation from pores may not be the important mechanism affecting fatigue behavior if the pore sizes are below the critical value (around 25  $\mu\text{m}$  for their studied material) for crack initiation. Correspondingly, crack initiation and short crack propagation may play important roles in the overall fatigue life, especially when the applied stress amplitude is low.

**Quantity:** As a large number of pores reduce the effective bearing area of material, the quantity of pores has an influence on the fatigue behavior. According to (Buffière et al., 2001), the porosity level is a first order parameter which greatly alters both the average number of cycles to failure and the lifetime scatter, especially at high stress level.

**Shape:** Shape of porosity could also influence the fatigue behavior as a sharp shape is more prone to stress concentration. However, according to (Gall et al., 2001), shape has a negligible effect on fatigue crack initiation compared to other significant factors such as size.

Fewer studies were focused on the influence of pores on fatigue behavior in LCF compared with that in HCF. Nevertheless, pores were also determined as the most probable crack initiation sites in LCF (Firouzdor et al., 2007). An increase of porosity content can cause degradation in thermal-fatigue resistance of cast aluminum alloys in LCF (Arami et al., 2008). A very fine porosity remaining after the alloy processing is claimed to have no influence on fatigue crack nucleation and growth in LCF in (Stolarz et al., 2001).

### 2.3.1.2 Oxide films

Oxide films is another important casting defect in Al-Si alloys as previously mentioned in 2.2.2 section, although they are often less detrimental to fatigue life than pores (Wang et al., 2006) (Song et al., 2011).

## Chapter 2 Literature review

---

According to (Cao and Campbell, 2003), the mechanical properties and reliability of cast aluminum alloys are mainly limited by the large and uncontrolled number of double oxide films, which act as cracks in the liquid metal and the castings. Location and size of oxide films are considered as the most influential parameter for fatigue behavior (Yi et al., 2006) (Wang et al., 2006). An oxide film present at or close to the specimen surface is more likely to act as a favorable crack initiation site. With an increase of oxide films size, the fatigue life decreases. However, in the same way as for porosity, there exists a critical defect size for fatigue crack initiation, below which the crack initiates from other intrinsic initiators. In a Sr modified A356 alloy, this critical size is 50  $\mu\text{m}$ , which is twice the critical size for pores in the same material (Wang et al., 2001a). This may explain why oxide films are less detrimental to fatigue life than pores. In addition, HIP process, which can reduce the porosity, has little effect on oxide films (Boileau and Allison, 2003). As previously mentioned, oxide films are not the key defects in the LFC Al-Si alloy of this study so that their influence could be ignored.

### 2.3.2 Influence of microstructural constituents/features

Besides the casting defects, microstructural constituents and features of alloys, such as hard inclusions, SDAS, grain boundaries, may also have an influence on the fatigue life. They are originally responsible for fatigue crack propagation once cracks have initiated from casting defects (Ammar et al., 2008a). However, in the absence of large defects, hard inclusions and slip bands, are possible initiation sites (Yi et al., 2006). More studies have focused on their influence on fatigue behavior in HCF than in LCF. Therefore, if not specified, the research works presented in the following subsection are in the HCF range.

#### 2.3.2.1 Hard inclusions

Various hard inclusions may affect the fatigue properties of Al-Si alloy (Moffat, 2007) (Wang et al., 2001b) (Firouzdor et al., 2007). Si particles, iron intermetallics, copper containing phases and magnesium containing phases are the most important hard inclusions in the material of this thesis. Their influences are presented separately in the following.

##### ✓ Eutectic silicon particles

When shrinkage porosity is controlled or when the maximum internal defect (oxide or pore) size is small (less than 100  $\mu\text{m}$ ), the relevant microstructural initiation sites are often the large Si particles within eutectic regions as a result of high local stress-concentrations (Gall et al., 2000b) (Stolarz et al., 2001) (McDowell et al., 2003) (Ma et al., 2014) (Zeng et al., 2014). Whether the cracks initiated from casting defects or hard inclusions, including Si particles, or elsewhere, the Si phase is often found to have an influence on cracks propagation (Boileau and Allison, 2003) (Chan et al., 2003) and on the



## Chapter 2 Literature review

crack path (Zhang et al., 2007). According to (Zeng et al., 2014), Si phase may act as a barrier for cracks propagation due to its higher strength and hardness.

The size and aspect ratio of silicon particles have a significant influence on mechanical properties (Saigal and Fuller Jr., 2001) (Fan et al., 2001). Silicon particles with large aspect ratios are most prone to cracking. As a result, Sr-modified alloys with small and round silicon particles have longer fatigue lives than unmodified alloys (Wang et al., 2001b). Increasing size of Si-particles, and/or decreasing the free space between them, result in high stress/strain concentrations reducing the fatigue resistance (Gao et al., 2004). The initiation and propagation of cracks at Si particles can occur via debonding or fracture depending on the size, shape and orientation of these particles, on the loading conditions and on the strength of Al matrix-particle interface (Mbuya, 2011). For example, Si particles are claimed to be prone to fracture in (Verdu et al., 1996). The fracture and debonding of silicon particles are reported (Gall et al., 2000b) to only depend on their shape and alignment when all of the silicon particles are intact before any loading is applied.

Figure 2-20 shows an example of the interaction of a fatigue crack with Si particles in an Al-Si alloy (Chan et al., 2003): two fatigue cracks originating from grain boundaries deflect to propagate around particles by debonding or fracture. Then they linked up when both grew across the matrix ligament.

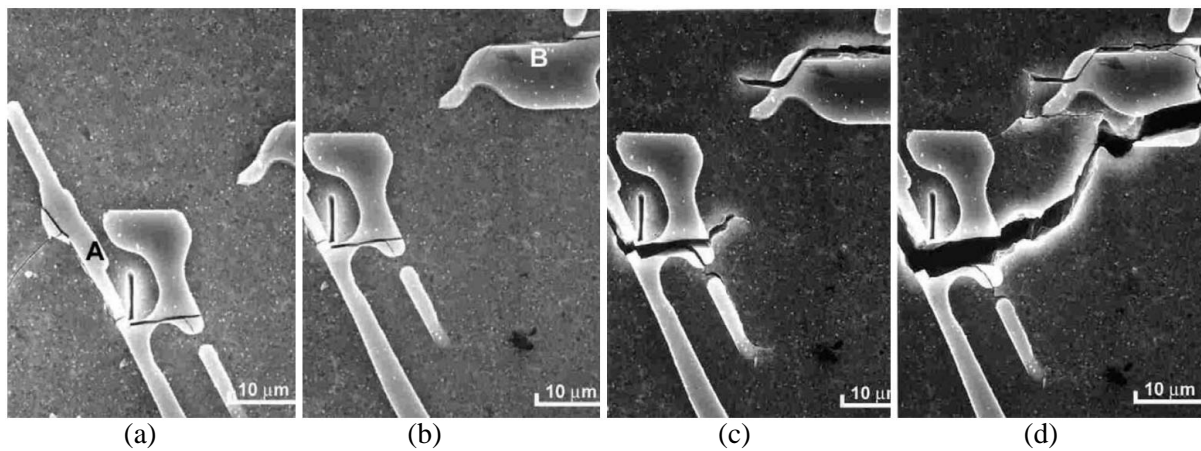


Figure 2-20 Interaction of a fatigue crack with Si particles: (a) at  $\Delta K=6 \text{ MPa}\sqrt{\text{m}}$ , a fatigue crack along a grain boundary (left) ran into a Si particle (A) and deflected to follow the interface, causing the particle A to fracture; (b) interface and particle fracture at Si particle (B) located ahead of the crack tip; (c) linkage of the main crack with particle cracks at  $\Delta K=8 \text{ MPa}\sqrt{\text{m}}$ ; and (d) crack coalescence by fatigue crack growth through the matrix ligament at  $\Delta K=10 \text{ MPa}\sqrt{\text{m}}$ . The loading axis is vertical (Chan et al., 2003).

In the LCF range, Si particles are also possible initiation sites in the absence of large casting defects, and the cracks propagate across Al layers that separate neighboring Si particles and form structural barriers (Stolarz et al., 2001). The propagation of a fatigue crack can also be resisted by Si particles (Zeng et al., 2014). Si modification by addition of Sr can capably enhance thermal fatigue life in LCF, especially thermal-shock fatigue (Firouzidor et al., 2007).

## Chapter 2 Literature review

### ✓ Iron intermetallics

The presence of Fe-intermetallic plates in eutectic region increases local stress level and localizes plastic strain, and thus results in the fatigue damage limit being reduced by 20% (Gao et al., 2004). Microcracks are found at iron intermetallics both in HCF (Yi et al., 2004) and LCF (Tabibian et al., 2010). Iron intermetallics can have an important influence on crack propagation in interaction with Si particles (Boileau and Allison, 2003) (Ammar et al., 2008a). However, in the absence of large casting defects, iron intermetallics can also provide possible cracks initiation sites both in HCF (Song et al., 2011) (Ma et al., 2014) and in LCF (Stolarz et al., 2001) (Firouzdor et al., 2007).  $\alpha$  and  $\beta$ , which are the most common iron intermetallics phases, are the two types of iron intermetallics present in the studied material. Figure 2-21 shows one example of these two phases in a fracture surface. Usually, when they are both present,  $\beta$  phase is considered to be more harmful than  $\alpha$  phase due to its sharper morphology (Belmares-Perales et al., 2008).

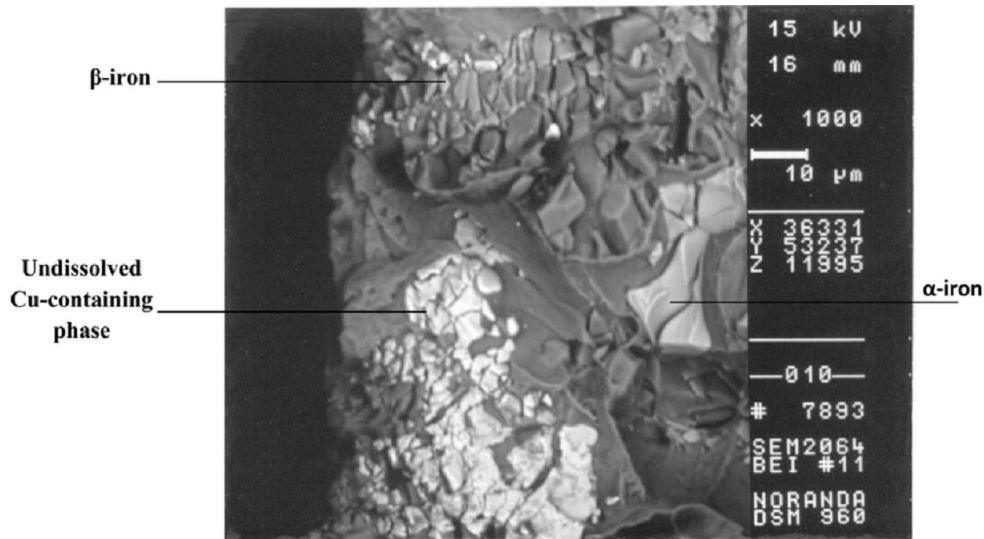


Figure 2-21 SEM micrograph showing fracture of both iron and copper intermetallics in an Al-Si alloy with 0.8%Fe (Ma et al., 2014).

In the absence of other defects, fatigue **crack initiation** in both Low-Fe and High-Fe Al-Si alloys appears dominated by the local plastic deformation accumulation within the micro-cells (a micro-cell consisting of an  $\alpha$ -Al secondary dendrite, eutectic Si-particles and Fe-rich intermetallic particles) intersecting the specimen surface (Yi et al., 2004). Large Fe-rich intermetallic particles in High-Fe alloys promote the formation of fatigue crack, thus increasing Fe content decreases the crack initiation life (Yi et al., 2004). In addition, at high iron levels and low cooling rates (0.8% Fe, 83  $\mu$ m DAS), crack initiation is more prone to occur through the cleavage of  $\beta$ -phase platelets rather than by their decohesion from the matrix (Ma et al., 2014).

## Chapter 2 Literature review

---

Once cracks have initiated at iron intermetallics or at other hard inclusions in an unmodified alloy, they mainly propagate through the coalescence of fractured Si particles, except where  $\beta$  intermetallics are present, in which case the latter takes priority in **crack propagation**. In Sr-modified alloy, the morphology of hard inclusions is refined and most of the Al matrix is involved when cracks propagate through the linkage of fractured/debonded Si particles and fragmented  $\beta$  intermetallics (Ma et al., 2014). The direction of crack propagation depends largely on the morphology of  $\beta$  platelets (individual or branched), which can cause retardation in the small-crack growth when inclined to the crack growth path (Yi et al., 2004). Thus increasing Fe content increases the crack propagation life due to the retardation effect of large Fe intermetallics on crack propagation (Yi et al., 2004).

Several authors observed that increasing **Fe content** reduces the fatigue life in the long lifetime regime ( $>10^6$  cycles) (Yi et al., 2004), particularly for alloys with large SDAS (Wang et al., 2001b). Indeed, the fatigue damage is dominated by crack initiation stage in the long life-time regime and increasing Fe content decreases the crack initiation life. Increasing Fe content slightly increases the fatigue life in the short lifetime regime ( $<10^5$  cycles) as the small crack propagation stage, which could be increased with the increasing Fe content, dominates the total fatigue life (Yi et al., 2004). Fe content has no effect for medium fatigue life ( $>10^5$  and  $<10^6$  cycles) due to the offset between the two situations above (Yi et al., 2004).

In the presence of casting defects (Gall et al., 2000a), during the initial stages of fatigue crack growth from a defect of the order of 100  $\mu\text{m}$ , a crack was observed to propagate almost only through the Al–1% Si dendrite cells, to avoid the Al–Si eutectic and to follow the  $\alpha$  intermetallic particles only when they are in line with the crack plane. During the later stages of fatigue, the fatigue cracks are apt to propagate through damaged  $\alpha$  intermetallics and silicon particles. The final overload fracture occurs almost only through cleavage-like fracture in  $\alpha$  intermetallics and ductile tearing in the Al–Si eutectic phase. Once a crack has initiated from a casting defect (Mbuya et al., 2012), it tends to avoid Si and intermetallic particles at low  $\Delta K$  (Range of stress intensity factor) levels until a mid  $\Delta K$  of  $\sim 7 \text{ MPa}\sqrt{m}$ . At higher levels of  $\Delta K$ , the crack increasingly seeks out Si and intermetallic particles until a  $\Delta K$  of  $\sim 9 \text{ MPa}\sqrt{m}$  after which propagation through intermetallic particles in the 0.67wt.% Si alloy or Si and intermetallics in the 6.9 wt. %Si alloys becomes more favorable. The authors observed that crack interaction with intermetallics results in crack deflections that cause roughness induced crack closure and possibly oxide induced crack closure at low to mid  $\Delta K$ .

### ✓ **Copper containing phases and magnesium containing phases**

As presented in § 2.2.2, magnesium is sometimes mixed with copper and forms phases such as AlCuMgSi so that the influence of copper and magnesium containing phases on the fatigue properties is presented together here.

## Chapter 2 Literature review

In LCF, cracks propagate through these brittle phases rather than through the more ductile matrix (Tabibian, 2011) (Firouzdor et al., 2007). Figure 2-21 presents an example of cracks propagation through the fracture of  $\text{Al}_2\text{Cu}$  or other Cu-intermetallics such as  $\text{Al}_7\text{Cu}_2\text{Fe}$ , as well as through fragmented Si particles (Ma et al., 2014). The thermal-fatigue cracks passing across Cu rich and Cu–Mg rich intermetallics were observed in (Arami et al., 2008) (see Figure 2-22). Compared with the crack propagation through these phases, only a few studies reported crack initiation at these phases. In (Ma et al., 2014), at low iron levels and high cooling rates (0.4% Fe, 23  $\mu\text{m}$  DAS), cracks initiate at  $\text{Al}_2\text{Cu}$  particles in an unmodified A319 alloy.

The shape and alignment of these particles are the most dominant parameters influencing initial particle fracture and debonding (Gall et al., 2000b). However, Fan et al. (Fan et al., 2003) consider that particle aspect ratio, at least over the range of 1.0 ~ 1.65, has less influence than spacing effects or the number of particles in the cluster, especially in the HCF regime.

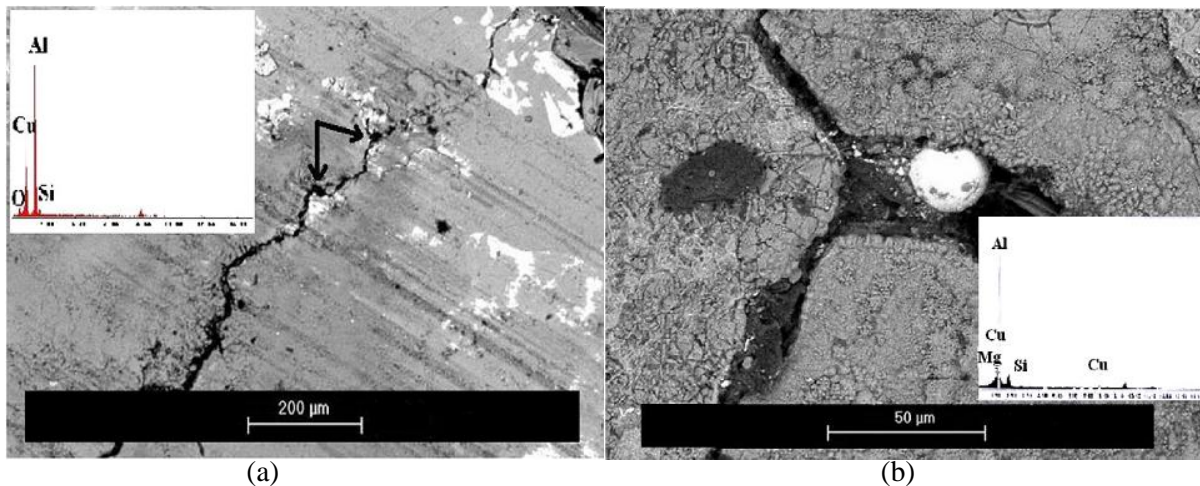


Figure 2-22 Typical SEM image and EDAX analysis from a thermal-shock crack propagated through the pores and developed by debonding and cracking of (a) large Cu rich and (b) Cu–Mg rich intermetallics in an A319 alloy (Arami et al., 2008).

### 2.3.2.2 Microstructural features

Besides hard inclusions, some microstructural features, such as SDAS, slip bands and grain boundaries, are also observed to influence the fatigue properties in the absence of large casting defects.

#### ✓ SDAS

Several authors propose to use SDAS to predict the fatigue life of A356 alloys without large pores (Wang et al., 2001b) and with large pores (Zhang et al., 2000) in HCF.

In the absence of large pores, cracks are observed to initiate at slip bands and oxide films (Wang et al., 2001b) and the fatigue life for unmodified and Sr-modified A356-T6 alloys is a function of SDAS as

## Chapter 2 Literature review

shown in Figure 2-23. In unmodified alloys, fatigue life decreases with increasing SDAS in both fine (SDAS < 40  $\mu\text{m}$ ) and coarse (SDAS > 60  $\mu\text{m}$ ) structures; while in microstructures with intermediate SDAS values (SDAS: 40-60  $\mu\text{m}$ ), the fatigue life seems constant with SDAS. In Sr-modified material having fine microstructures (SDAS < 60  $\mu\text{m}$ ), fatigue life decreases with increasing SDAS values, while in coarser microstructures (SDAS > 60  $\mu\text{m}$ ), fatigue life increases with increasing SDAS values.

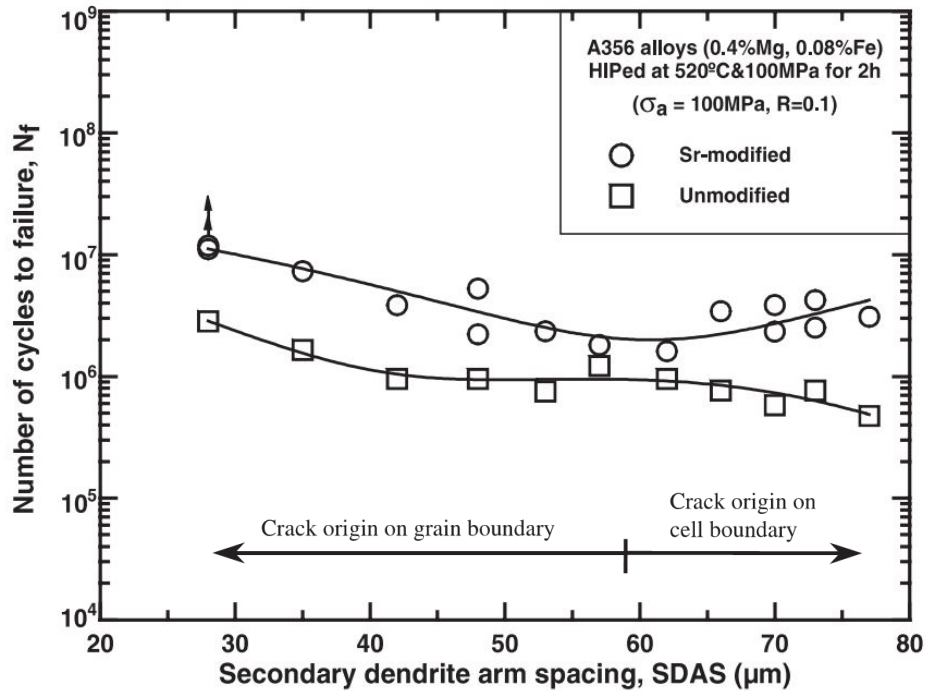


Figure 2-23 Fatigue life for unmodified and Sr-modified A356-T6 alloys as a function of SDAS (Wang et al., 2001b).

The influence of SDAS on fatigue behavior is ascribed to its influence on dispersion hardening (Hart, 1972), including the dislocation slip distance (dendrite cell size) (Hull and Bacon, 2001), and the degree of interaction between dislocation, eutectic particles, and dendrite cell/grain boundaries (Wang et al., 2001b). In coarse microstructure (large SDAS), the interaction between dislocations and cell boundaries dominates the image stress. The slip distance of dislocations increases at increasing SDAS thus hardening rate and image stress are lower. However, in fine microstructures (small SDAS), the hardening is dominated by dislocations interacting with grain boundaries. The hardening rate and the image stress is lower than that in coarse structures due to longer slip distances of dislocations in fine structures (Caceres et al., 1996). Thus intermediate SDAS (about 60  $\mu\text{m}$  for Sr-modified alloys) results in a maximum image stress as the cell boundaries 'become distinct' and interaction between dislocations and cell boundaries replace interaction between dislocations and grain boundaries. Hence microcracks are assumed to occur along grain boundaries in fine microstructure, while they are assumed to take places at cell boundaries in coarse structures (Figure 2-23) (Wang et al., 2001b). The large and elongated eutectic particles in unmodified alloys lead to distinct cell boundaries at lower



## Chapter 2 Literature review

SDAS and thus results in a smaller intermediate SDAS (about 40  $\mu\text{m}$ ). They also decrease the fatigue life with SDAS in the very coarse microstructures.

The evolution with SDAS is different when large pores exist such as in the Sr-modified A356 alloy used by (Zhang et al., 2000). When SDAS is less than 30  $\mu\text{m}$ , the fatigue life fluctuates slightly with SDAS. As the SDAS increases beyond 30  $\mu\text{m}$ , fatigue life drops by about 3 times under LCF and about 100 times under HCF at  $R = 0.1$ . Fatigue cracks initiate at or near surface eutectic regions when the SDAS is less than  $\sim 27$   $\mu\text{m}$ . When the SDAS is greater than 30  $\mu\text{m}$ , porosity becomes the dominant crack initiation site. A SDAS of 30  $\mu\text{m}$  corresponds to a critical pore size of 80-100  $\mu\text{m}$ , which may be used as a parameter to predict the fatigue behavior of this casting alloy.

In the LCF range, according to (Sehitoglu et al., 2000), rapidly solidified material, i.e. with a small SDAS ( $< 30$   $\mu\text{m}$ ), displays the highest cyclic stress-strain amplitudes, with the stress levels decreasing gradually as the SDAS approaches 100  $\mu\text{m}$ . The decrease of the copper content in solution as the SDAS increases would explain the softer response of microstructures with large SDAS. Decreasing of SDAS increases would explain the softer response of microstructures with large SDAS. Decreasing of SDAS could improve thermal fatigue life (Firouzdor et al., 2007). Fracture surface of the fine SDAS samples present more traces of plastic deformation, whilst fracture surface of large SDAS samples shows even cleavage fracture.

### ✓ Slip bands and grain boundaries

In the absence of casting defects, cracks were observed to initiate at slip bands (Figure 2-24) in (Ammar et al., 2008a), as these slip bands constitute highly stressed regions of the sample surface.

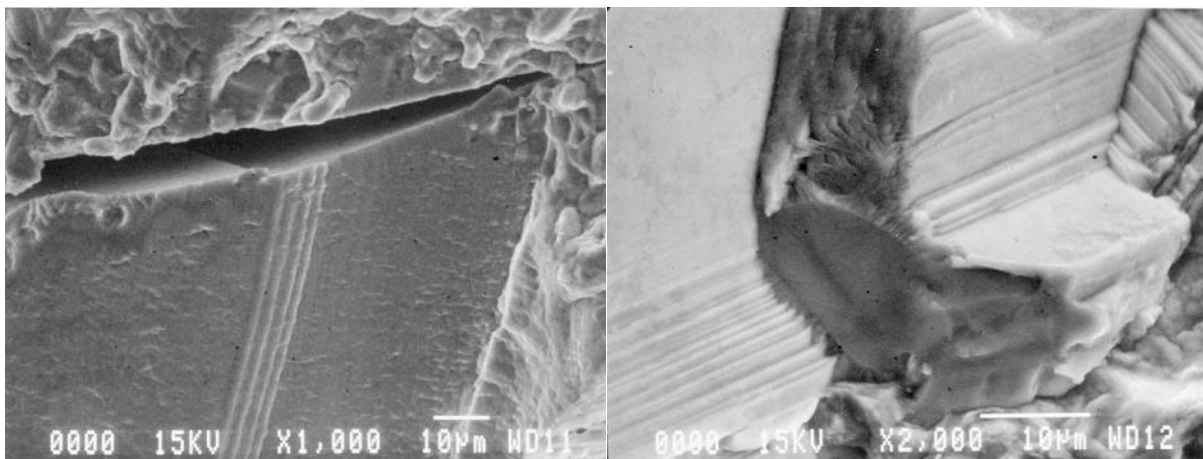


Figure 2-24 Examples of slip bands on the fracture surface indicating the local yielding and dislocation movement (Wang et al., 2001b).

According to (Zeng et al., 2014), there are two mechanisms for crack initiation in the LCF regime: it could initiate as a PSB (Persistent slip bands) crack in a grain, or around eutectic Si particles. Figure

## Chapter 2 Literature review

2-25 shows the fracture surface of an initiated fatigue crack in LCF. The apparent facet shown in the fracture surface that corresponds to the initiated crack suggests that the crack initiated at the PSBs.

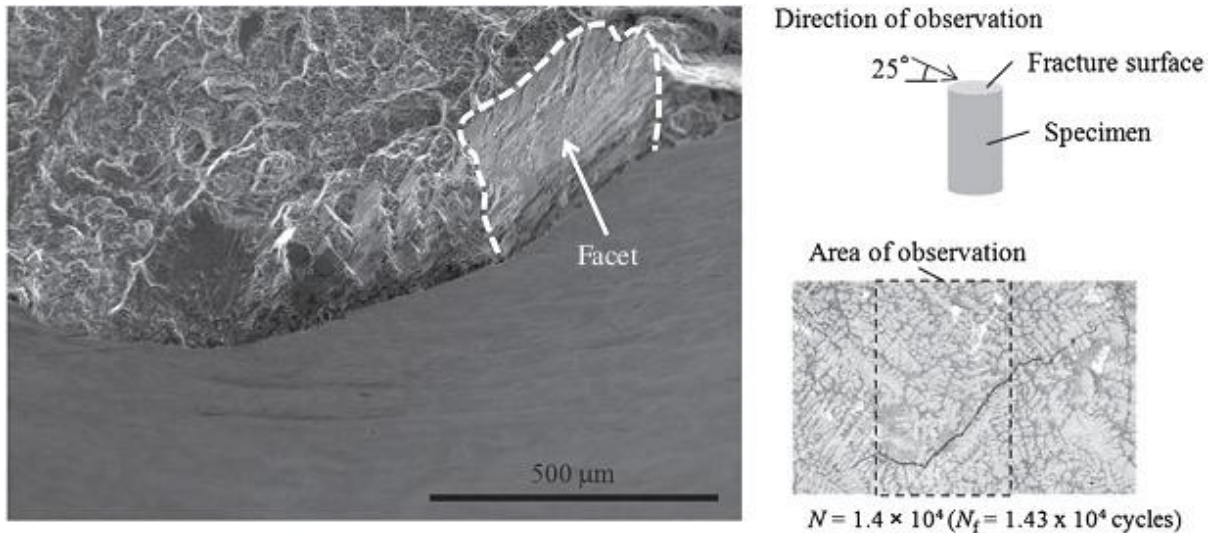


Figure 2-25 SEM image showing a PSB crack in A356 alloy (Zeng et al., 2014)

Crack initiation is favored by the presence of a well oriented grain boundary at the edge of a pore in (Buffière, 2004), while crack propagation occurs along grain boundaries in (Chan et al., 2003). The grains are observed on a large proportion of the fracture surface and are generally oriented parallel to the long axis of the wedge casting in (Boileau and Allison, 2003). However, grain boundaries could also act as efficient barriers against crack propagation (Buffière et al., 2001) (Buffière, 2004) (Chan et al., 2003). In the LCF regime, cracks initiating from and propagating along grain boundaries were observed (Song et al., 2011) (Zeng et al., 2014).

### 2.4 Summary of literature review

Al-Si casting alloys are widely used in automotive industry due to their light weight, environmentally-friendly, excellent mechanical properties and casting performances. The additives change the microstructure of the alloy and form various constituents while they improve various properties of Al-Si alloys. The main microstructure constituents and casting defects are listed in Table 2-2. Chemical composition, additions of element, casting temperature and cooling rates have important influence on microstructure. In manufacturing of cylinder heads, the Lost Foam Casting (LFC) process progressively replaces the traditional die casting process to save the cost. However, the slower cooling rate of LFC process results in a coarser microstructure (large SDAS, large size of intermetallics and Si phases) and a large volume fraction of pores. Although microstructure of the LFC A319 and A356 alloys studied in this thesis were characterized using SEM in a previous Ph.D. thesis (Tabibian, 2011), AlCuMgSi phase was not revealed. More importantly, the limited information given by a 2D characterization did not allow fully understanding the spatial morphologies of various constituents.

## Chapter 2 Literature review

---

Thus a 3D characterization is necessary to reveal their 3D morphologies and sizes that may affect mechanical properties.

The casting defects, microstructure constituents and features have an important influence on the fatigue properties. The main micromechanisms of fatigue damage in Al-Si alloys reported in the literature are summarized in Table 2-3. Large casting defects including pores are considered to be the most probable crack initiation sites if they are above a critical size. In the absence of large casting defects, hard inclusions, including Si phase, iron intermetallics, Al<sub>2</sub>Cu phase, and grain boundaries and slip bands also become possible crack initiation sites. No matter where cracks initiated, they are likely to propagate along hard inclusions and/or grain boundaries although they may also be resisted by hard inclusions. The size, shape, orientation of hard inclusions, and loading conditions have an influence on damage mechanisms of hard inclusions, i.e. decohesion or fracture. SDAS also has influence on fatigue life. Increasing SDAS reduces fatigue life except in an Sr-modified A356-T6 alloy in (Wang et al., 2001b) for coarse microstructures (SDAS > 60 μm) where fatigue life increases with increasing SDAS values.

Most of the studies were performed in the HCF instead of in LCF regime. Few materials, studied in both HCF and LCF regime, present large pores like in the studied material. Although postmortem analysis in the previous Ph. D. thesis (Tabibian, 2011) revealed cracks at hard inclusions in the same material, it did not allow following cracks initiation and propagation until final failure. Thus the damage mechanisms of this material are still not clear and need to be further studied using the experimental protocol developed in this thesis.



## Chapter 2 Literature review

Table 2-2 Main microstructure constituents and casting defects in Al-Si alloy

Microstructure constituents or casting defects		Morphologies	Influence factors	
Microstructure constituents	<b><math>\alpha</math>-Aluminum</b>		Dendritic structure	
	<b>Si phase</b>		Compact, massive precipitates or branched plates	
	<b>Iron intermetallics</b>	<b><math>\alpha</math>-AlFeMnSi phase</b>	‘Chinese script’ morphology	Higher cooling rate enables the $\alpha$ -AlFeMnSi phase to solidify in a fine compact morphology and the lower cooling rate results in the formation of compact and star-like Chinese script $\alpha$ -AlFeMnSi phase.
		<b><math>\beta</math>-AlFeSi phase</b>	‘plate-like’ morphology	Addition of Sr, increasing casting temperature, increasing the Mn content or decreasing the iron content could promote the formation of a more compact and less harmful $\alpha$ -AlFeMnSi phase and reduce the formation of harmful $\beta$ -AlFeSi phase, and vice versa.
	<b>Cu containing phases</b>	<b>Al<sub>2</sub>Cu phase</b>	Block like or eutectic morphology	Affected by the addition of Ce, Sr or Fe.
		<b>AlCuMgSi phase</b>	Small pieces attached to large Al <sub>2</sub> Cu phases.	It forms when Cu content is more than 2% and its amount increases with increasing Cu content.
	<b>Mg containing phases</b>	<b>Mg<sub>2</sub>Si</b>	Mg <sub>2</sub> Si phase having small black script morphology in SEM observations presents clearly a coral like connectivity in 3D.	-
	Casting defects	<b>Pores</b>	<b>gas porosity</b>	‘round ball’
<b>shrinkage porosity</b>			Complex structure	
<b>Oxide films</b>		Oxide films exhibit different morphologies because of their different chemical compositions, thickness, strength and interaction with the melts.		

## Chapter 2 Literature review

Table 2-3 Micromechanisms of fatigue damage in Al-Si casting alloys

		Crack initiation		Crack propagation	
		HCF	LCF	HCF	LCF
Casting defects	<b>Pores</b>	Above a critical size (also related with their locations, number, and shape).	Above a critical size (also related with their number).	Accelerating crack growth	
	<b>Oxides films</b>	Critical size: oxides films > pores.	-		
Hard inclusions	<b>Si particles</b>	In the absence of large casting defects		1. Cracks propagate along Si particles but are also resisted by the Si particles; 2. debonding or fracture depending on its size, shape, orientation, loading conditions etc.; 3. Sr modification increases the fatigue life.	
	<b>Iron intermetallics</b>	In the absence of large casting defects, High-Fe content promotes fatigue crack initiation		1. $\beta$ phase is more harmful than $\alpha$ phase; 2. cracks propagate along iron intermetallics but are also resisted by iron intermetallics; 3. debonding or fracture depending on phase morphology, loading conditions etc. .	
	<b>Cu containing phases</b>	In the absence of large casting defects, and at low iron levels, in unmodified condition.	-	Propagation along these phases. Debonding or fracture depending on the shape and alignment of these phases	
	<b>Mg containing phases</b>	-	Increasing Mg content decrease fatigue life.		
					Increasing Fe-content reduces the fatigue life.
				Increasing Fe-content slightly increases the fatigue life.	
Microstructural features	<b>Grain boundary</b>	In the absence of large casting defects.		Propagation along grain boundaries.	
	<b>Slip bands</b>			Depending on its orientation.	
	<b>SDAS</b>	Increasing SDAS reduces fatigue life (except in an Sr-modified A356-T6 alloy in (Wang et al., 2001b) for coarse microstructures (SDAS > 60 $\mu\text{m}$ ) where fatigue life increases with increasing SDAS values)			

# Chapter 3 Material Characterization

## Contents

---

<b>3.1</b>	<b>Introduction.....</b>	<b>- 37 -</b>
<b>3.2</b>	<b>Characterization methods .....</b>	<b>- 38 -</b>
3.2.1	Optical microscope observation.....	- 38 -
3.2.2	SEM observation.....	- 39 -
3.2.3	X-ray microtomography observation .....	- 39 -
3.2.3.1	X-ray microtomography principle.....	- 39 -
3.2.3.2	Experimental protocol of X-ray tomography .....	- 42 -
3.2.4	Image analysis process.....	- 45 -
3.2.4.1	Image processing.....	- 46 -
3.2.4.2	Image analysis.....	- 48 -
3.2.4.3	Image quantification .....	- 48 -
<b>3.3</b>	<b>'Phases' morphologies and sizes .....</b>	<b>- 50 -</b>
3.3.1	Microstructure of A319 alloy.....	- 50 -
3.3.1.1	Pores.....	- 50 -
✓	3D characterization with a 1.5 $\mu\text{m}$ voxel size (Specimen 1).....	- 51 -
✓	3D characterization with a voxel size of 3 $\mu\text{m}$ (Specimen 2) .....	- 55 -
3.3.1.2	Si .....	- 60 -
3.3.1.3	Iron intermetallics .....	- 62 -
3.3.1.4	Copper containing phases .....	- 67 -
3.3.1.5	Pb .....	- 73 -
3.3.2	Microstructure of A356 alloy.....	- 75 -
<b>3.4</b>	<b>Comparisons .....</b>	<b>- 79 -</b>
<b>3.5</b>	<b>Summary.....</b>	<b>- 82 -</b>

---

# Chapter 3 Material Characterization

## 3.1 Introduction

As the purpose is to study the influence of the casting microstructure of Al-Si alloy on initiation and propagation of cracks in low cycle fatigue at room temperature, it is of primary importance to characterize this microstructure. Besides, the characterization of defects is also necessary for the fatigue life prediction (Charkaluk et al., 2014) (Szmytka et al., 2014) (Nanakasse, 2013).

Two alloys, A319 and A356, were studied. Their chemical compositions and their phases or constituents studied in 3D are listed in Table 3-1 and Table 3-2, respectively. Both alloys are Sr-modified and non-aged, but A319 alloy is without heat treatment and A356 alloy is with a T7 heat treatment. The microstructure of A319 alloy, which is the main studied material, was analyzed using optical microscope and Scanning Electron Microscope prior to the 3D characterization with X-ray computed tomography.

Table 3-1 Chemical composition of Lost Foam Casting A356 and A319 alloys (wt.%)

Material	Si	Fe	Cu	Mn	Mg	Ni	Zn	Pb	Sn	Ti	Other elements*	
											each	total
A319	5.3 - 7.5	≅ 0.6	3- 3.80	≅ 0.50	0.25- 0.40	≅ 0.30	≅ 0.40	≅ 0.10	≅ 0.05	≅ 0.20	≅ 0.03	≅ 0.1
A356	6.5 - 7.5	≅ 0.30	≅ 0.10	≅ 0.10	0.25- 0.40	≅ 0.1	≅ 0.10	≅ 0.1	≅ 0.05	≅ 0.20	≅ 0.02	≅ 0.1

\*Other elements: Zr, V, P and Sr.

Table 3-2 Phases or constituents studied in 3D in A356 and A319 alloys

Material	phases or constituents
A319	Pores, iron based intermetallics, Al <sub>2</sub> Cu, Pb, Si
A356	Pores, iron based intermetallics

This chapter is divided into four sections, including this introduction. The characterization methods, i.e. optical microscope, SEM-EDS, laboratory and synchrotron X-ray tomography, and analysis process are presented in the second section. Then, in the third section, A319 alloy is fully characterized both in 2D and 3D whereas A356 alloy is only roughly characterized as the study of A319 alloy is the main objective of this thesis. The main conclusions about materials characterization are summarized in the last section.

### 3.2 Characterization methods

The samples extracted from the fire deck areas of prototype cylinder heads were characterized using Optical Microscope (OM) and Scanning Electron Microscopy (SEM) on surface (2D characterization) and using laboratory and synchrotron X-ray tomography in volume (3D characterization). OM observations require a fine polishing of flat surface, thus the samples were polished using abrasive papers of grades up to 4000 grits in succession and then using polishing cloths and suspensions up to  $1/4\ \mu\text{m}$ . SEM observations have less stringent requirements for the polishing than OM observations, so the polishing performed with polishing cloths and suspensions up to  $3\ \mu\text{m}$  is enough. The polishing is not necessary for the samples characterized with X-ray tomography.

#### 3.2.1 Optical microscope observation

Optical Microscope (OM) observations were performed with an Olympus PMG3 inverted metallurgical microscope equipped with a JVC colour video camera and a Nikon YM-EPI light microscope equipped with a Sony colour video camera. The polished samples were observed with a magnification from  $2.5\times$  to  $50\times$ .

A key work for the following tensile and fatigue tests with 2D in-situ observations is the development of an etching solution in order to give a natural texture to the aluminum dendrites by revealing segregation of Si (Figure 3-1). A texture is necessary to make Digital Image Correlation, which will be presented in chapter 4, feasible to an acceptable resolution without adding a speckle pattern that will also mask the microstructure. Many etching methods were tried and the composition of the etchant used is 100ml distilled water, 4g potassium permanganate and 1g sodium hydroxide. The etching time is 15 seconds (Zwieg, 2003).

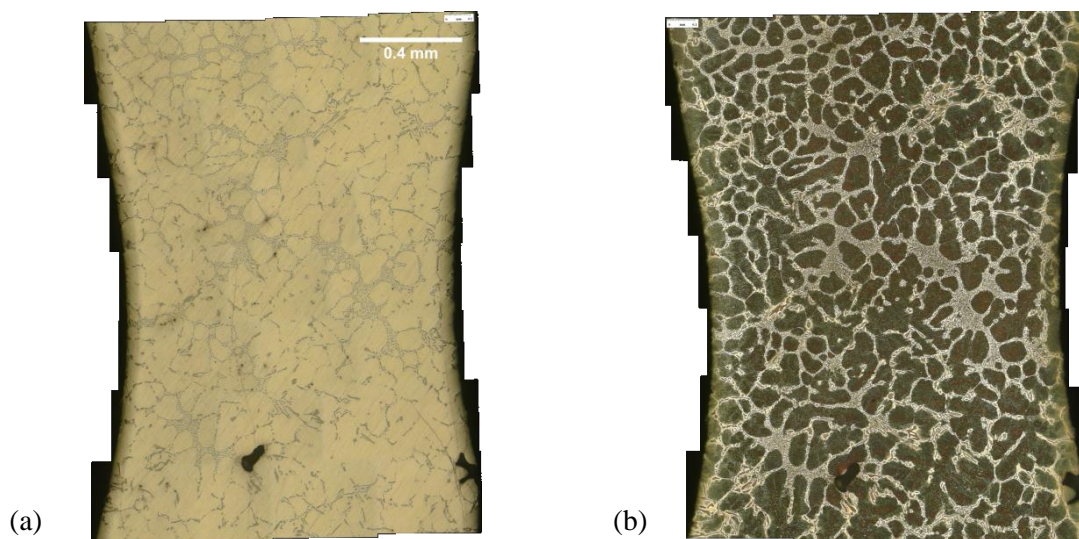


Figure 3-1 OM images of an A356 specimen (a) before and (b) after etching

## Chapter 3 Material Characterization

---

### 3.2.2 SEM observation

The Scanning Electron Microscopy (SEM) is a technique of electron microscopy capable of producing high resolution images of the surface using the principle of electron interactions (Joy, 2006) (Krumeich, 2011). Signals generated due to the interaction of matter with the beam of electrons are Secondary Electrons (SE) and Back Scattered Electrons (BSE). While SE is very sensitive to the surface topography, there is no significant relationship between the yields of secondary electrons and atomic number, thus SE signal cannot be used for chemical analysis. On the contrary, as the yield of BSE increases with an increase of atomic number, it could be used for chemical analysis. The higher the atomic number of one feature the brighter it appears in the BSE image. Energy-Dispersive X-ray Spectroscopy (EDS) is a technique used for elemental analysis or chemical characterization. X-ray fluorescence is generated due to the interaction of the beam of electrons with atoms from the sample surface. Each element produces X-ray photons with characteristic energy, which are collected by the EDS microanalysis system. Then these collected X-rays are sorted and plotted by energy. The elements corresponding to the peaks in this energy distribution are identified automatically by the EDS analysis software (Joy, 2006). The chemical composition at a point or in an area is thus obtained. Based on this basic principle, the X-ray mapping function of EDS allows identifying the element distribution in the analyzed zone. The number of X-ray photons of specified energy detected at each point over a fixed counting time, while the electron beam is rastered over a rectangular area, is converted into a brightness value for one pixel of the digital image. Then pixels in the analyzed zone are mapped to a single-band image with 0-255 levels. The image can be displayed as a grayscale image or assigned false colors based on a look-up table. Thus, the distribution of a specified element in the analyzed zone could be revealed in the X-ray mapping image by a specified color or gray level (Newbury, 1986).

A319 alloy was characterized using SEM/EDS system. Observations were performed using HITACHI 3600N SEM, and the EDS analyses were performed using the equipped NORAN System SIX X-ray Microanalysis System. Images were taken using BSE signal in order to reveal the different compositions, which were further identified using EDS.

### 3.2.3 X-ray microtomography observation

#### 3.2.3.1 X-ray microtomography principle

The principle of X-ray Computed Tomography (CT) is illustrated in Figure 3-2(a) (Salvo et al., 2010): The sample is placed on a rotating stage between the X-ray beam source and the detector. A scintillator converts the X-rays transmitted through the sample into visible light, which is recorded by specific optics, such as a CCD or CMOS camera. A set of  $N$  radiographs, i.e. a scan, corresponding to

## Chapter 3 Material Characterization

$N$  angular positions of the sample are taken while the sample is rotated through  $180^\circ$  or  $360^\circ$  along its vertical axis. The three dimensional (3D) image with a 16 bit gray scale color is reconstructed using these radiographs (Herman, 2010). The grey levels reflect the optical properties of different absorbing medium.

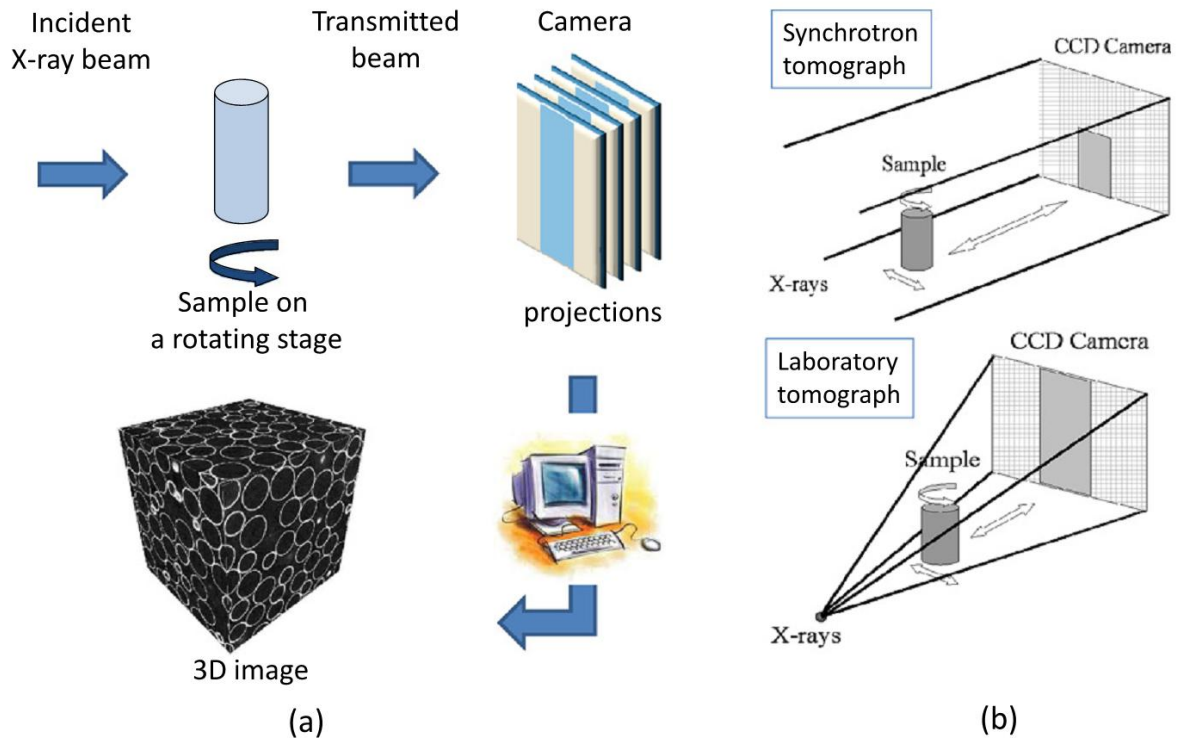


Figure 3-2 (a) Principle of tomography; (b) Synchrotron and laboratory tomography. (Salvo et al., 2010)

Figure 3-3 illustrates the imaging principle of X-ray tomography (Cloetens et al., 1997) (Baruchel et al., 2000): Complex refractive index  $n$ , which is a main optical constant of absorbing medium, is related to absorption coefficient  $\beta$  and decrement of refractive index  $\delta$ . X-rays can be treated as electromagnetic waves. When they pass through an object, both their amplitude and phase are altered. The amplitude of transmitted X-rays relates to the absorption coefficient, which is a function of the density and the atomic number of the elements. Thus different microstructure features present different grey levels in the reconstructed 3D images thanks to the different amplitudes of transmitted X-rays. The contrast provided by different absorption coefficients is called ‘absorption contrast’. The phase-shift of the transmitted X-rays is related to the decrement of refractive index, which also depends on the atomic number, and it provides the so-called ‘phase contrast’. However, the decrement of refractive index  $\delta$  is more sensitive to the atomic number than the absorption coefficient  $\beta$ , especially for light elements (Momose et al., 1996). Two features having adjacent atomic numbers, such as Al and Si, which could not be distinguished by absorption contrast, can be revealed thanks to phase contrast (see Figure 3-4). Besides, the borders and interfaces between sample matrix and



## Chapter 3 Material Characterization

inclusions also have more phase contrast as they produce a highly-localized change in the refractive index of the sample.

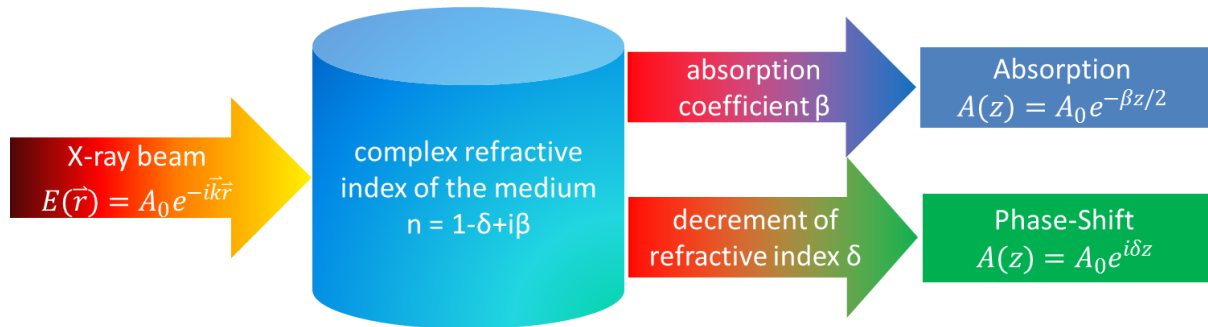


Figure 3-3 Absorption contrast and phase contrast.

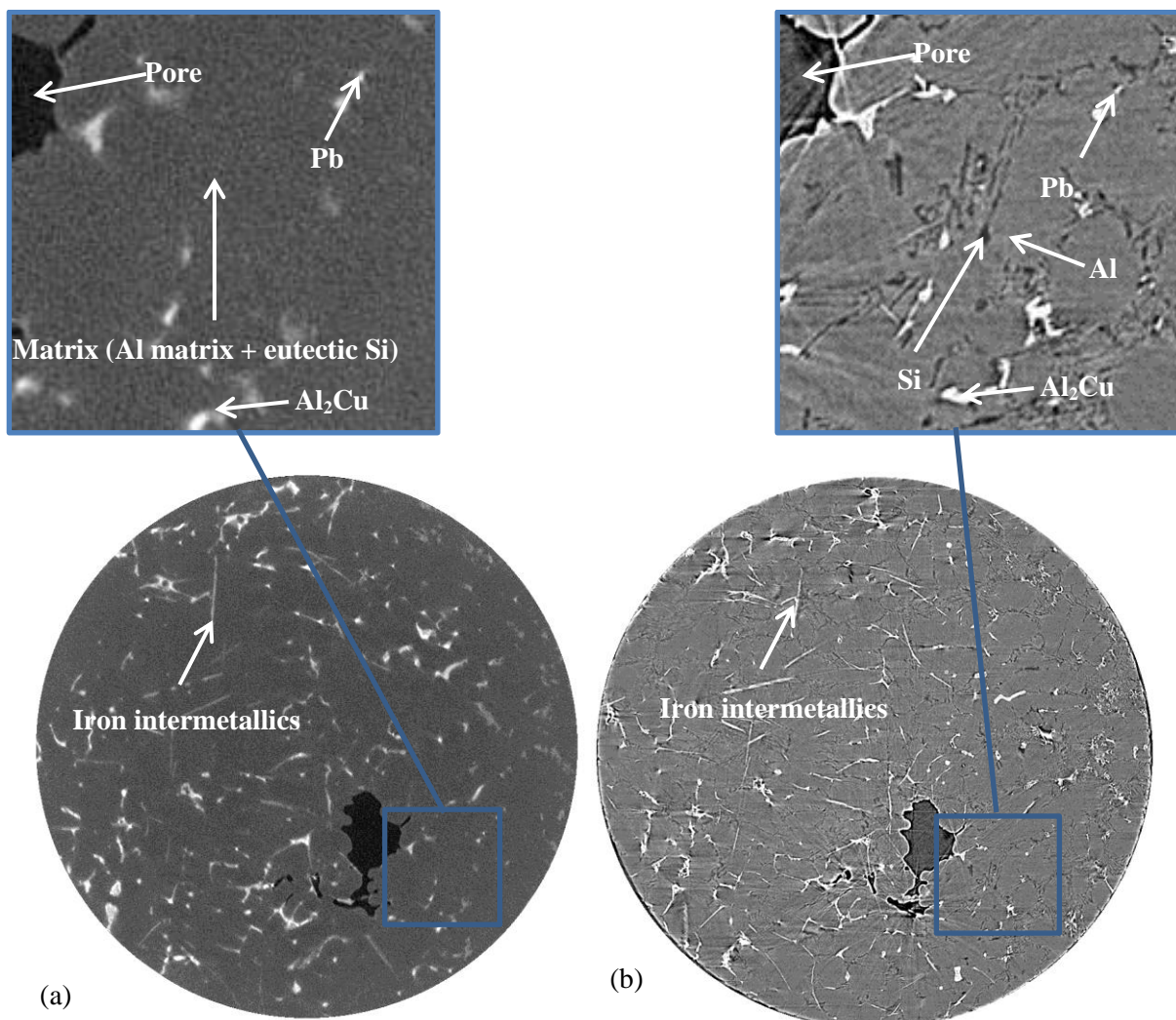


Figure 3-4 A CT slice of an A319 alloy from: (a) Lab-CT (only absorption contrast) and (b) SR-CT (absorption and phase contrasts).

Depending on the X-ray source, there is two categories of tomography (Salvo et al., 2010): Synchrotron Radiation tomography (SR-CT) and laboratory tomography (Lab-CT) (Figure 3-2 (b)).



## Chapter 3 Material Characterization

---

The X-ray beam of Lab-CT is divergent and polychromatic. The sample rotates around  $360^\circ$  for one scan, which lasts about several minutes in a fast scan mode and 15 – 45 minutes in a more typical mode (Limodin et al., 2009a). In a typical mode, 4 images are taken at a given angular position: the first image is ignored to avoid the afterglow effect of the detector, and the other 3 images are averaged as the final radiograph in this angular position. The spatial resolution that varies from several hundreds of nanometers to hundreds of microns depends directly on the distance between the sample and the X-ray tube: a smaller distance will give a higher resolution and a smaller scan volume. Only absorption contrast is provided by Lab-CT.

The X-ray beam of SR-CT is parallel, polychromatic or monochromatic. The sample rotates around  $180^\circ$  for one scan (Limodin et al., 2009b). Thanks to the high brilliance of the X-ray source, the exposure time reduces significantly compared to Lab-CT, typically only a few minutes and even less than 1 second with fast cameras. The spatial resolution, which depends on the equipment used, such as the scintillator, the optics and the pixel size of the camera, varies from several tens of nanometers to hundreds of microns (Salvo et al., 2010). Both absorption and phase contrasts are provided by SR-CT.

For a given detector, which results in a specific size of image in pixels, a larger scan volume yields a lower resolution. Thus only small size specimen is suitable for X-ray tomography in order to ensure a sufficient resolution. In order to obtain high quality 3D images, an appropriate energy of X-ray beam, i.e. acceleration voltage of the electron gun for Lab-CT or photon energy for SR-CT should be selected to ensure at least a 10% transmission of the X-ray beam through the sample (Limodin et al., 2009a).

### 3.2.3.2 Experimental protocol of X-ray tomography

Three specimens extracted from cylinder heads were analyzed using X-ray microtomography (Table 3-3):

- ◆ Specimen 1, which is a cylindrical sample, was scanned in eight adjacent volumes along its height  $H$  (Figure 3-5(a)).
- ◆ Specimen 2, which is a macroscopic fatigue specimen, was scanned in the central part of the gauge length (Figure 3-6(a)).
- ◆ Specimen 3, which is a small flat tensile test specimen, was also scanned in the central part (Figure 3-7 (a)).

## Chapter 3 Material Characterization

Table 3-3 Specimens studied in this chapter

Name of specimen	Material	Specimen size (mm)
Specimen 1	A319	$\Phi 2.55$
Specimen 2	A319	$\Phi 5.14$
Specimen 3	A356	$1.53 \times 1.36$

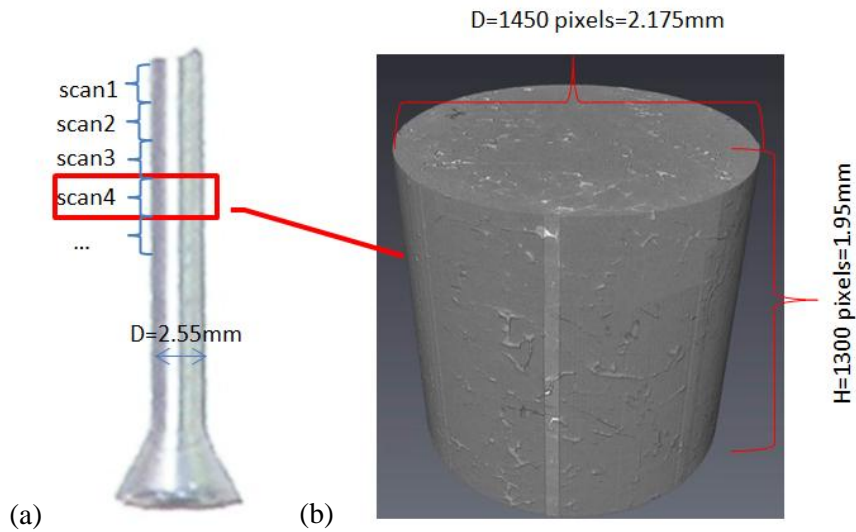


Figure 3-5 (a) Locations of the scans in Specimen 1 (A319) and (b) 3D rendering of the region analyzed in 'scan4'

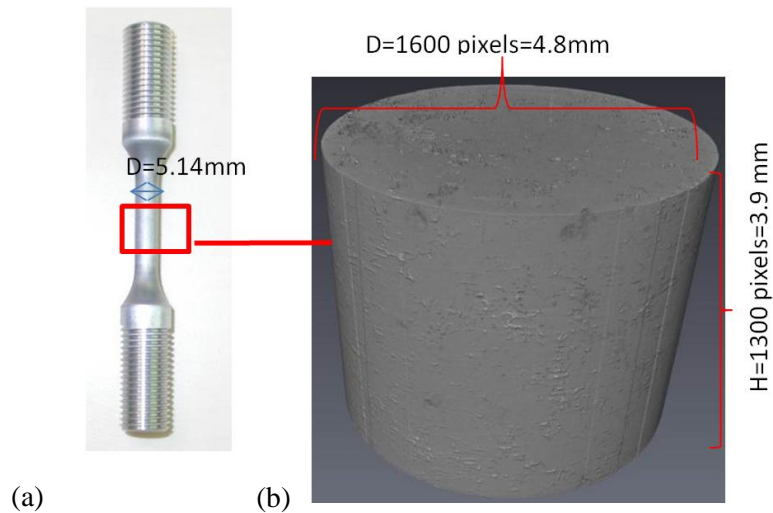


Figure 3-6 (a) Location of the scan in Specimen 2 (A319) and (b) 3D rendering of the analyzed region

## Chapter 3 Material Characterization

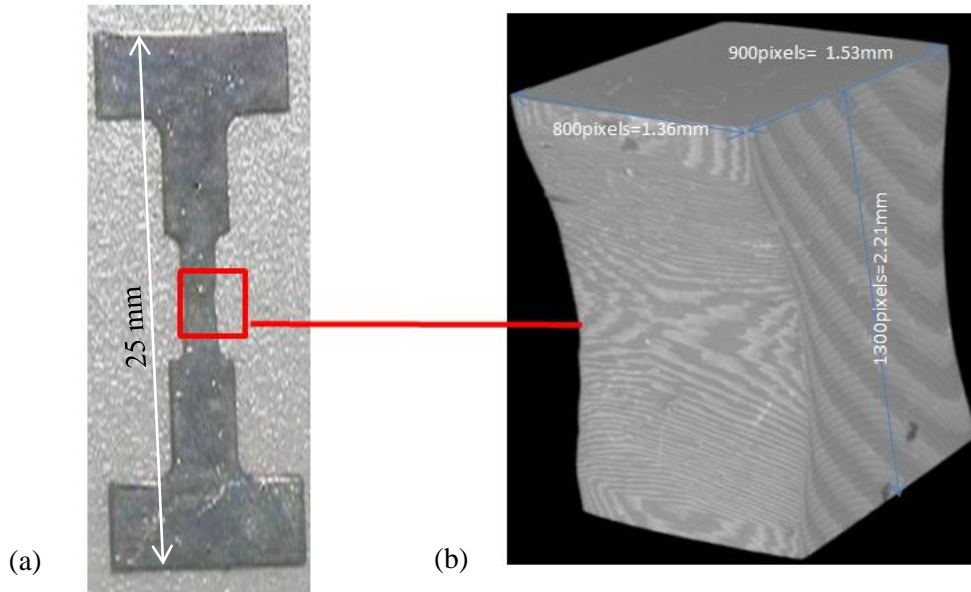


Figure 3-7 (a) Location of the scan in Specimen 3 (A356) and (b) 3D rendering of the analyzed region

Lab-CT was realized in Laboratoire Matériaux, Ingénierie et Sciences (MATEIS) at INSA-Lyon. The experiments were performed using a V-Tomex CT system (Phoenix X-ray) fitted with a nanofocus tube (tungsten target) whose acceleration voltage can be adjusted from 10 to 160 kV, and whose focal spot size is tuneable from 6  $\mu\text{m}$  to 1  $\mu\text{m}$ . Specimens were placed on the rotating stage in the tomography chamber between the X-ray source and an amorphous silicon diode array detector of dimensions  $1920 \times 1536$  voxels. Specimen 1, 2 and 3 were characterized using the parameter settings listed in Table 3-4. Reconstruction of the tomographic data was performed with a filtered back-projection algorithm using `datos|x-acquisition` software developed by Phoenix. Definition of a Region Of Interest (ROI) that is centered on the sample was used to reduce the image size, which is listed in Table 3-4 for each specimen.

Table 3-4 Parameter settings of laboratory X-ray microtomography

Specimen name	Voxel size ( $\mu\text{m}$ )	acceleration voltage (kV)	filament current ( $\mu\text{A}$ )	number of radiographs in a scan ( $N$ )	acquisition time per image (ms)	Image size after ROI selection (voxels)
Specimen 1	1.501	86	173	1500	667	$1600 \times 1600 \times 1300$ ( $2.4 \times 2.4 \times 2.05 \text{ mm}^3$ )
Specimen 2	2.995	90	145	1500	667	$1700 \times 1700 \times 1300$ ( $5.1 \times 5.1 \times 3.9 \text{ mm}^3$ )
Specimen 3	1.7	60	240	720	1000	$800 \times 900 \times 1300$ ( $1.36 \times 1.53 \times 2.21 \text{ mm}^3$ )

Synchrotron X-ray tomography was performed on TOMCAT (Tomographic Microscopy and Coherent radiology experiments) beamline at the Swiss Light Source (SLS) in Villigen, Swiss. Part of Specimen 1 was scanned at a voxel size of about 1.61  $\mu\text{m}$ . A monochromatic X-ray beam having

## Chapter 3 Material Characterization

photon energy of 25 keV was used. During one scan, 1500 radiographs were taken at an exposure time of 300 ms per image; one scan lasted about 7 min. Reconstruction of the acquired tomographic data was performed using the reconstruction platform developed by SLS (Marone et al., 2010). The ROI focused on Specimen 1 is  $1680 \times 1680 \times 1850$  voxels ( $2.7 \times 2.7 \times 2.98$  mm<sup>3</sup>).

### 3.2.4 Image analysis process

Results of quantitative 2D characterization on the studied material are from (Tabibian, 2011). 2D measurements were performed with ImageJ software on BSE images with one pixel size of  $0.8 \sim 2.5$   $\mu$ m. The total surface analyzed was about 51.2 mm<sup>2</sup> for A319 alloy and 63.6 mm<sup>2</sup> for A356 alloy. The basic steps of image analysis are the same with that for 3D images presented in the following (Figure 3-8). For more details about the measurement method, please refer to (Charkaluk et al., 2014).

The 3D images were processed and analyzed using ImageJ/Fiji and Avizo Fire softwares. The main steps of the analysis process are shown in Figure 3-8.

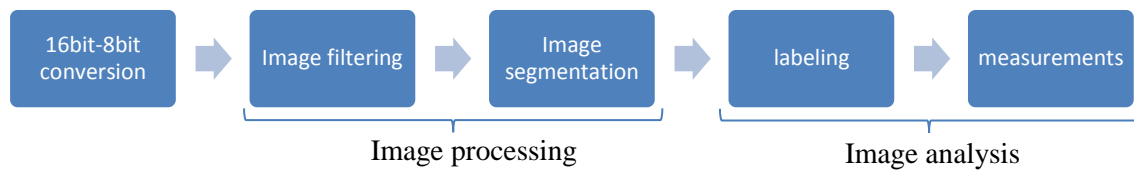


Figure 3-8 Scheme of image processing and analysis

After reconstruction, 16 bit images were reduced to 8 bit in order to minimize the files size. The conversion process is as follow. The distribution of gray values in the 3D 16-bit image was calculated, and plotted in a histogram. Then the brightness and contrast were adjusted to the peak range of the histogram (set the minimum and maximum values of the peak range as the minimum ('min') and maximum display values ('max') separately). Afterwards, the 16-bit image was converted to 8-bit image by linearly scaling from min-max to 0-255 (Ferreira and Rasband, 2012).

The analysis of Specimen 1 performed with Lab-CT was focused on the mid-length of the cylindrical sample ('scan4' in Figure 3-5(a)). A cylindrical ROI (Table 3-5) was further selected as the region analyzed using Fiji software, and its 3D rendering image is shown in Figure 3-5(b). Similarly, an ROI (Table 3-5) was also selected for the analysis of the SR-CT scan of Specimen 1.

For Specimen 2 (Figure 3-6(b)), the use of a larger voxel size, i.e. 3  $\mu$ m instead of 1.5  $\mu$ m, allowed a larger scan volume to be obtained, i.e. approximately 10 times the volume of Specimen 1.

The ROI of Specimen 3 (A356) was extracted using a mask (Figure 3-7 (b)), as it has not a regular but a cubic shape with a notch at each side. The analysed volume (Table 3-5) is only 5% of that of Specimen 2.

## Chapter 3 Material Characterization

Table 3-5 Size and volume of analysed volume for each specimen

Specimen	X-ray source	Size of analysed volume		Analysed volume (mm <sup>3</sup> )
		Diameter (pixels)	Height (pixels)	
Specimen1	synchrotron	1500 (2.415 mm)	1750 (2.8175 mm)	12.91
	laboratory	1450 (2.175 mm)	1300 (1.95 mm)	7.24
Specimen2		1600 (4.8mm)	1300 (3.9 mm)	70.54
Specimen3		-	-	3.58

### 3.2.4.1 Image processing

The 3D images processing was performed either with Avizo Fire or ImageJ softwares. ImageJ is a public domain, Java-based and free image processing program. Custom acquisition, analysis and processing plugins can be developed using ImageJ's built-in editor and a Java compiler (ImageJ Software, 2013). Avizo is a general-purpose commercial software with more tools, but the program code is not open.

Filtering was applied prior to segmentation in order to reduce the noise in the image. Images were sequentially filtered by 3D median and anisotropic diffusion filters in Avizo software except for Specimen 3 (A356) that was filtered with a binning process to reduce both image size and noise. Some very fine details in the tomography images may be lost due to the applied filters, thus appropriate parameters should be selected for the balance between the noise reduction and the lost information. The principles of median filter, anisotropic diffusion filter, and binning and the main parameters of filters selected for Specimens 1 and 2 are presented in Appendix I. The original image size of Specimen 3, i.e. 800×900×1300 voxels (1 voxel = 1.7×1.7×1.7 μm<sup>3</sup>), was reduced to 400×450×650 voxels (1 voxel = 3.4×3.4×3.4 μm<sup>3</sup>) after binning. Some examples of filtering by using Avizo and ImageJ are shown in Figure 3-9 and Figure 3-10.

## Chapter 3 Material Characterization

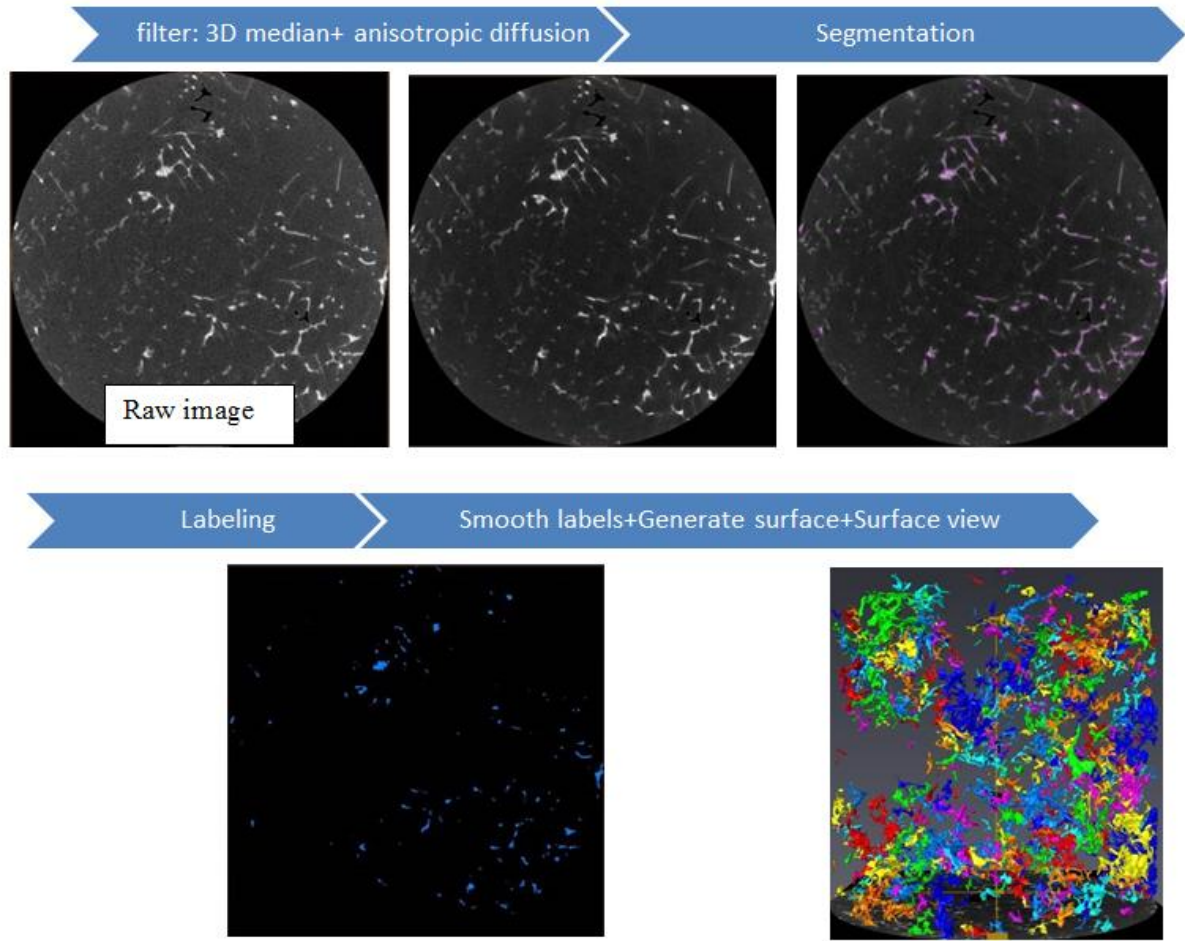


Figure 3-9 Scheme of image processing and analysis for Specimens 1 and 2 in Avizo

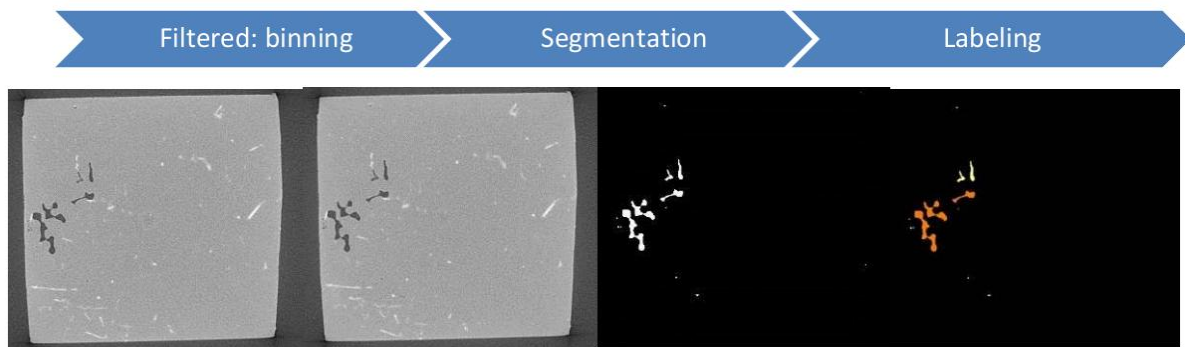


Figure 3-10 Scheme of image processing and analysis for Specimen 3 in ImageJ

The segmentation of the different phases or constituents was realized by simple grayscale thresholding, i.e. by selecting the minimum and the maximum grey levels that belong to the studied phase, either by using the “Threshold Tools” in Avizo for Specimens 1 and 2 (Figure 3-9) or by using the ‘adjust threshold’ function in ImageJ for Specimen 3 (Figure 3-10). The threshold ranges selected for the different phases are listed in Appendix I. In addition, Specimen 3 was segmented as a whole object (matrix + pores + intermetallics) in order to calculate its volume of  $3.58 \text{ mm}^3$ , which cannot be obtained directly from specimen’s dimensions due to the presence of an irregular notch.



## Chapter 3 Material Characterization

---

In SR-CT image, due to the strong phase contrast, the grey values inside the porosity are sometimes similar with the grey values of the eutectic Si and/or Al matrix and thus it affects the segmentation of both porosity and eutectic Si. Besides, a bright fringe, which has a grey value in the range of iron intermetallics or Al<sub>2</sub>Cu phase, is found around the pores (cf. Figure 3-4(b)). Thus the segmentation of iron intermetallics and Al<sub>2</sub>Cu phase is difficult. Although pores, iron intermetallics and Al<sub>2</sub>Cu phase in the SR-CT image are not studied in this chapter, they will be segmented in Chapter 5. Therefore, a series of pre-treatment methods, which are presented in Appendix I, are necessary to solve these problems.

Because the choice of a threshold range will vary from one user to the other for a same image, a preliminary segmentation test, which is detailed in Appendix I, was performed for the intermetallics in the Lab-CT image of Specimen 1 to study the influence of the selected threshold interval on the results. A segmentation test for the Si phase in the SR-CT image was also performed using a similar method and will be explained in §3.4.1. The lower resolution of Specimens 2 (voxel size = 3 μm) and 3 (voxel size = 3.4 μm) after binning was not enough to segment properly intermetallics, Al<sub>2</sub>Cu phase and Pb particles, hence only some basic analysis, e.g. volume fraction, was performed for these phases while a more detailed analysis was performed on the pores.

### 3.2.4.2 Image analysis

The thresholded phases or constituents were labeled with Avizo software for Specimen 1 or 2 and with the “Analysis\_3D” plugin in Fiji software for Specimen 3; this plugin has been developed at SIMAP-GPM2 (Boulos et al., 2012). After labeling, voxels that belong to a same 3D object are given a same color (grey level) and different objects are marked with different colors (grey level) or labels; see Figure 3-10 and Figure 3-9. In Avizo, all the boundaries of the labeled regions were smoothed (‘2’ was selected as the size and “3d Volume” was selected for the Mode) before surface generation. A 3D view could be obtained by using ‘generate surface’ function and ‘surface view’ function. ‘Generate surface’ function computes a triangular approximation of the interfaces between different material types in a Label Field and can use the probability information to generate smoother surfaces. ‘Surface view’ function allows visualizing the generated surface (ZIB (Zuse Institute Berlin) and VSG (Visualization Sciences Group), 2012). The 3D rendering images can also be shown filtered by the different parameters (such as Feret diameter, ‘sphericity (F)’), which will be explained in the following of the objects.

### 3.2.4.3 Image quantification

The “Quantification tools” (ZIB and VSG, 2012) in Avizo Fire were used to get quantitative analysis for Specimens 1 and 2. The granulometric analysis (with Octahedron as a structural element) for all



## Chapter 3 Material Characterization

the specimens and the quantitative analysis for Specimen 3 were performed with the “Analysis\_3D” plugins.

The main parameters adopted herein are: equivalent diameter, Feret diameter, granulometry and sphericity (F).

The **equivalent diameter in 2D** is the diameter of a disk surface that would have the same surface  $A_p$  as the object. It is defined according to equation (3-1) (Tabibian, 2011),

$$D_e = 2 \sqrt{\frac{A_p}{\pi}} \quad (3-1)$$

The **equivalent diameter in 3D** is the diameter of a sphere that would have the same volume  $V$  as the object, and it is calculated according to equation (3-2),

$$D_{eq} = 2 \times \left(\frac{3V}{4\pi}\right)^{\frac{1}{3}} \quad (3-2)$$

**Feret diameter** is the distance between the two farthest points on the boundary of the object. An example of measurement of Feret diameter performed in a plane (2D) is illustrated in Figure 3-11(a); it refers to the measurement of the object size with a caliper so that the Feret diameter is also called the caliper diameter. Feret diameter in the “Analysis\_3D” plugin was estimated from the length of the longest side of the minimum bounding box (Figure 3-11(b)). Herein the axis-aligned bounding box, which is the smallest rectangular parallelepiped that contains the object, was adopted as the minimum bounding box. Feret diameter in Avizo was defined as the maximum of the ‘Feret diameters’ over a range of angles so that it corresponds to a true assessment of the Feret diameter. For 3D images, this list contains 31 couples of values  $(\theta, \phi)$  in the coordinate system shown in Figure 3-11(c) (ZIB and VSG, 2012).

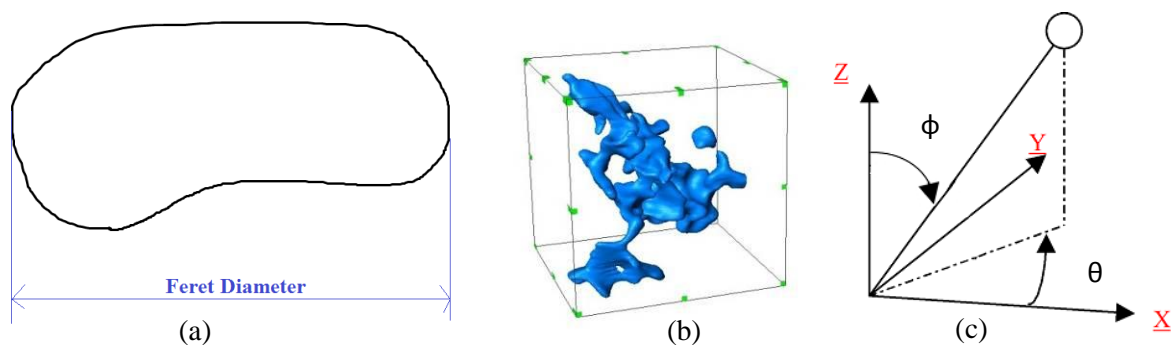


Figure 3-11 Illustrations of (a) Feret diameter, (b) minimum bounding box and (c) 3D coordinate system in Avizo software (ZIB et al. 2012)

A **granulometric analysis** was performed in ImageJ to measure the thickness distribution of a given phase. Granulometry estimates objects sizes using morphological opening operations: openings are performed step by step with an increasing structuring element size until all objects in the volume have

## Chapter 3 Material Characterization

---

disappeared in the input binary image. The number of positive pixels still present in the image is collected after each step, i.e. opening operation. Then the distribution of the volume fraction of objects as a function of structuring element size could be computed (Boulos et al., 2012). For a sphere, Equivalent diameter = Feret diameter = Maximum value of Granulometry.

A custom parameter ‘**sphericity** (F)’ was introduced according to equation (3-3) in the “Quantification tools” of Avizo in order to differentiate segmented pores with different 3D shape according to the proposition in (Kastner et al., 2011). This parameter corresponds to the ratio between the object volume and the volume of a sphere having the same surface as the object:

$$F = 6\sqrt{\pi} \frac{volume}{\sqrt{surface^3}}, \text{ ideal sphere } F=1 \quad (3-3)$$

Objects that are less than 8 voxels in volume were neglected in the analysis as they were considered as below the image resolution. This filtering operation cannot be achieved reasonably in two-dimensional analysis, because small objects in a 2-D plane (even as small as one pixel) may be part of a larger object with a complex structure or the boundary of a large object.

### 3.3 ‘Phases’ morphologies and sizes

The studied A319 alloy has been fully characterized in 2D using SEM/EDS and OM for a detailed understanding of its microstructure constituents and features. Then, it was characterized in 3D using laboratory and synchrotron tomography. Besides, A356 alloy, which was also used in this study, was roughly characterized in 3D in order to compare with A319 alloy. The quantitative analysis results of 2D characterization in (Tabibian, 2011) were used for comparison purpose.

#### 3.3.1 Microstructure of A319 alloy

Pores, intermetallics, Al<sub>2</sub>Cu, Pb and Si phases in Specimen 1 (A319) were analyzed deeply in this part. As presented in Appendix I, although the phase segmentation could not be performed accurately using synchrotron and laboratory tomography, the error in the quantitative analysis remains limited. Due to the lower resolution in Specimen 2 (A319), only pores were analyzed thoroughly.

##### 3.3.1.1 Pores

The typical casting defects, i.e. shrinkage and gas pores, are revealed by using OM in Figure 3-12 and by using SEM in Figure 3-13 . They have the minimum grey value (closest to the black) in the BSE images and could be distinguished by their morphologies. Shrinkage porosity presents coral-like appearance with complex microstructure, whereas gas porosity has an approximate spherical shape.

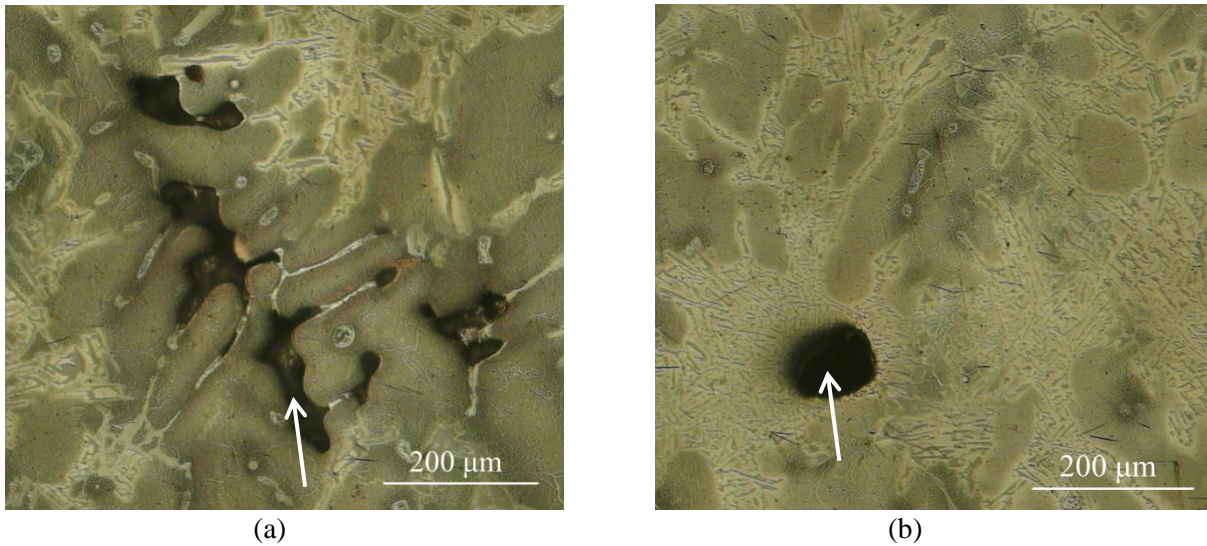


Figure 3-12 OM images of A319 alloy: (a) shrinkage and (b) gas pores (after etching)

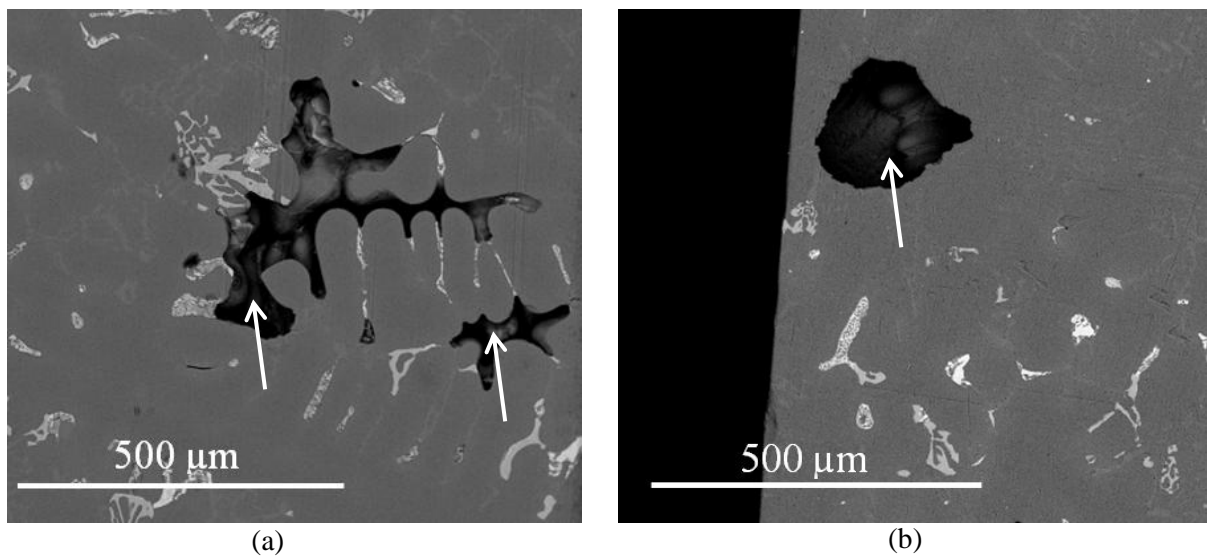


Figure 3-13 BSE images of A319: (a) shrinkage and (b) gas pores

Pores in A319 alloy were characterized in 3D using Lab-CT at two resolutions: a high resolution (voxel size = 1.5  $\mu\text{m}$ ) in a small volume for Specimen 1 and a low resolution (voxel size = 3  $\mu\text{m}$ ) but in a larger volume for Specimen 2.

### ✓ 3D characterization with a 1.5 $\mu\text{m}$ voxel size (Specimen 1)

The relation between equivalent and Feret diameters in Figure 3-14 shows that the difference between the two is not large for small pores, which are expected to be almost spherical. However, the gap between the two definitions of diameter is growing larger for some pores (e.g. pores marked with a green circle in Figure 3-14) with an increase of the object size; this implies that the morphology of these large objects is more complex than for other more rounded pores (e.g. pores marked with a black circle in Figure 3-14) for which the gap remains small. In fact, this conclusion matches the 3D morphologies shown well in Figure 3-15. The small pores whose Feret diameter is less than 20  $\mu\text{m}$  are

## Chapter 3 Material Characterization

usually small spheres as shown in Figure 3-15(a); they probably correspond to round gas pores. The largest pore, either in Feret or equivalent diameter, is marked out in Figure 3-15(c) and marked with a red circle in Figure 3-14. This is a shrinkage pore with a complex structure, which is shown in a close-up view in Figure 3-16. A few large pores may also have spherical morphology, e.g. pores marked with a dark circle in Figure 3-14 as shown in Figure 3-15(c).

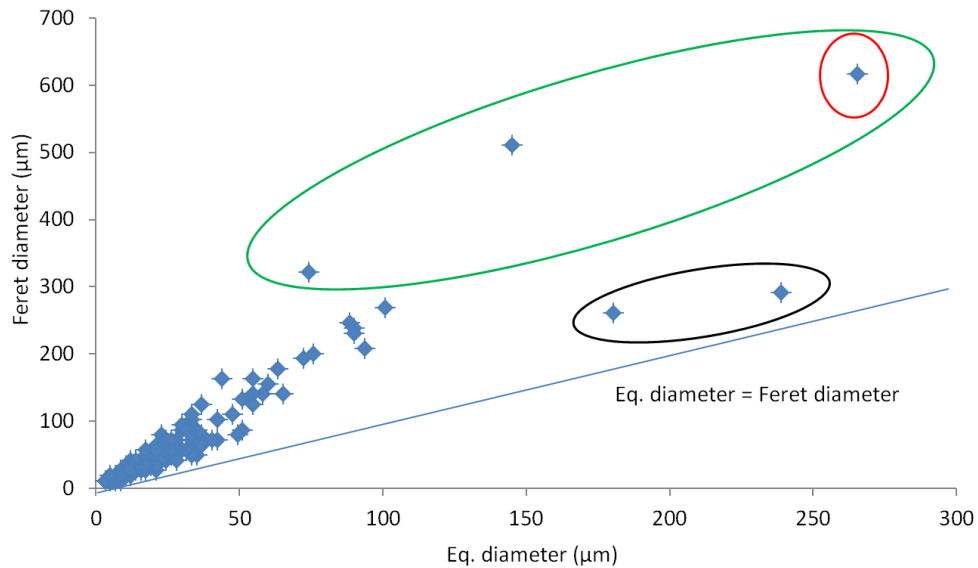


Figure 3-14 Relation between equivalent and Feret diameters of pores (Specimen 1)

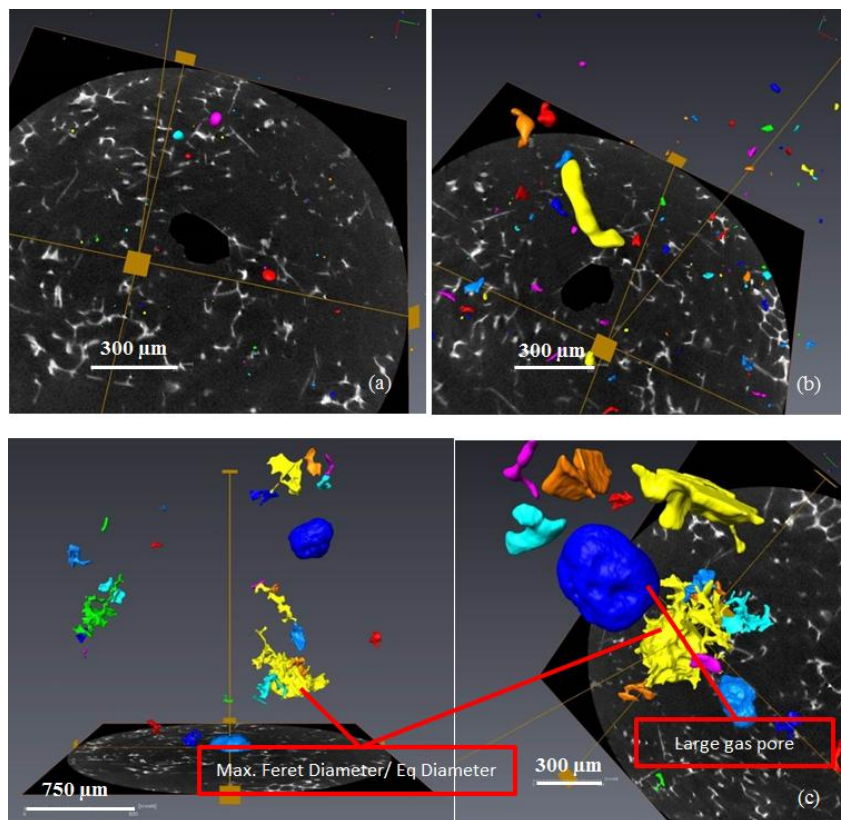


Figure 3-15 3D renderings of pores having a Feret diameter (a) less than 20 μm, (b) 20-100 μm, (c) more than 100 μm (Specimen 1)

## Chapter 3 Material Characterization

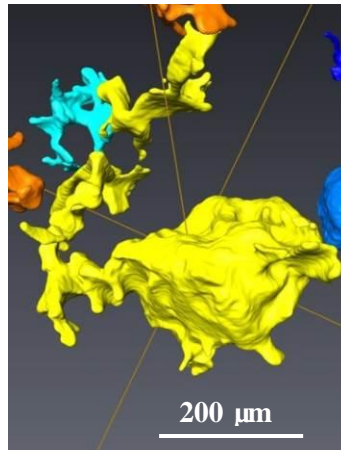


Figure 3-16 A close-up view of the largest pore (in yellow) in Figure 3-15

The quantitative analysis of pores in Specimen1 is presented in Table 3-6 in order to compare with the 2D analysis results. The maximum and average equivalent diameters were larger in the 3D results for the same reasons as an interconnected large pore in 3D may be divided into several objects in 2D measurements.

Table 3-6 2D and 3D results of pores in A319 alloy

	3D Results (Specimen 1)	2D Results(Tabibian, 2011)
Max Eq. diameter ( $\mu\text{m}$ )	267	211.1
Average Eq. diameter ( $\mu\text{m}$ )	13	10
Max Feret diameter ( $\mu\text{m}$ )	615	-
Average Feret diameter ( $\mu\text{m}$ )	25	-
Number of objects	628	-
Volume fraction %	0.37	0.56

The volume fraction of the large pores marked with a red circle in Figure 3-17 represents more than 90% of the total volume of pores. Large pores are all the more important to analyze as they are expected to have a critical influence on fatigue. The Feret diameter is able to characterize not only the volume of pores, like the equivalent diameter does, but also their morphology, which is very important for the fatigue behavior. However, several peaks situated around 20  $\mu\text{m}$  and between 120 and 250  $\mu\text{m}$  in granulometry distribution (Figure 3-18) cannot reflect the reasonable size of pores in Figure 3-15. Granulometry reflects the local thickness statistically instead of the size of each object. As a result, **the Feret diameter is more suitable to reflect the 3D size of the pores. Hence Feret diameter is chosen for the following analysis.**



## Chapter 3 Material Characterization

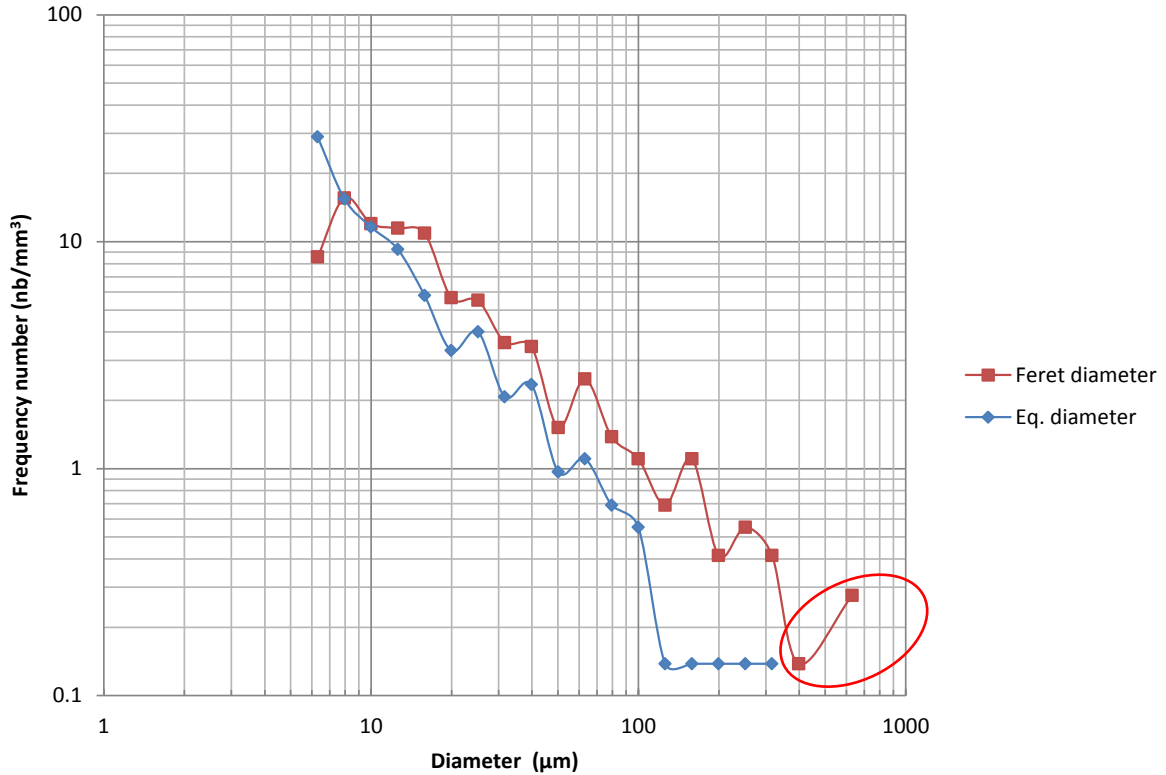


Figure 3-17 Distributions of pores as functions of equivalent and Feret diameters (Specimen 1)

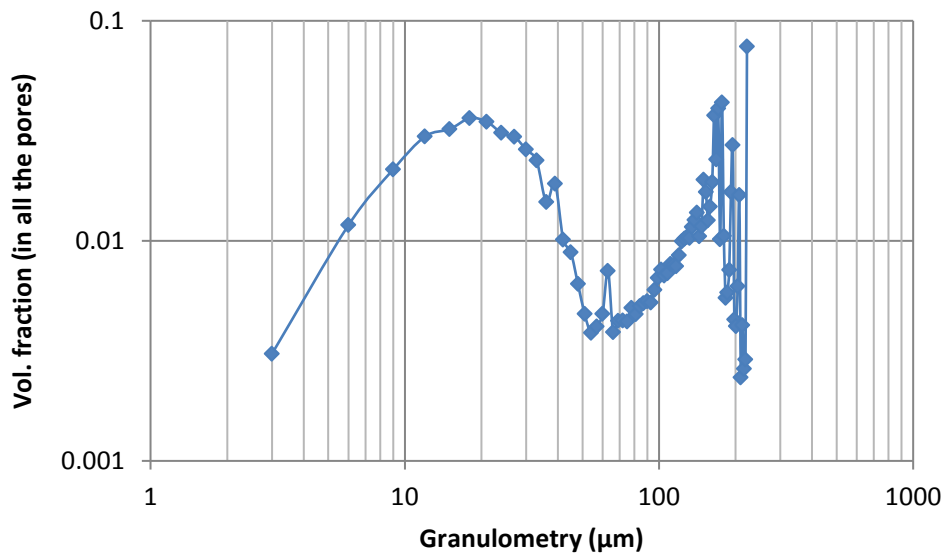


Figure 3-18 Granulometry distribution of pores (Specimen 1)

The porosity in Specimen 1 was analyzed separately in the eight scans performed. The main 3D parameters (maximum and average Feret diameter and volume fraction obtained with the “Analysis\_3D” plugin) are illustrated in Figure 3-19. Large differences were observed in the maximum Feret diameter and volume fraction between the eight scans (which correspond to different

## Chapter 3 Material Characterization

parts of the sample). **Therefore a large scan volume is required to obtain a representative characterization of pores.**

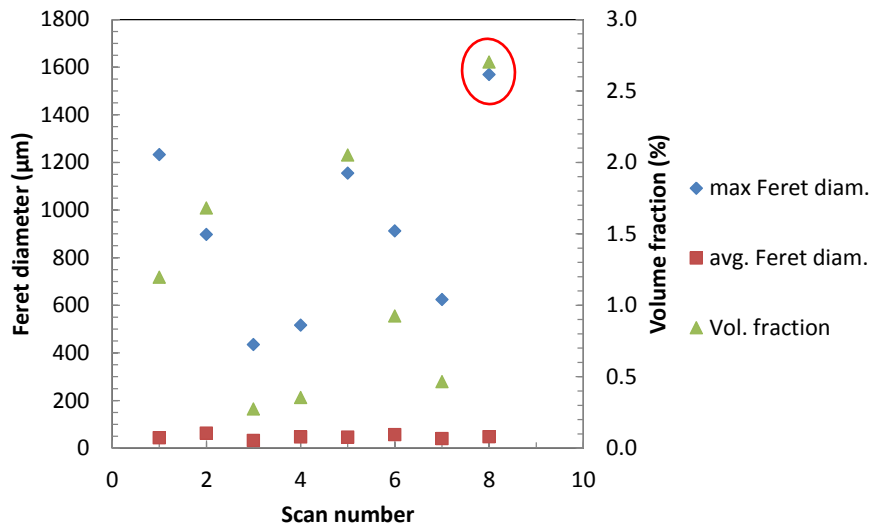


Figure 3-19 Variability of 3D analysis results of pores between scans (Specimen 1)

### ✓ 3D characterization with a voxel size of 3 μm (Specimen 2)

A much larger volume was then scanned for Specimen 2, and the basic 3D results for pores are listed in Table 3-7. The distributions as a function of the Feret diameter for Specimens 1 and 2 are plotted in Figure 3-20. The volume fraction of pores in Specimen 2 is very close to the average volume fraction of the eight scans in Specimen 1 (Figure 3-19). However, the analysis of Table 3-7 and Figure 3-20 proves that an increase of the scan volume results in a significant increase in the maximum and average diameters (either with an equivalent or Feret definition) in the 3D results of Specimen 2. For the maximum diameter, this can easily be explained as the large pores could be cut off or absent in the 3D images of smaller scan volume. Indeed, Figure 3-20 shows that, with an increase of the scanned volume, larger pores are revealed. The size of the largest pore in Specimen 2 (1516 μm in Table 3-7) is close to the maximum Feret diameter among all the eight scans performed on Specimen 1 (marked with a circle in Figure 3-19).

The evolution of the average diameter with the scanned volume should be considered with more caution as the change in pixel size results in a large change in the minimum pore's size considered in the analysis, i.e. objects less than 8 voxels ( $27\mu\text{m}^3$  for Specimen 1 and  $216\mu\text{m}^3$  for Specimen 2) in volume are indeed neglected.



## Chapter 3 Material Characterization

Table 3-7 3D and 2D results of pores in A319 alloy

	3D Results		2D Results Studied surface = 51.27 mm <sup>2</sup> (Tabibian, 2011)
	Specimen 1 voxel size 1.5 $\mu\text{m}$ Studied volume = 7.24 $\text{mm}^3$	Specimen 2 Voxel size 3 $\mu\text{m}$ Studied volume = 70.54 $\text{mm}^3$	
Max Eq. diam. ( $\mu\text{m}$ )	267	502	211.1
Average Eq. diam. ( $\mu\text{m}$ )	13	30	10
Max Feret diam. ( $\mu\text{m}$ )	615	1516	-
Average Feret diam. ( $\mu\text{m}$ )	25	66	-
Number of objects	628	1531	-
Volume fraction (%)	0.37	0.99	0.56

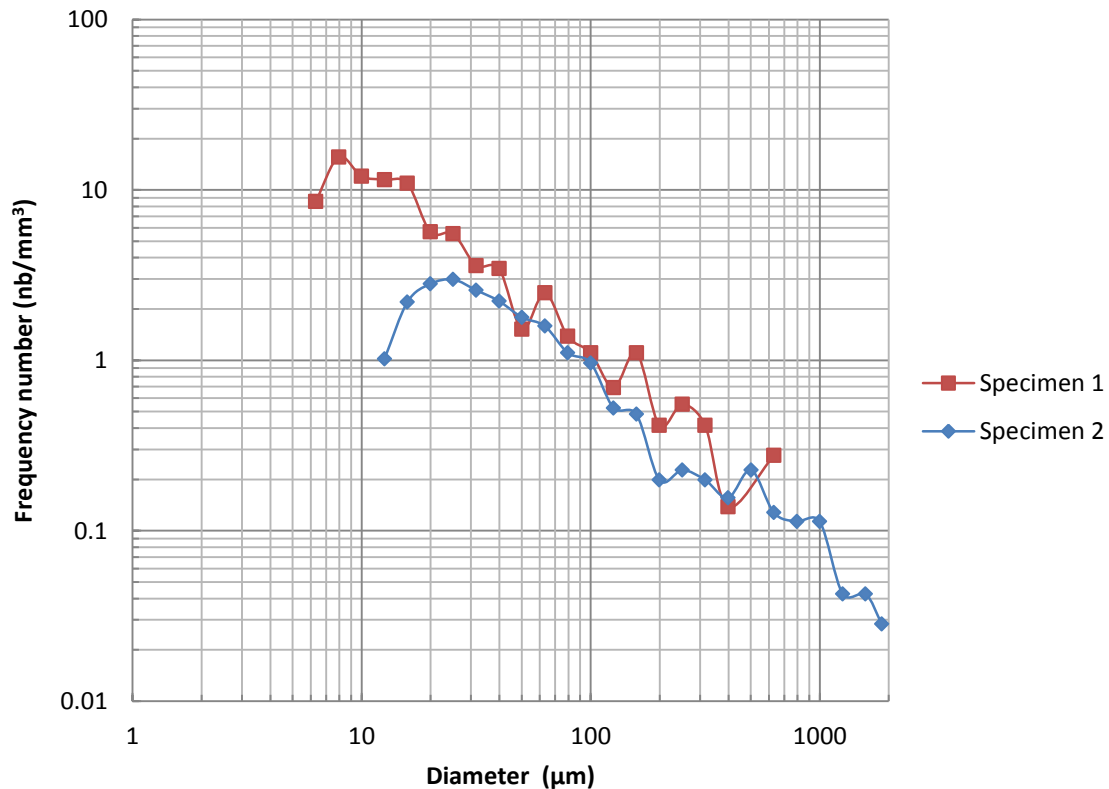


Figure 3-20 Distributions of Feret diameter of pores in Specimens 1 and 2

The 3D renderings of pores in Specimen 2 are shown in Figure 3-21 for different ranges of Feret diameter. Compared to Specimen 1 (Figure 3-15), larger shrinkage pores were revealed in a larger scan volume. The largest pore in this scan, which has the largest volume (equivalent diameter) and the largest Feret diameter, is marked out in Figure 3-21(d). The quantitative analysis shows that the volume fraction of the largest 50 pores among a total population of 1531 pores is more than 90% of

## Chapter 3 Material Characterization

the total volume of pores; this suggests that the large pores may play a more important role than the small pores. Due to its large size, Specimen 2 allowed studying a larger population of pores in one single scan and especially revealing more large pores, which are of utmost importance for fatigue, while the loss in resolution remains limited.

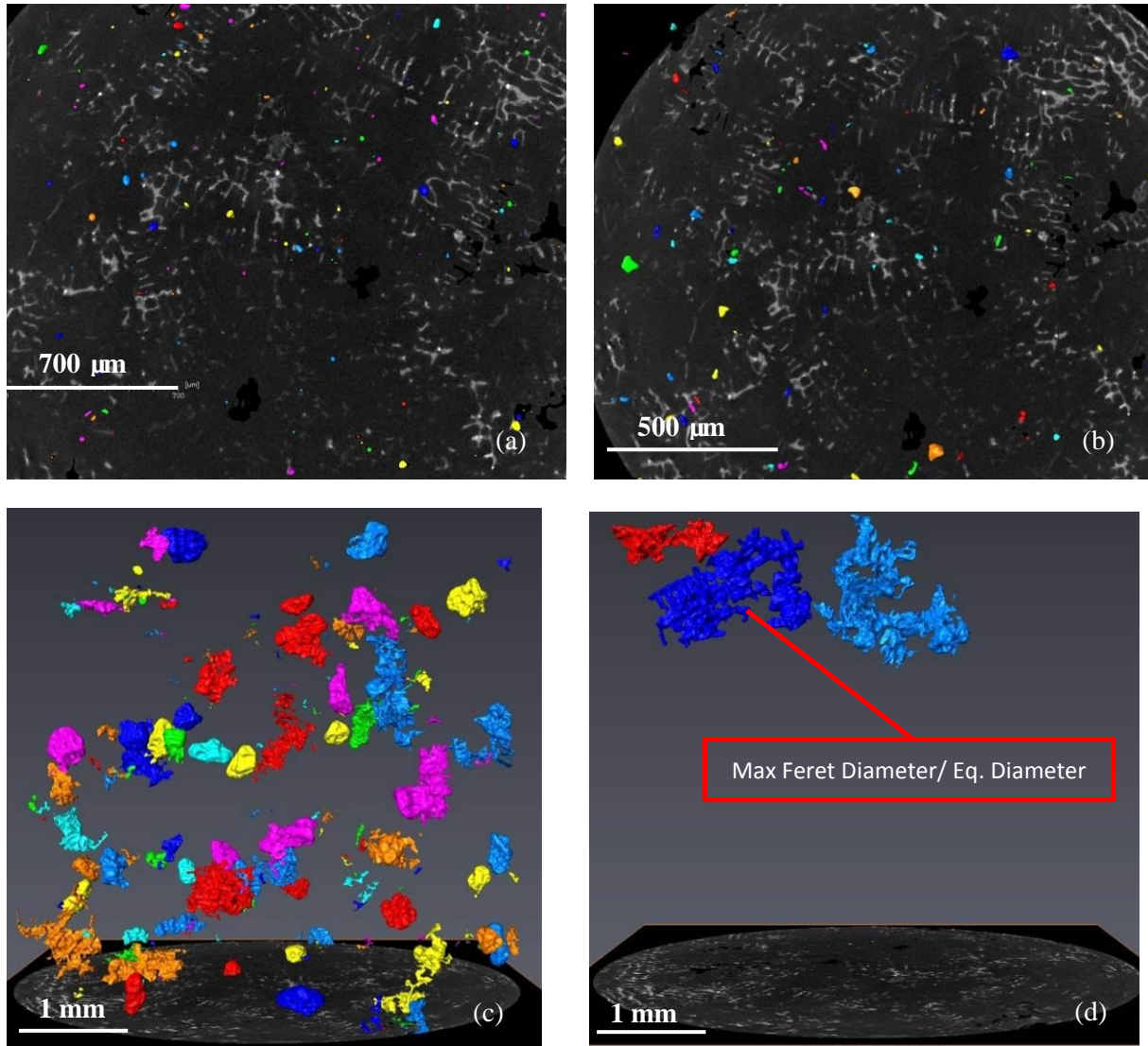


Figure 3-21 3D renderings of pores having a Feret diameter (a) less than  $60\ \mu\text{m}$ , (b)  $60\text{-}100\ \mu\text{m}$ , (c)  $100\text{-}1200\ \mu\text{m}$  and (d) more than  $1200\ \mu\text{m}$  (Specimen 2)

Among the parameters that were tested to filter the pores with different morphology, the custom parameter ‘sphericity (F)’ (see §3.2.4.3) was found to be extremely effective. After some trials (filtering tests performed with different ‘sphericity (F)’ values) it appears that pores with different morphology, i.e. rounded or tortuous, could be differentiated according to  $F > 0.4$  and  $F < 0.4$ .

3D images of pores with  $F > 0.4$  are shown in Figure 3-22(a) and their distributions as a function of Feret diameter are shown in Figure 3-23. The pores with  $F > 0.4$  are usually spherical and have a relatively small volume. Their number is 1430, which is 93.4% of the total number of 1531, but their

## Chapter 3 Material Characterization

volume is only 23.37% of the total volume of pores. The morphology of pores with  $F > 0.4$  is close to the spherical shape of gas porosity.

The 3D images of pores with  $F < 0.4$  are shown in Figure 3-22(b). Pores with  $F < 0.4$  usually have complex structures and relatively large volumes. Stress concentration is more likely to occur at the tip of pores having a tortuous microstructure. Their number is only 101, which is only 6.6% of the total number of 1531, but their volume is 76.63% of the total volume of pores. The morphology of pores with  $F < 0.4$  is like shrinkage porosity.

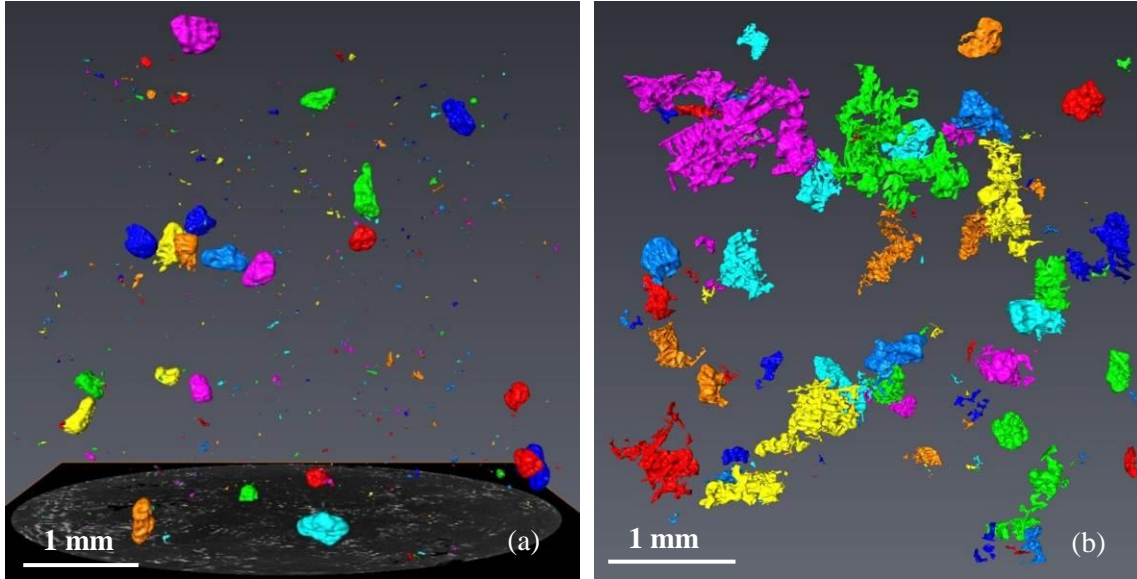


Figure 3-22 3D rendering of pores having sphericity factor: (a)  $F > 0.4$  and (b)  $F < 0.4$  (Specimen 2)

Charkaluk et al. recently proposed a method to establish and identify a probability density function characterizing the fatigue lifetime (Charkaluk et al., 2014). This method is initiated with a quantitative analysis of the microstructure of the A319 alloy based on SEM observations, which provides the initial probability distribution of defects. The formula and the parameters (shown in (equation (3-4)) in (Charkaluk et al., 2014) are adopted here as the material is exactly the same as the studied A319 alloy. The curve so obtained (in Figure 3-23) fits well to the distribution of pores having sphericity factor larger than 0.4. However, the second peak in the tail of the distribution cannot be fitted.

$$Pa = \frac{1}{a\sigma\sqrt{2\pi}} \exp\left[-\frac{[\ln(x)-\mu]^2}{2\sigma^2}\right], \sigma = 0.991, \mu = -3.264 \quad (3-4)$$

Actually, the curves drawn using equation (3-4) cannot fit the distribution of pores having sphericity factor smaller than 0.4 (see Figure 3-23) even if the parameters  $\sigma$  and  $\mu$  are adjusted.

A probabilistic thermal-mechanical fatigue criterion for LFC aluminum alloys based on 3D porosity distribution obtained from the 3D characterization in Specimen 2 has been developed in a report of École Polytechnique (Palaiseau, France) (Nanakasse, 2013) and in the works of Szmytka et al.

## Chapter 3 Material Characterization

(Szmytka et al., 2014). Thus a thorough characterization of the pores in A319 alloy also provides a strong support for fatigue life prediction.

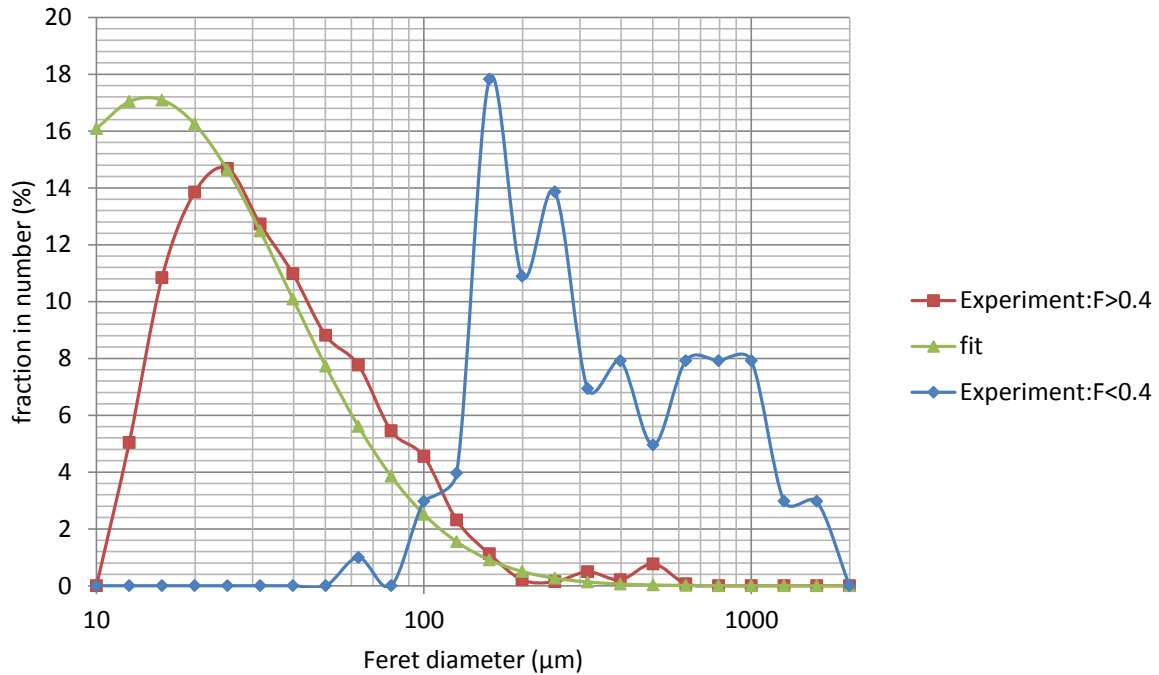


Figure 3-23 Distributions of pores ( $F > 0.4$  and  $F < 0.4$ ) as functions of Feret diameter as compared to the fitting curve in (Charkaluk et al., 2014).

3D characterization of pores also allows Dendrite Arm Spacing (DAS) being measured in 3D. These measurements were performed directly on the surface of 3D rendered shrinkage pores in Specimen 2 (see Appendix I). DAS measured in the 3D structure is shown in Table 3-8. The final measurements performed in 2D in (Tabibian, 2011) is 73.7  $\mu\text{m}$ . Unlike the measurements of pores size (Table 3-7), the difference of DAS measurements between 2D and 3D is small and less than the variability observed in one sample (either in 2D or 3D).

Table 3-8 DAS values measured on 3D images (Specimen 2)

number	L ( $\mu\text{m}$ )	n	DAS ( $\mu\text{m}$ )
1	301.86	4	75.47
2	254.87	4	63.72
3	266.65	3	88.88
4	175.93	3	58.64
5	345.02	3	115.01
6	630.94	9	70.10
<b>average</b>			<b>78.64</b>



## Chapter 3 Material Characterization

### 3.3.1.2 Si

Al matrix and eutectic Si are revealed in Figure 3-24 (a) using SEM and in Figure 3-24 (b) using OM. Al matrix occupies the largest surface area and presents dendritic morphology. In BSE image, Al matrix has the minimum grey value after porosity, and eutectic Si is just brighter than the Al matrix.

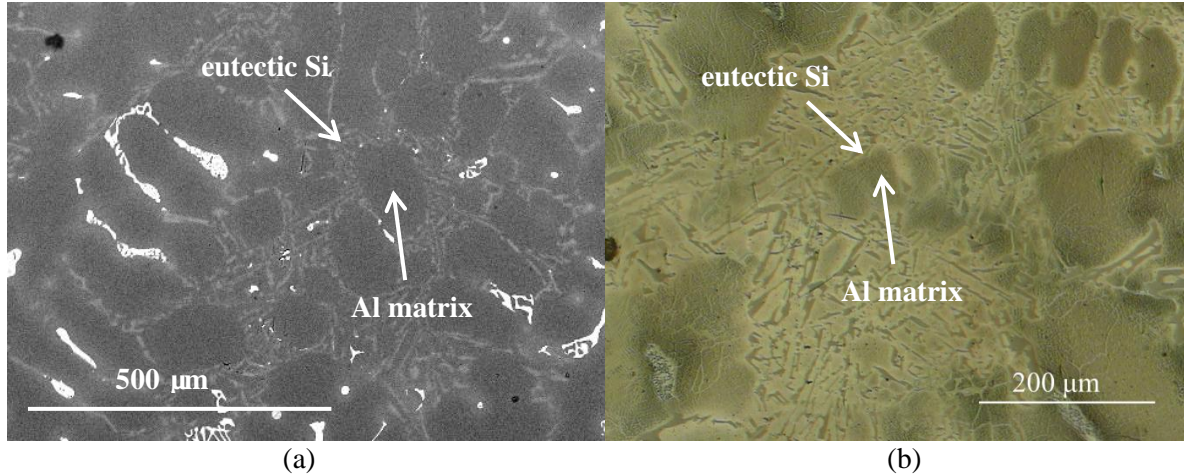


Figure 3-24 Al matrix and eutectic Si (A319, after etching) in (a) BSE and (b) OM images

Si phase, which cannot be distinguished from the Al matrix using Lab-CT due to the insufficient absorption contrast between Si and Al, was revealed using SR-CT with phase contrast. 3D renderings of Si phase (Specimen 1) are shown in a volume of  $500 \times 500 \times 500 \mu\text{m}^3$  in Figure 3-25(a) and in a small subvolume in Figure 3-25(b). The Si phase has a complex connected microstructure. Compared with the segmentation problem encountered for the intermetallics (see Appendix I), the segmentation of Si was even more difficult. As shown in Figure 3-26, if a large fraction of Si phase is not selected at a given threshold range, a large fraction of Al matrix is already selected due to noise. These effects can be observed in the results of segmentation tests shown in Table 3-9. Even if the threshold range varies by only one unit, the volume fraction of Si will vary by about 1% and this uncertainty could not be accepted. The maximum Feret diameter remains unchanged whatever the threshold range, because it already corresponds to the largest dimension of the studied volume. Thus Feret diameter is not suitable to characterize such a highly interconnected microstructure. This also tends to indicate that the networks of Si phase extend to the whole volume. However, the maximum object's volume changes dramatically with the variations of threshold range as shown in Table 3-9. The segmentation of Si phase is thus too sensitive to the selected threshold. Besides, by observing the BSE image in Figure 3-24 (a) and even the slice of SR-CT image in Figure 3-4(b), the Si phase, which is often very fine, could not be revealed precisely with the present resolution of tomography (voxel size =  $1.61 \mu\text{m}$ ). As a result, a quantitative analysis of Si phase could not be performed. Nevertheless, considering the complex connected microstructure of Si phase shown in Figure 3-25, **the granulometry**, which

## Chapter 3 Material Characterization

reflects the local thickness instead of the extent of the interconnected microstructure, **could be recommended to characterize the size of Si phase when it could be revealed more precisely.**

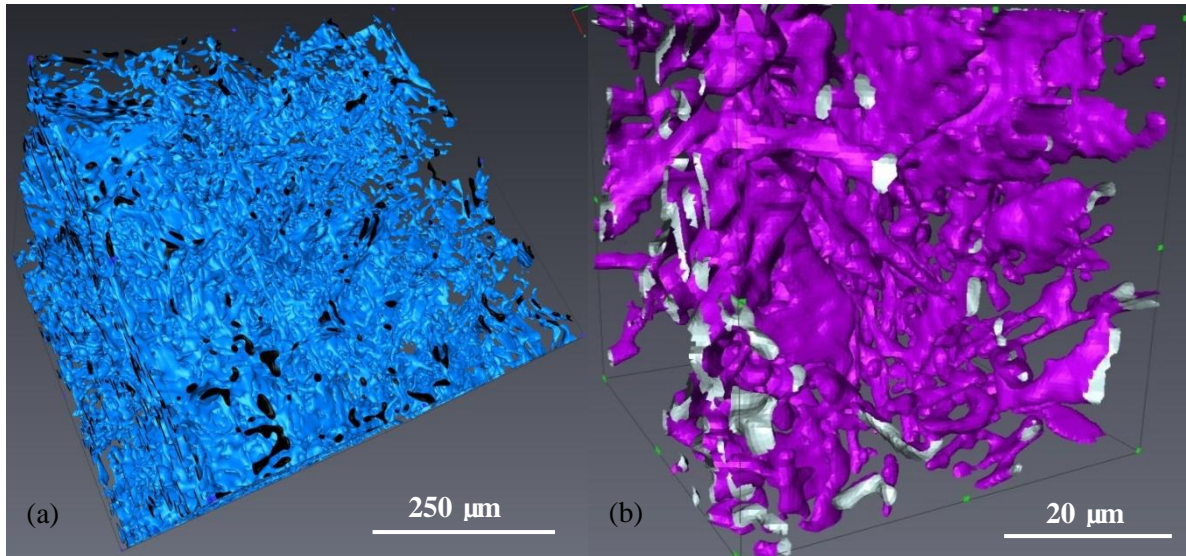


Figure 3-25 3D renderings of Si phase in (a) a volume of  $500 \times 500 \times 500 \mu\text{m}^3$  and (b) a subvolume

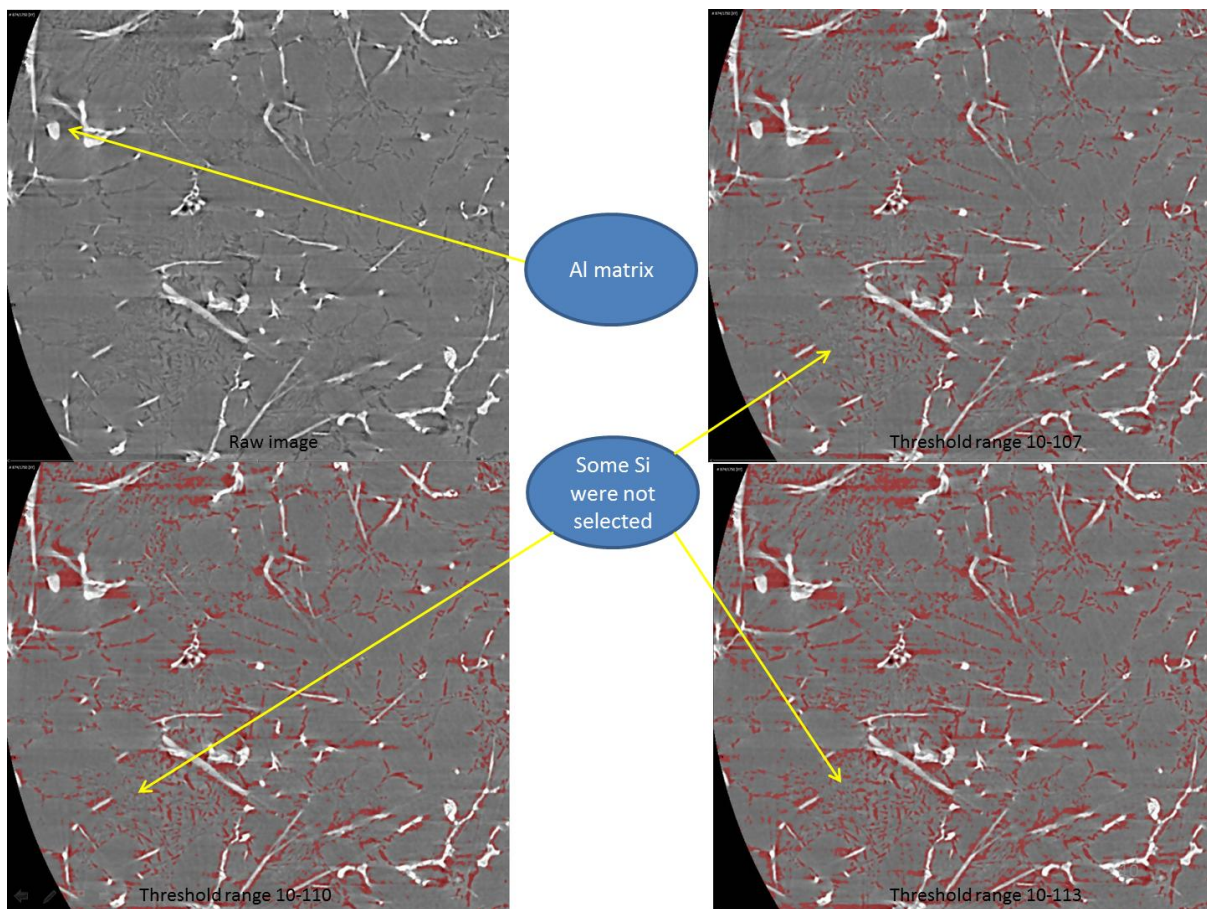


Figure 3-26 Illustration of the problem of threshold range selection for Si



## Chapter 3 Material Characterization

Table 3-9 Results of segmentation tests for Si phase

Range of thresholds	10-113	10-109	10-108	10-107	10-106
Max. Feret Diam. ( $\mu\text{m}$ )	3700	3701	3701	3701	3701
Volume of the object having max. Eq. and Feret diam. ( $\text{mm}^3$ )	1.97	1.23	1.10	0.97	0.86
Volume fraction (%)	16.11	10.61	9.73	8.95	8.25

### 3.3.1.3 Iron intermetallics

The iron intermetallics ( $\alpha$  and  $\beta$ ) revealed using OM in Figure 3-27 are confirmed using SEM, as OM cannot always distinguish them from other hard inclusions, such as Si phase and copper containing phase, while, they are easy to recognize using SEM (Figure 3-28). Thanks to chemical contrast, they are brighter than the Al-Si eutectic in the BSE image. Having close compositions,  $\alpha$  and  $\beta$  phases have similar gray values, so that it is impossible to distinguish them by their color. However, their morphologies are quite different.  $\alpha$  phase usually presents "Chinese script" morphology, while  $\beta$  phase almost always presents needle-like morphology. In addition, a method using SEM/EDS system proposed in (Rosefort et al., 2011) can be used to identify  $\alpha$  and  $\beta$  via the ratio  $\mu$  (equation (3-5)) of silicon to manganese plus iron content in the AlFeSi-phase:

$$\mu = \frac{\text{Si wt.}\%}{\text{Fe wt.}\% + \text{Mn wt.}\%} \quad (3-5)$$

$\alpha$  phase has a lower value of  $\mu$ , than  $\beta$ . The critical value of  $\mu$  used to distinguish the two phases in (Rosefort et al., 2011) and in this study is 0.5. In fact, in the present A319 alloy, there is usually no significant manganese content (less than 1 wt. %) detected in the  $\beta$  phase. Besides,  $\beta$  phase is less observed than  $\alpha$  phase. This proves that the use of Mn addition has worked effectively to favor  $\alpha$  rather than  $\beta$  intermetallic.

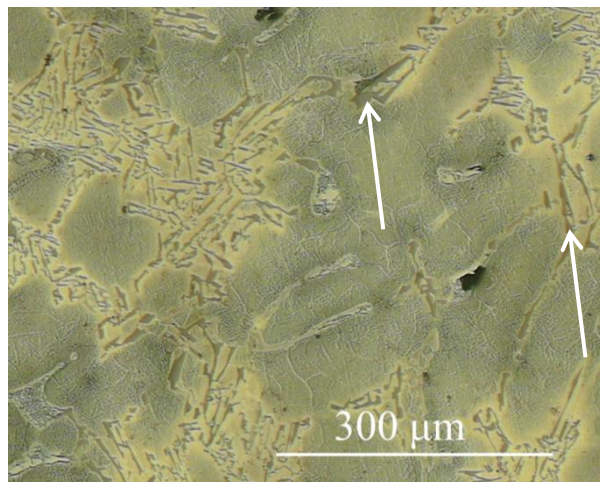


Figure 3-27 Iron intermetallics in OM image (A319, after etching).



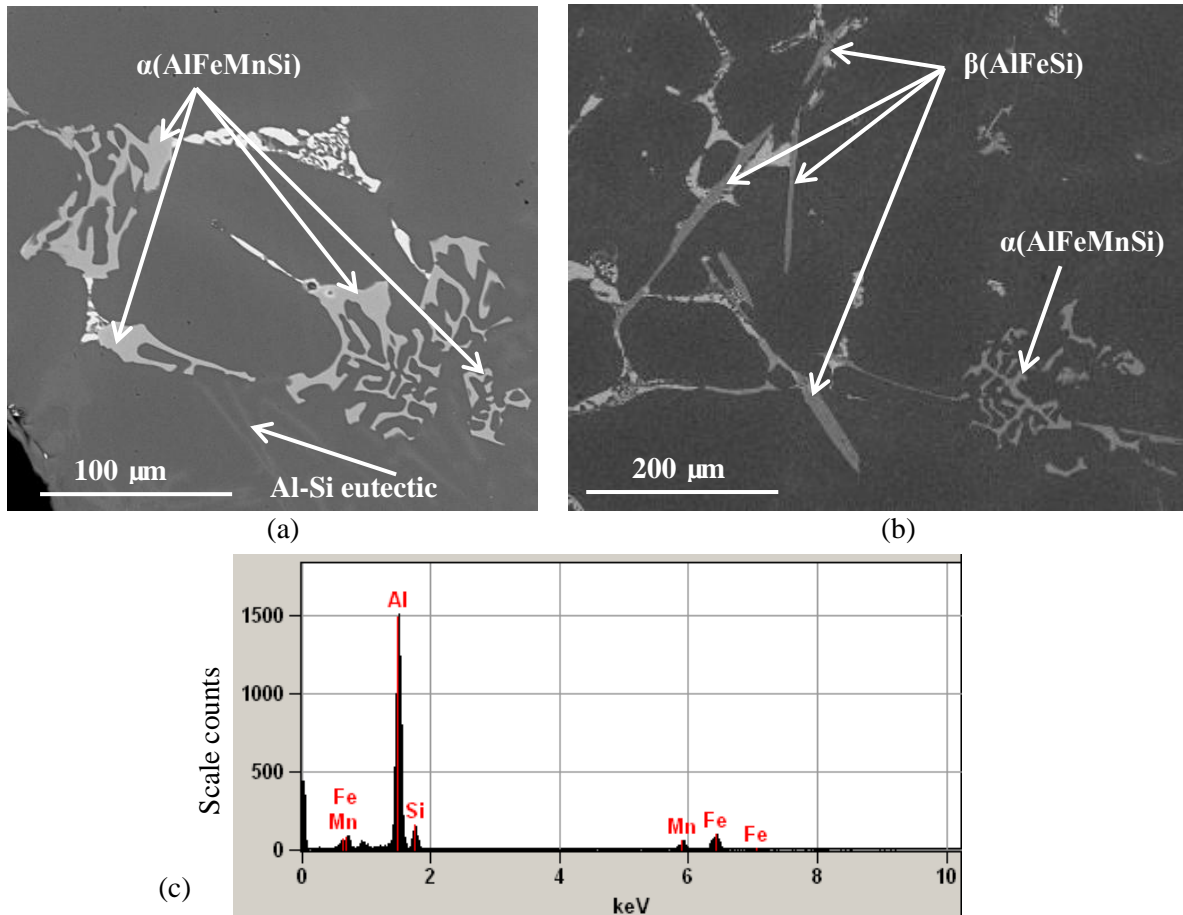


Figure 3-28 BSE image: (a)  $\alpha$  phase with "Chinese script" morphology; (b)  $\alpha$  phase and needle-like  $\beta$  phase (A319). (c) An example of EDS analysis on  $\alpha$  phase.

Volume fraction of the intermetallics phase in Specimen 2 is 5.18% whereas it is 7.36% in Specimen 1, which was scanned with a higher resolution. This result and the segmentation problems reported in Appendix I underline that the lower resolution (Specimen 2) and the lower contrast (Specimens 1 and 2) have a serious influence on the results although this difference may also be due to the different studied volume. Hence a higher resolution and a sufficient contrast are necessary to better characterize the intermetallics even if only a smaller volume could be characterized. The following 3D quantitative analysis of iron intermetallics was performed with a higher resolution, i.e. in Specimen 1. The results are shown in Table 3-10 in order to compare with the 2D analysis results. The maximum and average equivalent diameters are larger when measured in 3D as the complex microstructure cannot be characterized in 2D images where large structures are divided into a lot of smaller structures.

## Chapter 3 Material Characterization

Table 3-10 Comparisons between 3D and 2D results of iron intermetallics

	3D Results (Specimen 1)	2D Results (Tabibian, 2011)
Max Eq. diameter ( $\mu\text{m}$ )	924	188.81
Average Eq. diameter ( $\mu\text{m}$ )	13	10
Max Feret diameter ( $\mu\text{m}$ )	2917	-
Average Feret diameter ( $\mu\text{m}$ )	23	-
Number of objects	18569	-
Volume fraction (%)	7.36	3.45

The 3D renderings of intermetallics are shown in Figure 3-29 for different ranges of Feret diameter. The morphology of small objects (less than  $60\ \mu\text{m}$ ) is spherical at the present resolution. With the increasing of the object size, the morphologies of objects become more complex. The largest intermetallic in Figure 3-29 (d) has a complex connected microstructure that extends over the whole scan volume. Its size ( $2917\ \mu\text{m}$ ) is nearly the maximum dimension in the characterized volume and is much larger than for the other intermetallics (less than  $1000\ \mu\text{m}$ ).

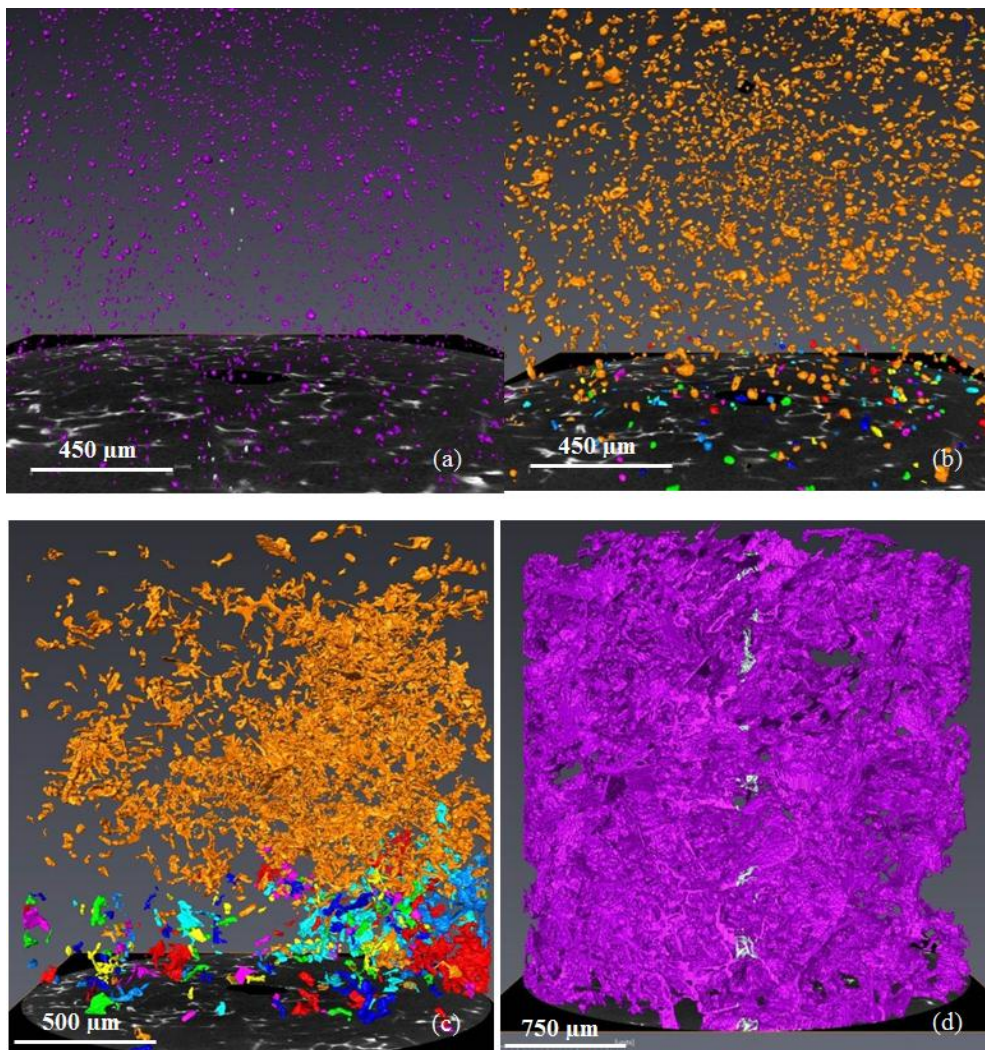


Figure 3-29 3D renderings of intermetallics having a Feret diameter (a) less than  $20\ \mu\text{m}$ , (b)  $20\text{--}60\ \mu\text{m}$ , (c)  $60\text{--}1500\ \mu\text{m}$ , (d) more than  $1500\ \mu\text{m}$

## Chapter 3 Material Characterization

A 2D cross-section from the 3D image and a 3D rendering of the intermetallics are shown in Figure 3-30 in order to illustrate the relation between the 2D and 3D microstructures. An intermetallic with a ‘Chinese script’ morphology is shown in a slice in Figure 3-31(a) and its 3D microstructure is shown in Figure 3-32(b). In fact this ‘Chinese script’ intermetallic is a part of the largest object shown in Figure 3-29(d).

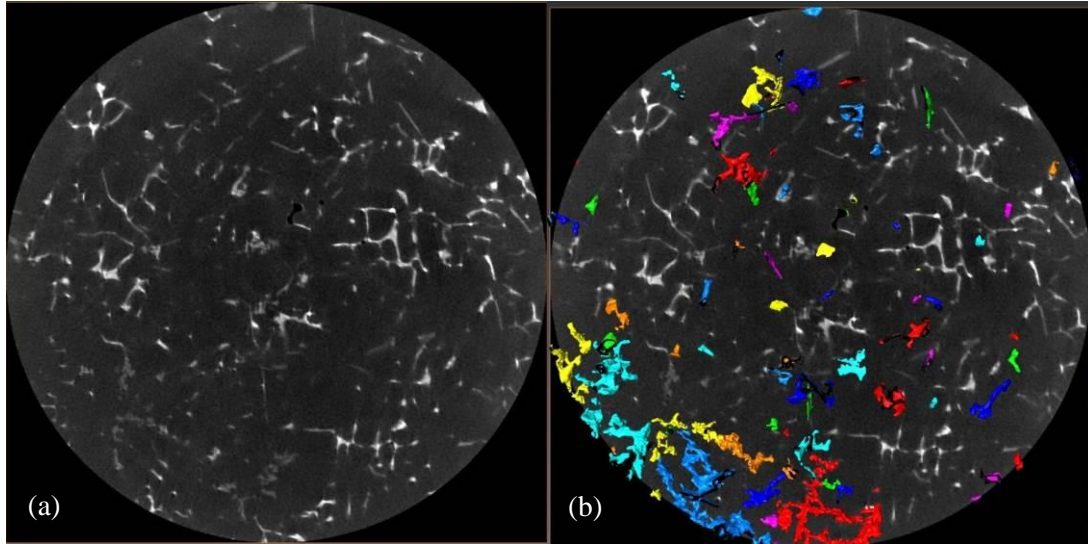


Figure 3-30 (a) A slice from the Lab-CT image with (b) 3D rendering of intermetallics

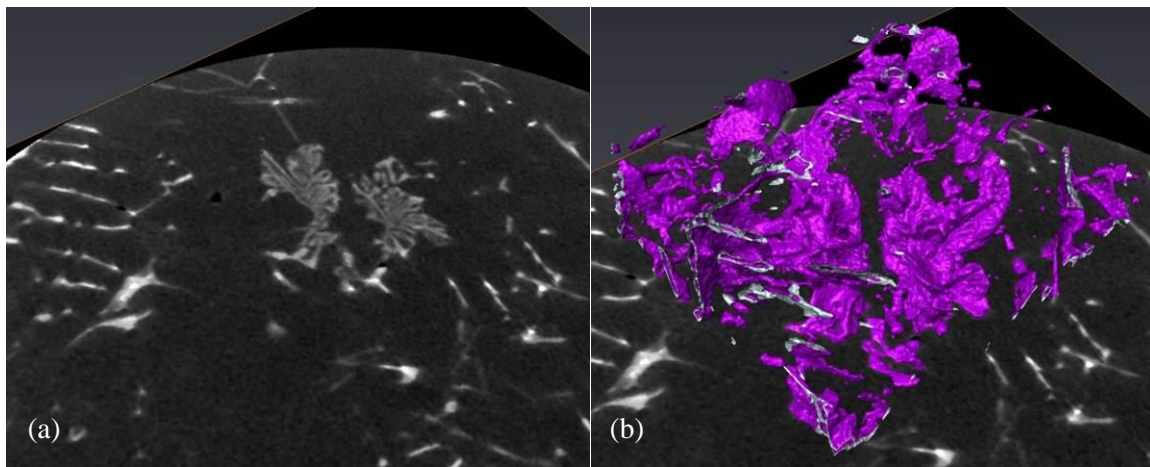


Figure 3-31 (a) A ‘Chinese script’ morphology with (b) 3D rendering

The distributions of iron intermetallics as functions of the equivalent and Feret diameters in Figure 3-32 are similar (more small size than large size objects in number). However, large intermetallics have larger sizes in Feret diameter than in equivalent diameter due to their complex and non-spherical morphologies (Figure 3-29(c) and (d)). The granulometry distribution of intermetallics in Figure 3-33 shows that their average thickness is slightly less than 10  $\mu\text{m}$  in the studied volume. Although the maximum thickness is about 28  $\mu\text{m}$ , the volume fraction of iron intermetallics with thickness larger than 20  $\mu\text{m}$  is very low (less than 1%).



## Chapter 3 Material Characterization

Neither the equivalent diameter nor Feret diameter (Figure 3-32) was fair to characterize the size of the intermetallics as their values are usually too large. The maximum Feret diameter corresponds to the largest dimension of the characterized volume as it is representative of the extent of the intermetallics network (Figure 3-29 (d)). This extended network is similar with that of Si phase. Although the maximum equivalent diameter is less than the maximum Feret diameter, it is only suitable for the characterization of objects having spherical morphologies and also relates to the extent of the intermetallics network as a large characterized volume results in a large volume of the maximum object. The distribution of granulometry (Figure 3-33) could better characterize the size of interconnected intermetallics. **Hence granulometry was recommended to characterize the size of intermetallics.**

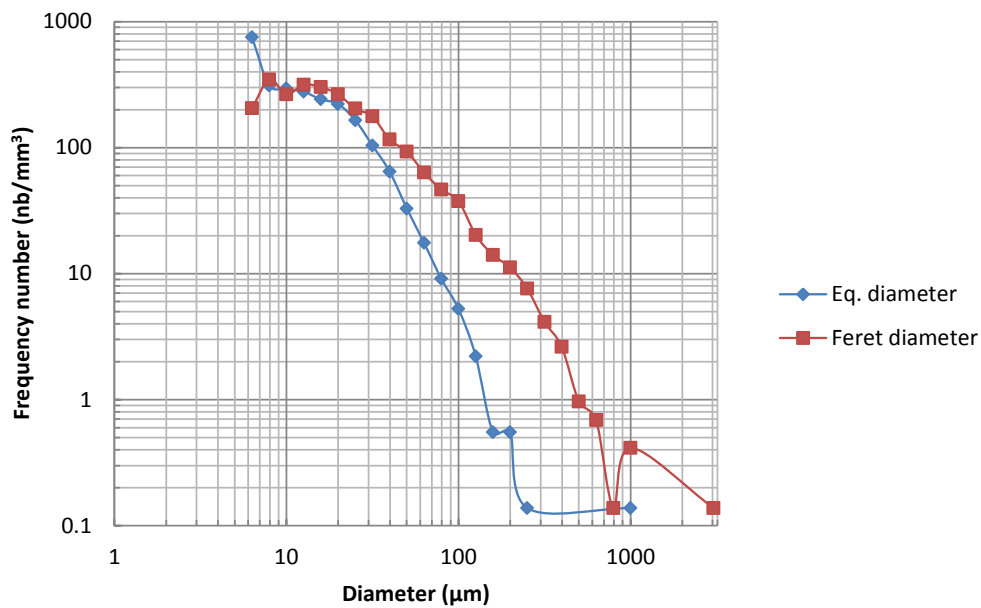


Figure 3-32 Distributions of intermetallics as functions of equivalent and Feret diameters

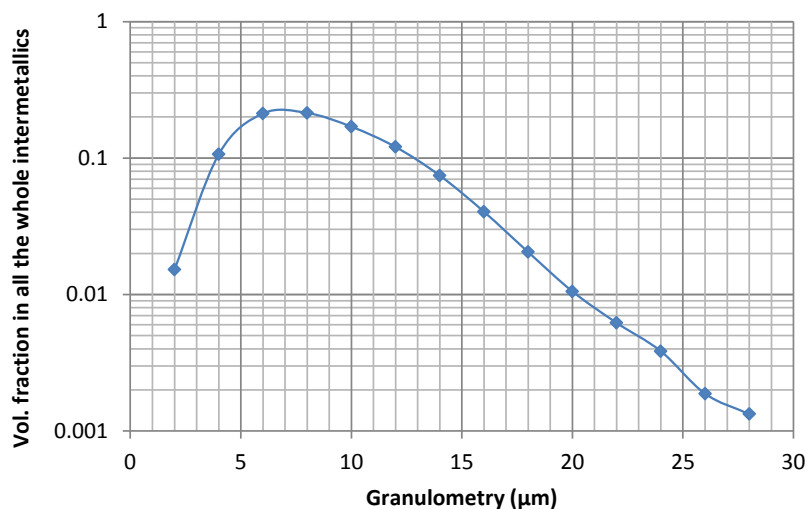


Figure 3-33 Granulometry distribution of intermetallics

## Chapter 3 Material Characterization

### 3.3.1.4 Copper containing phases

The copper containing phases ( $\text{Al}_2\text{Cu}$  and  $\text{AlCuMgSi}$  phases), are simultaneously revealed using OM in Figure 3-34, as  $\text{AlCuMgSi}$  phase cannot be distinguished from  $\text{Al}_2\text{Cu}$  phase and Al matrix due to the limit of resolution and contrast. They are better revealed using SEM in Figure 3-35. In the BSE images,  $\text{Al}_2\text{Cu}$  phase is brighter than the iron intermetallics and could thus be identified by its grey level.  $\text{AlCuMgSi}$  phase is a little darker than iron intermetallics but brighter than Al-Si eutectic, and it is always connected with the  $\text{Al}_2\text{Cu}$  phase. Both phases have a very complex microstructure. In Figure 3-35, the smaller size  $\text{AlCuMgSi}$  phase is attached to the larger size  $\text{Al}_2\text{Cu}$  phase. Besides, a localized densely punctate microstructure was also observed (marked with a circle in Figure 3-35). More examples of this kind of structure are shown in Figure 3-36(a) and in Figure 3-36 (b) at a higher resolution. In fact, they correspond to the connected microstructure of small size  $\text{Al}_2\text{Cu}$  and  $\text{AlCuMgSi}$  phases. The thickness of  $\text{AlCuMgSi}$  phase is usually less than 1  $\mu\text{m}$ , and that of  $\text{Al}_2\text{Cu}$  phase less than 10  $\mu\text{m}$  and sometimes less than 1  $\mu\text{m}$ . The copper containing phases may exist in the Al matrix as the connected microstructure (Figure 3-35), or it may connect with the Al-Si eutectic phase (Figure 3-36(a)), and sometimes with iron intermetallics ( $\alpha$  and  $\beta$ ) (Figure 3-37).

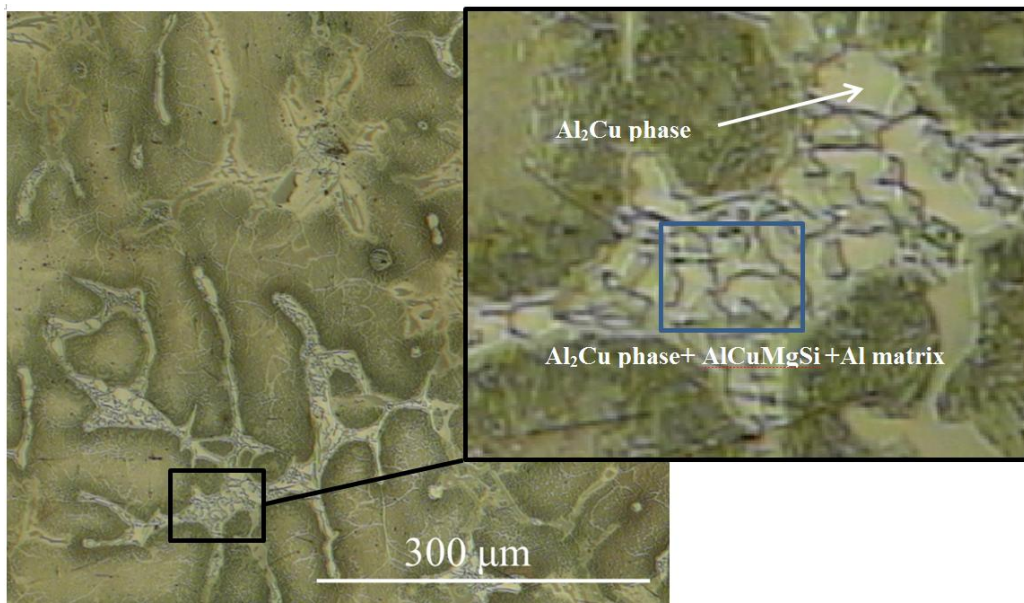


Figure 3-34 Copper containing phases ( $\text{Al}_2\text{Cu}$  and  $\text{AlCuMgSi}$ ) in OM image (A319, after etching).

## Chapter 3 Material Characterization

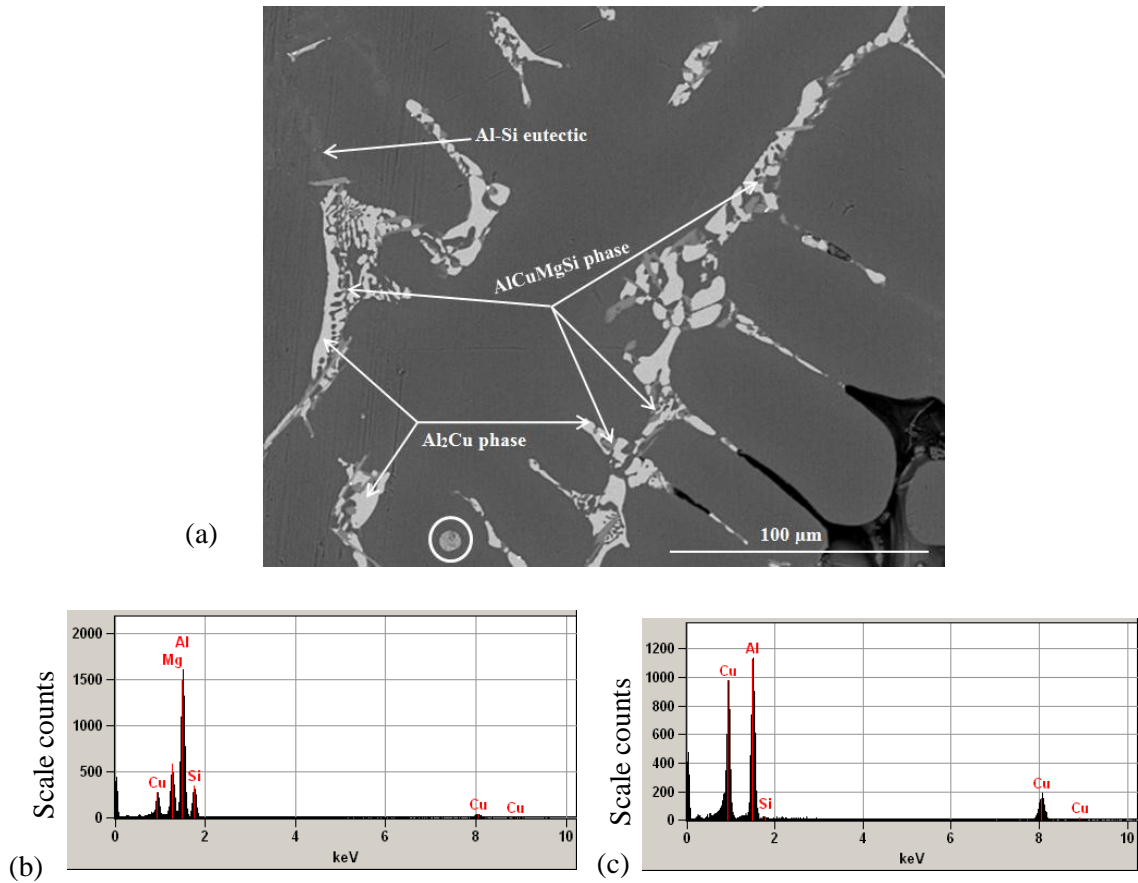


Figure 3-35 (a) BSE image: copper containing phases, Al<sub>2</sub>Cu and AlCuMgSi (A319), and a small connected microstructure of Al<sub>2</sub>Cu and AlCuMgSi phases marked with a circle. Examples of EDS analysis on (b) AlCuMgSi and (c) Al<sub>2</sub>Cu.

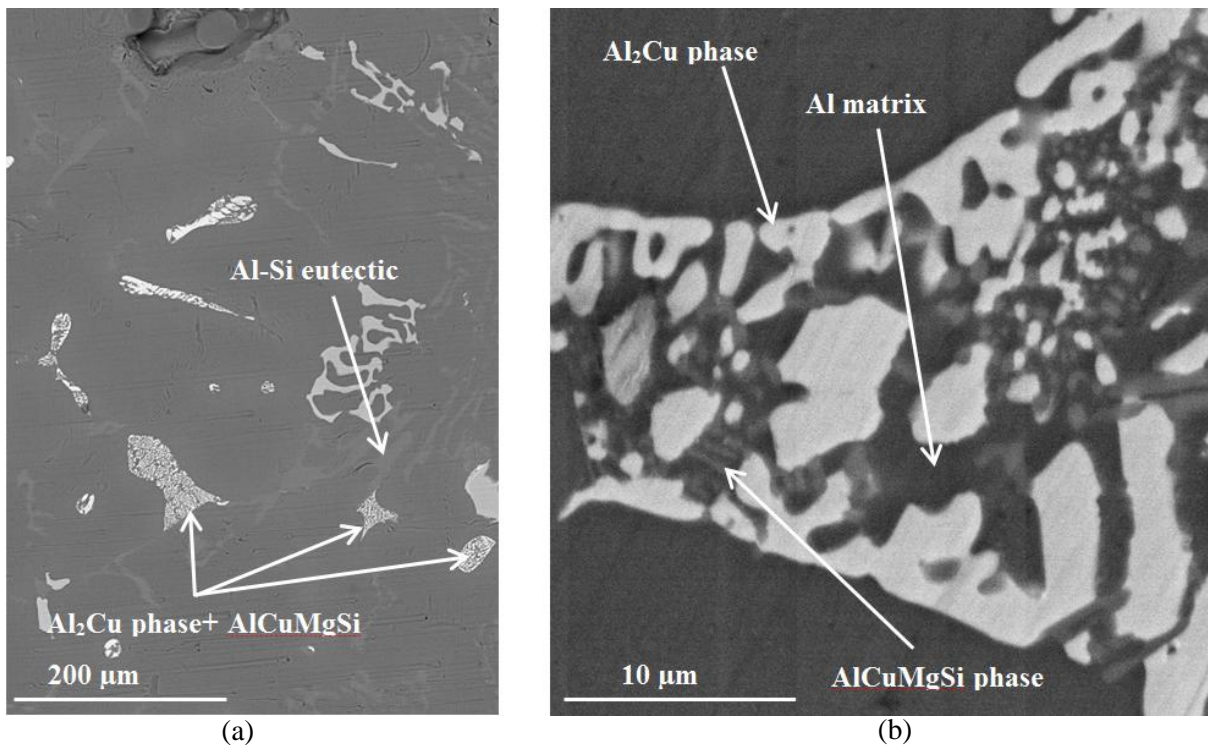


Figure 3-36 BSE images: (a) some small connected microstructure of Al<sub>2</sub>Cu and AlCuMgSi phases, and (b) a zoom on one example of this connected microstructure.

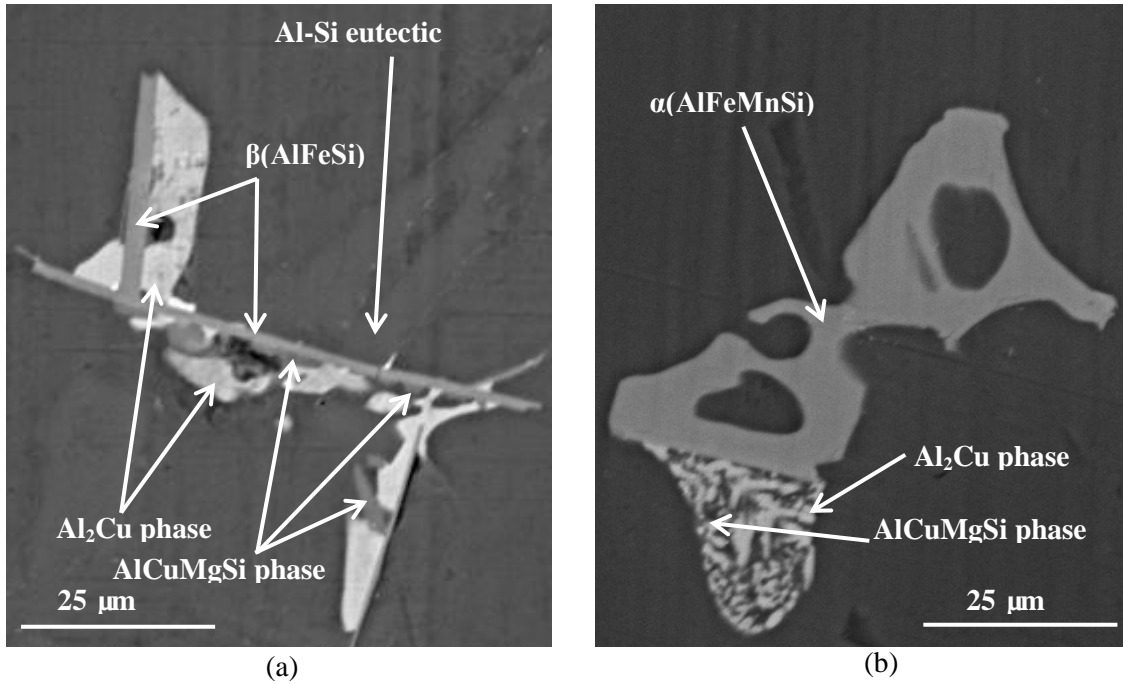


Figure 3-37 BSE images: copper containing phases connected with (a) Al-Si eutectic and  $\beta$  intermetallics and (b) with  $\alpha$  intermetallics

As mentioned above, the size of AlCuMgSi phase is usually too small, so it cannot be revealed with the present resolution of tomography. As a result, only Al<sub>2</sub>Cu phase was characterized in 3D. Despite the lower resolution for Specimen 2, the measured volume fraction of Al<sub>2</sub>Cu phase is 1.28% which is close to that in Specimen 1 (1.28%). Thus the lower resolution does not seem to have a significant effect on volume fraction. However, considering that the size of Al<sub>2</sub>Cu in 2D is usually less than 5  $\mu\text{m}$  and sometimes less than 1  $\mu\text{m}$ , a lower resolution cannot reveal the size of such a fine microstructure although the overall volume fractions are almost the same. Thus a higher resolution is necessary to the quantitative analysis of this phase. The 3D quantitative analysis of the Al<sub>2</sub>Cu phase was performed in Specimen 1 in the following. Results are summarized in Table 3-11 in order to compare with the 2D analysis results. The volume fractions in 3D and 2D are close; the maximum and average equivalent diameters are again larger in the 3D results as the complex microstructure cannot be characterized in 2D images where large structures are cut.

Table 3-11 Comparison of 3D and 2D results of Al<sub>2</sub>Cu

	3D results (Specimen 1)	2D results (Tabibian, 2011)
Max Eq. diameter ( $\mu\text{m}$ )	202	118.35
Average Eq. diameter ( $\mu\text{m}$ )	15	10
Max Feret diameter ( $\mu\text{m}$ )	987	-
Average Feret diameter ( $\mu\text{m}$ )	31	-
Number of objects	10802	-
Volume fraction %	1.28	1.30



## Chapter 3 Material Characterization

The 3D renderings of  $\text{Al}_2\text{Cu}$  are shown in Figure 3-38 for different ranges of Feret diameter. Similar with iron intermetallics, the small objects (less than  $20\ \mu\text{m}$ ) present spherical morphologies while large objects have morphologies that become more complex at increasing size. The object with the maximum volume and the object with the maximum Feret diameter are not the same as shown in Figure 3-38(d).

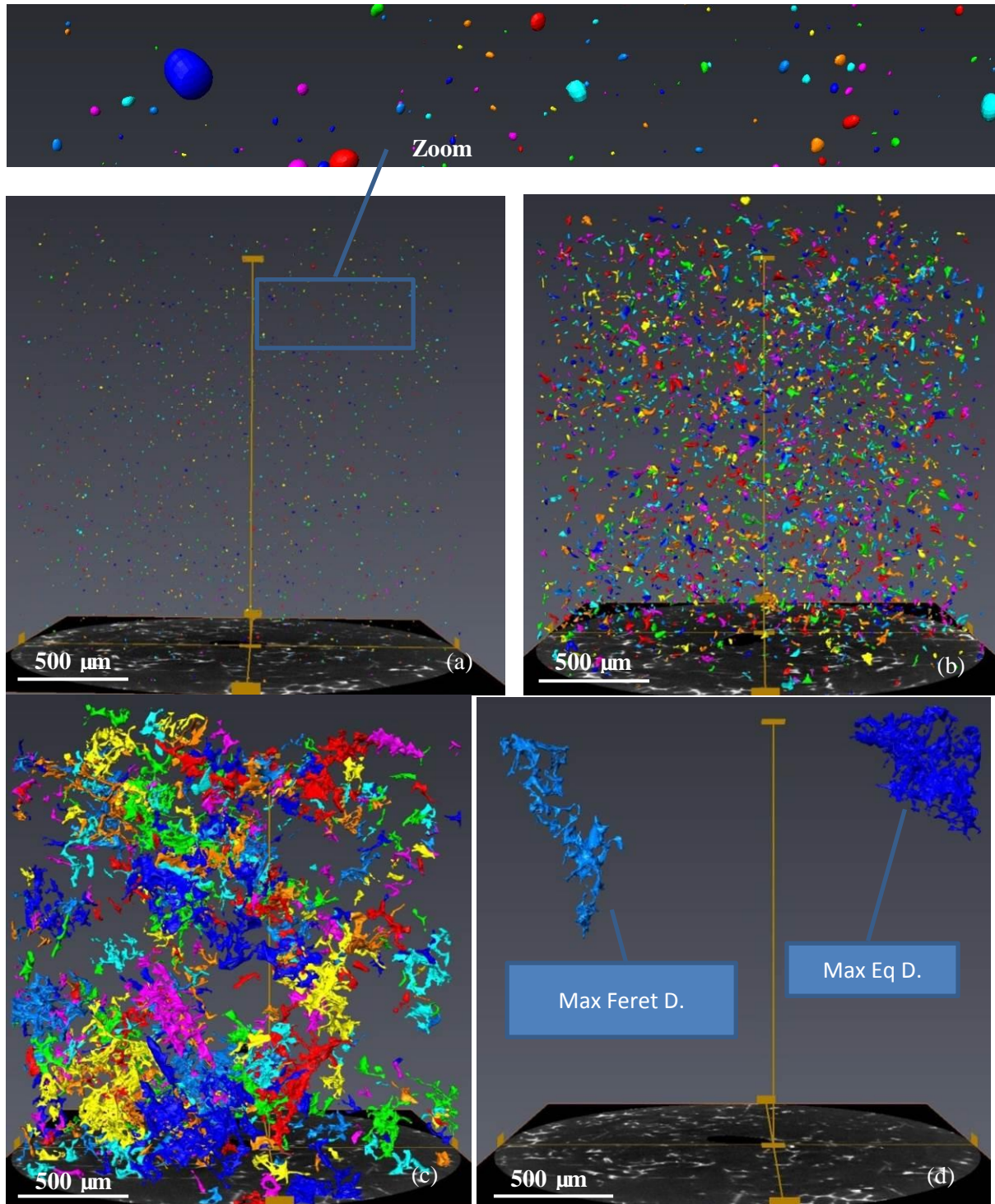


Figure 3-38 3D renderings of  $\text{Al}_2\text{Cu}$  having a Feret diameter (a) less than  $20\ \mu\text{m}$ , (b)  $20\text{-}90\ \mu\text{m}$ , (c)  $90\text{-}750\ \mu\text{m}$ , (d) more than  $750\ \mu\text{m}$

## Chapter 3 Material Characterization

A 2D cross-section from the 3D image and the corresponding 3D microstructure of  $\text{Al}_2\text{Cu}$  are shown in Figure 3-39 in order to observe the relation between the 2D and 3D microstructures.

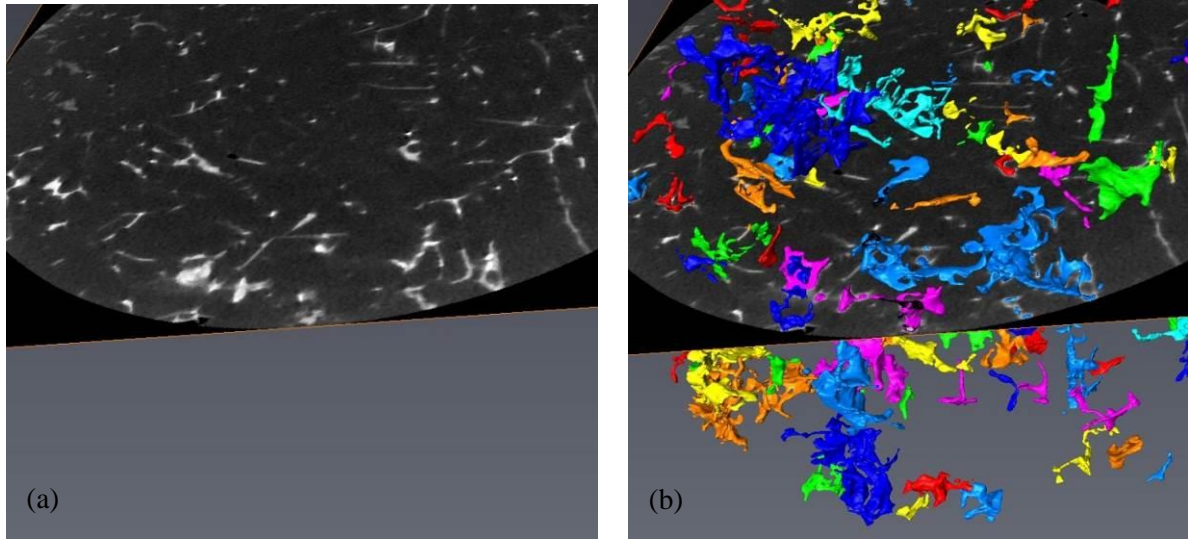


Figure 3-39 (a) A slice from the Lab-CT image and (b) a 3D rendering of  $\text{Al}_2\text{Cu}$

The size distributions in number as a function of the equivalent and Feret diameters and the size distribution in volume using granulometry are shown in Figure 3-40 and Figure 3-41. The average thickness of  $\text{Al}_2\text{Cu}$  phase is a little less than  $10\ \mu\text{m}$  which is close to that of iron intermetallics. Unlike for the intermetallics, the maximum Feret diameter of  $\text{Al}_2\text{Cu}$  phase is much less than the maximum dimension of the studied volume and the maximum Feret and equivalent diameters do not depend on size of the characterized volume. Also considering Figure 3-38, networks of  $\text{Al}_2\text{Cu}$  are less extended than that of intermetallics. Nevertheless, as the morphologies of large objects are far from spherical in Figure 3-38, the Feret diameter would be more suitable to characterize the complex microstructure of  $\text{Al}_2\text{Cu}$  phase than the equivalent diameter. However, although the  $\text{Al}_2\text{Cu}$  phase is less interconnected than iron intermetallics (Figure 3-29(d)), a local thickness seems more suitable to characterize such an interconnected microstructure rather than the global size of each object, i.e. Feret diameter or Equivalent diameter. **The granulometry is thus recommended to characterize the size of  $\text{Al}_2\text{Cu}$ , which possesses a complex and interconnected 3D microstructure.**

# Chapter 3 Material Characterization

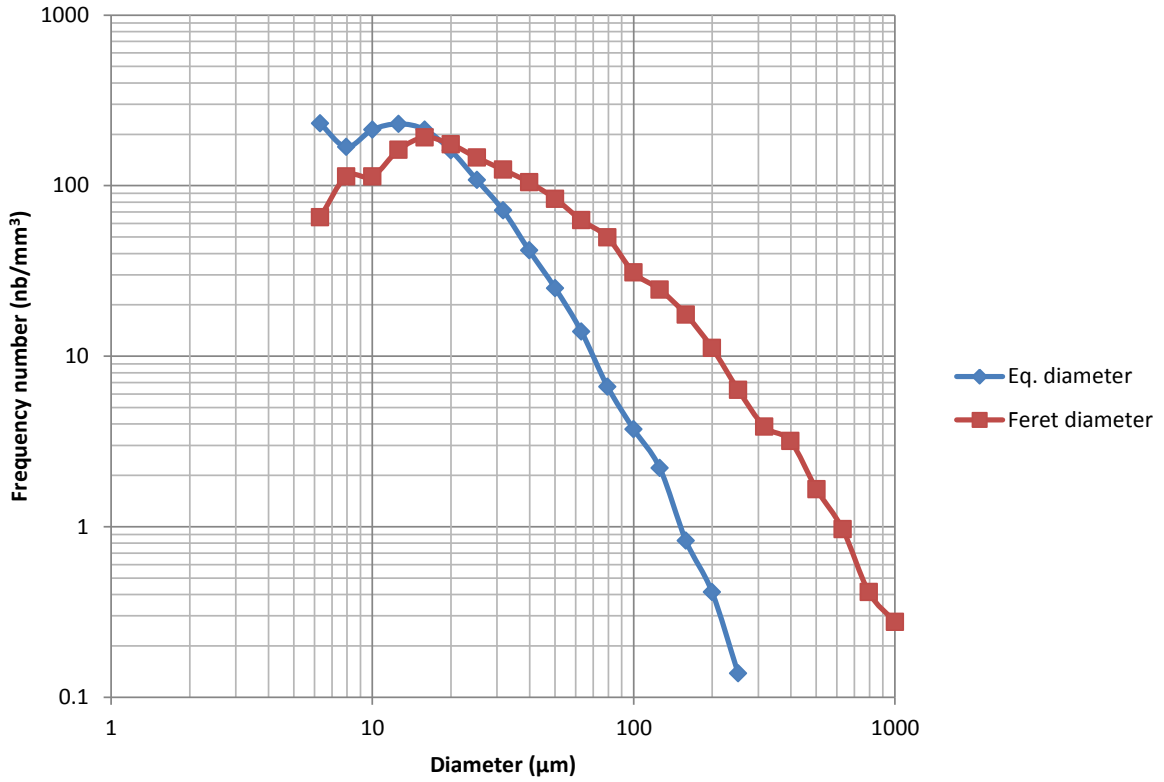


Figure 3-40 Distributions of Al<sub>2</sub>Cu as functions of equivalent and Feret diameters

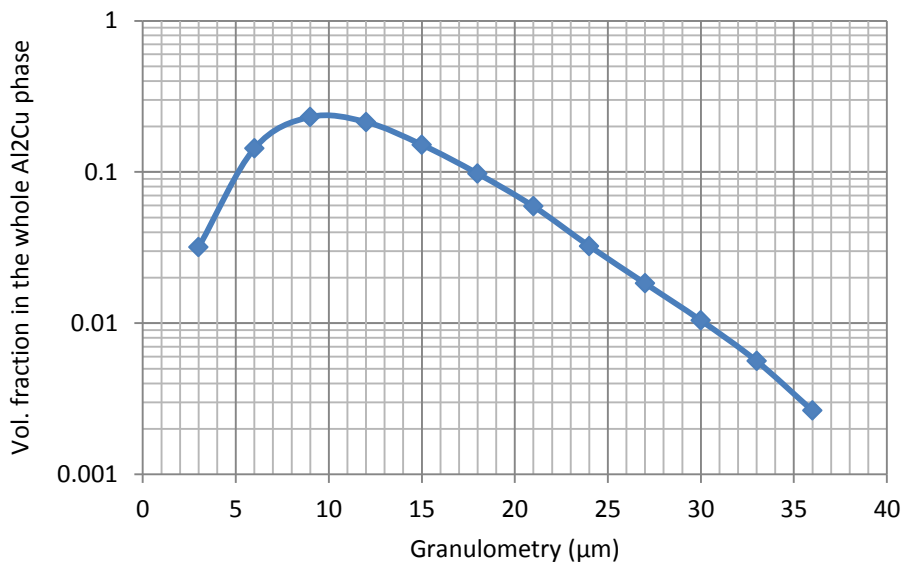


Figure 3-41 Granulometry distribution of Al<sub>2</sub>Cu phase

## Chapter 3 Material Characterization

### 3.3.1.5 Pb

Pb is present as an impurity, i.e. less than 0.1 wt. %, in the studied alloy. Pb particles, which were revealed using SEM in Figure 3-42, show a point-like morphology. In the BSE images, they are the brightest among all the constituents observed in the studied A319 alloy. These particles cannot be revealed using OM due to their small size, low content and inadequate contrast.

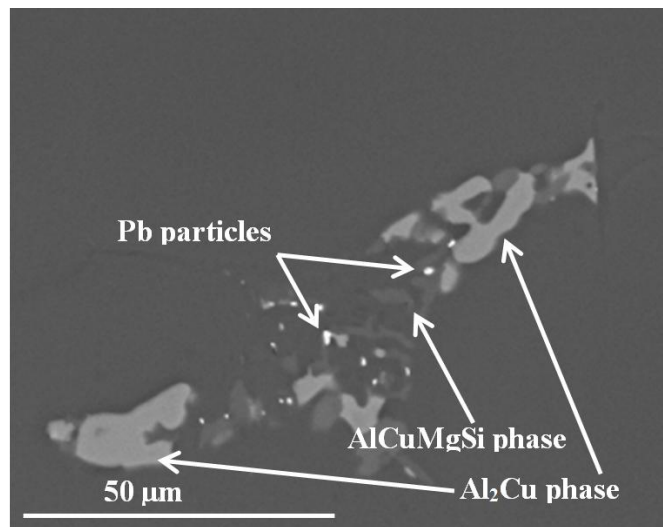


Figure 3-42 BSE images: Pb particles in A319 alloy

Different resolution used yield different volume fraction of Pb: 0.06% at a high resolution (Specimen 1) and 0.19% at a low resolution (Specimen 2). The lower resolution strongly influences the measured volume fraction of Pb due to its small size, although the different studied volume may also be a reason. **Hence a higher resolution is necessary to characterize the Pb.** Besides, due to the quite low volume fraction of Pb, **a larger characterized volume is also necessary under the premise of ensuring a sufficient resolution.** Thus the following 3D quantitative analysis of Pb was performed on the scan with the highest resolution (Specimen 1). The main parameters are listed in

Table 3-12; there is no 2D result to compare with. The comparison with the 3D results of intermetallics in Table 3-10 and Al<sub>2</sub>Cu in Table 3-11 shows that the Pb particles are much smaller.

Table 3-12 3D results of Pb (Specimen 1)

Max Eq. diameter (μm)	48
Average Eq. diameter (μm)	10
Max Feret diameter (μm)	167
Average Feret diameter (μm)	18
Number of objects	4694
Volume fraction%	0.06



## Chapter 3 Material Characterization

The 3D renderings of Pb for different ranges of Feret diameter in Figure 3-43 show that small objects (see Figure 3-43(a)) are again likely to be spherical at the present resolution. The content of Pb particles is very small (volume fraction is only 0.06%), and unlike the intermetallics and Al<sub>2</sub>Cu, Pb particles have not a complex and interconnected morphology.

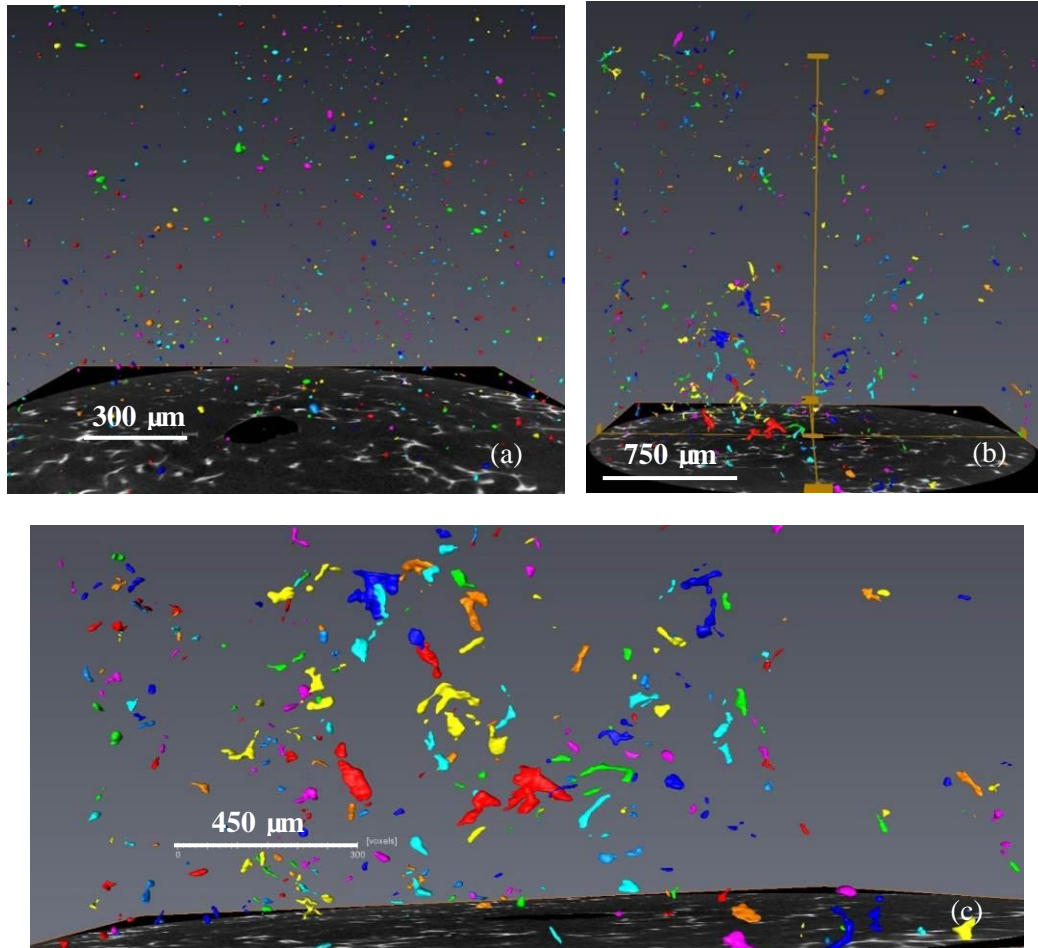


Figure 3-43 3D renderings of Pb having a Feret diameter (a) less than 30 μm, (b) more than 30 μm, and (c) close-up view of objects in figure (b)

The size distributions of Pb as functions of the equivalent and Feret diameters are shown in Figure 3-44. There is a significant difference between the two distributions: Again Feret diameter reflects larger sizes than equivalent diameter. Considering the non-spherical shape of the largest Pb particles shown in Figure 3-43(c), Feret diameter seems more suitable than equivalent diameter. **Hence the Feret diameter is recommended to characterize the size of Pb.**

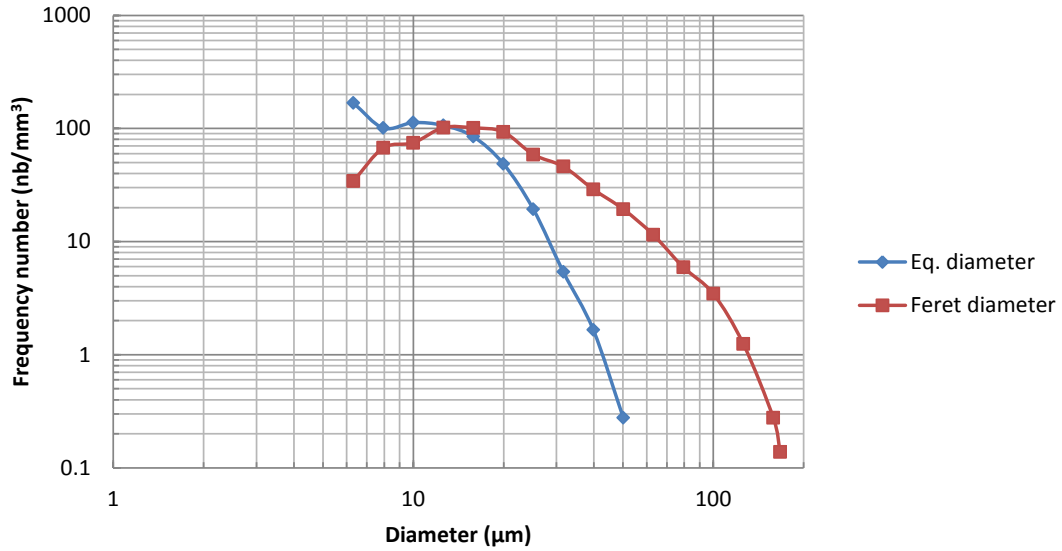


Figure 3-44 Distributions of Pb as functions of equivalent and Feret diameters

### 3.3.2 Microstructure of A356 alloy

The main microstructural features of A356 alloy, which were revealed using SEM and OM (Figure 3-45), are: pores, Al-matrix, Si phase and iron intermetallics. Contrary to A319 alloy, many ‘β platelet’ iron intermetallics are observed in A356 alloy, while only a few α ‘Chinese script’ iron intermetallics are observed. This is due to the lower Mn content in A356 alloy than in A319 alloy which reduces the content of α phase as reviewed in Chapter 2.

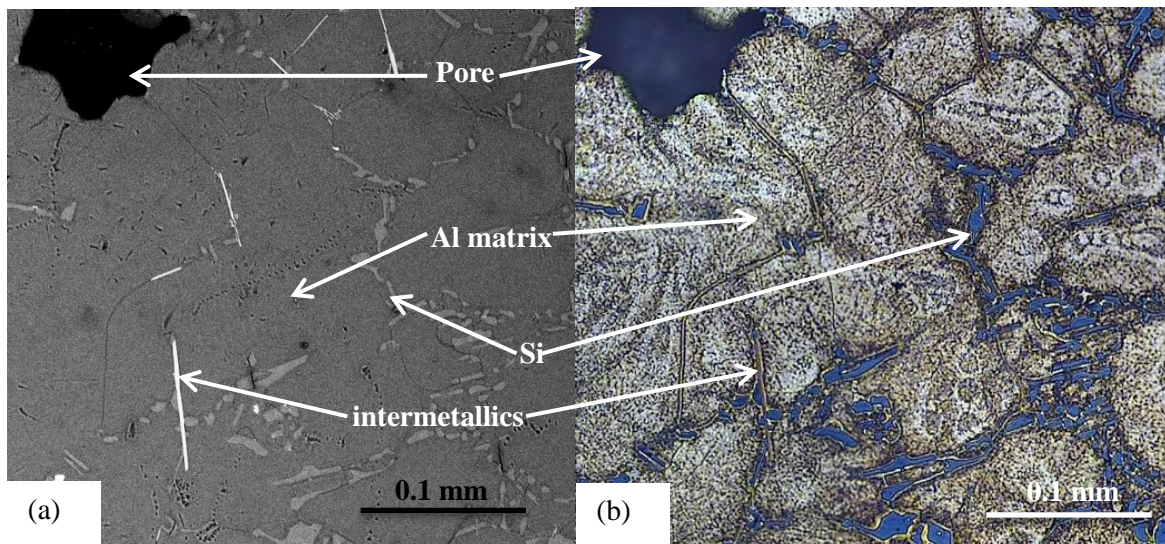


Figure 3-45 Microstructure of A356 alloy (after etching): (a) BSE image, (b) OM image

In A356 alloy, the constituents revealed with lab-CT are identified as iron intermetallics and porosity, as shown in Figure 3-46. The 3D renderings of pores and intermetallics in Specimen 3 are shown in Figure 3-47(a) and (b). The morphologies of pores in A356 alloy are similar with that in A319 alloy.



## Chapter 3 Material Characterization

Thus Feret diameter is again used to characterize pores. The intermetallics in A356 alloy (Figure 3-47(b)) are less interconnected than that in A319 alloy (Figure 3-29(d)). Using lab-CT with a voxel size of 0.9  $\mu\text{m}$ , the morphology of iron intermetallics in A356 alloy was revealed in Figure 3-47(c). As it was already observed in 2D, more  $\beta$  plates than  $\alpha$  phase were found.

The main results of the quantitative 3D analysis are listed in Table 3-13. The average and maximum equivalent diameter measured in 3D are larger than in 2D for the same reason as for the intermetallics in A319 alloy (§ 3.3.1.3). Unlike intermetallics in A319 alloy, the maximum Feret diameter of intermetallics in A356 alloy is much less than the dimension of the scan volume (Figure 3-7(b)). Iron intermetallics are thus less extended in A356 than in A319 alloy. This indicates that the highly interconnected networks of iron intermetallics in A319 alloy may be ascribed to: (1) the high Fe content that leads to more iron intermetallics; (2) the high Mn content that leads to more  $\alpha$  ‘Chinese script’ phase. Considering 3D morphologies in Figure 3-47(c),  $\beta$  plates look like individual objects instead of interconnected networks. Thus Feret diameter may also be a suitable parameter to characterize the size of intermetallics in A356 alloy. Nevertheless, the statistical thickness distribution is also necessary as the iron intermetallics may form a connected network locally as shown in Figure 3-47(b). The following quantitative analysis of intermetallics in A356 alloy is performed using granulometry to allow comparison with A319 alloy.

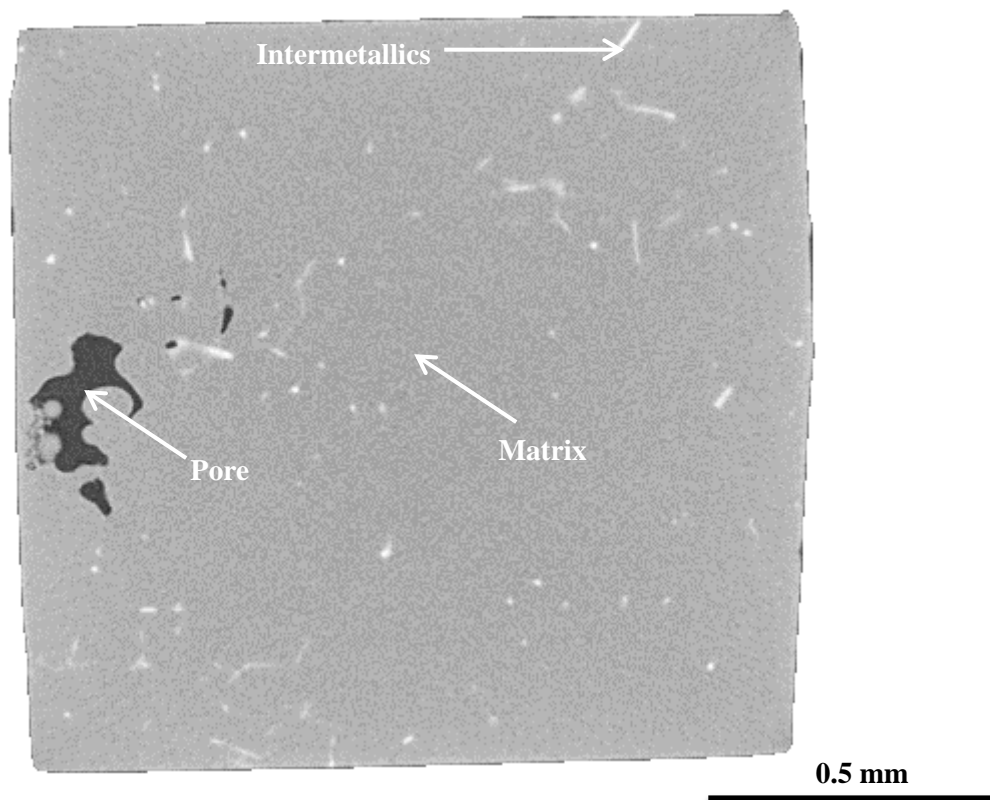


Figure 3-46 Example of one lab-CT slice (Specimen 3, A356 alloy, voxel of 3.4  $\mu\text{m}$  after binning) that presents intermetallics, porosity and Al matrix

## Chapter 3 Material Characterization

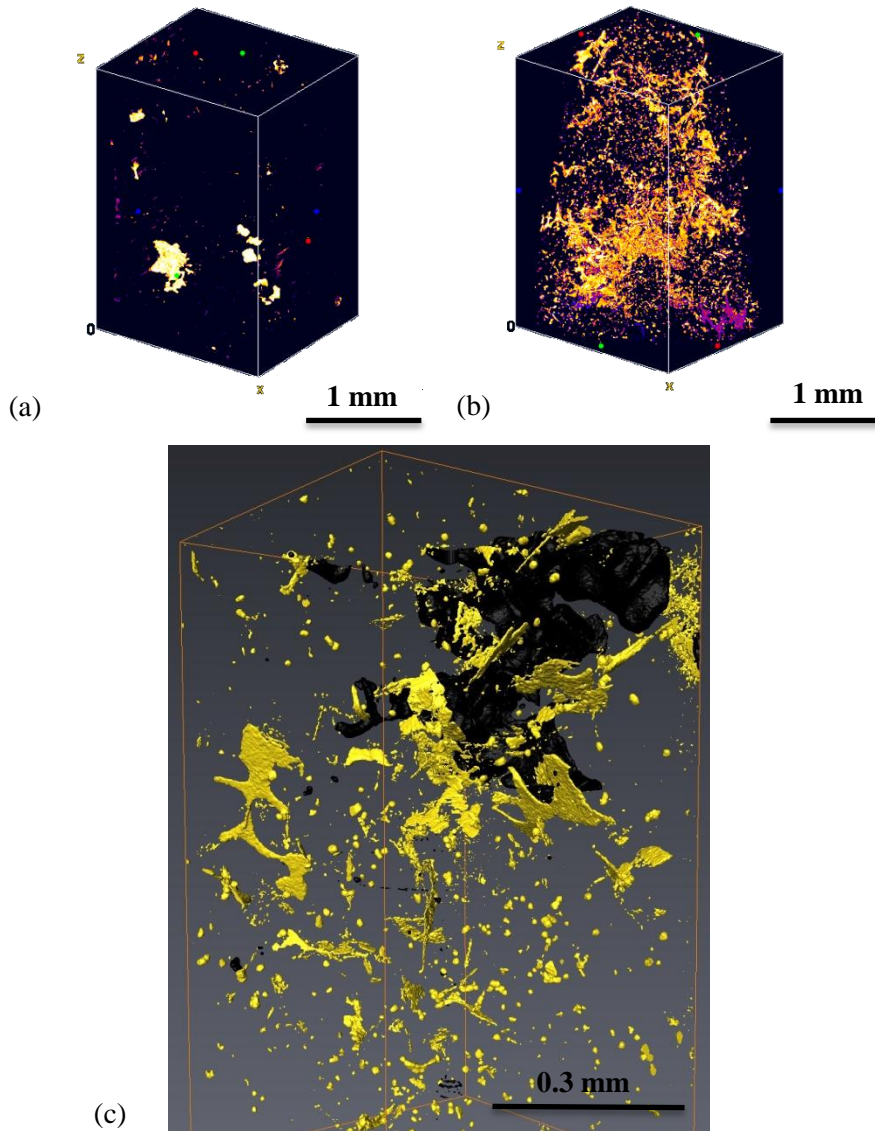


Figure 3-47 3D view of (a) pores and iron intermetallics at (b) a  $3.4\ \mu\text{m}$  voxel size (Specimen 3) and at (c) a  $0.9\ \mu\text{m}$  voxel size (courtesy of RX-Solutions); intermetallics are in yellow and pores in black

Table 3-13 3D vs. 2D results of pores and intermetallics in A356

Pores	Intermetallics
<p>❑ <b>Results 3D (Specimen 3)</b>                      Max Eq. diam. = <math>195\ \mu\text{m}</math>                      Average Eq. diam. = <math>16\ \mu\text{m}</math>                      Max Feret diam. = <math>466\ \mu\text{m}</math>                      Average Feret diam. = <math>33\ \mu\text{m}</math>                      Fraction vol.= 0.20%</p> <p>❑ <b>Results 2D (thesis of S. Tabibian)</b>                      Average Eq. diam. = <math>10\ \mu\text{m}</math>                      Fraction vol.=0.6%</p>	<p>❑ <b>Results 3D (Specimen 3)</b>                      Average Eq. diam. = <math>14\ \mu\text{m}</math>                      Max Feret diam. = <math>761\ \mu\text{m}</math>                      Average Feret diam. = <math>25\ \mu\text{m}</math>                      Fraction vol.= 1.49%</p> <p>❑ <b>Results 2D (thesis of S. Tabibian)</b>                      Average Eq. diam. = <math>7\ \mu\text{m}</math>                      Fraction vol.=0.76%</p>

## Chapter 3 Material Characterization

The size distributions of pores as a function of Feret diameter in A356 alloy (Specimen 3) is shown in Figure 3-48 in order to compare with that in A319 alloy (Specimen 2). The distributions in both alloys can be considered as close except for the large pores. Indeed, the scan volume of Specimen 3 is  $3.58\text{mm}^3$  which is only 5% of that of Specimen 2. Consequently some large pores present in Specimen 2 may be missed in Specimen 3 due to the smaller sampled volume.

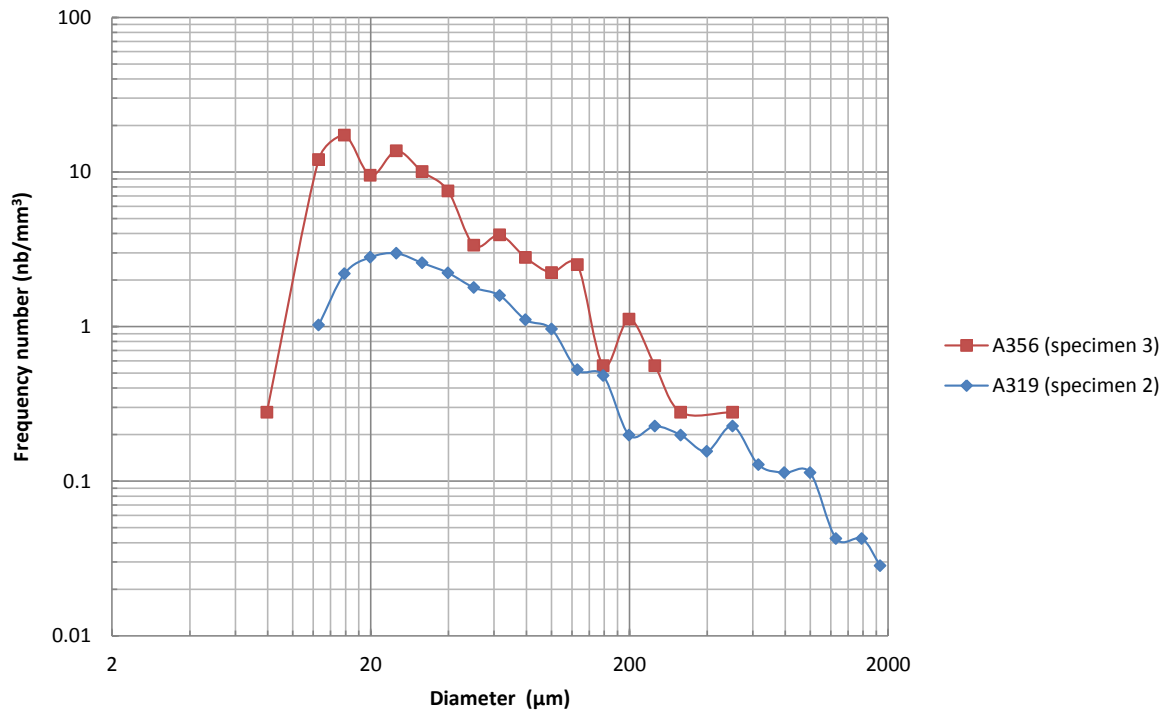


Figure 3-48 Distributions of Feret diameter of pores in A356 and A319

The granulometry distributions of intermetallics in A356 (Specimen 3) and in A319 (Specimen 1) are shown in Figure 3-49. Although the distribution in Specimen 3 is less reliable than that for Specimen 1 due to the limited resolution of the binned image, the average sizes of iron intermetallics in both alloys are close. The maximum thickness of iron intermetallics in A319 alloy was found to be larger than that in A356 alloy in Figure 3-49. There are some possible reasons: (1) a higher iron content (see Table 3-1) in A319 than in A356 results in iron intermetallics having a larger size; (2) variability between samples; (3) a variety of errors, such as the difference between the tomography images qualities for these two specimens, the different resolutions used for the analysis or errors during the segmentation of phases.

The comparison of results in Table 3-10, Table 3-11 and Table 3-13 shows that A319 alloy has a volume fraction of natural tracers (distributed phases revealed using laboratory X-ray tomography) about 10 times higher than A356. In particular it has eutectic Al-Al<sub>2</sub>Cu phases that are not present in A356 alloy.

## Chapter 3 Material Characterization

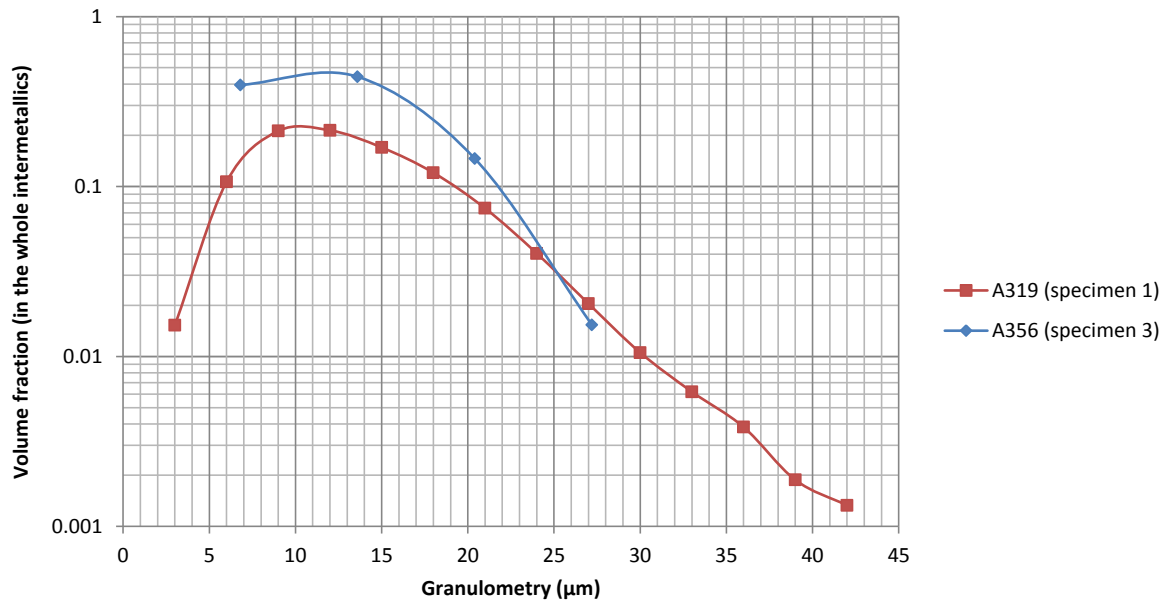


Figure 3-49 Granulometry distributions of intermetallics in A319 and A356

### 3.4 Comparisons

The main constituents and features in A319 and A356 alloys were characterized using OM and SEM/EDS in 2D and using laboratory and synchrotron (only for A319 alloy) X-ray tomography in 3D.

Table 3-14 Comparison of the different characterization methods used

Characterization method	Operation	Cost	Requirement of polishing	Contrast	Resolution	Characterization spatial
OM	Easy	Low	High	Low	Medium	2D
SEM	Medium	Medium	Medium	Very high	High	
Lab-CT	Medium	High	Low	Medium	Medium	3D
SR-CT	Medium	Very High	Low	High	Medium	

OM observation is the easiest one implemented thanks to its simple principle, easy operation and low-cost equipment. But it can only be performed in 2D, and a high quality OM image has a high requirement for polishing. Pores and Al matrix are very easy to identify using OM because they usually present quite different colours and morphologies compared with inclusions and because they have large size. Porosity is the only feature that is black in OM image. Al matrix, which occupies the largest surface fraction, has an enough contrast with pores and inclusions. However, it is not always easy to make out the different inclusions, i.e. Si phase, AlCuMgSi phase, iron intermetallics, Al<sub>2</sub>Cu phase, Pb particles due to: (1) insufficient contrast; (2) similar morphologies in 2D, i.e. long strips,

## Chapter 3 Material Characterization

---

punctate or block like. Although the used etching method gives more contrast for the following DIC measurement, it does not allow for the different inclusions to be distinguished easily.

SEM observation could be performed with a very high resolution compared with other methods and provides images with enough contrast for the studied material. Besides, SEM-EDS analysis allows identifying chemical compositions of constituents. According to the grey values in BSE images from low to high atomic number, i.e. from darker to brighter, the constituents and features are ranked as: Porosity, Al matrix, eutectic Si particles, AlCuMgSi phase, iron intermetallics, Al<sub>2</sub>Cu phase, Pb particles. These differences in grey levels, which reflect differences in atomic number and density, are an important basis for the segmentation of constituents and features in the tomography images where the contrast also depends on atomic number. In addition, the distinction between gas and shrinkage pores, or between  $\alpha$ (AlFeMnSi) and  $\beta$ (AlFeSi) phase could be made based on their different morphologies. SEM characterization is the only method that allows revealing all the main constituents and features among the four used characterization methods. However it is limited to 2D characterization.

Although characterization using X-ray tomography provides images with lower resolution and lower contrast than SEM and although its cost, especially for SR-CT, is high, it gives access to 3D information. SR-CT is more expensive than Lab-CT but allows revealing Si phase thanks to phase contrast. The morphologies of constituents and features revealed in 3D show that the individual objects in 2D may connect in 3D and even form highly extending networks. 2D measurements only measure the local cross sections of a 3D connected microstructure. Comparison of measurement performed in 3D and in 2D indicates that 3D measurement can better reflect the size of microstructure when the same parameter is used. Besides, small objects (noises) can be reasonably removed which cannot be realized easily in 2D analysis (a small object in the 2D image may be part of a 2D cross-section of a large object, so it cannot be deleted reasonably).

The most suitable 3D parameter was selected for each constituent in A319 alloy: Feret diameter was chosen to characterize the size of individual objects such as pores and Pb particles, and granulometry was chosen to characterize the size of the phases with a complex interconnected microstructure, i.e. iron intermetallics and Al<sub>2</sub>Cu. The volume fraction distribution of the four phases or constituents (pores, iron intermetallics, Al<sub>2</sub>Cu and Pb) in A319 as a function of size is shown in Figure 3-50. The size of pores is much larger than that of Pb, iron intermetallics and Al<sub>2</sub>Cu (**Size: Pores > Pb > iron intermetallics & Al<sub>2</sub>Cu**). The Feret diameter of the majority of pores, i.e. pores with volume fraction above 10%, is more than 400  $\mu\text{m}$  in a volume of 70.54  $\text{mm}^3$ . In the same time, that of Pb is between 18  $\mu\text{m}$  and 60  $\mu\text{m}$  and the local thickness of iron intermetallics and Al<sub>2</sub>Cu is only between 6  $\mu\text{m}$  and 18  $\mu\text{m}$ . Thus the pores are first assumed to be the most critical defects in the volume.

## Chapter 3 Material Characterization

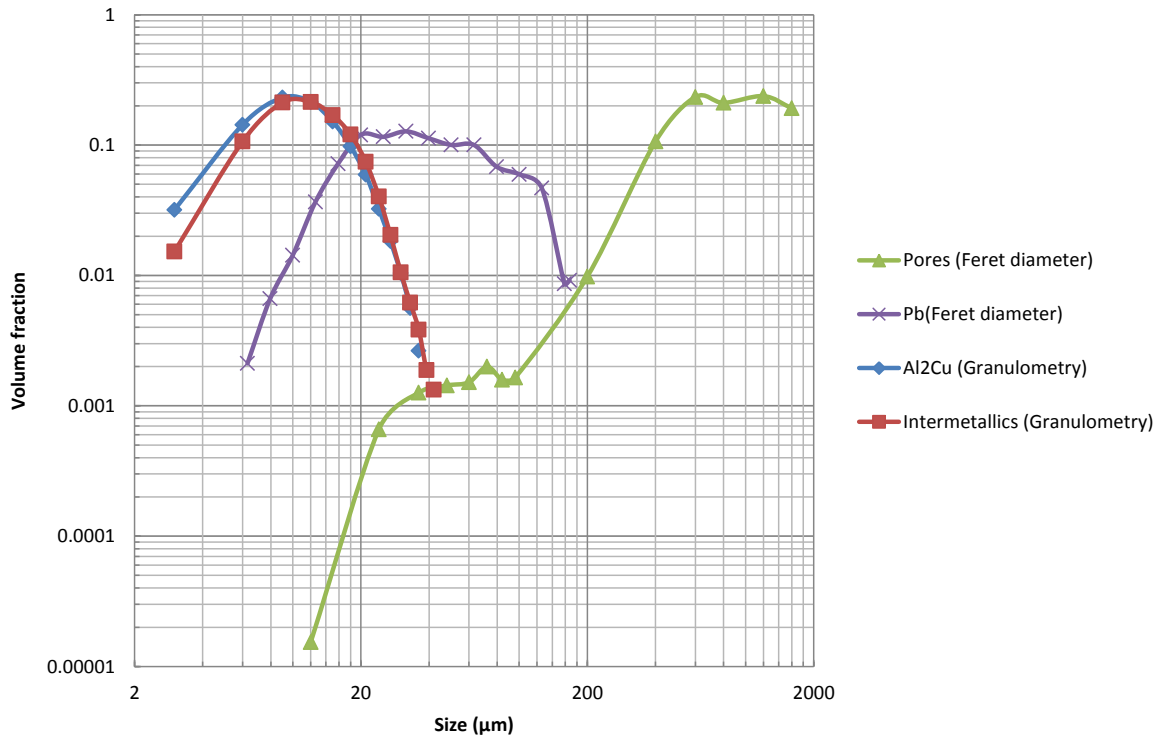


Figure 3-50 Distributions of pores, intermetallics,  $\text{Al}_2\text{Cu}$ , Pb as a function of size (Ferret diameter for pores and Pb, granulometry for intermetallics and  $\text{Al}_2\text{Cu}$ )

Feret diameter is selected to characterize the size of pores, as it could better reflect the global shape than Equivalent diameter. But Feret diameter gives no information on the local shape or the orientation of a pore even using the ‘sphericity’ factor. The location of pores, i.e. the distance between pore and surface, which is also an important factor as reviewed in Chapter 2, was not characterized neither. Although Feret diameter is not enough to fully characterize pores, it is the most suitable parameter according to the author’s knowledge.

Although average size of Pb particles is larger than that of hard inclusions, i.e. iron intermetallics and  $\text{Al}_2\text{Cu}$ , Pb is more ‘soft’ than Al matrix (Table 3-15 (Wikipedia, 2014a) (Wikipedia, 2014b)). Thus Pb particles are more likely to behave as ‘pores’ in Al matrix rather than as hard inclusions. Considering their size distribution (Figure 3-50) and morphologies (Figure 3-43), they could be compared to ‘small pores’ in the material.

Table 3-15 Mechanical properties of Al and Pb

Element	Young's modulus	Mohs hardness	Brinell hardness
Al	70 GPa	2.75	245 MPa
Pb	16 GPa	1.5	5.0 MPa



## Chapter 3 Material Characterization

---

Granulometry is used to characterize the interconnected microstructures i.e. hard inclusions. It is based on statistical thickness measurement. Thus such a measurement performed in 2D can also characterize the studied material reasonably if a surface large enough is studied. A 3D image usually has 1000 to 2000 slices, in other words, a 3D image can be analyzed as a stack of 2D images that have been acquired at the same time. For this kind of analysis, the advantage of X-ray tomography is that a large “surface” is scanned at once but the drawback is the rather coarse resolution whereas SEM images have higher resolution and higher contrast, which are better to characterize the hard inclusions, especially for Si phase. Although AlCuMgSi phase can be well revealed using SEM, its 3D microstructure is unknown. Although granulometry is selected to characterize the size of hard inclusions, it cannot reveal their extent in 3D. Analysis using the maximum Feret diameter shows that Al<sub>2</sub>Cu network is less extended than iron intermetallics and Si phase networks, which may extend to the whole volume.

In 356 alloy, Feret diameter is also the most suitable parameter to characterize the size of pores. However, granulometry and Feret diameter are both suitable to characterize the size of iron intermetallics as iron intermetallics in A356 alloy are less extended and less interconnected. Anyway, similar with A319 alloy, no matter which parameter is chosen it cannot fully characterize these microstructures.

### 3.5 Summary

A319 and A356 alloys were characterized using OM and SEM/EDS in 2D and using laboratory and synchrotron X-ray tomography in 3D (Table 3-16). OM is easy to operate and is not expensive but it provides images with low contrast and low resolution. An etching method gave markers on sample surface for the following DIC measurements although it does not allow identifying the different inclusions. SEM provides images with very high resolution and high contrast and, when it is equipped with EDS, the chemical composition could be identified. Although X-ray tomography is more expensive than OM and SEM and provides images with lower resolution and lower contrast than SEM, it permits 3D non-destructive characterization. In spite of very high cost, SR-CT allows Si phase, which is not revealed using Lab-CT, being revealed thanks to phase contrast.

A simple grayscale thresholding method was used for the segmentation of different constituents and features from tomographic image. A pre-treatment process is proposed to solve the segmentation problem caused by the phase contrast of synchrotron tomography. 3D analysis combining Avizo and ImageJ softwares allows the complex microstructure of A356 and A319 Al-Si alloys to be characterized in 3D thoroughly.

3D characterization shows that the individual objects in 2D may be parts of one 3D object and even form large extended networks. Thus measurements in 3D are usually more reliable than in 2D. Feret

## Chapter 3 Material Characterization

---

diameter better characterizes the size of individual objects such as pores and Pb particles while granulometry better characterizes the size of interconnected phases, such as iron intermetallics, Al<sub>2</sub>Cu and Si phases. However, no matter which parameter is selected to characterize the size of 3D objects, it does never allow a thorough characterization of all the parameters that are of known importance in fatigue. For example, Feret diameter cannot reflect the local shape, orientation and location of the individual objects, while granulometry cannot reveal the extent of interconnected microstructure.

In A319 alloy, Al<sub>2</sub>Cu phase is less extended than iron intermetallics and Si phase which extend to the whole volume. The highly extended iron intermetallics is ascribed to the high Fe and Mn in A319 alloy which results in more 'Chinese script'  $\alpha$  phase than platelet  $\beta$  phase. Although their average size is larger than hard inclusions, Pb particles can be compared to 'small pores' if one considers their sizes, morphologies and mechanical properties. The average size of porosity is more than 10 times that of other constituents, thus pores are first assumed to be the most critical defects in the volume. A probabilistic thermal-mechanical fatigue criterion for LFC aluminum alloys, which has been initially developed based on 2D porosity distribution (Charkaluk et al., 2014), has been improved using the 3D characterization of pores (Szmytka et al., 2014).

A356 alloy contains more  $\beta$  phase than  $\alpha$  phase due to its lower Mn content than A319 alloy; the iron intermetallics are thus less extended. A319 alloy was found to have a volume fraction of natural tracers (microstructure constituents) about 10 times higher (in the case of Lab-CT) than A356, in particular it has eutectic Al-Al<sub>2</sub>Cu phases that are not present in A356 alloy.

## Chapter 3 Material Characterization

Table 3-16 Summary of 2D and 3D characterization

Alloy	Grey level <sup>1</sup>	Microstructure		2D Characterization	3D characterization			
					Morphology	Size	Recommended Scan conditions	
A319	0 Low	Pore	Gas pore <sup>2</sup>	Approximately spherical	Rounded individual object sphericity $\approx 1$	Feret diameter: Majority >400 $\mu\text{m}$	Lab-CT or SR-CT Large scan volume	
			Shrinkage pore <sup>2</sup>	Coral-like	Tortuous individual object sphericity $\approx 0$			
	↓  High 255	Al		Matrix				
		Si		Plat-like	Highly interconnected networks, extended in the whole volume	Granulometry	Only SR-CT High resolution	
		AlCuMgSi		Densely punctate, thickness < 1 $\mu\text{m}$ , around Al <sub>2</sub> Cu	Due to the present resolution, cannot be revealed.			Lab-CT or SR-CT High resolution
		Iron intermetallics	$\alpha^3$	'Chinese script' More Mn content than $\beta$ .	Highly interconnected networks, extended in the whole volume	Granulometry: Majority 6~18 $\mu\text{m}$		
			$\beta^3$	Needle-like, plate Less Mn content than $\alpha$ .				
		Al <sub>2</sub> Cu		Thickness : < 1 $\mu\text{m}$ ~ 10 $\mu\text{m}$	Complex structures, less extended than Si and intermetallics	Granulometry: Majority 6~18 $\mu\text{m}$		
Pb		Small points	Individually object (smaller than pores)	Feret diameter: Majority 18~ 60 $\mu\text{m}$	Lab-CT or SR-CT High resolution and Large scan volume			
A356	Low ↓ High	Pore		X	Similar with that in A319			X
		Al			Matrix			
		Iron intermetallics			More $\beta$ plate, less extended than A319	Average size close to A319		

1. Grey level in BSE or 8bit tomography images;

2. / 3. Similar grey levels, but different morphologies.

# Chapter 4 Experimental methods

## Contents

---

<b>4.1</b>	<b>Introduction.....</b>	<b>- 85 -</b>
<b>4.2</b>	<b>Extraction of specimens.....</b>	<b>- 86 -</b>
<b>4.3</b>	<b>Preparation and selection of specimens .....</b>	<b>- 89 -</b>
<b>4.4</b>	<b>Experimental protocol .....</b>	<b>- 93 -</b>
4.4.1	In-situ observation methods .....	- 93 -
4.4.1.1	2D in-situ observations on surface.....	- 93 -
4.4.1.2	3D in-situ observations in volume .....	- 94 -
4.4.2	Mechanical.....	- 95 -
4.4.2.1	Tensile tests .....	- 95 -
4.4.2.2	Fatigue tests .....	- 96 -
4.4.3	Postmortem analyses.....	- 97 -
<b>4.5</b>	<b>Field measurements .....</b>	<b>- 99 -</b>
4.5.1	Basic principles.....	- 99 -
4.5.2	DIC.....	- 100 -
4.5.2.1	Application conditions .....	- 100 -
4.5.2.2	DIC using Elastix.....	- 101 -
4.5.3	DVC.....	- 103 -
4.5.4	Measurement uncertainty .....	- 105 -
<b>4.6</b>	<b>Summary.....</b>	<b>- 108 -</b>

---

## 4.1 Introduction

In order to study the influence of the casting microstructure upon the damage micromechanisms of Al-Si alloy in LCF, an experimental protocol has been set up based on the coupling of kinematic field measurements at the microstructure scale on surface and in volume. This protocol, which is detailed in this chapter, has been validated in monotonic tensile tests before being applied in fatigue tests.

## Chapter 4 Experimental methods

The most suitable specimens extracted from cylinder heads, as well as the Region Of Interests (ROI), where in-situ observations were performed, were selected through a series of methods (see § 4.2 and 4.3). During tensile and fatigue tests (see § 4.4), a Questar long distance microscope was used for 2D in-situ observations on surface while laboratory and synchrotron X-ray tomography was used for 3D in-situ observations in volume. Digital Image Correlation (DIC) and Digital Volume Correlation (DVC) techniques were used for field measurements on surface and in volume respectively (see § 4.5). Postmortem analyses were performed with OM, SEM and EDS (see § 4.4).

### 4.2 Extraction of specimens

Table 4-1 summarizes the procedure of extraction, preparation and selection of specimens. Figure 4-1 shows the extraction area of specimens from prototype cylinder heads. Specimens were extracted from A319 prototype cylinder heads manufactured using LFC process, except some specimens coming from A356 cylinder heads. These later ones have been used for 2D tensile tests in the context of a preliminary study. The characterization of pores and intermetallics in A356 alloy (Specimen 3 in Chapter 3) has shown that their size distribution is close to that in A319 alloy although intermetallics are less extended in A356 than in A319. Thus A356 alloy cylinder head could be used to validate the experimental protocol in tensile tests.

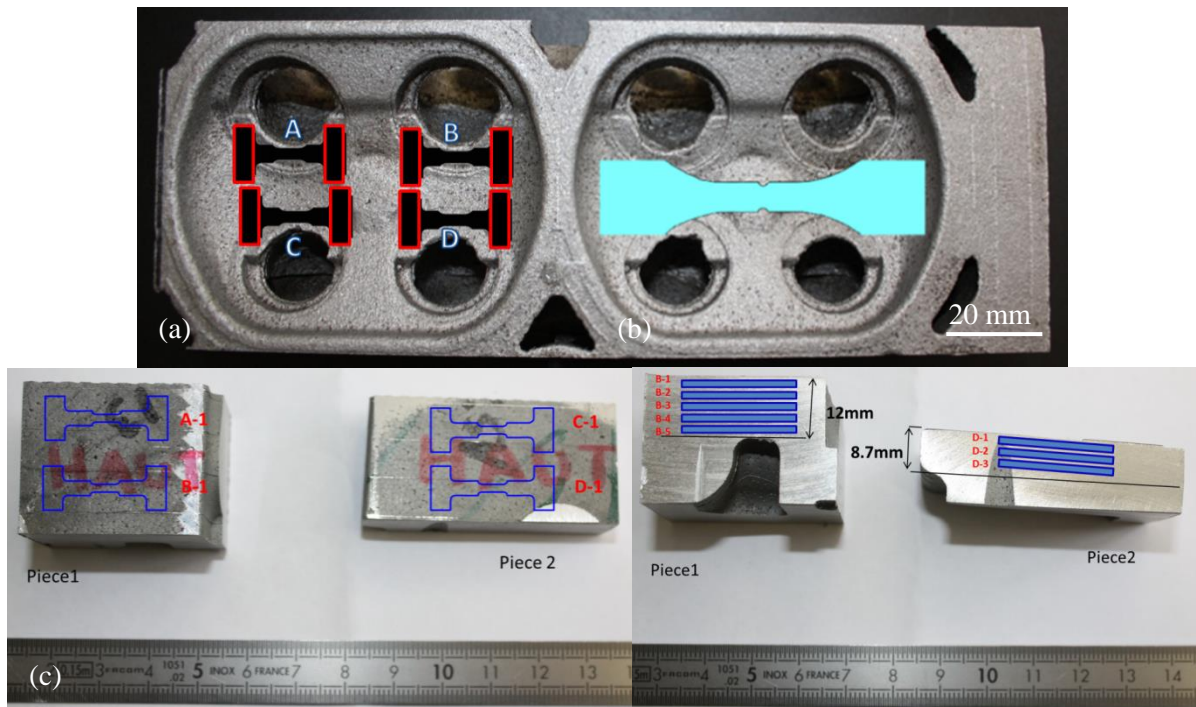

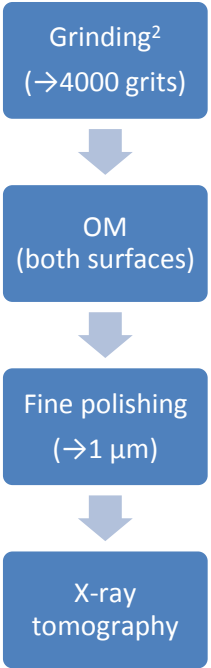
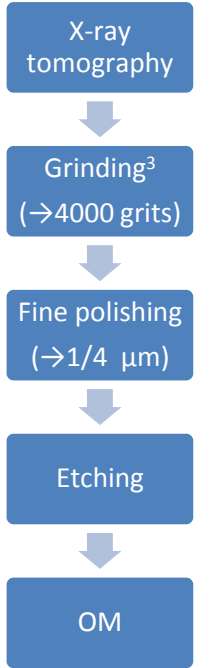
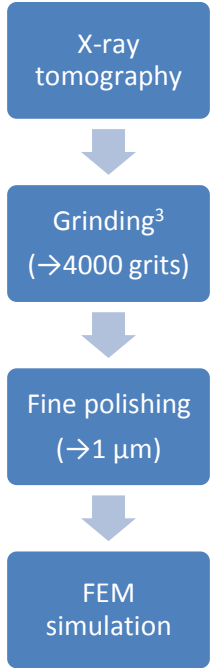


Figure 4-1 Extraction of specimens from prototype cylinder heads: (a) small and (b) large size specimens from the fire deck areas and (c) from small pieces.

## Chapter 4 Experimental methods

Table 4-1 Extraction, preparation, selection and in-situ observations of specimens

Type	Test	Tensile		Fatigue					
	In-situ observation method	2D		3D		2D		3D	
Extraction of specimens	Material	A356		A319					
	Areas of prototype cylinder heads	fire deck Figure 4-1(a)		small pieces Figure 4-1(c)		fire deck Figure 4-1(b)		fire deck Figure 4-1(a)	
	Size	Small size Figure 4-2(a)			Large size Figure 4-2(b)		Small size Figure 4-2(c)		
	Number of extracted specimens	20		16		4		36	
Preparation and selection	Protocol								
	Selected specimen name	T1	T2	T3		F1	F2	F3	F4
In-situ Observations	Number of Questar images	6	4	-		6	6	-	-
	pixel/voxel size (μm)	0.34		1.695		0.38		1.625	
	Element size (DIC/DVC)	32 pixels 10.2 μm		16 voxels 27.2 μm		32 pixels 12.0 μm		16 voxels 26.0 μm	

**Notes:**

1. Grinding was only performed on the observed surface.
2. Grinding was performed on both flat surfaces for the postmortem analysis using SEM.
3. Grinding was performed on four sides and each corner of specimens to ensure that all the surfaces are smooth and thus prevent the generation of stress concentration.



## Chapter 4 Experimental methods

Almost all the specimens were extracted from the fire deck area (Figure 4-1(a) and (b)) that is the most critical area in cylinder head. Only specimens for 3D tensile tests were extracted from two pieces (Figure 4-1 (c)) of an A319 cylinder head outside this area because of a lack of an entire cylinder head at the time the tests were planned. Due to different cooling rates, the coarseness of the microstructure, which is reflected by DAS, will vary in different parts of a cylinder head. Thus, the DAS of the two used pieces was measured to ensure that they are indeed representative for the coarseness of the microstructure in the fire deck. The mean DAS of the two parts being about 55 - 63  $\mu\text{m}$ , i.e. close to the DAS value of 73.7  $\mu\text{m}$  in the fire deck area (Tabibian, 2011), representativity for the critical zone of the cylinder head was assumed.

Small size specimens (Figure 4-2(a)) were used for tensile and fatigue tests with 3D in-situ observation and tensile tests with 2D in-situ observations. Large size specimens (Figure 4-2(b)) with notches ( $K_t$  (Stress concentration factor) = 2.45 (resp. = 2.3) for Specimen F1 (resp. Specimen F2)) were used for fatigue tests with 2D in-situ observations. As the resolution of tomographic image decreases with the increasing scan volume, only small size specimens, which could be scanned with a resolution (voxel size = 1.5 ~ 1.625  $\mu\text{m}$ ) that allows revealing hard inclusions, are suitable for 3D in-situ observations. 2D in-situ tensile tests also used small size specimens as we did not have enough material for the large specimen geometry.

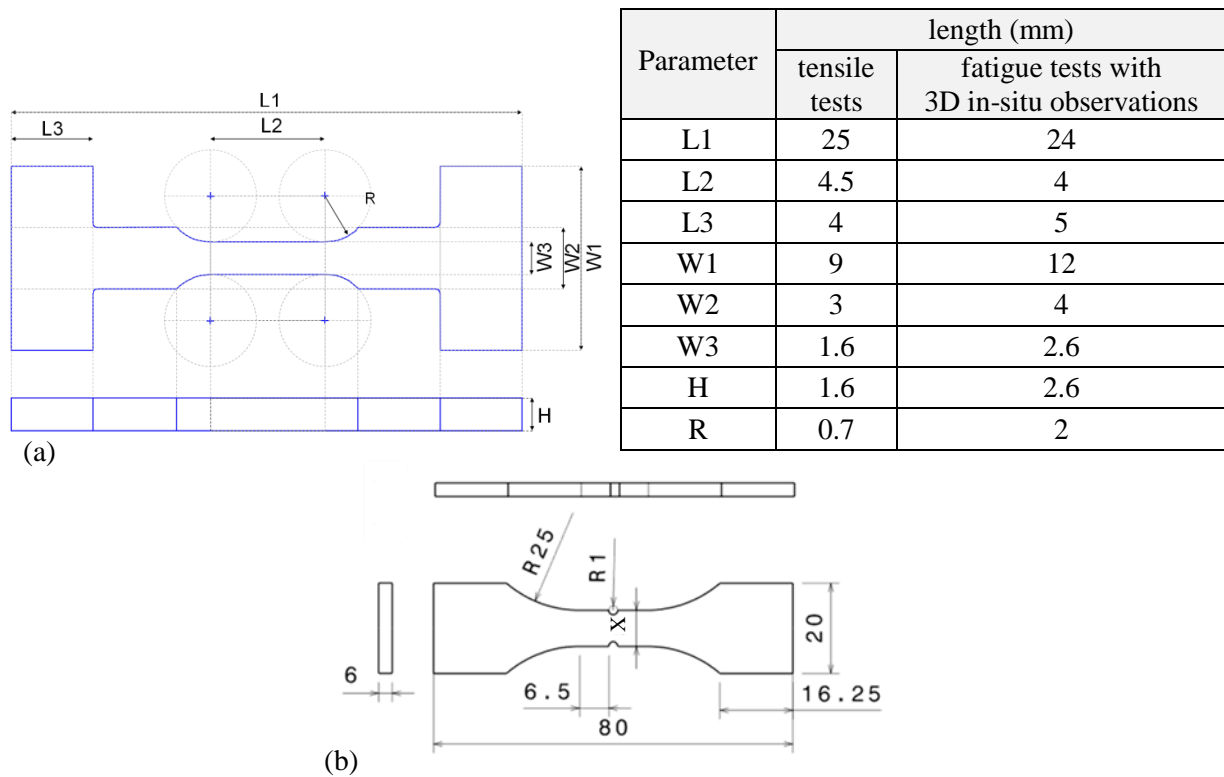


Figure 4-2 Size of extracted specimens (in mm) for (a) tensile tests and fatigue tests with 3D in-situ observations, (b) fatigue tests with 2D in-situ observations (X=10 for Specimen F1, and X=8 for Specimen F2).

### 4.3 Preparation and selection of specimens

The protocol of specimen preparation and selection for each test is shown in Table 4-1. The grinding was performed using abrasive papers of grades up to 4000 grits in succession; this process was improved gradually in this thesis (see notes of Table 4-1). The fine polishing was performed using polishing cloths and suspensions up to 1 or 1/4  $\mu\text{m}$  for surface observations. Different observation methods were used for selection of specimens either individually or in succession: (i) OM image revealed surface breaking casting defects, (ii) two X-ray radiography images taken perpendicular to the flat surfaces of specimens allowed revealing the projections of 3D casting defects in a direction perpendicular to the specimen surface, and (iii) X-ray tomography image revealed 3D casting defects in volume. As reviews in Chapter 2, large pores are assumed to be the most critical initiation sites and surface pores are considered more critical than subsurface pores, thus the above ways to reveal pores in 2D or 3D meet the following objectives:

- (1) To select the most suitable specimens: The chosen specimens have no large defects near the shoulders while they have defects with a size compatible with the specimen cross-section in the gauge length.
- (2) To select ROI where in-situ observations will be performed: the selected areas have a cluster of subsurface pores or pores near the surface.

**Tensile tests with 2D in-situ observation:** Radiography was performed using lab-CT (MATEIS) with a 3.58  $\mu\text{m}$  voxel size at two perpendicular positions per specimen. Two specimens were selected from 20 extracted specimens. ROI was identified by the comparison between radiographies and OM images.

**Tensile tests with 3D in-situ observation:** Grinding and fine polishing were performed on both flat surfaces; it allows casting defects being revealed on both sides in OM images and allows postmortem analysis being performed. Ten specimens were selected from 16 extracted specimens using OM observations (see Figure 4-3(a) and (b) for examples), then final selections were performed using lab-CT (MATEIS) in the fast scan mode, i.e. the scan lasts about 5 minutes, at a 4.5  $\mu\text{m}$  voxel size. These medium resolution images allow revealing the size and shape of the large pores rapidly. The height of the tomographic image is 1100 pixels, i.e. 4.95 mm, and the size of cross section is  $800 \times 650$  pixels<sup>2</sup>, i.e.  $3.6 \times 2.9$  mm<sup>2</sup>. Thus the whole gauge length between the specimen's shoulders (length = 4.5 mm, see Figure 4-2(a)) could be characterized. ROI was selected by using the 3D rendering of pores.

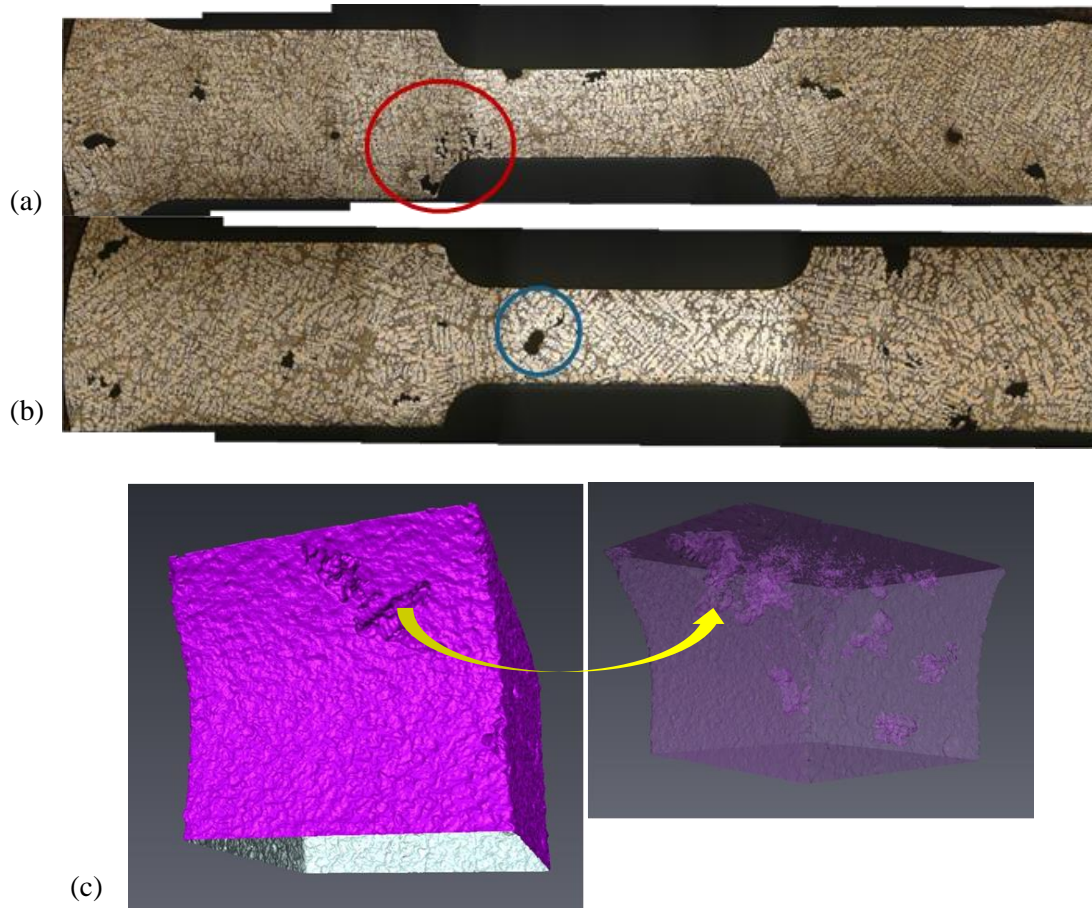


Figure 4-3 Examples of OM images on the surface of grinded specimens: (a) unselected and (b) selected. (c): One example of a large casting defect in the shoulder area on the 3D rendered surface (left) and in volume with the material set transparent (right)

**Fatigue tests with 2D in-situ observation:** the analysis of tensile tests with 2D in-situ observation (see Chapter 5) showed that the radiography was not enough to select ROI, which was thus selected using lab-CT (LML, see Figure 4-4) with voxel size of  $6.35\mu\text{m}$  for Specimen F1 and  $6.00\mu\text{m}$  for Specimen F2. These resolutions allow the large casting defects in the whole critical volume, i.e. notched area, to be revealed. A 90kV acceleration voltage was selected. A set of 1440 radiographies was recorded while the specimen was rotating over  $360^\circ$  along its vertical axis and one scan lasted about one hour. ROI was identified by the comparison between 3D rendering of pores and OM image.

## Chapter 4 Experimental methods

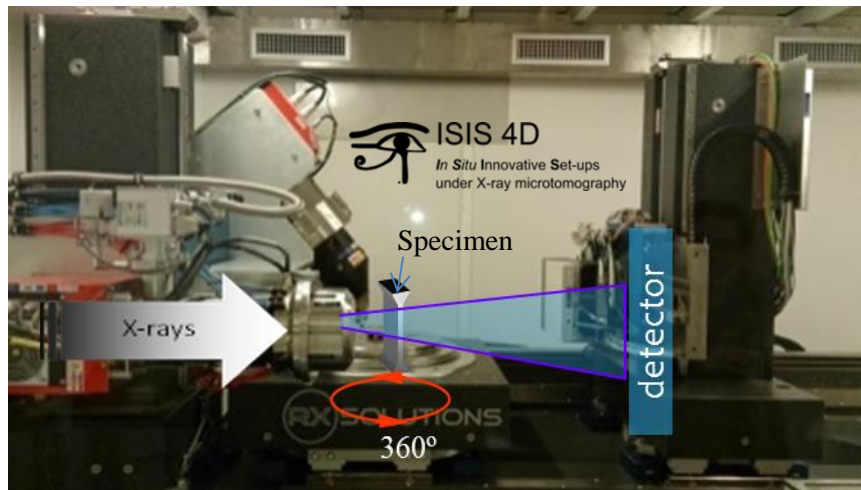


Figure 4-4 Lab-CT at Laboratoire de Mécanique de Lille (LML)

**Fatigue tests with 3D in-situ observation:** Ten specimens were selected from 36 extracted specimens by using lab-CT (MATEIS) in the fast scan mode, i.e. the scan lasts about 6 minutes, at a  $5.0 \mu\text{m}$  voxel size. The height of the tomographic image is 1400 pixels, which covers the length of 7 mm for the scanned specimen, including the notched areas. Figure 4-3(c) shows an example during the selection of specimens at this step. Based on FEM simulations performed for the tensile tests with 3D in-situ observation (see Chapter 5), FEM simulation (see Appendix II) was used to select ROI. Fatigue tests were performed on eight specimens, but only two specimens, i.e. Specimen F3 and F4, are analyzed in this thesis.

The selections of all the specimens listed in Table 4-1 are detailed in Appendix III.

In order to check if the selected small size specimens are representative for the studied material (characterized in Chapter 3), each specimen was analyzed in 3D. The pores were characterized using the scan with a low resolution (voxel size =  $4.5 \sim 5.0 \mu\text{m}$ ) but in a large volume. The scan with a higher resolution (voxel size =  $1.6 \sim 1.7 \mu\text{m}$ ) but in a smaller volume taken in the beginning of the test ('reference image, will be presented in § 4.4') was used to characterize hard inclusions. Herein, Specimen T3 is used as an example to illustrate this process.

As reviewed in Chapter 2, large pores have an important influence on both crack initiation and propagation. Large pores in the studied material characterized in Chapter 3 indicated that a large volume is required to characterize pores due to their large size. A small volume may not represent the distribution of pores in the studied material. Thus it is necessary to check if the distribution of pores in the selected small specimen could represent the distribution in a larger volume. The distributions of pores in Specimen T3 (analyzed volume is about  $8.2 \text{ mm}^3$ ) and in Specimen 2 (presented in Chapter 3, analyzed volume is about  $70 \text{ mm}^3$ ) were compared in Figure 4-5. The green (resp. red) curve and histogram stand for the pores distributions in the small Specimen T3 (resp. studied material, i.e. Specimen2) characterized with a voxel size of  $4.5 \mu\text{m}$  (resp.  $3 \mu\text{m}$ ) in number and volume frequency,

## Chapter 4 Experimental methods

respectively. The small difference between Specimen T3 and Specimen 2 for the first peak, which corresponds to small rounded gas pores, in the number distribution may be caused both by the different resolutions used, which control the detectability of small pores, and by the scattering in cylinder head microstructure. Besides, in Specimen T3, the volume fraction of porosity is 0.88%, which is close to that measured in Specimen 2 (1.17%), and the maximum size of pores is about 1.05 mm, which is a typical size for large defect in this material as presented in Chapter 3. This largest pore is a subsurface shrinkage pore and a close-up view showing its complex microstructure is shown in Appendix III. The selected Specimen T3 is thus representative of the studied material in terms of the size distribution of small pores and most importantly of large pores, which correspond to the peak in the volume distribution in Figure 4-5, that are believed to play the most important part in damage initiation.

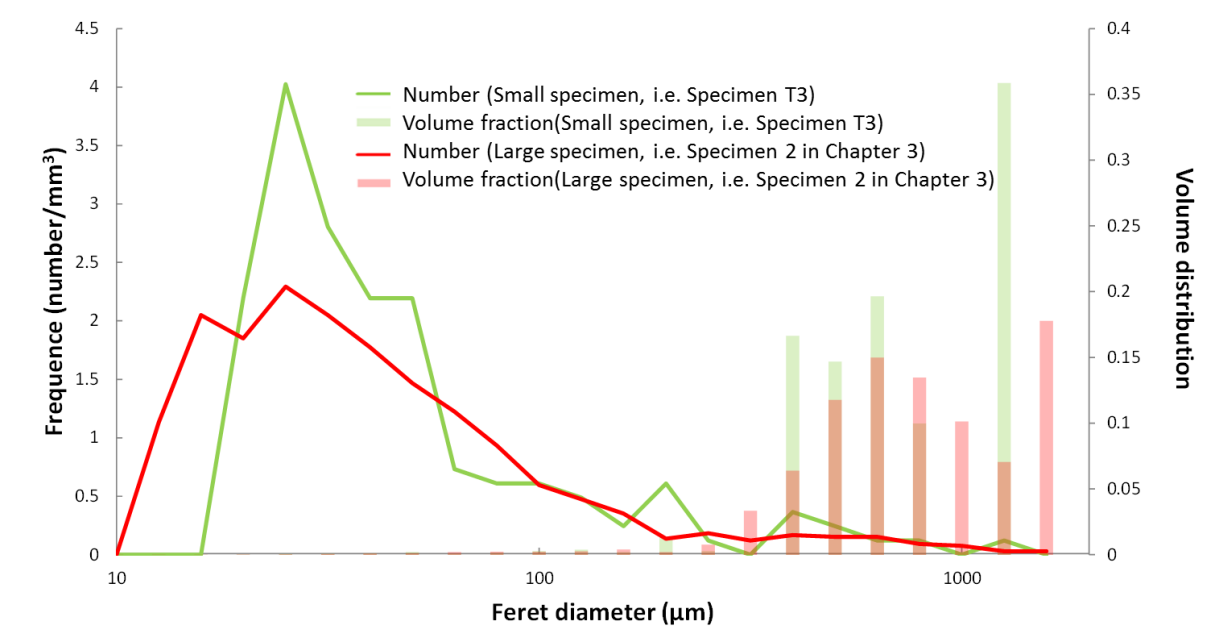


Figure 4-5 Size distributions of pores in Specimen T3 and in a larger sample (Specimen 2)

The reference image taken with a high resolution (1pixel = 1.695μm) was used to characterize the interconnected phases, i.e. iron intermetallics and Al<sub>2</sub>Cu phases. Therefore, the analyzed volume in the ROI of the selected specimen is only 2.68mm<sup>3</sup>. The granulometry distributions of iron intermetallics and Al<sub>2</sub>Cu phases (Figure 4-6) in Specimen T3 and in the larger Specimen 1 (presented in Chapter 3, analyzed volume is about 7.24mm<sup>3</sup>) were compared. Although there are only a little difference between their maximum sizes, the volume fractions of these large size hard inclusions are very low, i.e. less than 1%. These differences may be due to the different characterized volumes. As the average size are almost the same, the distribution of iron intermetallics and Al<sub>2</sub>Cu phases in the selected ROI in the small specimen could also represent this material.

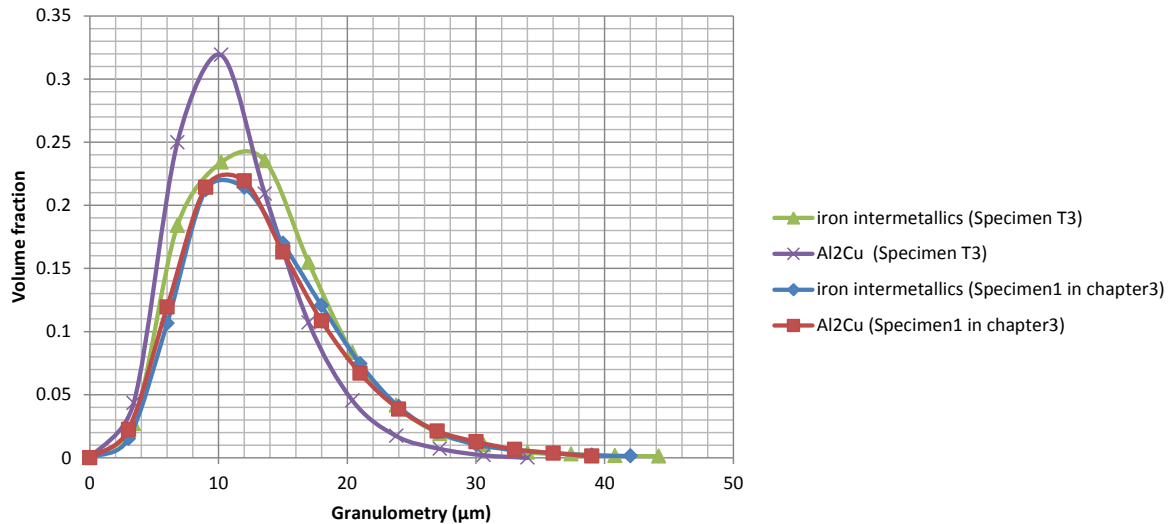


Figure 4-6 Comparison of granulometry distributions of iron intermetallics and Al<sub>2</sub>Cu phases in Specimen T3 and in larger Specimen 1

### 4.4 Experimental protocol

The methods of in-situ observations in 2D on surface and in 3D in volume are introduced at first in this section. Then the procedures for tensile and fatigue tests are detailed. Postmortem analysis methods are introduced in the end of this section.

#### 4.4.1 In-situ observation methods

##### 4.4.1.1 2D in-situ observations on surface

2D in-situ observations were performed at microstructure scale on surface. Observations were performed using Questar long distance microscope equipped with JAI 500 CCD camera (Figure 4-7). Questar was mounted on translation stage which allows displacement in three directions. The resolution, i.e. the pixel size, could be modified with additional lens and by changing the distance between the specimen and the camera. The resolution used for each specimen is listed in Table 4-1. The field of view, i.e. the diagonal length of one image of size  $2456 \times 2050$  pixels<sup>2</sup>, can vary from 0.88 mm to 0.28 mm depending on the resolution. A coaxial lighting was used for surface observations, and its intensity was adjusted to give an appropriate texture for DIC.



## Chapter 4 Experimental methods

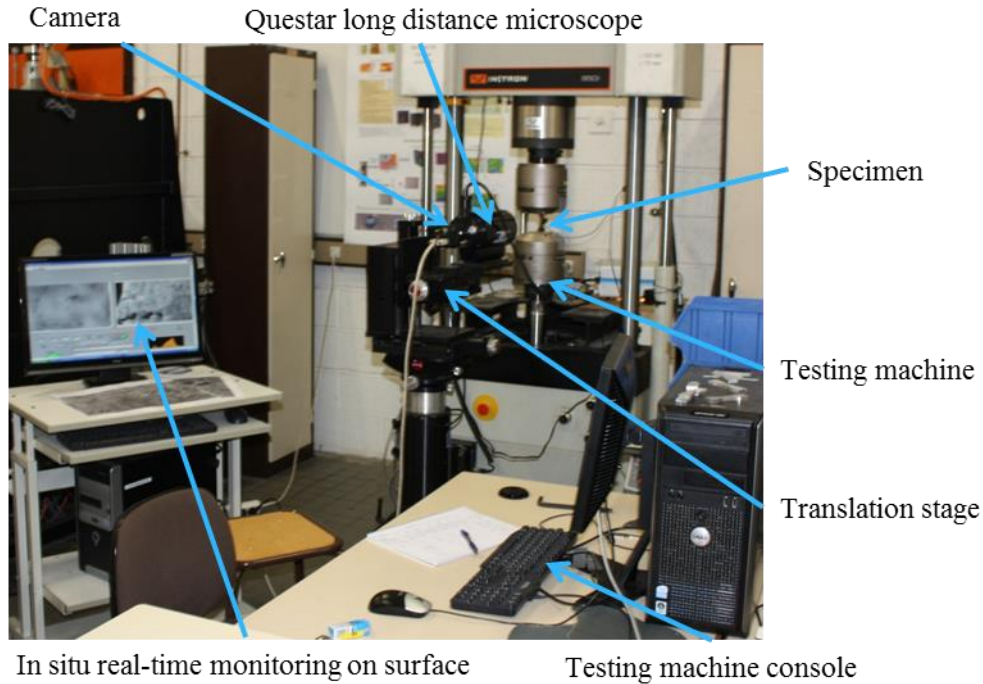


Figure 4-7 2D in-situ observation equipment

At each load step, several images (number for each specimen is listed in Table 4-1) were taken in order to cover the selected ROI (Figure 4-8). An appropriate overlap between adjacent images is necessary for the further stitching of the images to a larger image. As several hundred images needed to be stitched in the following tests, automatic Image Stitching plugins in ImageJ were used (Preibisch et al., 2009).

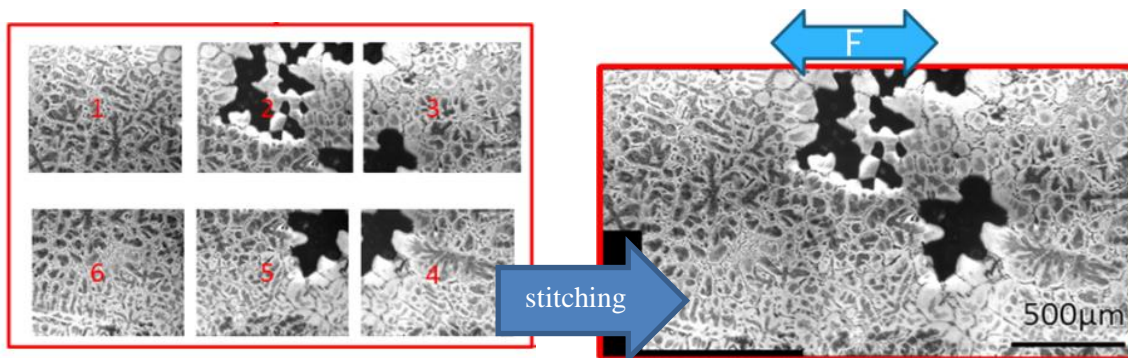


Figure 4-8 Example of images taken at one step using Questar and stitching of images

### 4.4.1.2 3D in-situ observations in volume

3D in-situ observations in volume were performed at the MATEIS laboratory for tensile tests and on TOMCAT beamline at SLS for fatigue tests. The parameters for these tomography experiments are listed in Table 4-2. The resolution for each specimen is listed in Table 4-1 in order to compare with that for 2D in-situ observations.

## Chapter 4 Experimental methods

Table 4-2 Parameter settings for 3D in-situ observations

Test type	Tensile test	Fatigue test
Tomography	Lab-CT (MATEIS, Lyon, France)	SR-CT (TOMCAT, SLS, Swiss)
Acceleration voltage /photon energy	80kV	25KeV
Number of radiographies per scan	900	1500
Acquisition time per image	500 ms	300 ms
Scan time	45 min	7 min
Reconstructed image size	800×820×1000 voxels	1450×1560×2160 voxels

### 4.4.2 Mechanical

#### 4.4.2.1 Tensile tests

In 2D, tensile tests were performed with an Insight 100 SL Material Testing Systems (MTS) electromechanical load frame. A specially designed fixture (Figure 4-9(a)) was used to mount the small specimen in the testing machine. In 3D, an in-situ test rig developed at MATEIS (Buffiere et al., 2010) was installed in the tomography chamber to load the specimen (Figure 4-9(b)). A force sensor allows recording the applied load during the tests that were performed in displacement control mode at a speed of 1  $\mu\text{m/s}$  for both types of tensile tests. The specimen was loaded step by step until fracture except for Specimen T3, which was loaded until the loss of connection with the force sensor. Images were taken in the selected ROI before loading and at each load step when the test was interrupted and the specimen held under load; it was of course necessary to wait for stress relaxation to occur before recording an image (Figure 4-10).

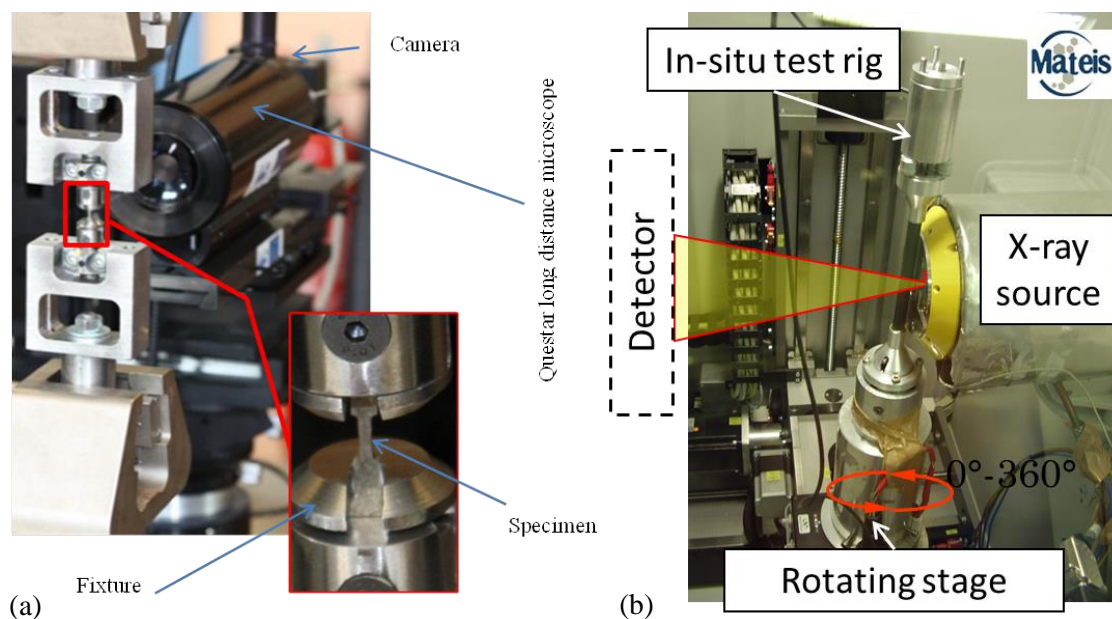


Figure 4-9 Tensile tests with (a) 2D and (b) 3D in-situ observations

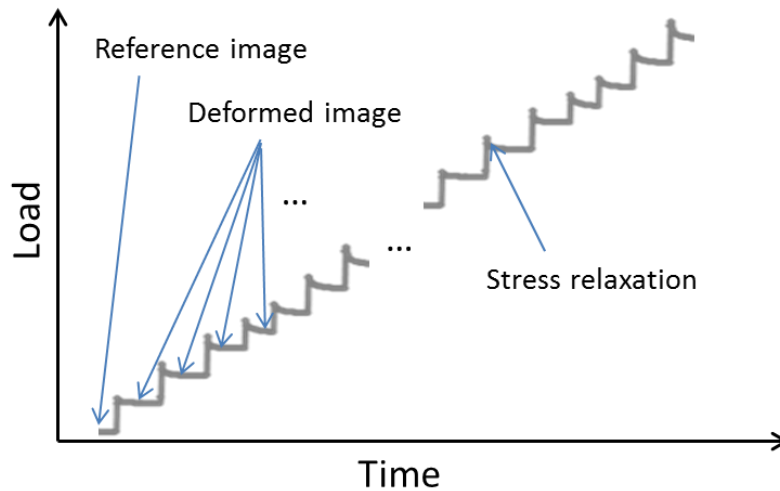


Figure 4-10 Tensile tests process

### 4.4.2.2 Fatigue tests

2D fatigue tests were performed with an Instron 8501 servohydraulic dynamic testing machine. The cyclic loading was controlled in displacement at a speed between 0.003 mm/s and 0.15 mm/s. A smaller speed was applied during the monotonic tensile stage in the 1<sup>st</sup> cycle or when only a few cycles were launched in one step, while a higher speed was applied when a large number of cycles were launched in one step. During the test, the applied load was recorded and an extensometer, which was installed across the notched area of the specimen, was used to measure the macroscopic deformation (Figure 4-11(a)).

In 3D, a specially designed fatigue rig (Figure 4-11(b)) from MATEIS laboratory was used to load the specimen in situ under synchrotron tomography. The cyclic loading was controlled in displacement mode but only the load could be monitored with a force sensor in real time. The cyclic frequency was between 0.3 Hz and 10 Hz. The fatigue test ( $R \approx 0.1\sim 0.2$ ) was performed step by step, only a few cycles were launched between each step. Images were acquired before fatigue cycling and at minimum and maximum loads at each step (Figure 4-12).

Due to stress relaxation, cyclic softening and cracks propagation, the load decreases during the tests. If a significant decrease occurred for the maximum load or if the minimum load fell close to 0 N (in this case, the sample will no longer be held in the grips in 3D or it may come in compression in 2D), the displacement will be manually corrected in order to ensure the cyclic loading is in an ideal state.

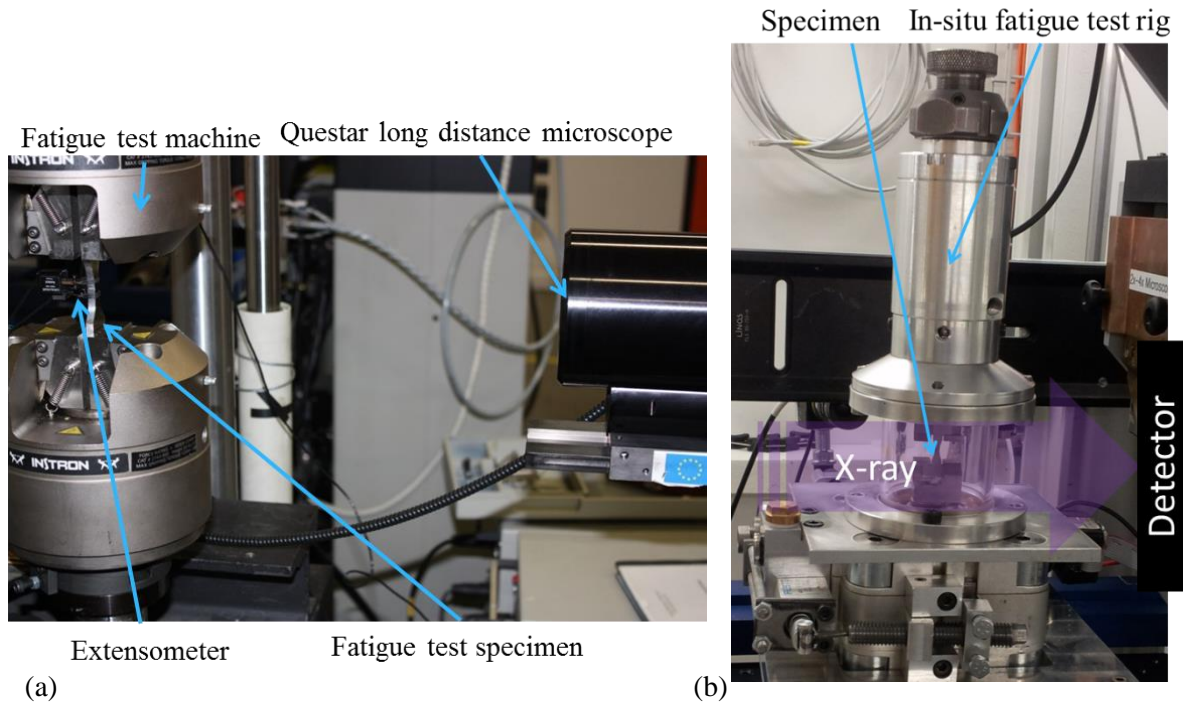


Figure 4-11 Fatigue tests with (a) 2D and (b) 3D in-situ observations

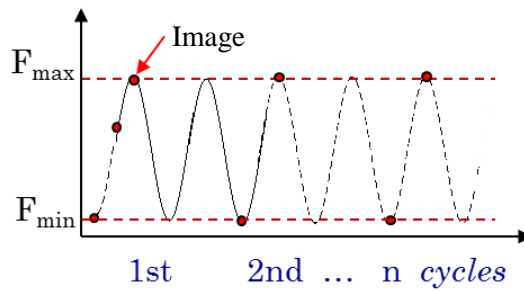


Figure 4-12 Images taken during fatigue tests

### 4.4.3 Postmortem analyses

Postmortem analyses were performed using OM and SEM in order to identify the microcracks on surface and the microstructure along final fracture on flat surface. Fracture analysis was performed using SEM to identify the possible cracks initiations sites in fatigue and to study the fracture morphologies. A scan was also performed on one of the two parts of the broken specimen for each fatigue test with 3D in-situ observations to allow identifying the fracture locations in 3D.

X-ray mappings were performed on all the fracture surfaces of fatigue specimens to identify the damage mechanisms of hard inclusions. Due to the too large size of Specimens F1 and F2, i.e. specimens for 2D fatigue tests, X-ray mappings were only performed on the areas below ROI on flat surface instead of on the whole fracture surfaces (Figure 4-13). The dwell time for each image is 20-



## Chapter 4 Experimental methods

30 seconds which allows revealing the distributions of the studied elements. 30-50 images are acquired for one X-ray mapping image to obtain the necessary contrast for each analyzed element; thus total acquisition time for one map is about 2-3 hours. Each obtained X-ray map is registered on the BSE image in order to observe the relations between the microstructure of the fracture surface and the element distribution, i.e. the distribution of the constituents. Both fracture surfaces images of each specimen are placed side by side (Figure 4-14). Symmetry and rotation transformations are performed on one of the two images to allow comparison of the constituents in the same position on the two fracture surfaces. If the same constituents are identified in the same location on both fracture surfaces, the failure mechanism is fracture of hard particles. Otherwise, the failure mechanism is decohesion/debonding.

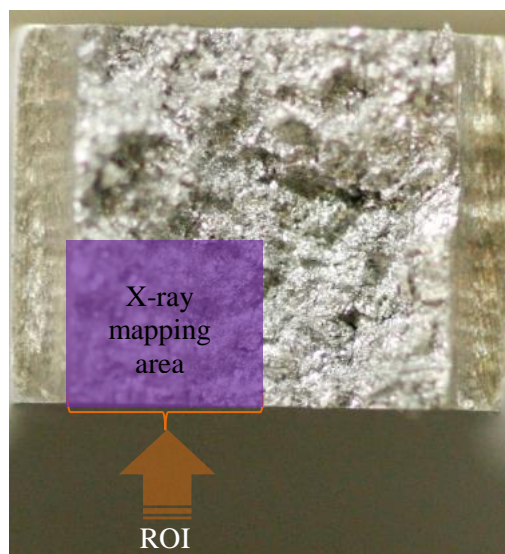


Figure 4-13 Schematic diagram illustrating X-ray mapping area for large size specimens

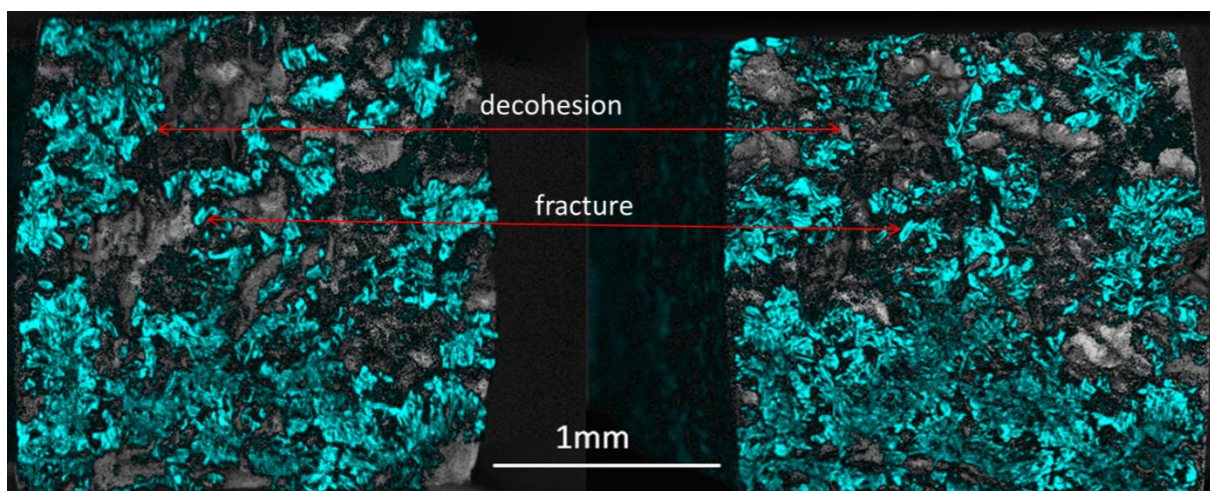


Figure 4-14 Example showing decohesion and fracture of eutectic Si in X-ray mapping images of two fracture surfaces of the same specimen

### 4.5 Field measurements

#### 4.5.1 Basic principles

The measurements on the observed surface and volume were performed by using Digital Image Correlation (DIC) and Digital Volume Correlation (DVC) techniques. DIC, which appeared in the early 1980s, is an optical metrology based on digital image processing and numerical computing. It directly provides displacements and strains full-fields by comparing the digital images of the specimen surface in the un-deformed (or reference) and deformed (or moving ) states respectively (Sutton et al., 2009) (Grediac and Hild, 2012). DVC technique is an extension of the well-developed DIC method and their principles are similar. DVC was developed from the end of 1990s (Bay et al., 1999), and is now widely used due to the development of 3D advanced imaging devices (Sutton et al., 2009) (Limodin et al., 2009) (Pan et al., 2012) .

The first step for correlation is to divide the 2D or 3D image into a virtual grid so that the displacements are computed at each node of this grid. One example for 2D image is shown in Figure 4-15 where the calculation area (i.e. ROI) in the reference image has been divided into a regular-spaced virtual grid. The principle of correlation is the tracking (or matching) of the same points (or pixels) between two images recorded before and after deformation (Sutton et al., 2009).  $\mathbf{X}$  is the vector denoting the position of the current point with respect to the volume coordinate system and  $\mathbf{u}$  is the unknown displacement vector field. Each image is identified by its grey level function representing the volume of the sample:  $f$  for the reference image taken before deformation,  $g$  for the deformed image taken after deformation (Hild and Roux, 2006) (Lachambre et al., 2014). The optical flow equation in (4-1) assumes that the grey level variations are due to the displacement of the material points only:

$$f(\mathbf{X}) = g(\mathbf{X} + \mathbf{u}(\mathbf{X})) \quad (4-1)$$

Herein, only  $\mathbf{u}(\mathbf{X})$  is unknown. This problem could be solved by evaluating the similarity degree between the reference subset and the deformed subset, thus an appropriate criterion coefficient is necessary (Sutton et al., 2009) (Pan, 2007) (Pan et al., 2012):

$$C_{f,g}(\vec{u}) = \text{Corr}\{f(\mathbf{X}), g(\mathbf{X} + \mathbf{u}(\mathbf{X}))\} \quad (4-2)$$

The matching procedure is completed through searching the peak position of the distribution of correlation coefficient. Some commonly used correlation coefficients could be found in the literature such as in (Bay et al., 1999), (Verhulp et al., 2004), (Roux et al., 2008), (Smith et al., 2002), (Moës et al., 1999), (Réthoré et al., 2008), (Bornert et al., 2004), (Pan et al., 2009), (Pan et al., 2012), (Sutton et al., 2009).



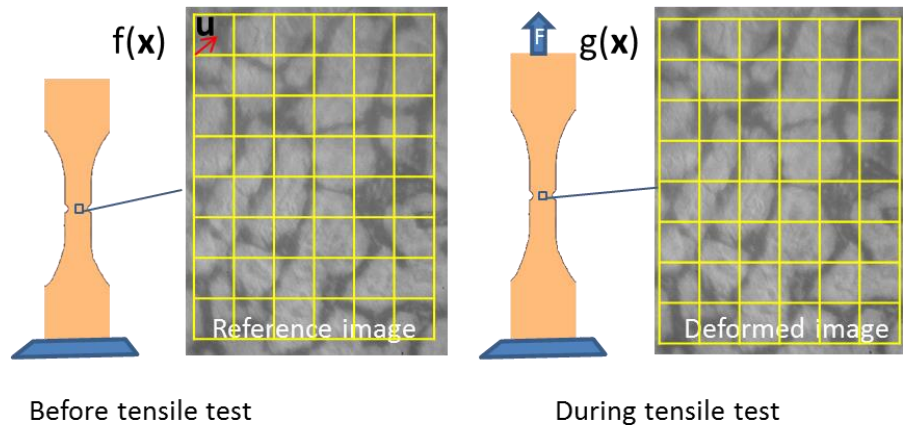


Figure 4-15 Schematic illustration of the two images recorded before and after deformation: a “reference” and a target (or deformed) images.

Once the displacement field has been obtained by the DVC or DIC technique, the strain field could be calculated from the displacement field using the Strain-Displacement Relations.

### 4.5.2 DIC

#### 4.5.2.1 Application conditions

DIC method measures the in-plane displacement if the measurement system and the deformed status satisfy some conditions (Pan, 2007) (Pan et al., 2009):

- (1) The specimen surface must be a flat or an approximately flat plane. If the fluctuating heights on the object surface are small enough, it can be considered as an approximation flat. The well-polished specimens should satisfy this condition.
- (2) The deformation should remain in the same plane parallel to the CCD sensor during loading and the out-of-plane motion of the specimen during loading should be small enough to be neglected. Normally, the out-of-plane motion can be somewhat alleviated by using a telecentric imaging system or placing the camera far from the specimen to approximate a telecentric imaging system. The Questar long distance microscope could ensure that the camera is far from the specimen surface.
- (3) The imaging system should not suffer from geometric distortion. This means that an ideal linear correspondence should exist between the physical point on the measured object surface and the imaged point. The deviation between the optical axis and the surface normal of the measured object always exists, and the geometric distortion is more or less present in an actual optical imaging system or other high-resolution imaging system (e.g. SEM). However, the influence of geometric errors of the imaging system is usually small and thus could be

## Chapter 4 Experimental methods

neglected. If the influence of geometric distortion cannot be neglected, corresponding distortion correction techniques (Sutton et al., 2007a)(Sutton et al., 2007b) should be applied.

- (4) A random gray intensity distribution (i.e. the random speckle pattern), which deforms together with the specimen surface as a carrier of deformation information, is required on the specimen surface. Herein, the used etching method (presented in Chapter 3) could provide natural tracers on specimens' surfaces.

### 4.5.2.2 DIC using Elastix

Elastix software (Klein et al., 2010) is a publicly available computer program for intensity-based image registration and consists of a collection of algorithms that are commonly used to solve medical image registration problems. Some basic methods used in this thesis are introduced in the following, for more details please refer to (Klein and Staring, 2012) and the cited references. One can also refer to a Ph.D. thesis (Wang, 2014) in the laboratory in which Elastix was used. One example of the parameters used is given in Appendix IV.

The minimization problem (in equation 4-2) is solved with an iterative optimization method, usually in a multiresolution setting. The general components of a parametric registration algorithm in a block scheme are shown in Figure 4-16 (Klein and Staring, 2012). Some components used in this thesis are presented later. More details illustrating this scheme could be found in (Klein et al., 2010).

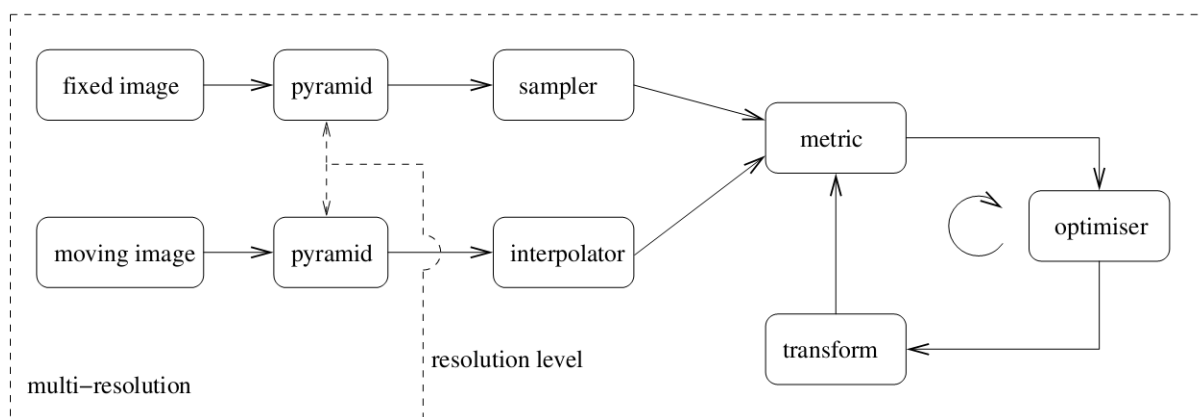


Figure 4-16 The basic registration components (Klein and Staring, 2012)

- The commonly used similarity measure (i.e. '**metric**' in Figure 4-16) in Elastix software are Sum of Squared Differences (SSD), Normalized Correlation Coefficient (NCC), Mutual Information (MI), Normalized Mutual Information (NMI), Kappa Statistic (KS); they are detailed in (Klein and Staring, 2012). The Normalized Correlation Coefficient (NCC), i.e. Advanced Normalized Correlation metric, which assumes a linear relation between the intensity values of the fixed and moving image, was used here.

## Chapter 4 Experimental methods

---

- In Elastix software, the transformation is defined as a coordinate mapping from the fixed image domain to the moving image domain. The used transformation model determines what type of deformations between the fixed and moving image one can handle. The common transformation types are the translation, the rigid, the similarity, the affine, the non-rigid B-spline and the non-rigid thin-plate spline like transformations. Here, B-splines **Transform**, which is often used as a parameterization for the category of non-rigid transformations, was used. The transformation of a point can be computed from only a couple of surrounding control points as B-splines have local support. This is conducive to model local transformations, and to fast computation. More explanations about B-splines Transform could be found in (Klein and Staring, 2012) (Unser, 1999) (Rueckert et al., 1999).
- The commonly used **optimisers** in Elastix are gradient descent (GD), Robbins-Monro (RM), quasi-Newton (QN), nonlinear conjugate gradient (NCG) (Klein et al., 2007). Herein, Adaptive Stochastic Gradient Descent (Klein et al., 2009), which is a more advanced version of GD, was used as it sets less parameter and is more robust.
- Gaussian **pyramid** (Lester and Arridge, 1999), i.e. Fixed Recursive Image Pyramid and Moving Recursive Image Pyramid, which applies smoothing and down-sampling, was used as the multiscale resolution strategy, i.e. “pyramid “ in Figure 4-16. This is a timesaving pyramid as image contains much fewer voxels in the first resolution levels.
- $N$ -th order B-Spline **Interpolator** (Unser, 1999) was selected as the interpolator; a better quality requires a higher order and more computation time. A first order B-spline interpolation, i.e.  $N = 1$ , commonly gives satisfactory results for registration, while a higher-order interpolation is generally required for the deformed results of the registration.  $N = 3$  is recommended in (Klein and Staring, 2012).
- Random **sampler** (Klein et al., 2007), which randomly selects a user-defined number of pixels from the fixed image, was used as ‘sampler’ in Figure 4-16. It allows each voxel being selected with equal chance. A mask which covers the pores and the area outside the specimen was made using ImageJ to restrict the DIC computation, i.e. Image sampler, to the surface of specimen.

In order to reduce the noises in the measured fields, a bending energy penalty term was added to the cost function. It penalizes sharp deviations of the transformation (e.g. no high compression followed by a nearby high expansion), and can be used to regularize the non-rigid transformation (Klein and Staring, 2012) (see Figure 4-17). The two user-defined constants that weigh similarity (Metric0) against regularity (Metric1), i.e. ‘Metric0 Weight’ and ‘Metric1 Weight’, were adjusted for each test.

## Chapter 4 Experimental methods

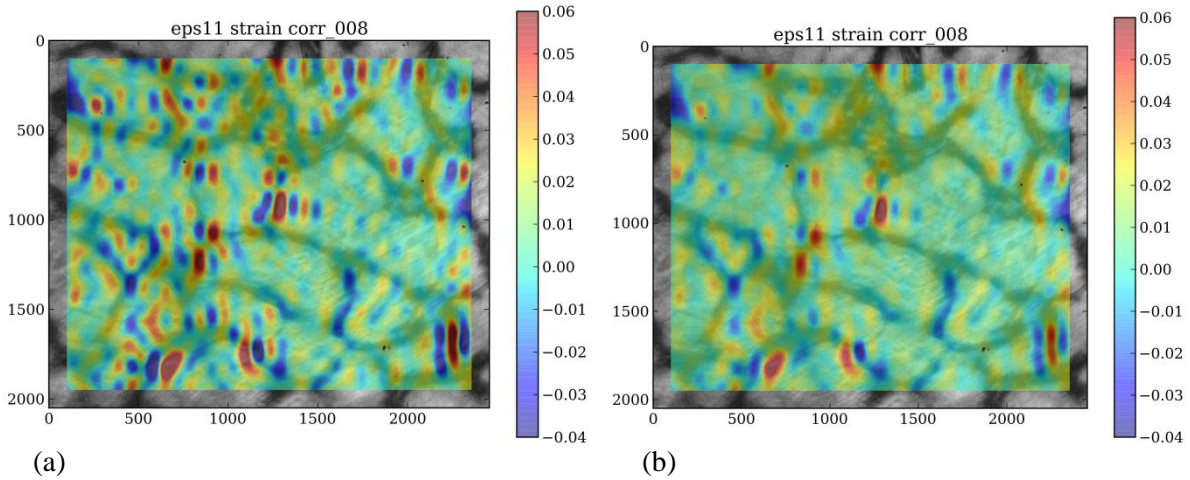


Figure 4-17 Examples of a strain field calculated: (a) without and (b) with bending energy penalty term ('Metric0 Weight = 1.0' and 'Metric1 Weight = 100').

Tensile tests with 2D in-situ observations were also performed on another three selected A356 specimens. The experimental protocol is the same as that for Specimens T1 and T2 besides a much larger magnification was applied. The used pixel size is about  $0.17 \mu\text{m}$ , which is only half of that for Specimens T1 and T2. However, depth of field (DOF), which is the distance between the nearest and farthest objects in a scene that appear acceptably sharp in an image, reduces with the increasing magnification. With the experimental equipment used in this thesis, a good focus was difficult to obtain in the case of a  $0.17 \mu\text{m}$  pixel size and the images become a little blurred. There is always too much noise in the measured fields from DIC by using these high resolution images, although a variety of means have been tried to reduce the noise to an acceptable level. Thus the in-situ tensile tests with the higher resolution on A356 alloy were failed. An equipment, which could provide an enough DOF with a higher resolution for the imaging systems, would give exploitable results at a higher resolution. However, under the present experimental conditions, the fatigue tests with 2D in-situ observations on A319 alloy were performed with the medium resolution (1 pixel  $\approx 0.34 \mu\text{m}$ ) used for the well validated tensile tests performed on A356 alloy.

### 4.5.3 DVC

Field measurements using DVC for tensile tests were performed using the Mechanical Image Correlation (MIC3D) algorithm developed by J. Réthoré (LaMCoS, France). The analyzed image size for DVC is  $800 \times 820 \times 800$  voxels ( $1.36 \times 1.39 \times 1.36 \text{mm}^3$ ). The volume inside the specimen was selected as ROI for the DVC measurements, and its size is  $688 \times 768 \times 768$  voxels ( $1.17 \times 1.3 \times 1.3 \text{mm}^3$ ). The correlation was performed between the reference image and each deformed image, the displacement and strain fields at each step were thus obtained. As only the applied load was known through the in-situ test rig, the average strain was calculated with DVC in order to obtain a stress-strain curve. The displacement discontinuity induced by the crack avoids matching the reference

## Chapter 4 Experimental methods

---

image to the image corrected by the measured displacement field. This so-called residual error, which could be calculated as 'Reference image + calculated displacement fields – moving image', is maximum at the cracks locations and gives information about the crack geometry. The thresholding of the original tomographic image is difficult due to the limited opening of the crack compared to the voxel size. Thus the residual error provides a less arbitrary way to extract the cracks than greyscale thresholding from the tomography image (Limodin et al., 2009) (Réthoré et al., 2012) (Lachambre, 2014).

The tomographic images of fatigue tests were filtered with a binning process to reduce both image size and noise for the following DVC measurements. After binning, the size of one image is  $725 \times 780 \times 1080$  voxels, and one pixel =  $3.25 \mu\text{m}$ . A 2D/3D image correlation platform based on C++ has been recently developed at LML. This platform, which is optimized for treating large data set in a limited time, was used for rigid registration and DVC measurements for the fatigue tests:

- (1) Rigid displacement and rotation may exist between different images taken during the fatigue tests because:
  - The upper grip of the in-situ fatigue test rig is fixed and the load is applied through the lower grip. Thus this results in a unidirectional overall displacement.
  - The in-situ fatigue machine for tomography does not allow the heads of specimen to be rigidly fixed in the grips as in standard fatigue machines. This results both in rigid displacement and rotation.
  - The specimen was reloaded when a significant decrease in the maximum or minimum load occurred. This also results both in rigid displacement and rotation.
  - Dust may progressively adhere to the scintillator of the detector during one fatigue test and cannot be easily removed so that an in-plane displacement has to be applied to the scintillator in front of the detector to allow image recording away from the dust.

The above mentioned rigid displacement and rotation made the comparison between different cycles difficult. Thus, using the correlation platform, all the tomographic images were rigidly registered with the image taken before the fatigue test, i.e. at the minimum load of the 1<sup>st</sup> cycle. The principle of image registration (Sotiras et al., 2013) (Zitová and Flusser, 2003) is the same with DVC. The following analysis and DVC were performed after rigid registration.

- (2) DVC measurements were performed between the minimum and maximum loads of the same cycle. The following results were obtained:
  - ✓ The displacement field and strain field in the bulk of the specimen at different cycles.
  - ✓ Only the applied load could be directly measured during the in-situ fatigue tests. The average deformation along the loading direction at different cycles was computed from DVC in the absence of an extensometer.

## Chapter 4 Experimental methods

---

- ✓ Field of Crack Opening Displacement (COD). COD was computed using two slices of the displacement field perpendicular to the loading direction: one above and one below the studied crack. The subtraction operation between these two slices yields the COD map. This method of COD calculation was used to study crack propagation in the works of (Limodin et al., 2009) (Limodin et al., 2010).
- (3) DVC measurements performed at the minimum load between the 1<sup>st</sup> cycle and the other cycles allow obtaining the shape of plastic deformation zones at different cycles (Lachambre, 2014).
- (4) DVC measurements performed between the minimum loading of the 1<sup>st</sup> cycle and the maximum loading at the other cycles are expected to yield the 3D cracks using the residual error field (Limodin et al., 2010) .

### 4.5.4 Measurement uncertainty

Measurement uncertainty (Rabinovich, 1999) was used to assess the measurement accuracy of DIC (Amiot et al., 2013) and DVC (Reu, 2013). The measurement uncertainty of DIC or DVC is usually evaluated through the comparison between a prescribed displacement and the displacement measured from DIC or DVC (Limodin et al., 2014) (El Bartali, 2007). The displacement may be a translation of the virtual image or a translation of the physical object (Lachambre, 2014). The first case is used to test the algorithm and the texture of the image (Roux et al., 2008) and the second allows in addition to take into account all the image acquisition system, e.g. reconstruction artifacts (Limodin et al., 2011). Therefore, the second method was used here. The uncertainty is estimated from the standard deviation of the displacement field measured by DIC / DVC between two images, i.e. one at a reference position and another one after translation (Roux et al., 2008) (Passieux and Périé, 2012) (Gomes Perini et al., 2014). How to apply this translation differs according to the cases presented below:

**Uncertainty of the displacement field from DIC (in 2D):** The reference image was taken on the specimen surface. Then a given displacement (10  $\mu\text{m}$  in the present case) was imposed on the Questar translation stage in a direction perpendicular to the specimen surface and the moving image was taken at this position.

**Uncertainty of the displacement field from DVC (in 3D):** Two methods were used for lab-CT and SR-CT separately.

Lab-CT (both A356 and A319 alloys): Two scans were taken: one at a reference position and another one after a translation along the beam direction. As the beam of lab-CT is conical, the voxel size is changed (from 1.7 to 1.695 $\mu\text{m}$  in the present case). Thus a known displacement field in all directions,



## Chapter 4 Experimental methods

i.e. a dilatation, which corresponds to a maximum displacement of 1.5 voxel, was applied (Limodin et al., 2014).

SR-CT: As in the 2D uncertainty assessment from DIC, the reference scan was taken at a reference position and the moving image was recorded after a small displacement (10  $\mu\text{m}$  in the present case) of the specimen in a direction perpendicular to the beam direction and to the axis of rotation of the stage.

Figure 4-18 shows measurement uncertainties for A356 alloy, using (1) Questar microscope (Limodin et al., 2014) and (2) lab-CT (Limodin et al., 2014), and for A319 alloy, using (3) lab-CT and (4) SR-CT, as well as for other materials in the literature: polypropylene solid foam using SR-CT in (Roux et al., 2008), ferritic cast iron using lab-CT in (Limodin et al., 2009) and using SR-CT in (Limodin et al., 2010). The measurement accuracies in this thesis are acceptable as: (1) element size is much larger than uncertainties (about 50 ~ 100 times); (2) the uncertainties are generally smaller than that in the literature in the case of the same element size. Measurement accuracies in this thesis could be ranked from high to low as: A356 2D measurements > A319 SR-CT > A319 lab-CT > A356 lab-CT.

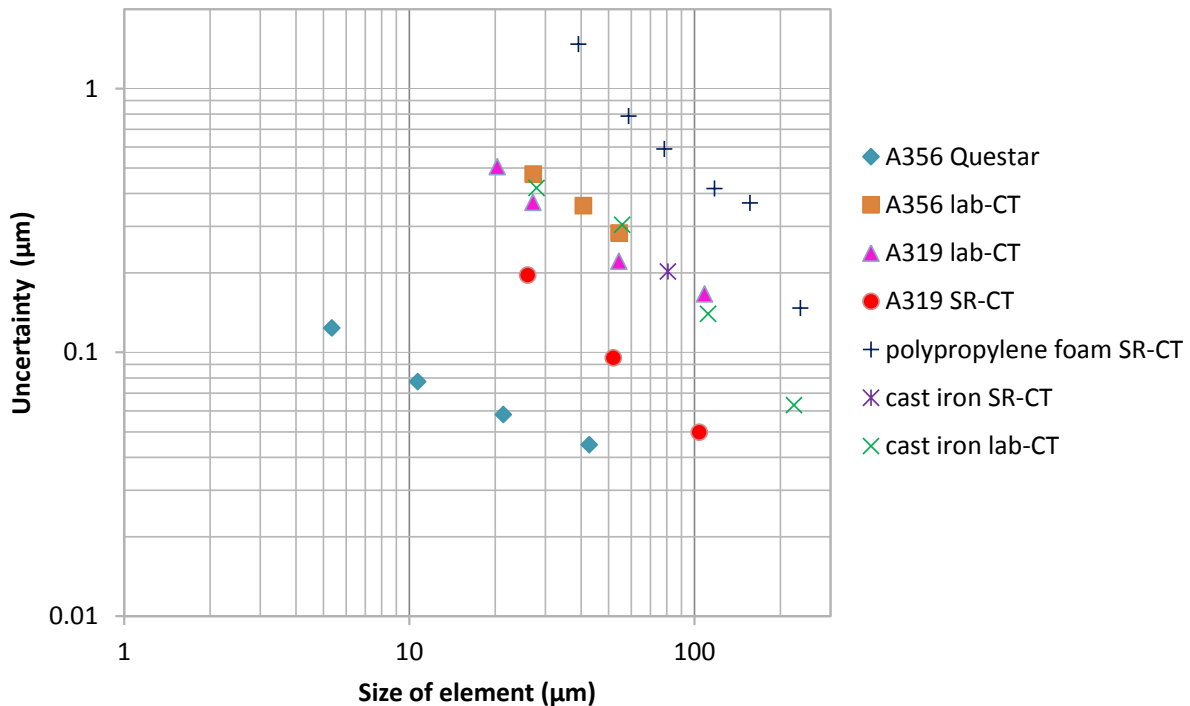


Figure 4-18 Measurements uncertainties

An etching method has been applied on 2D in-situ specimens to give the specimen surface the natural tracers that are necessary for DIC. In 3D, the microstructural features revealed by lab-CT (Table 4-3) were successfully used as natural markers for DVC. Resolution of DVC technique depends directly on the presence of numerous and finely dispersed microstructural features (Limodin et al., 2014). As characterized in Chapter 3, A319 alloy has a volume fraction of natural tracers about 10 times higher

## Chapter 4 Experimental methods

than A356; in particular it has eutectic Al-Al<sub>2</sub>Cu phases that are not present in A356 alloy. Thus DVC measurements using lab-CT images have higher accuracy for A319 than for A356 alloy for a given spatial resolution. SR-CT reveals Si phase that is not revealed in lab-CT. As more natural tracers are observed with SR-CT than with lab-CT, a higher measurement accuracy is obtained for the former. In contrast, the spherical nodules inside cast iron are used as the only natural markers for DVC either by using lab-CT (Limodin et al., 2009) or SR-CT (Limodin et al., 2010), thus their measurement accuracies are virtually the same. As shown in Figure 3-1, etching reveals segregation of Si that gives contrast to Al matrix. Thus 2D measurements on the etched surface have higher accuracy than the others.

Table 4-3 Natural tracers for DIC and DVC

Material	Observation mode	Natural tracers			
		Iron intermetallics	Copper containing phases	Si	Al matrix
A356	Questar	✓	-	✓	✓
	lab-CT	✓	-	-	-
A319		✓	✓	-	-
	SR-CT	✓	✓	✓	-
	Questar	✓	✓	✓	✓

Measurement uncertainty always depends on the element size, i.e. the grid spacing in Figure 4-15. It decreases with the increasing of element size, but a large element size will reduce the spatial resolution. For the balance between the measurement accuracy, i.e. uncertainty, and the spatial resolution, i.e. element size, an appropriate element size, which also corresponds to an acceptable uncertainty, was selected for each measurement; they are listed in Table 4-4.

Table 4-4 Selected element size for each measurement

Measurements	Element size		Uncertainty (μm)
	Pixels/voxels	μm	
A356 Questar	32	10.72	0.077
A356 lab-CT <sup>1</sup>	16	27.2	0.473
A319 lab-CT	16	27.2	0.370
A319 SR-CT	16 <sup>2</sup>	26.0	0.196

1. Experiments are presented in (Limodin et al., 2014).
2. 16 voxels in the original image, i.e. 8 voxels in the images after binning.

# Chapter 4 Experimental methods

## 4.6 Summary

Four types of tests (Figure 4-19), i.e. tensile/fatigue tests with 2D/3D in-situ observations, were presented here. The developed experimental protocol (Figure 4-20) was first validated in tensile tests and was then applied in fatigue tests. The basic information for each specimen is listed in Table 4-1, and one can refer to Appendix III for more details.

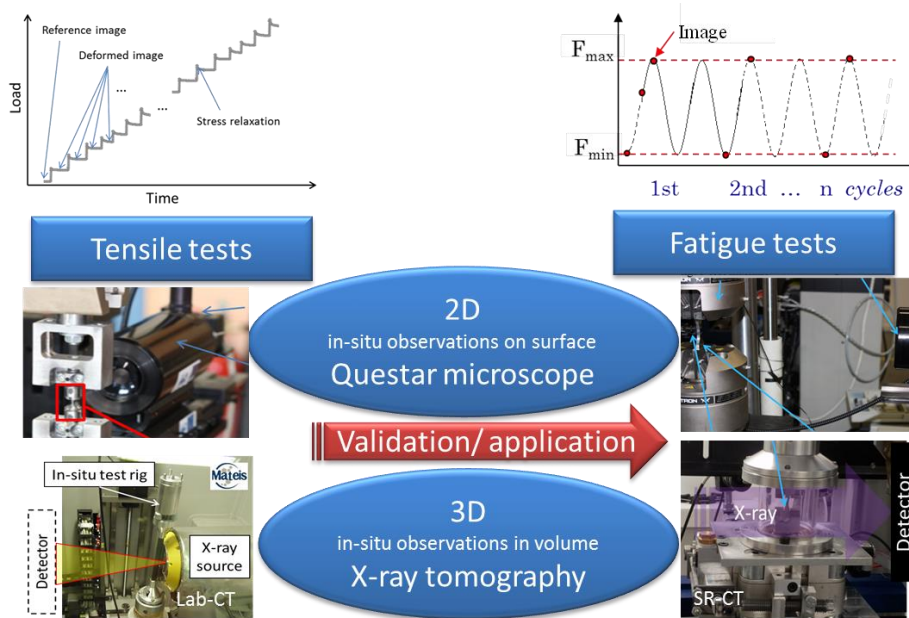


Figure 4-19 Four types of tests in this thesis

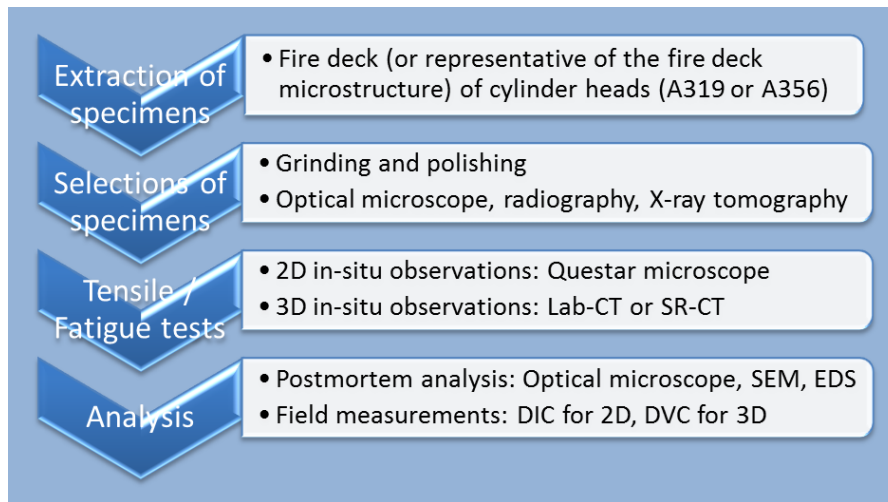


Figure 4-20 Basic experimental protocol in this thesis

# Chapter 5 Damage mechanisms in Al-Si alloys

## Contents

---

<b>5.1</b>	<b>Introduction.....</b>	<b>- 110 -</b>
<b>5.2</b>	<b>Tensile damage mechanisms .....</b>	<b>- 110 -</b>
5.2.1	Tensile tests with 2D in-situ observations .....	- 110 -
✓	Tests results.....	- 110 -
✓	Postmortem analysis .....	- 111 -
✓	DIC measurements.....	- 115 -
5.2.2	Tensile tests with 3D in-situ observations .....	- 120 -
✓	Tests results and DVC measurements.....	- 120 -
✓	Post-mortem analysis .....	- 124 -
✓	Crack initiation and growth.....	- 126 -
5.2.3	Discussion .....	- 128 -
5.2.3.1	Application of 2D in-situ tensile tests on A356 alloy .....	- 128 -
5.2.3.2	Application of 3D in-situ tensile tests on A319 alloy .....	- 130 -
<b>5.3</b>	<b>Fatigue damage mechanisms.....</b>	<b>- 132 -</b>
5.3.1	Fatigue tests with 2D in-situ observations .....	- 132 -
✓	Results of 2D fatigue tests .....	- 132 -
✓	Crack initiation.....	- 133 -
✓	Crack propagation.....	- 141 -
✓	Final fracture .....	- 146 -
✓	DIC measurements.....	- 148 -
5.3.2	Fatigue tests with 3D in-situ observations .....	- 152 -
✓	Results of 3D fatigue tests .....	- 152 -
✓	Cracks initiation .....	- 153 -
✓	Crack propagation.....	- 157 -
✓	Crack opening .....	- 163 -
5.3.3	Discussion .....	- 164 -
✓	Crack initiation.....	- 165 -

## Chapter 5 Damage mechanisms in Al-Si alloys

---

✓ Crack propagation .....	- 170 -
✓ Final fracture .....	- 171 -
✓ Damage mechanisms of hard inclusions .....	- 172 -
<b>5.4 Summary .....</b>	<b>- 173 -</b>
5.4.1 Experimental protocol.....	- 173 -
5.4.2 Damage mechanisms.....	- 174 -
5.4.2.1 A356 LFC alloy .....	- 174 -
5.4.2.2 A319 LFC alloy .....	- 174 -
✓ Tensile damage mechanisms.....	- 174 -
✓ Fatigue damage mechanisms .....	- 175 -

---

### 5.1 Introduction

The developed experimental protocol was first applied in tensile tests on A356 to validate 2D in-situ test and on A319 alloy to validate 3D in-situ tests. These results are presented separately at the beginning of § 5.2. Then the used experimental protocol and tensile damage mechanisms are discussed. Afterwards the validated experimental protocol was applied in LCF to study damage mechanisms in A319 LFC alloy. Section 5.3 first presents and analyzes the results of fatigue tests with 2D and 3D in-situ observations respectively. Then, damage mechanisms of A319 alloy are discussed and summarized. The first part of § 5.4 evaluates this experimental protocol according to its application in this study. Finally, some conclusions are drawn about damage mechanisms in tensile loading and in LCF for Al-Si LFC cast alloys.

### 5.2 Tensile damage mechanisms

#### 5.2.1 Tensile tests with 2D in-situ observations

##### ✓ Tests results

Preliminary tensile tests with 2D in-situ observations were realized on two A356 specimens, i.e. Specimen T1 and T2. These two specimens have different pores distributions, different shapes and different tensile strengths (see Table 5-1). Seven steps (resp. 16) for Specimen T1 (resp. Specimen T2) were performed before the final failure. While Specimen T1 failed from a crack inside the ROI at a normal stress of 73MPa and overall average strain of 0.5%, Specimen T2 failed outside the ROI at a normal stress of 246MPa and an overall average strain of 0.7%.

## Chapter 5 Damage mechanisms in Al-Si alloys

Table 5-1 Results of 2D tensile tests

Specimen		T1	T2
Shape		Unnotched	Notched
ROI cross-sectional areas		6780 × 3670 pixels, i.e. 2.31 × 1.25 mm	4570 × 3970 pixels, i.e. 1.55 × 1.35 mm
Steps before final failure		7	16
Final failure	Normal stress	73 MPa	246 MPa
	Average longitudinal strain (Extensometer)	0.5%	0.7%
	Location	Inside ROI	Outside ROI

### ✓ Postmortem analysis

Postmortem analysis shows that, in Specimen T1 (Figure 5-1(a)), the final fracture occurred in the selected ROI at a large cluster of surface breaking pores, which was observed both in the radiography and OM image. In Specimen T2 (Figure 5-2), the final fracture occurred outside the selected ROI although notches were added. Some sporadically distributed pores (white color in Figure 5-2) could be observed in the region that corresponds to the final fracture in the radiography image, although they are not as clear as the pore present in the selected ROI.

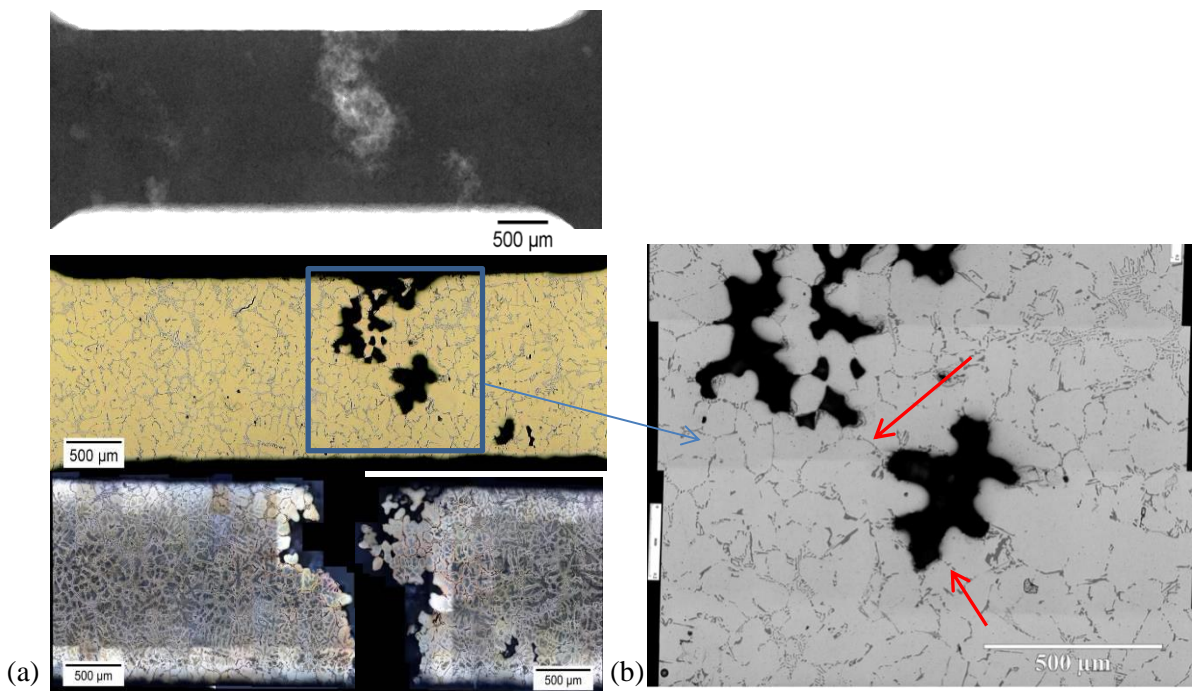


Figure 5-1 (a) Postmortem OM image (bottom) of Specimen T1 compared with radiography (top) and OM (middle) images taken before the tensile test, with (b) a larger magnification in the ROI marked by a rectangle.



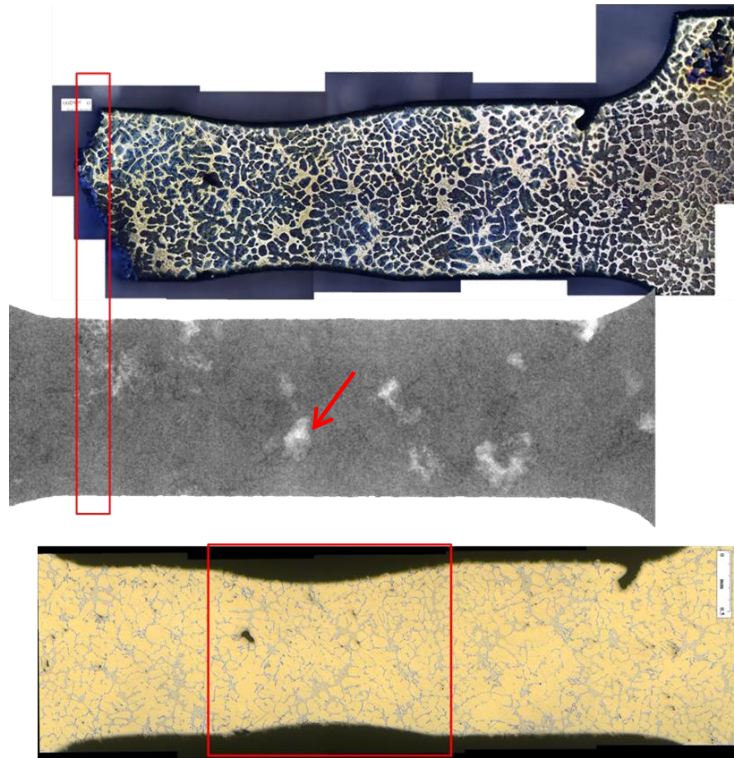


Figure 5-2 Postmortem OM image of Specimen T2 (top) compared with radiography (middle) and OM (bottom) images taken before the tensile test

The fracture analysis (Figure 5-3) reveals pores on fracture surfaces in both Specimens T1 and T2. A large cluster of pores (Figure 5-3(a)) occupies about half of the cross-sectional area of the fracture surfaces of Specimen T1. A single large pore (Figure 5-3(b)), which is very close to the surface (less than 0.01 mm below the surface), is observed in fracture surface of Specimen T2.

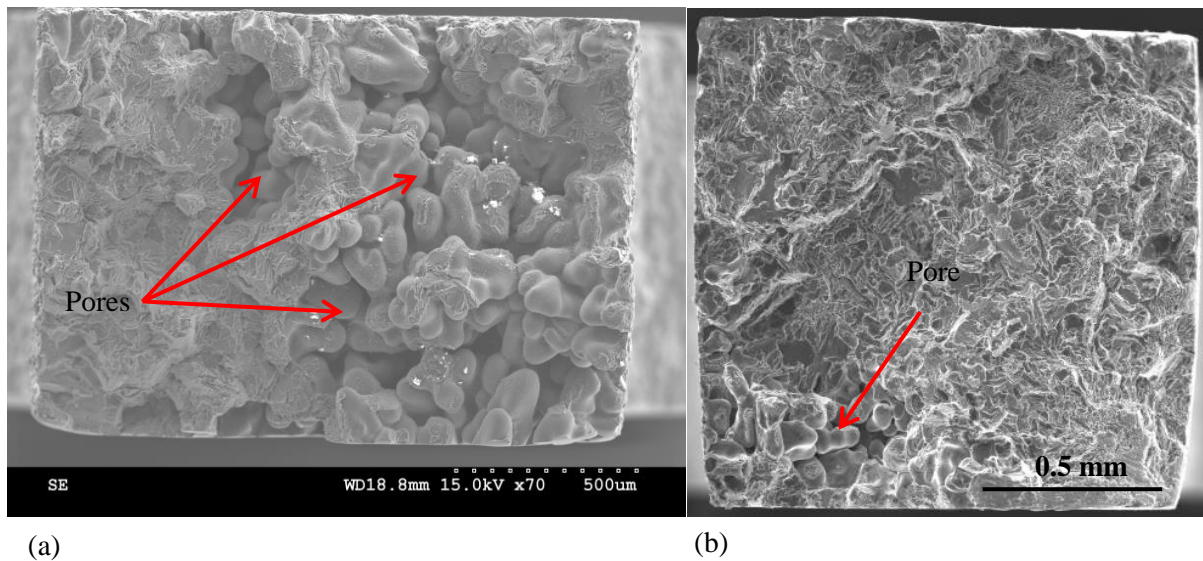


Figure 5-3 Fracture analysis of Specimens (a) T1 and (b) T2

## Chapter 5 Damage mechanisms in Al-Si alloys

Cracks were observed clearly in the Questar images of Specimen T1 (see large cracks marked by arrows in Figure 5-4(a)). They nucleate in the vicinity of large pores. Comparisons with OM image at a larger magnification (Figure 5-1(b)) shows that the cracks marked by arrows are along the Si particles. Postmortem SEM analysis could reveal microcracks and phases better as shown in Figure 5-5(a). Microcracks and the final failure occurred at hard inclusions, such as eutectic Si and iron intermetallics.

Although the overall deformation was measured in the Questar images of Specimen T2 during the tensile test, no large cracks could be observed directly in this area. However, SEM postmortem analysis in the selected ROI (Figure 5-5(b)) with a higher resolution shows that microcracks are present at hard inclusions, including eutectic Si and iron intermetallics, especially in the area where a large pore is marked by an arrow in the radiography image (Figure 5-2), and in the final fracture area.

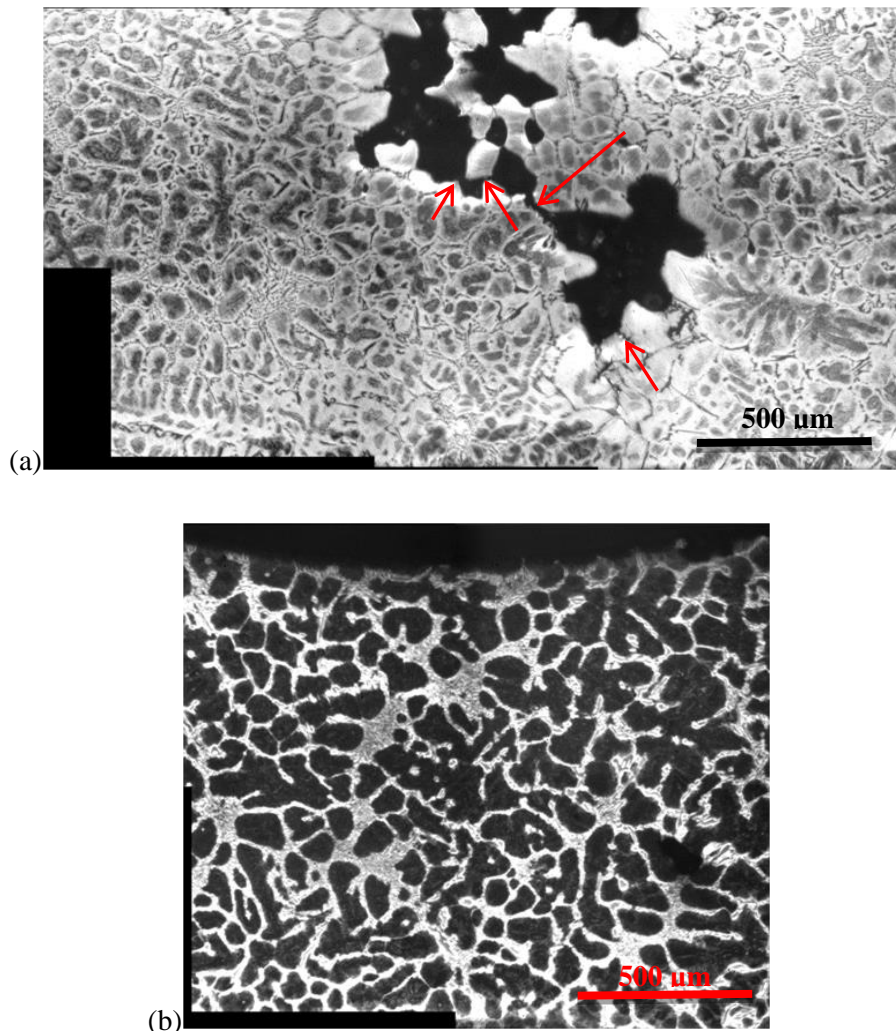


Figure 5-4 Stretched Questar images at the last step before failure: (a) 7<sup>th</sup> step of Specimen 1 at 71MPa (large cracks are marked by arrows); (b) 16<sup>th</sup> step of Specimen 2 at 237MPa

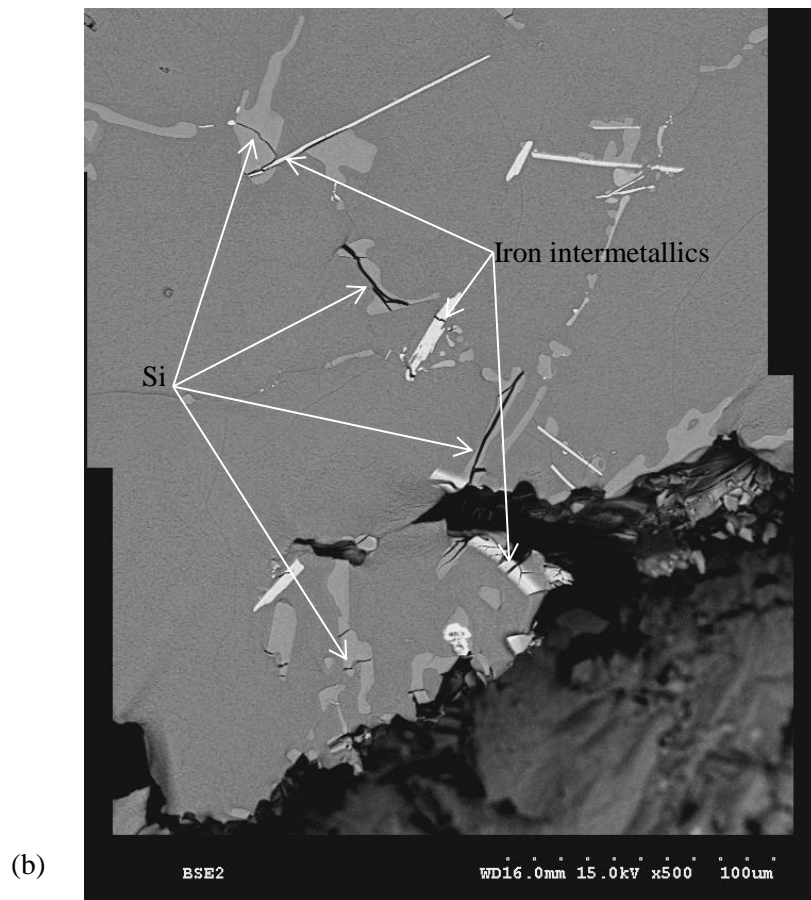
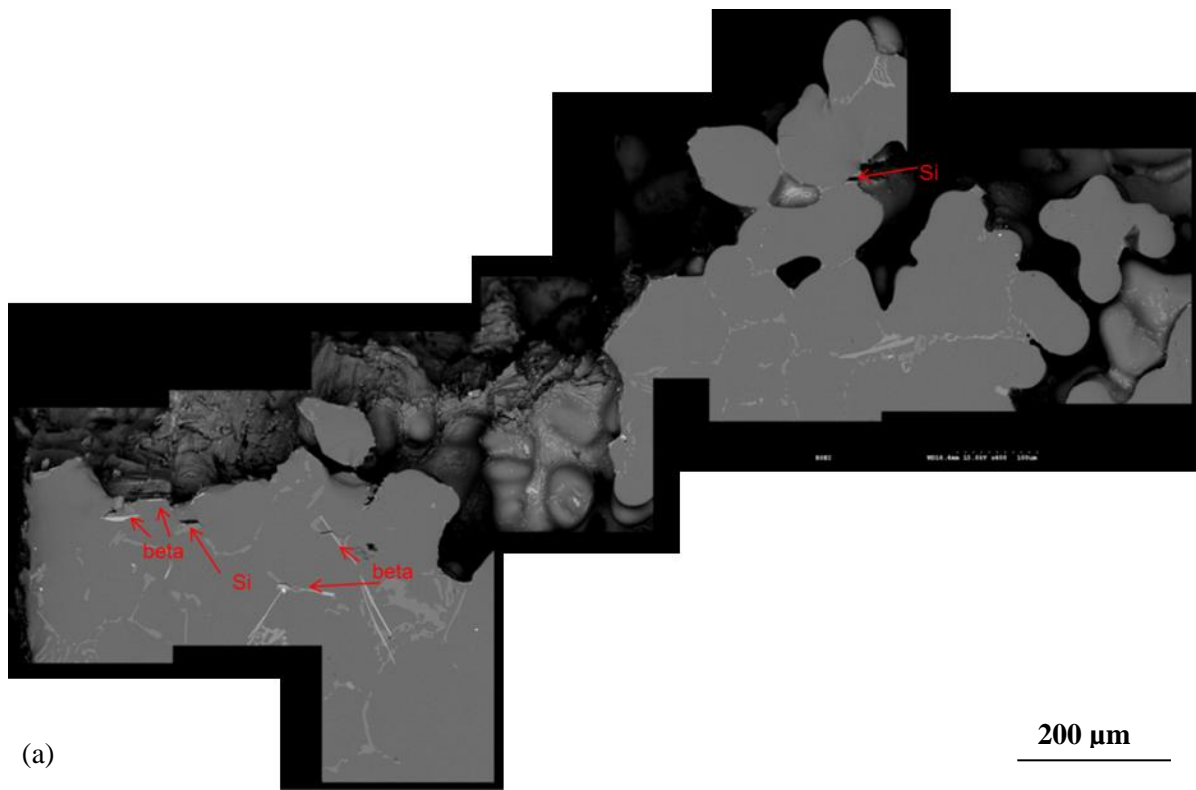


Figure 5-5 SEM postmortem analysis in Specimens (a) T1 and (b) T2: microcracks and final fracture at hard inclusions (Si particles, iron intermetallics).

### ✓ DIC measurements

The stress-strain curve from a standard test performed on A356 alloy with extensometer is shown in Figure 5-6. The average strain at each step calculated from DIC, was used to draw the stress-strain curves for the in-situ tests. Compared to the former, the stress-strain curve of Specimen T2 deduced from DIC measurements could be considered reliable. The stress-strain curve of Specimen T1 from DIC measurements is far below the stress-strain curve from the standard test. The reason will be discussed after.

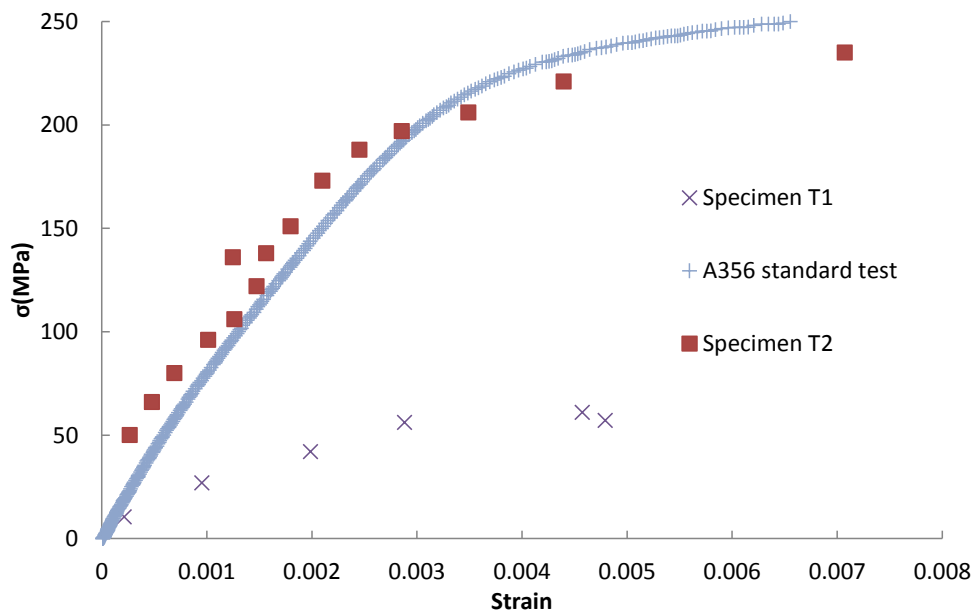


Figure 5-6 Stress-strain curves deduced from DIC measurements for Specimens T1 and T2 and from a standard test performed on A356 alloy.

In Specimen T1, the discontinuities in displacement fields along the loading direction (U1) were observed from the 3<sup>rd</sup> step (Figure 5-7 (a)). Then they increased at increasing load from Figure 5-7 (a) to Figure 5-7 (e). A good correlation is observed between these discontinuities in the displacement field (Figure 5-7 (f)) and the final fracture and microcracks at eutectic and intermetallic hard inclusions observed in SEM post-mortem analysis.



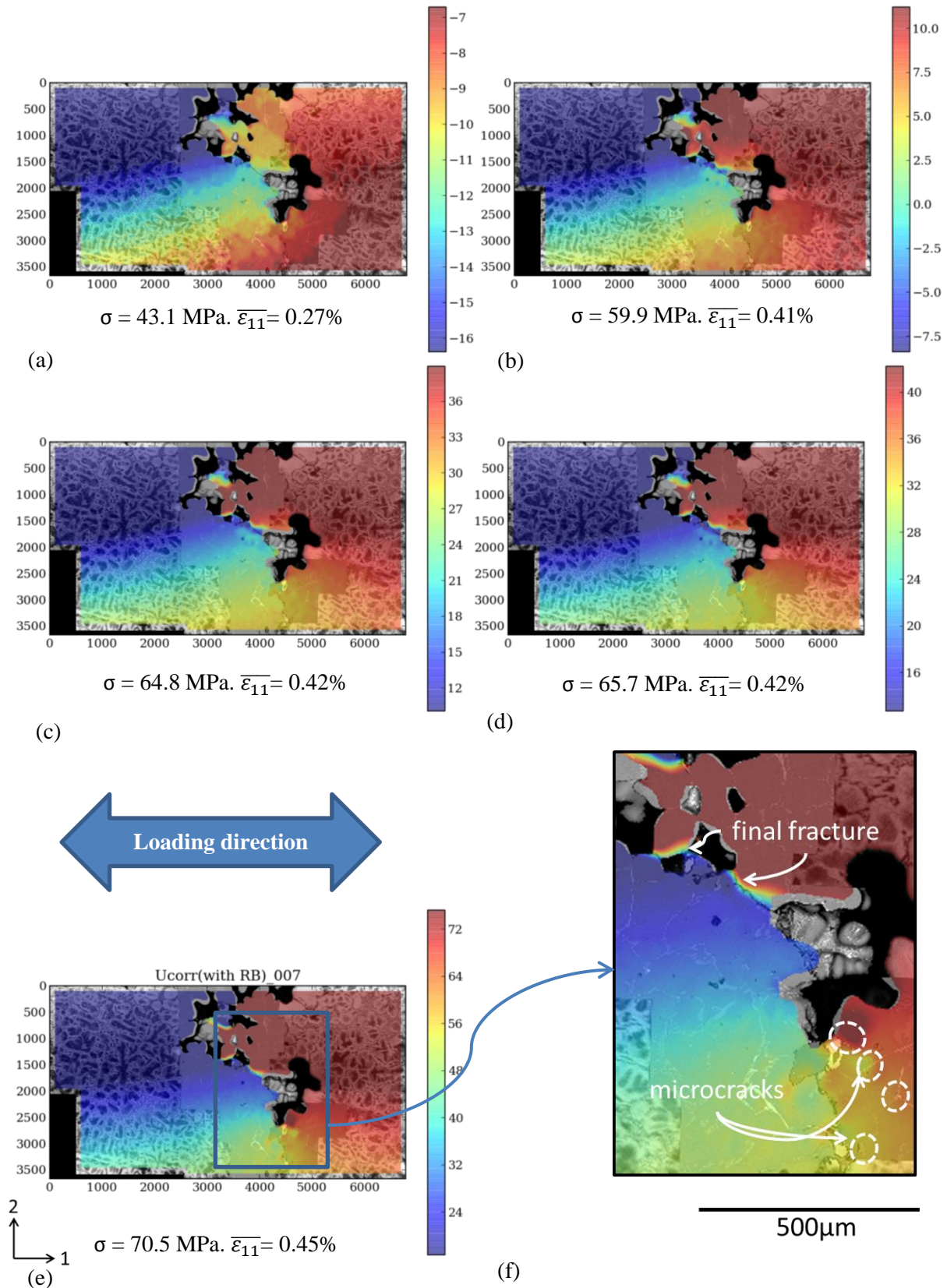


Figure 5-7 Displacement fields ( $U_1$ , in pixels, 1 pixel =  $0.34 \mu\text{m}$ ) of Specimen T1 in the loading direction at: (a) 3<sup>rd</sup> step, (b) 4<sup>th</sup> step, (c) 5<sup>th</sup> step, (d) 6<sup>th</sup> step, (e) 7<sup>th</sup> step with (f) a close-up view of the region marked with a rectangle in (e). Images obtained with post-mortem SEM are shown in transparency. The stress and mean strain calculated by DIC are specified for each step.

## Chapter 5 Damage mechanisms in Al-Si alloys

The longitudinal strain field ( $\epsilon_{11}$ ) for the 7<sup>th</sup> step (Figure 5-8) shows strain localizations. The correlation between strain localizations (Figure 5-8) and the final fracture and microcracks at hard inclusions revealed by SEM was also well observed.

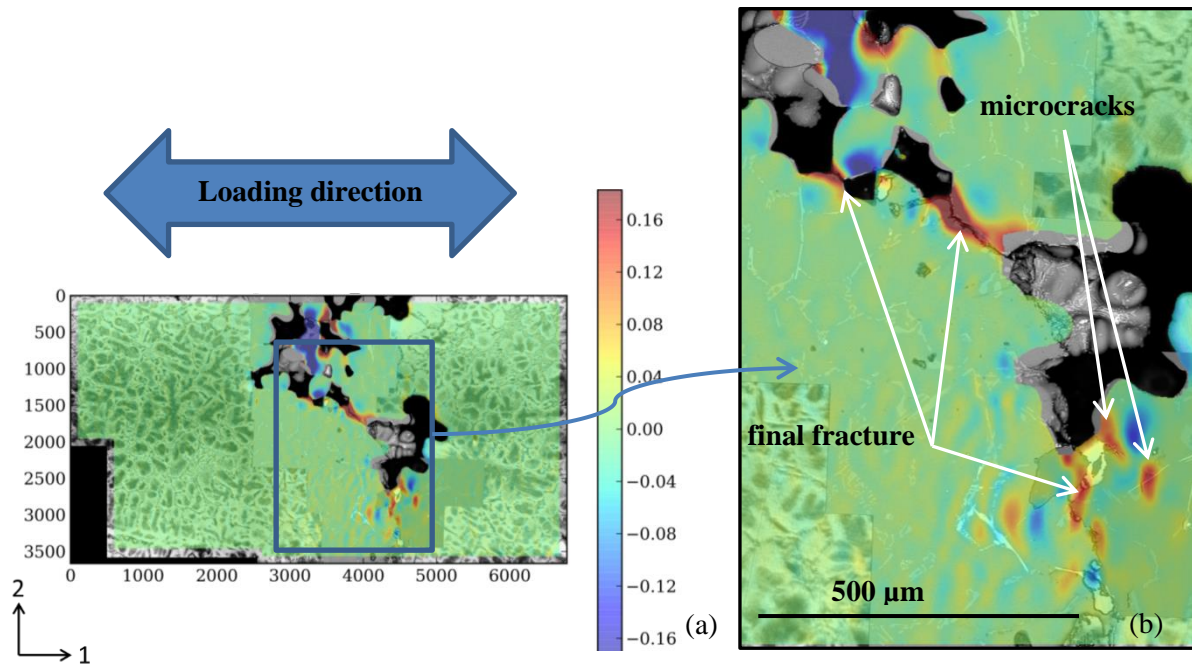


Figure 5-8 (a) Longitudinal strain field ( $\epsilon_{11}$ ) of Specimen T1 for the 7<sup>th</sup> step and (b) a close-up view of the region marked with a rectangle in (a). Images obtained with post-mortem SEM are shown in transparency.

In Specimen T2, no significant displacement discontinuities in Figure 5-9 was observed before the 15<sup>th</sup> step ( $\sigma = 220$  MPa). Although slight displacement discontinuities could be observed in Figure 5-9, they do not easily compare with the microcracks revealed by SEM.



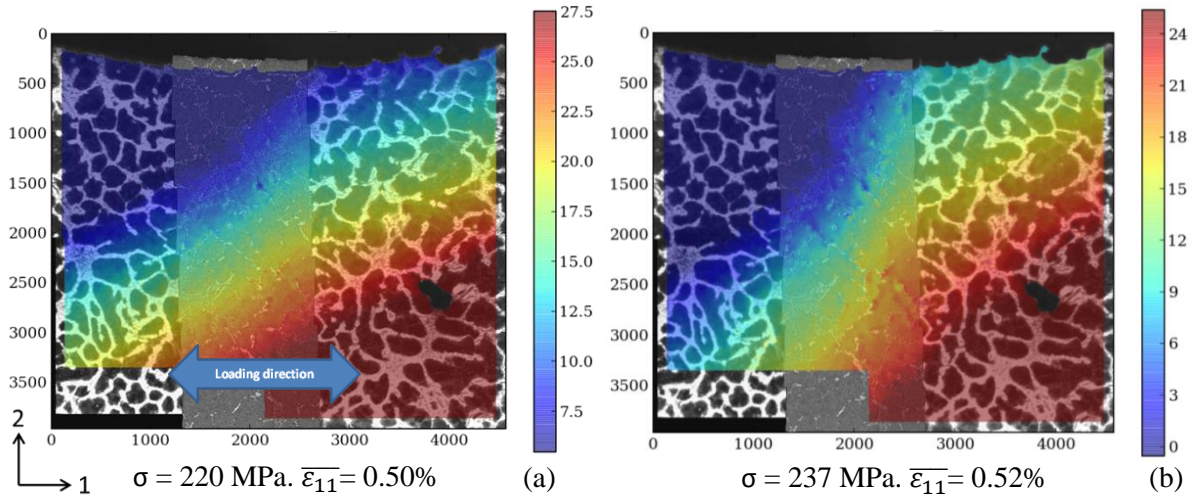


Figure 5-9 Displacement fields ( $U_1$ , in pixels) of Specimen T2 in the loading direction: (a) 15<sup>th</sup> step, (b) 16<sup>th</sup> step. Images obtained with post-mortem SEM are shown in transparency. The stress and mean strain calculated by DIC are specified for each step.

The longitudinal strain field ( $\epsilon_{11}$ ) ((Figure 5-10) (a) and (b)) is expected to give a better view of the relation between strain localization and cracks. However, unlike Specimen T1 in which large cracks and final fracture occurred in ROI, only several microcracks (Figure 5-10 (e)) were observed in ROI of Specimen T2. Although strain localizations were observed at increasing loading, i.e. from 15<sup>th</sup> step (Figure 5-10 (a)) to 16<sup>th</sup> step (Figure 5-10(b)), the relation between these microcracks and strain localizations was not always observed (Figure 5-10 (e)). The equivalent von Mises strain<sup>1</sup> field, which takes into account all the principal components of the deformation tensor, was then analysed. It is highly heterogeneous with a high density of “spots” of strain localization in a surface area (Figure 5-10 (c) and (d)) behind which a pore was detected in the radiography image (see arrow in Figure 5-2). The strain magnitude in these “spots” increases at increasing load, i.e. from 15<sup>th</sup> step (Figure 5-10 (c)) to 16<sup>th</sup> step (Figure 5-10(d)). The comparison of a close-up view of this area of strain localizations (Figure 5-10 (e)) with the corresponding SEM image (Figure 5-10(e)) proves that the zones with a large deformation are correlated to microcracks in the eutectic Si. These results will be further discussed later.

<sup>1</sup> The equivalent von Mises strain in 2D is defined as  $\epsilon^e = \frac{\sqrt{2}}{3} \sqrt{(\epsilon_1 - \epsilon_2)^2 + \epsilon_1^2 + \epsilon_2^2}$ , where  $\epsilon_1$  and  $\epsilon_2$  are the principal strains.

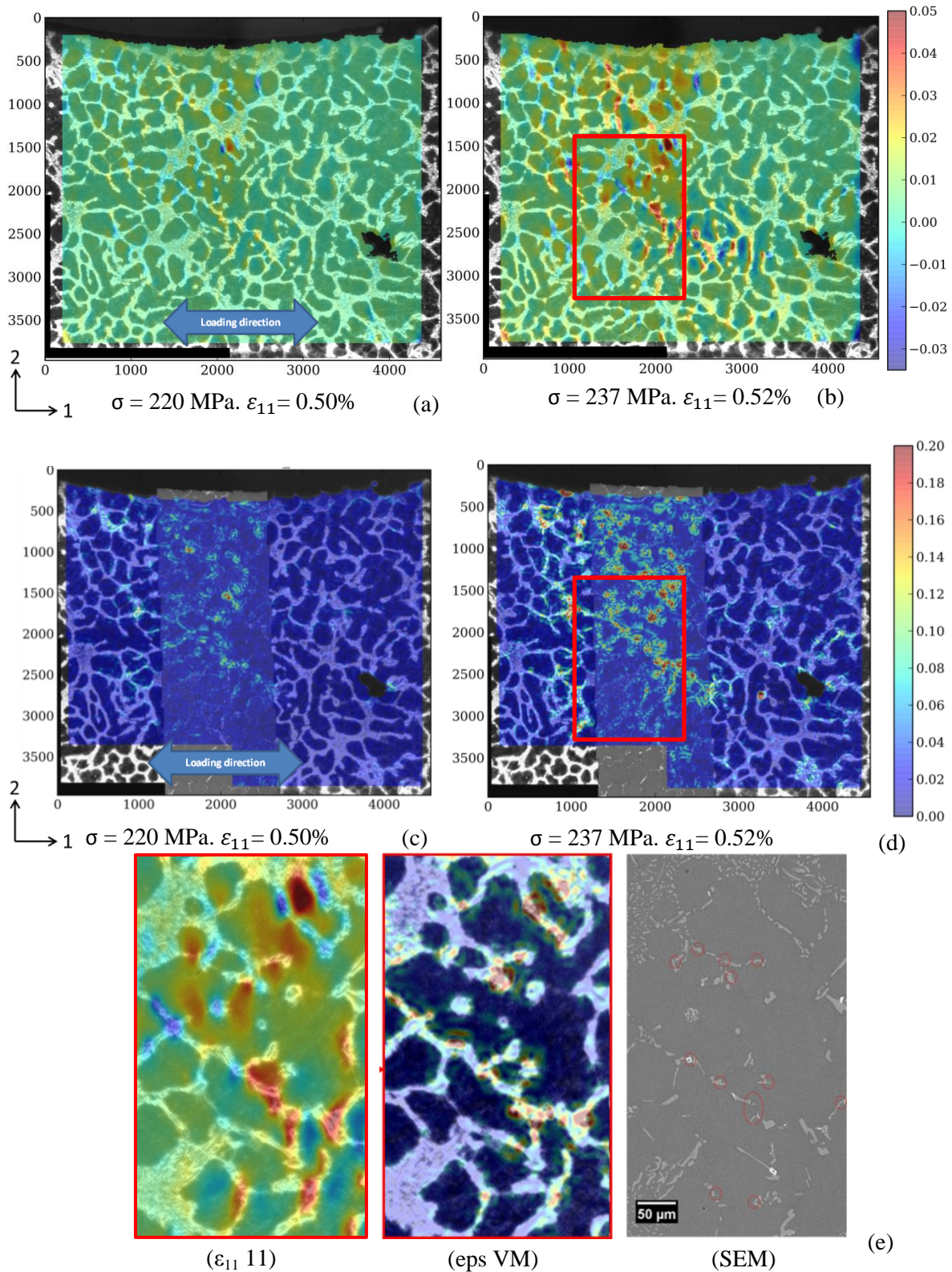


Figure 5-10 Longitudinal strain field ( $\epsilon_{11}$ ) of Specimen T2: (a) 15<sup>th</sup> step, (b) 16<sup>th</sup> step; Equivalent von Mises strain field at (c) 15<sup>th</sup> step, (d) 16<sup>th</sup> step; (e) A close-up view of the area marked in (b) and (d) compared with the microcracks (circled in red on the SEM image). Post-mortem SEM images (c) are shown in transparency in (c) and (d).

### 5.2.2 Tensile tests with 3D in-situ observations

#### ✓ Tests results and DVC measurements

Six loading steps were applied on Specimen T3 (A319) during the tensile test: the corresponding stresses are 147, 165, 176, 188, 192 and, 198 MPa respectively. The test ended not because of specimen failure but due to a loss of connection with the force sensor at the 6<sup>th</sup> step, i.e. at 198 MPa. However, at this last step, a number of cracks have already been observed in the tomography images that were analysed with DVC. The longitudinal strain field ( $\epsilon_{zz}$ ) was averaged over the whole volume at each loading step in order to determine the stress-strain curve (Figure 5-11). Compared with the curve of the same material obtained from a conventional test, i.e. with appropriate extensometer measurement on larger specimens, the curve derived from DVC can be considered reliable.

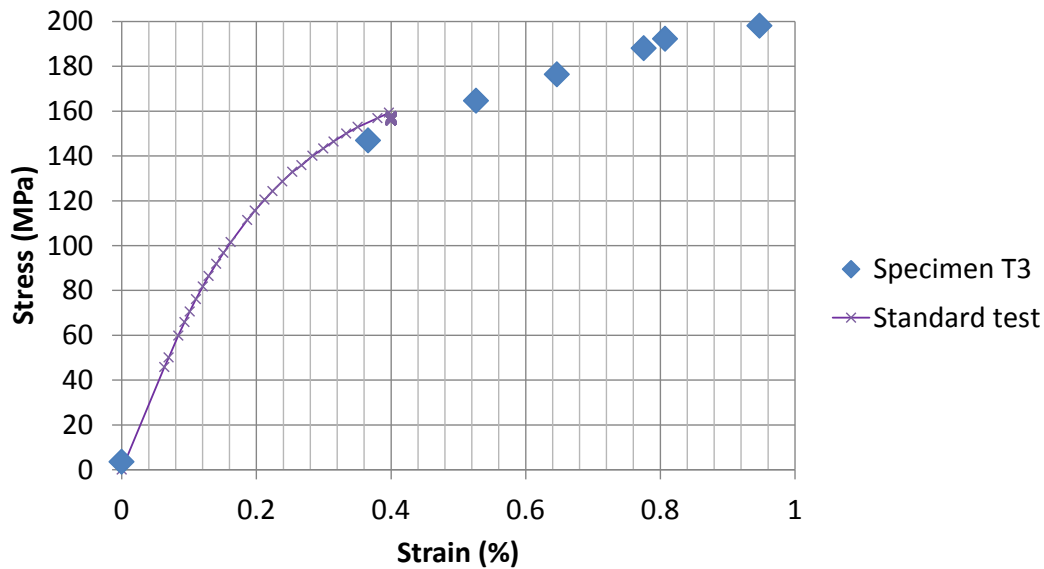


Figure 5-11 Comparison of stress-strain curves from DVC and from a standard test on A319 alloy

No obvious cracks were observed at the first step (147MPa) in the tomography image, and both the displacement and strain fields (Figure 5-12) are uniform. Cracks initiations were observed at the third step (176MPa) in the area marked with an arrow in the displacement field. Then displacement discontinuities and localizations in the strain field were observed to increase at increasing load.



# Chapter 5 Damage mechanisms in Al-Si alloys

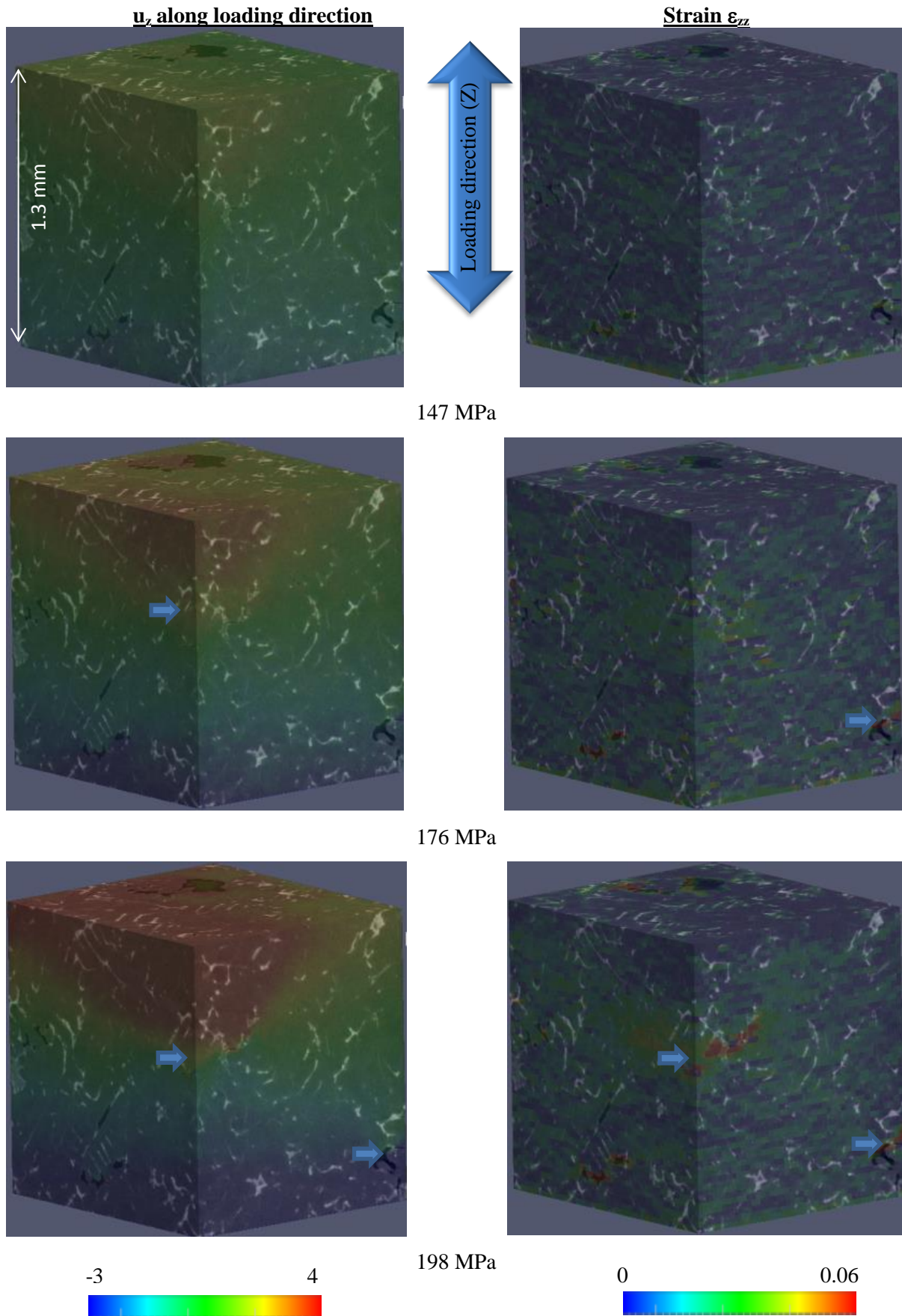


Figure 5-12 Displacement fields (in pixels, 1 pixel = 1.695  $\mu\text{m}$ ) and strain fields of Specimen T3

## Chapter 5 Damage mechanisms in Al-Si alloys

An example showing the comparison between the maximum residual error (in yellow) and 3D cracks segmented (in red color) from the tomography image is shown in Figure 5-13. A good correlation between the maximum residual error and cracks is observed. Thus 3D cracks in the following analysis were extracted using the maximum residual error.

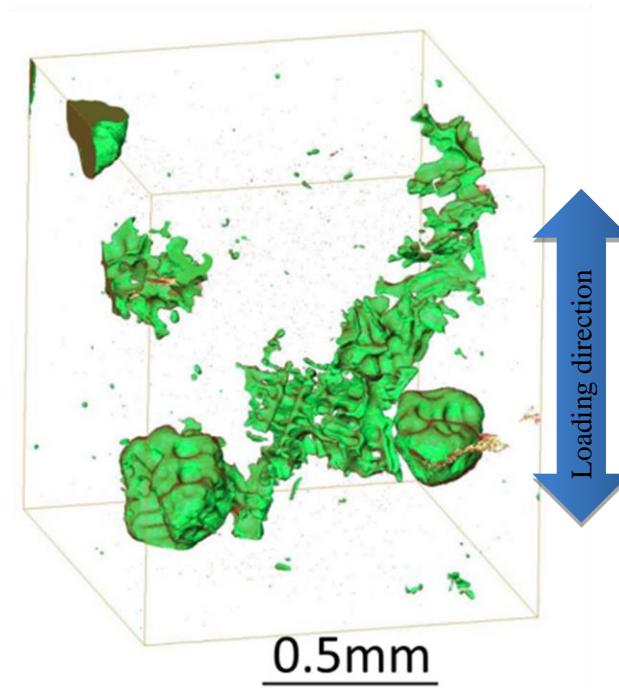


Figure 5-13 Comparison of 3D residual error in yellow and segmented cracks in red color in Specimen T3. Pores are rendered in green.

The damage mechanisms were followed from the last step (at 198 MPa) back to the step when crack initiation was observed. At the last step, the maximum of residual error (in red in Figure 5-14(a)) was thresholded to obtain a 3D rendering of cracks (in purple in Figure 5-14(b)-(f)). A good correlation is observed between displacement discontinuities (Figure 5-14(b)), strain localizations (Figure 5-14(c)) and the cracks. The cracks are located around the large pores in Figure 5-14(d), the relation between the cracks and the microstructure could be observed by comparing with the tomography image shown in Figure 5-14(e): cracks are along iron intermetallics, copper containing phases and matrix including eutectic Si and Al matrix.

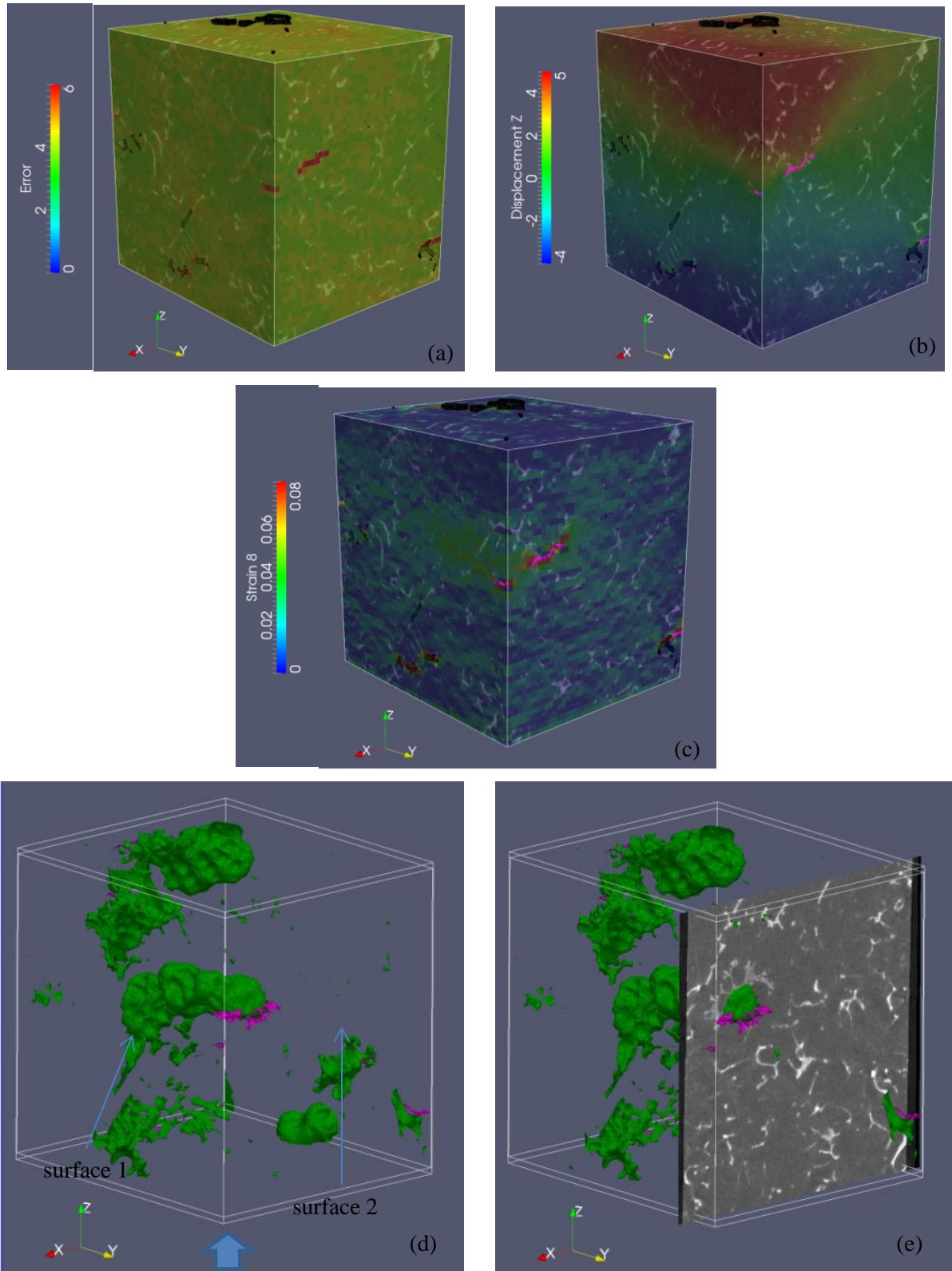


Figure 5-14 3D renderings of Specimen T3 at the 6<sup>th</sup> step (198MPa): (a) residual error, (b) displacement field (in pixels, 1 pixel = 1.695  $\mu\text{m}$ ) along loading direction (z-axis) and (c)  $\epsilon_{zz}$  strain field with pores shown in black and cracks in purple color; (d) Comparison between the cracks, in purple color, and pores, in green, with (e) the microstructure observed in one slice of tomography image.



## Chapter 5 Damage mechanisms in Al-Si alloys

### ✓ Post-mortem analysis

As Si phase could not be revealed by lab-CT, a comparison was made between the 3D in-situ observations and the 2D SEM analysis in order to reveal the relation between 3D cracks in bulk and cracks at hard inclusions on surface. The two polished flat surfaces of the specimen were named 'surface 1' and 'surface 2' in Figure 5-14(d) in order to locate the SEM post-mortem observation in the 3D tomography image. The crack observed in the residual error field (Figure 5-15(a)) and in the tomography image (Figure 5-15(b)) in a slice near surface 1 was also observed in the SEM image of surface 1 (Figure 5-15(c)). A SEM observation with a higher resolution (Figure 5-15(d)) shows that this crack goes through iron intermetallics (both  $\alpha$  and  $\beta$  phases) and eutectic Si although the relation between cracks and Si particles could not be revealed in-situ by using lab-CT.

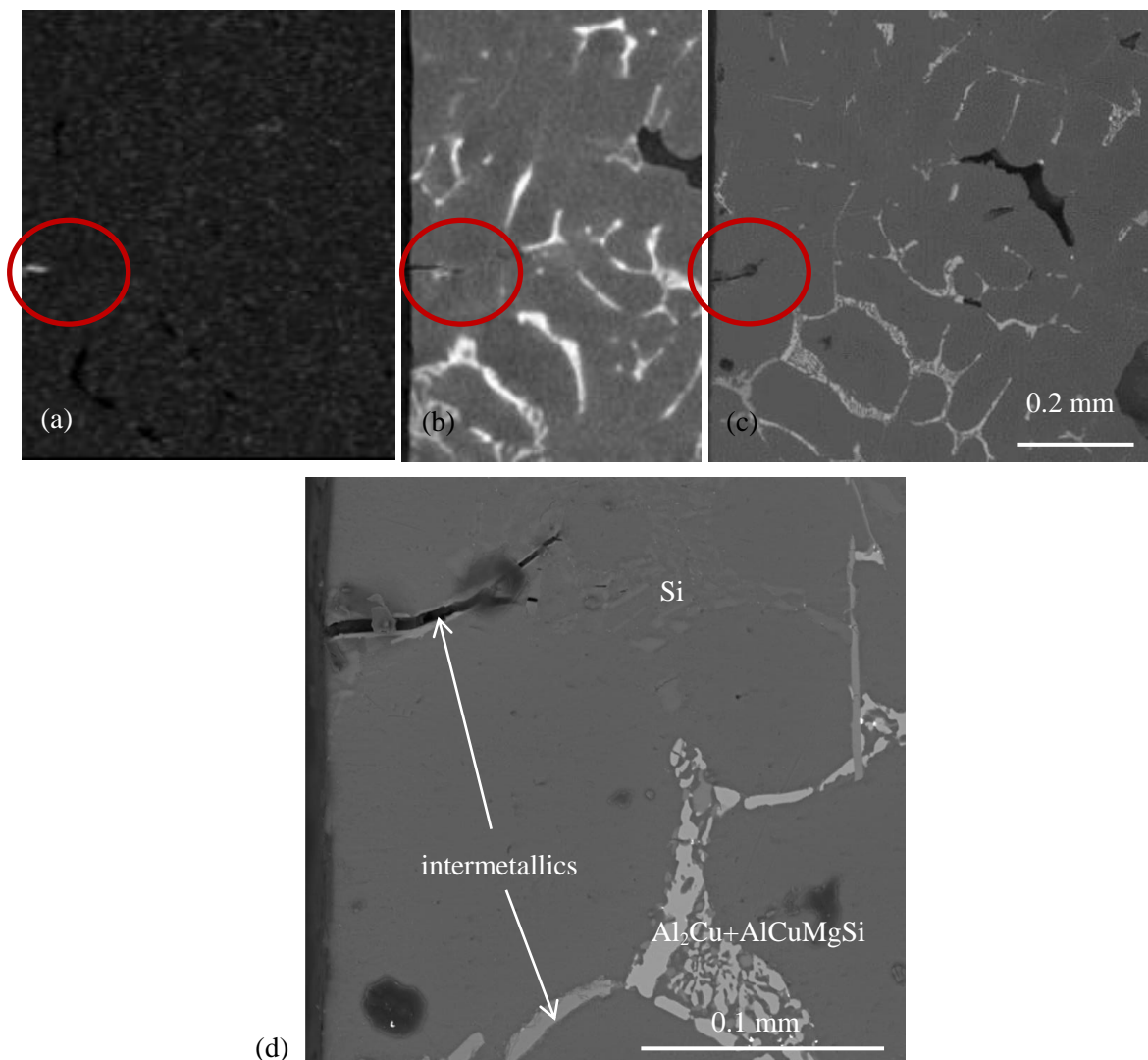


Figure 5-15 A partial view of (a) residual error field at 198MPa in one slice near the specimen's flat surface 1 and (b) of tomography image in the corresponding slice; (c) SEM image of surface 1 near the slice shown in (a) and (b) with (d) a higher resolution image on the area where a crack is marked with a red circle in (a)(b)(c)

## Chapter 5 Damage mechanisms in Al-Si alloys

The crack observed in the residual error field (Figure 5-16(a)) and in the tomography image in surface 2 (Figure 5-16(b)) was also observed at iron intermetallics and Si particles in the SEM images (Figure 5-16(c) and (d)). Some cracks were also observed at the  $Al_2Cu$  and  $AlCuMgSi$  phases (Figure 5-17).

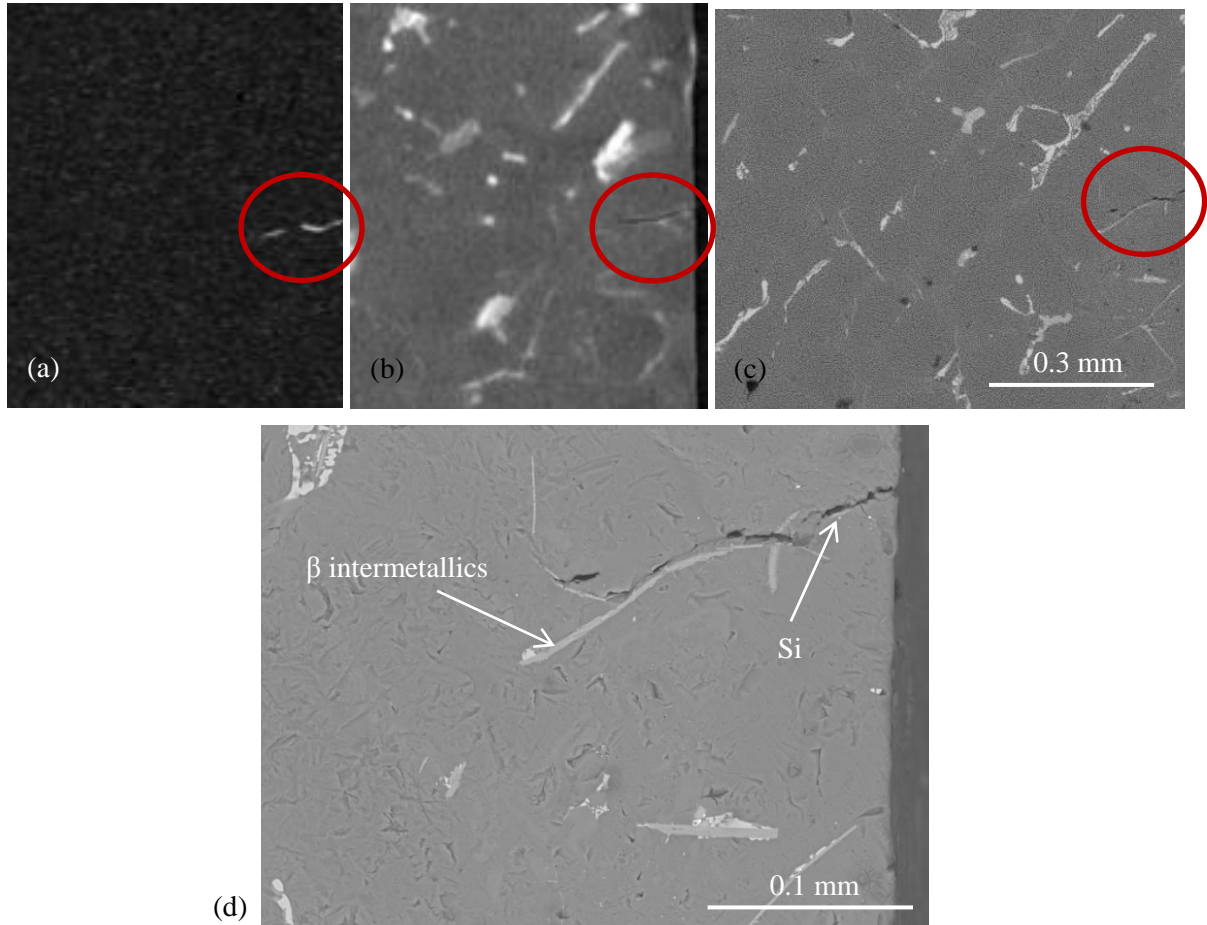


Figure 5-16 A partial view of (a) residual error field at 198MPa in one slice near surface 2 and (b) of tomography image in the corresponding slice; (c) the SEM image of surface 2, near the slice shown in (a) and (b), with (d) a higher resolution image on the area where a crack is marked with a red circle in (a)(b)(c)

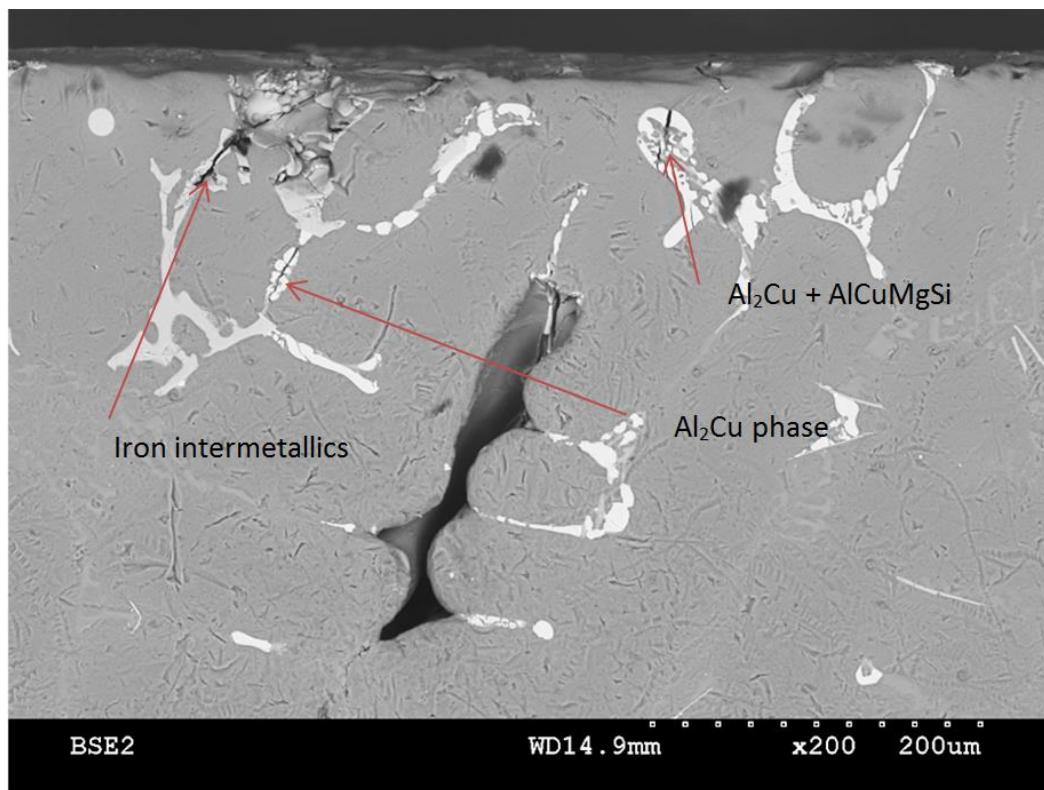


Figure 5-17 SEM image of Specimen T3 showing cracks at Al<sub>2</sub>Cu and AlCuMgSi phases

### ✓ Crack initiation and growth

The cracks growth during the six load steps of the tensile test is shown in Figure 5-18. The observation direction for these six images is along the loading direction and is marked by an arrow in Figure 5-14(d). The pores are shown in translucent grey and cracks in translucent yellow. These 3D rendering images restore the process of crack initiation and growth during tensile test. The cracks were observed to nucleate from large surface and subsurface pores at 176 MPa (Figure 5-18(c)). Then they were observed to grow with a further increase in the applied stress (Figure 5-18(c) ~ (f)). When cracks initiated from a subsurface pore, they are likely to initiate from the area near the free surface rather than from other area. Then these cracks propagated until the free surface.

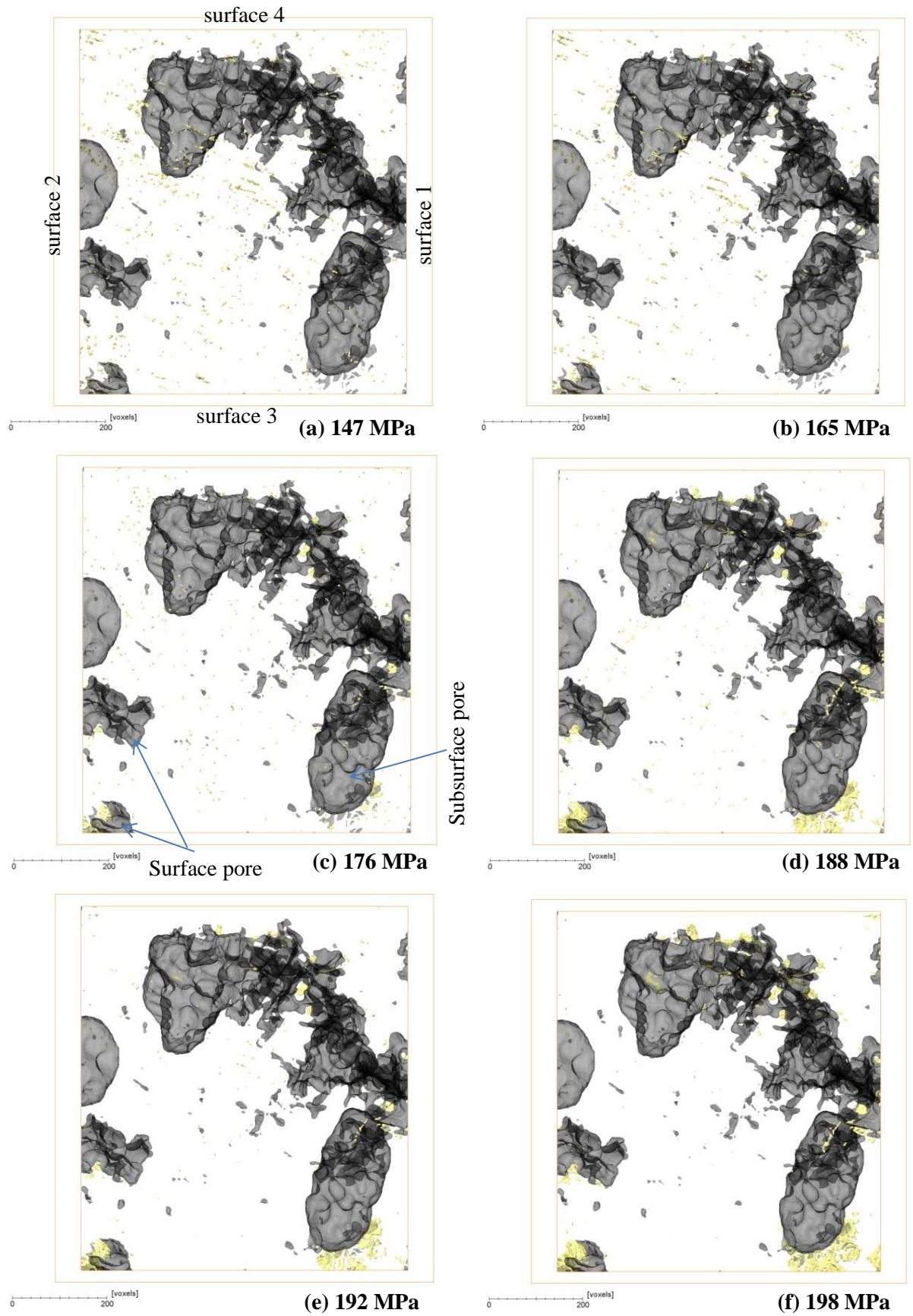


Figure 5-18 Cracks growth around pore in Specimen T3 during the tensile test (Pores in translucent grey and cracks in translucent yellow)



### 5.2.3 Discussion

#### 5.2.3.1 Application of 2D in-situ tensile tests on A356 alloy

Specimen T1 fractured at a normal stress far less than the ultimate tensile strength (more than 240 MPa) as shown in Table 5-1. Its stress-strain curve (Figure 5-6) is well below the stress-strain curve from the standard test while the stress-strain curve of Specimen T2 is close to that of the standard test. As reported in (Shore, 1968) and (Surappa et al., 1986), pores reduce tensile strength. Thus one possible explanation for this discrepancy is that more large pores were observed in Specimen T1 than in Specimen T2 both in the radiography and in the OM images (Figure 5-1(a) and Figure 5-2). The large pores are connected in fracture surface (Figure 5-3), thus it is actually one large surface pore. The size of this pore is as large as the thickness of specimen cross-section. Post-mortem analysis (Figure 5-1(a) and Figure 5-3) shows that the final failure of Specimen T1 was caused by this large surface pore that occupies half of the cross-sectional area in the fracture surface. Therefore the low tensile strength of Specimen T1 can be ascribed to this large surface pore which reduces the effective bearing area seriously.

However in Specimen T1, the projection of pores observed in radiography may contain other pores in addition to the pore involved in the final fracture, even if they might be small. The final failure may be caused by the coupling influence of these pores. In addition, the size of each pore in 3D, which is also an important parameter to analyse the damage mechanisms, cannot be known from radiography. Thus a 3D characterization of pores is necessary.

The final fracture of Specimen T2 did not occur in the selected ROI, although a notch was added, but in the area where there is a large pore (Figure 5-3(b)). Even though this is a subsurface pore it is very close to the surface (minimum distance < 0.01 mm). Although a cluster of subsurface pores was indeed found in ROI using radiography, their distance to the surface cannot be identified. As reported in (Gao et al., 2004) and (Ammar et al., 2008), the pores at or near surfaces are considered to be the most dangerous casting defects. Thus the most probable reason why the final fracture did not occur in the selected ROI can be ascribed to the large pore too close to the surface while the pores in selected ROI may be farther to surface.

However, one can also assume the influence of the size and shape of pore on final failure of Specimen T2. The pore in the fracture surface (Figure 5-3(b)) is a large shrinkage pore and its Feret diameter measured in 2D, i.e. in the fracture surface, is about 0.9 mm. The pore marked with an arrow in ROI (Figure 5-2) looks like 'a cluster' having a more rounded shape and its Feret diameter measured in 2D, i.e. in the radiography image, is about 0.5 mm. In other words, the pore in the final fracture may have a larger size and sharper shape than the pore in ROI. This may also explain why the final failure



## Chapter 5 Damage mechanisms in Al-Si alloys

---

occurred outside ROI; but this hypothesis cannot be confirmed without a 3D characterization of this pore. Hence 3D characterization of specimens is required to reveal the size, location and morphology of pores.

Although the role of size and location of pores is highlighted in the damage mechanisms of Specimens T1 and T2, some cases remain unclear without a 3D characterization of pores. Radiography is also not enough to select ROI. Thus tomography is required to understand the mechanisms better even in the tests with in-situ observation only on surface as well as to select ROI better. Therefore, tomography, which could reveal casting defects in 3D, has been used for the following fatigue tests with in-situ surface observation.

Microcracks (Figure 5-5(a)) were observed at hard inclusions around the large casting defects observed on the surface of Specimen T1. In fact, in the radiography image (Figure 5-1(a)), these pores were observed to extend deeper below the surface where these microcracks were observed. In Specimen T2, microcracks (Figure 5-5(b) and Figure 5-10(c)) were observed at hard inclusions on the surface area below which casting defects were found in the radiography image. In both specimens, SEM post-mortem analysis performed on the flat surface near the fracture surface has shown that the final fracture was more prone to occur along the hard inclusions. Thus, microcracks could have initiated from pores below the surface and have propagated along hard inclusions towards the free surface.

The tensile damage mechanisms of the same A356 alloy used in this study was studied in (Limodin et al., 2014). The in-situ tests with 3D in-situ observation using Lab-CT reveals that the cracks were observed to initiate from two surface breaking pores and the coalescence of cracks from these two neighbouring pores results in the final failure. This is consistent with this study: cracks initiate from pores. But the relation between cracks propagations and hard inclusions were not observed in their study as eutectic Si cannot be revealed by Lab-CT. However, numerous studies on other Al-Si alloys (Zhang et al., 2011) (Casari et al., 2013) (Tahamtan and Fadavi, 2010) indicated that hard inclusions, including eutectic Si and iron intermetallics, provide a path for crack propagation. This provides strong evidence to support the assumption in our study: once cracks initiate from pores they propagate along hard inclusions. Nonetheless, the tensile test with 3D in-situ observation using SR-CT which allows revealing eutectic Si is expected to prove this assumption directly.

DIC measurements reveal correlations between microcracks and/or final failure and displacement discontinuities and/or strain localizations. Deformation was localized in areas where the postmortem analysis using OM and SEM shows the presence of microcracks and/or the final fracture. These local deformation were significantly observed when the loading level is high enough (above 40 MPa for

## Chapter 5 Damage mechanisms in Al-Si alloys

---

Specimen T1 and above 220 MPa for Specimen T2), and their magnitude were observed to increase at increasing load. This implies that:

- (1) The cracks nucleation may need a sufficient stress concentration. Large pores in Specimen T1 may greatly increase stress concentration locally so that cracks initiated even at a low global stress level.
- (2) Cracks propagations are ascribed to the increasing deformation during the tensile test.

In addition, the microcracks, which could not be observed in the images taken with Questar long distance microscope during in-situ tensile test, could be followed by the displacement discontinuities or the strain localizations in the measured fields. This method will be further used to follow the cracks initiation and propagation during the process of cyclic deformation in the following fatigue tests.

### 5.2.3.2 Application of 3D in-situ tensile tests on A319 alloy

Cracks in Specimen T3 initiated from large subsurface and surface pores at 176MPa. Even if the surface pores are smaller than some other pores, many cracks initiated from them (Figure 5-18). This is consistent with (Ammar et al., 2008): surface pores are prone to act as crack initiation sites as they create regions of high stress concentrations. Many cracks also initiated from the largest pore, even if it is a subsurface pore. However, they are more likely to initiate from the areas near the free surfaces around this pore as a smaller distance between pore and surface produces a higher stress concentration (Fan et al., 2003).

The tomography image (Figure 5-14(e)) shows cracks propagated along iron intermetallics, copper containing phases and matrix including eutectic Si and Al matrix. The absorption contrast provided by Lab-CT is not enough to distinguish eutectic Si from Al matrix. However, when some of the cracks propagate until the free surface with the increasing loading (Figure 5-18), SEM post-mortem analysis (Figure 5-15 to Figure 5-17) shows cracks that propagated through hard inclusions, including eutectic Si, iron intermetallics, and copper containing phases. Thus cracks can be considered prone to propagate along eutectic Si instead of Al matrix even if Si cannot be distinguished using Lab-CT. This opinion is consistent with that in literature (Boileau and Allison, 2003) (Chan et al., 2003). Therefore in the studied A319 alloy, cracks could be considered to propagate along hard inclusions during tensile loading. Nevertheless, in-situ tests using SR-CT observation with additional phase contrast are required to reveal eutectic Si and to study its relation with the cracks directly.

The two surfaces between the shoulders of Specimen T3 are named as 'surface3' and 'surface4' in Figure 5-18. In Figure 5-18, more cracks were observed to propagate towards surface 3 than surface 1 or surface 2, thus more cracks would be expected on SEM observation of surface 3. However, as only

## Chapter 5 Damage mechanisms in Al-Si alloys

---

the two flat surfaces, i.e. surface1 and surface2, were polished before the tensile test, SEM observation could not be performed on the two unpolished surfaces, i.e. surface3 and surface4. Thus all these four surfaces of the specimen gauge length will be polished in the following fatigue tests.

Although 3D field measurement (16 voxels or 27.2  $\mu\text{m}$ ) has a lower spatial resolution than 2D field measurement (32 pixels or 10.2  $\mu\text{m}$ ), the former allows the measurement being performed in volume instead of only on surface. Using DVC measurements, correlations were observed between microcracks and displacement discontinuities and strain localizations (Figure 5-14). Deformation was localized in areas where 3D residual errors show the presence of microcracks. The magnitude of the local deformation was also observed to increase at increasing load (Figure 5-12). This indicates that the cracks propagations are due to the increasing deformation during the tensile test.

Under tensile loading, heterogeneities in the displacements and strain fields were observed at large pores if large pores were present such as in Specimen T3. To check if the strain distribution attributed to the pores coincides with the measured strain field, FEM simulation was performed (see Appendix II.2). The strain field from the FEM simulation is shown in Figure 5-19(a). The sub volume where the DVC measurement was performed is marked with a red rectangle in Figure 5-19(a) and shown at a higher magnification in Figure 5-19(b) in order to compare with the strain field at 198MPa from DVC in Figure 5-19(c). The similarity between the strain fields from FEM and from DVC confirms that the strain localization observed in the experimental fields can be mostly ascribed to pores. One can also consider that the shape of pore has an important influence on strain distribution. However one should keep in mind that the influence of hard 2<sup>nd</sup> phase particles may be below the actual resolution of DVC.

Because porosity has such an important influence on strain localization, FEM simulation was used to better select the specimens and the in-situ observation ROI for the following fatigue tests. The areas, where strain localizations are observed in the FEM strain field computed using an FE model representing solid matrix and pores, will be selected as ROI (see Appendix II).

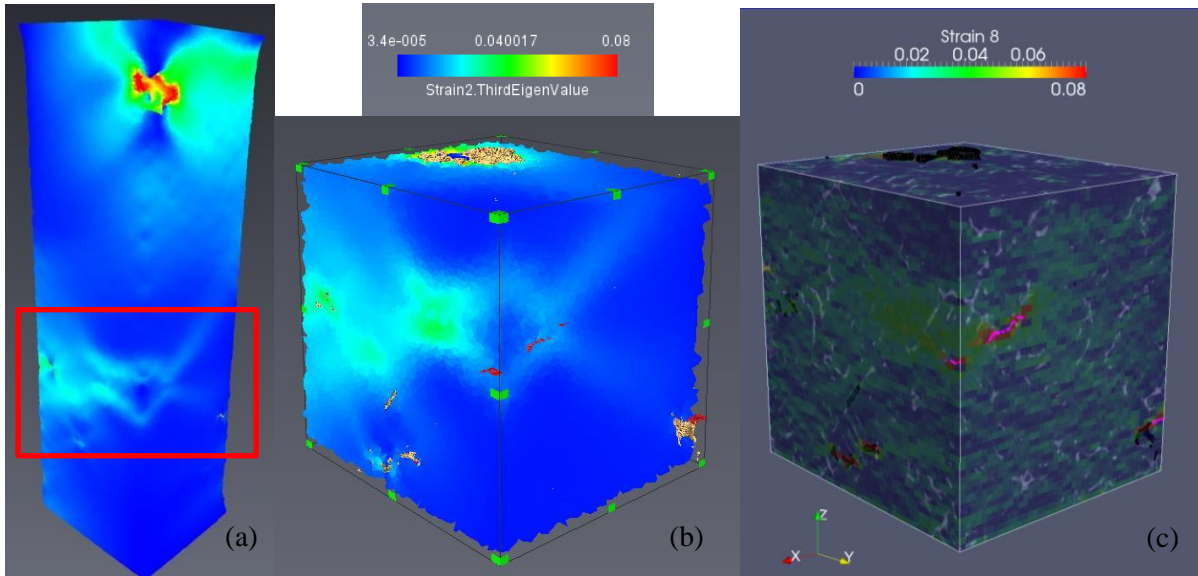


Figure 5-19 (a) Strain field ( $\varepsilon_{zz}$ ) from FEM with (b) a focus on the sub volume in the area marked with a red rectangle in (a) that corresponds to the area where the DVC measurements were performed (pores shown in golden, cracks in red) and corresponding strain field from DVC at 198MPa (pores shown in black and cracks in purple)

### 5.3 Fatigue damage mechanisms

The developed experimental protocol, which has been validated in tensile tests, has been improved for its application to the following fatigue tests: (i) **3D characterization of pores is necessary to select ROI and to analyse the results either for fatigue tests with 2D or 3D in-situ observations**, (ii) **FE simulation could be used to select ROI for fatigue tests with in-situ observation in volume**, (iii) **polishing should be performed on all the four surfaces of the test specimen for the post-mortem analysis**, and (iv) **SR-CT should be used to reveal eutectic Si**.

#### 5.3.1 Fatigue tests with 2D in-situ observations

##### ✓ Results of 2D fatigue tests

The main parameters of the fatigue tests performed on Specimens F1 and F2 are listed in Table 5-2. The maximum applied stress (Figure 5-20) shows fluctuations that are due to stress relaxation, cyclic softening, crack growth and reloading. Surface cracks were observed to initiate only in the selected ROI for both specimens. Thus the selection of ROI using lab-CT before fatigue tests was successful.

## Chapter 5 Damage mechanisms in Al-Si alloys

Table 5-2 Results of 2D fatigue tests

Specimen	F1	F2
Maximum stress (MPa)	110	80~110
R (Stress Ratio)	0.2	0.1~0.2
Maximum deformation measured by extensometer	0.15%	0.10%
Cracks initiation observed	After 7 000 cycles (step 52)	1 <sup>st</sup> cycle (during tensile stage)
Cracks propagation observed	Only in Zone 0	In all 6 zones
Final failure	About 100 000 cycles	20 430 cycles

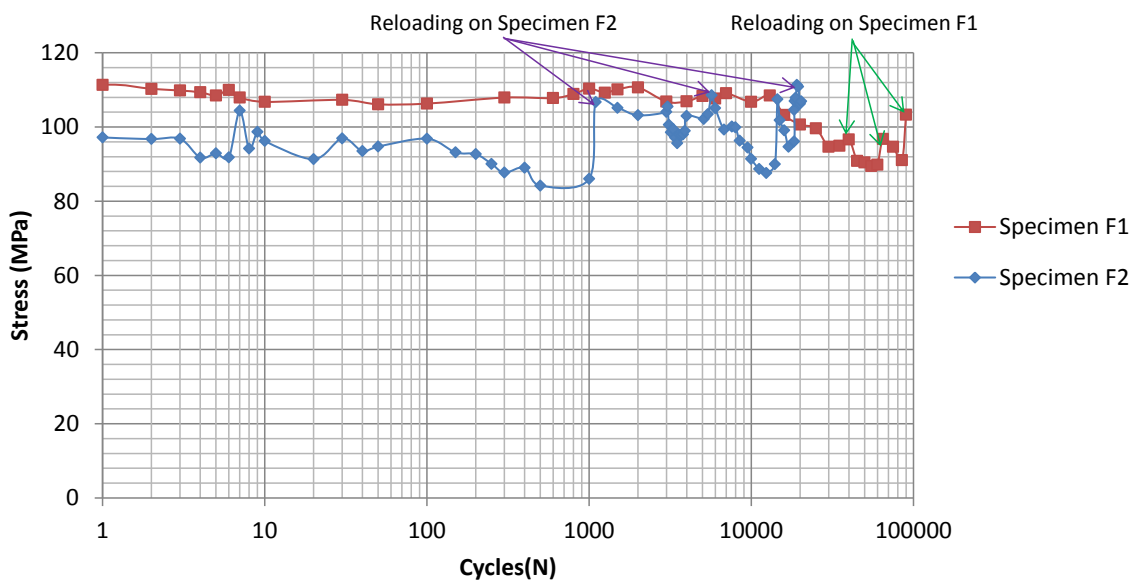


Figure 5-20 Maximum applied stress for Specimen F1 and F2 during 2D in-situ fatigue tests

### ✓ Crack initiation

Specimen F1 (Figure 5-21 and Figure III-4(c)) failed from a single crack nucleated at Si phase in front of the pore marked with arrows in Figure III-4(b). In order to check the influence of this pore on crack initiation, fracture analysis was performed.



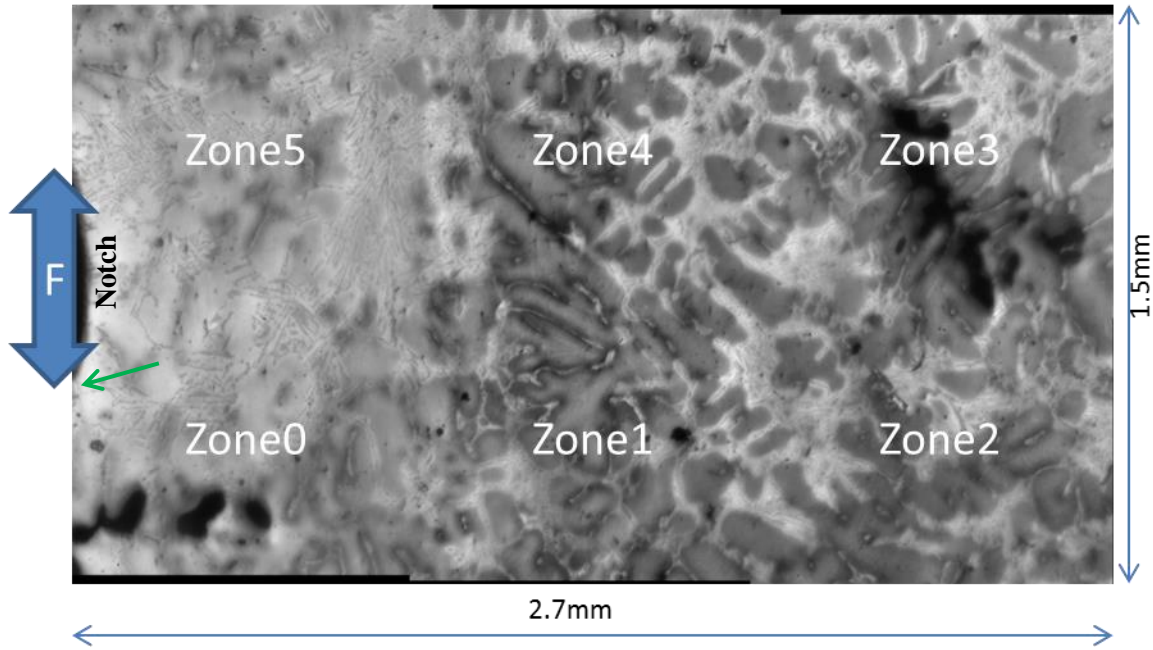
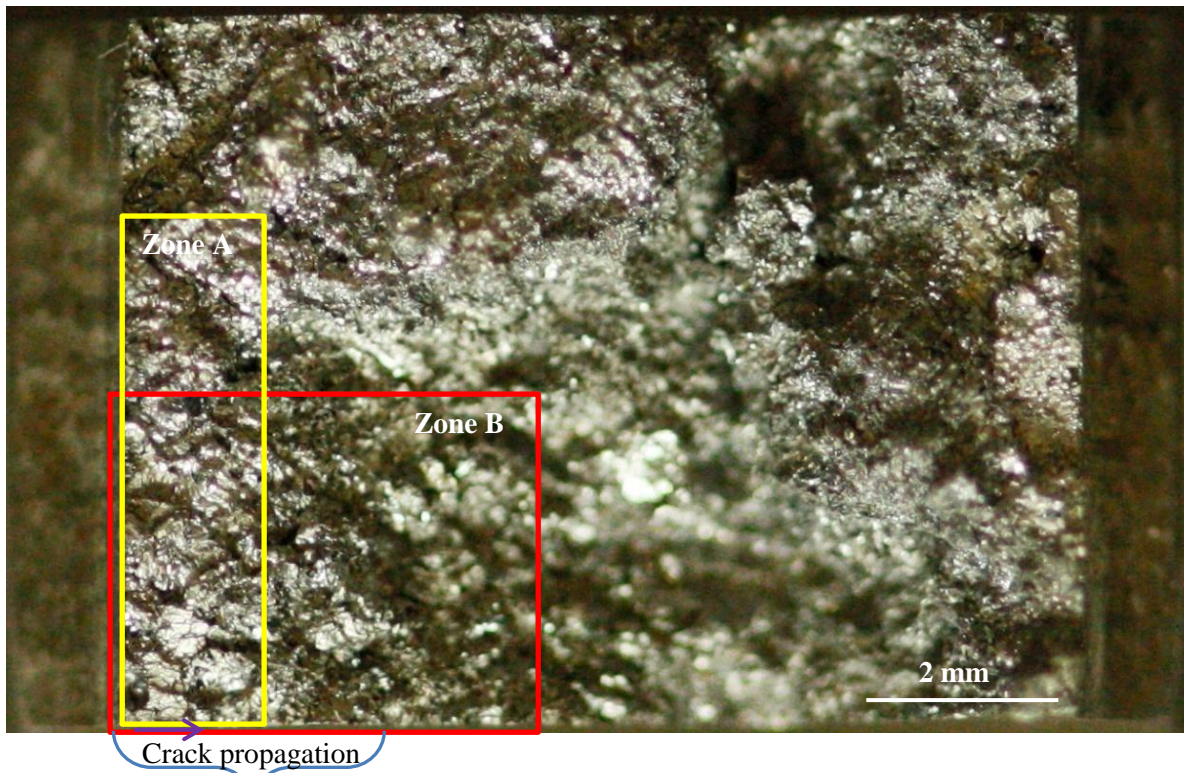


Figure 5-21 Stitched Questar image of Specimen F1 before the fatigue test. The crack initiation site after 7 000 cycles is marked by an arrow.

One half of the fractured specimen was observed using a single-lens reflex camera (Figure 5-22). Zone A is more likely to be crack initiation and propagation areas instead of final fracture area as it is more flat than other areas in fracture surface. Due to the limited DOF of the camera and to large fluctuations in the roughness of the fracture surface, some regions of the fracture surface were out of focus. Figure 5-23 shows SEM observation performed in Zone B, which was just below the ROI on surface. This surface ROI was selected due to the presence of a subsurface pore in the notch area, i.e. the pore marked with arrows in the tomography image used for specimens selection (Figure III-4(b)) and in the fracture surface (Figure 5-23). In Figure 5-24, SEM observation was performed with a higher resolution around this pore, i.e. in Zone C in Figure 5-23. River patterns (Schijve, 2008), of which the direction represents the direction of the crack propagation, were indeed observed around this pore. Thus the crack initiation, which was observed on the flat surface, could be ascribed to this pore that is surface-breaking in the notch area but is some distance below the flat surface where in-situ observations were done.



ROI in the flat surface

Figure 5-22 Fracture surface of Specimen F1. The SEM image in Zone B is shown in Figure 5-23.

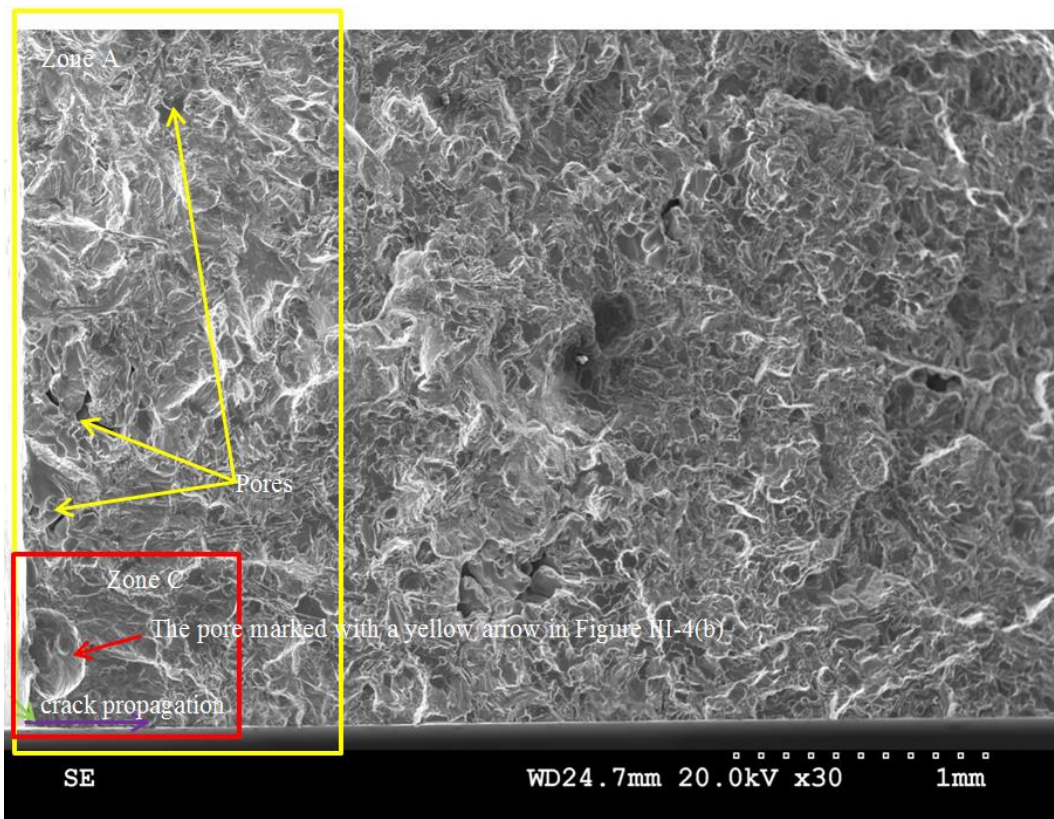


Figure 5-23 SEM image of the fracture surface of Specimen F1 in Zone B in Figure 5-22



## Chapter 5 Damage mechanisms in Al-Si alloys

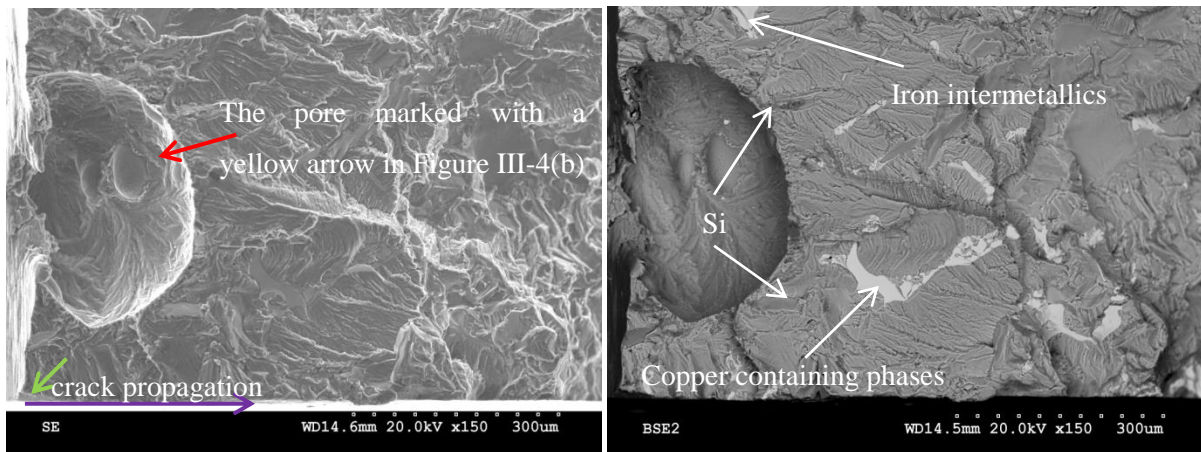


Figure 5-24 Zone C in Figure 5-23 observed using SEM with a higher resolution.

SEM observations were also performed on the whole fracture surface. The area, i.e. Zone A in Figure 5-22, where the river patterns were observed corresponds to the area where crack initiated and propagated. The other areas without river patterns are the fast fracture area in the final stage of fatigue test. This is consistent with the in-situ surface observation as cracks were only observed to grow in zone 0. A great difference could be observed between the left hand-side, i.e. crack propagation area, (more flat) and the right hand-side (high roughness), i.e. fast fracture area, of the fracture surface in Figure 5-23.

Several pores, marked by arrows in Figure 5-23, were found in the crack propagation area, i.e. Zone A. They present evidence of river patterns so that it is difficult to identify the first initiation site inside the specimen. There are several possible scenarios:

- (1) One crack initiated from one of these pores, and then grew through other pores towards the free surface.
- (2) Cracks initiated from several pores at the same time or at different cycles, and then coalesced during the propagation.
- (3) Cracks initiated from hard inclusions in bulk that are not connected with pores under the influence of the stress concentration induced by pores and then propagated through the pores.

By using 2D in-situ observations and post-mortem analysis, one cannot confirm which case is the true scenario for the crack initiation and propagation in bulk. However, the influence of pores below the observed flat surface on crack initiation on surface is certain.

In Specimen F2, cracks initiated from five different sites identified as A, B, C, D, and E in Figure 5-25(a). Cracks initiated from sites A and B (Figure 5-25 and Figure 5-26) before the maximum load of the 1<sup>st</sup> cycle was reached, i.e. below an applied stress of 80MPa. The opening of these two cracks became larger with a further increase of the stress up to the maximum value of the 1<sup>st</sup> cycle (Figure

## Chapter 5 Damage mechanisms in Al-Si alloys

5-26). Thus the maximum loading in the 1<sup>st</sup> cycle was stopped at about 98 MPa, which is lower than for Specimen F1.

SEM post-mortem analysis showed that these two cracks initiation sites on surface were not only at hard inclusions (Si particles, iron intermetallics, Al<sub>2</sub>Cu and AlCuMgSi phases) but also at Al matrix and that they are located just above Pore A (Figure 5-25, see Appendix III.3 for characterization of pores in Specimen F2). Thus the cracks were likely to have initiated from Pore A and then propagated to the flat surface.

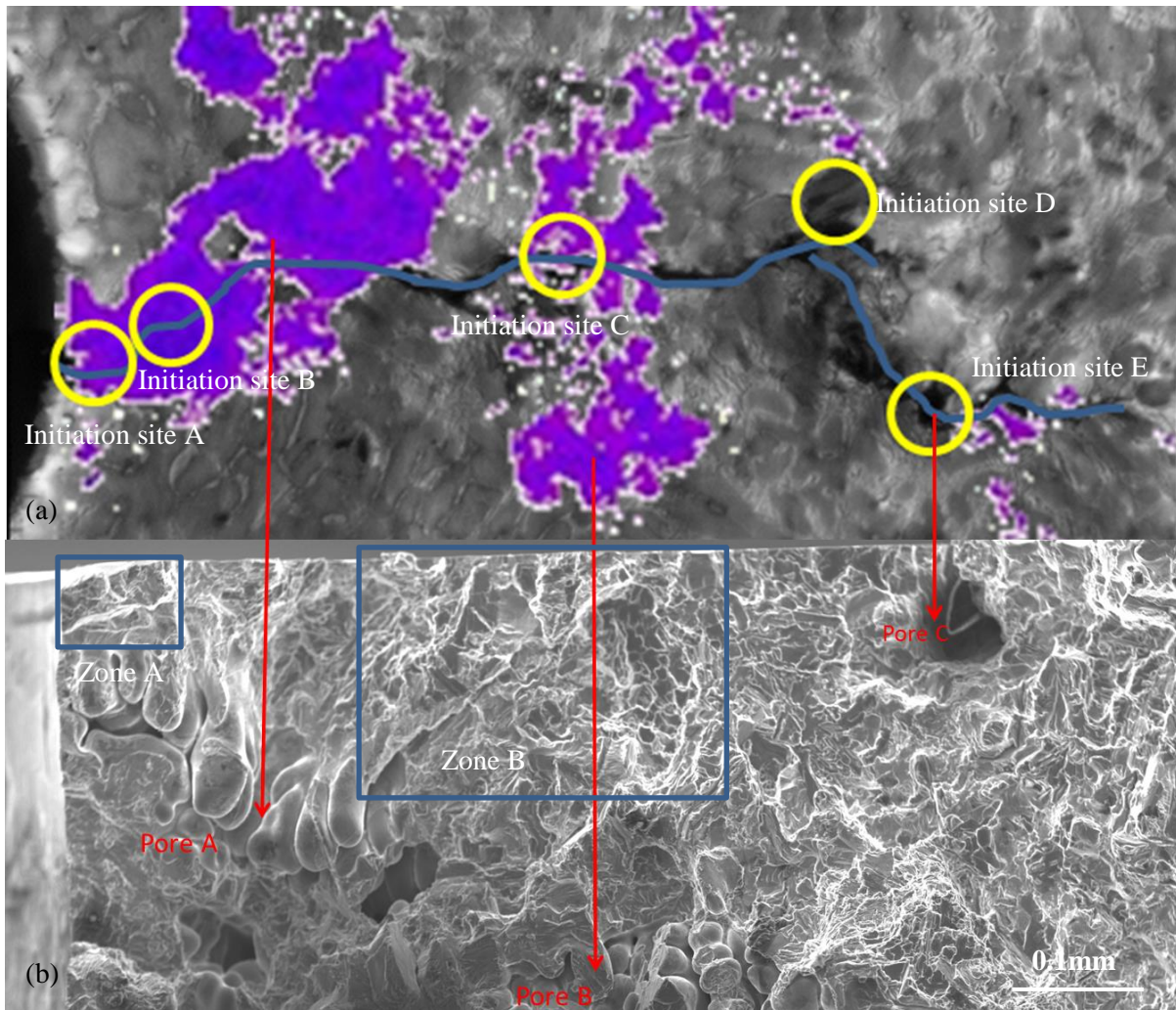


Figure 5-25 (a) Stacked Questar image of Specimen F2 after 20 300 cycles with the 2D projection of 3D pores from Figure III-5 in purple; the final fracture is marked with a blue line. (b) The fracture surface observed by SEM in the corresponding area shown in (a).



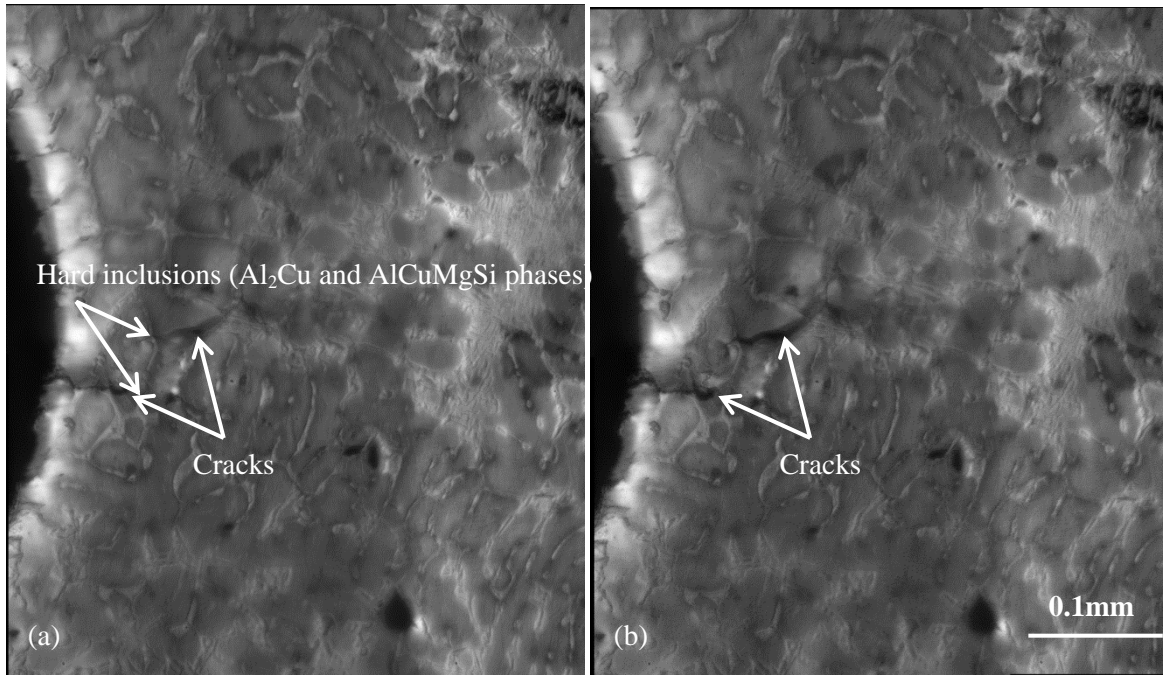


Figure 5-26 Stitched Questar images of Specimen F2 during the tensile stage at the 1<sup>st</sup> cycle at about (a) 80 MPa and (b) 98 MPa

Fracture analysis in Figure 5-27 shows that the distance between initiation sites A/B and Pore A is less than 0.1 mm. The cracks initiated on surface at initiation sites A/B during the tensile stage of the 1<sup>st</sup> cycle, thus the damage mechanism could not be ascribed to fatigue. Crack initiated at sites A/B because of the large stress concentration caused by the large Pore A in subsurface. This crack corresponds to brittle fracture zones with cleavage of Si (marked by a circle in Figure 5-27).

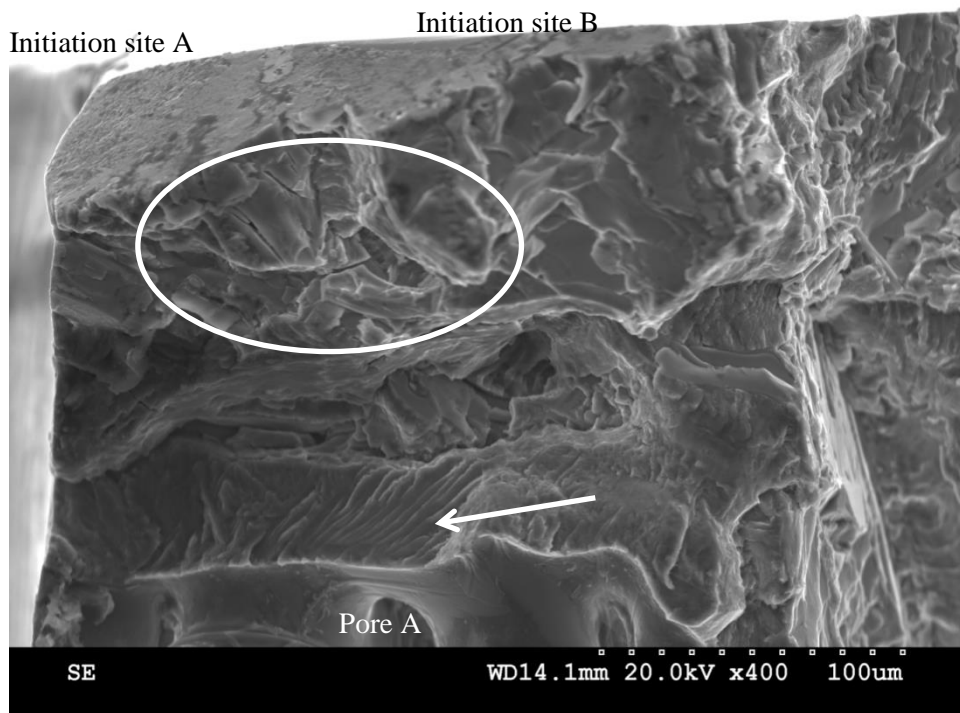


Figure 5-27 SEM image of Zone A marked in Figure 5-25(b)



## Chapter 5 Damage mechanisms in Al-Si alloys

Cracks were observed to initiate at sites C and D (Figure 5-25 and Figure 5-28) suddenly between the 15 860<sup>th</sup> cycle and the 15 890<sup>th</sup> cycle. These two initiation sites were across hard inclusions and Al matrix and cracks opened very quickly. Pore B is below the initiation site C (Figure 5-25) at a depth of about 0.8 mm as shown in Table III-1. Although the river patterns marked by a yellow circle in Figure 5-29 revealed the direction of cracks originated from the cleavage of a Si particle in a local area, one cannot obtain more information about crack propagation in a larger area. However, the ‘ridge’ line, which formed during the coalescence of cracks from two different planes (Verreman and Nie, 1991) and is marked by a red circle in Figure 5-29, was observed between initiation site C and Pore A. This implied that crack initiation C may be due to coalescence of two cracks.

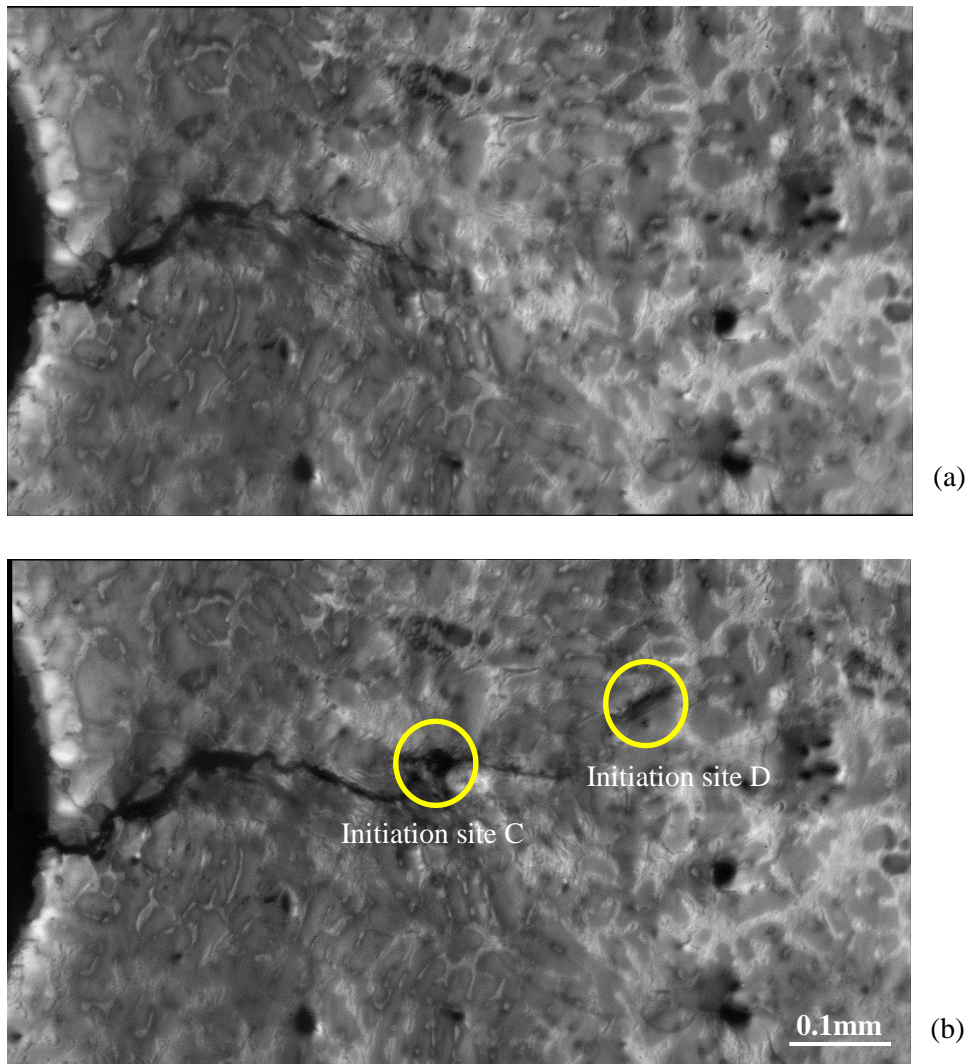


Figure 5-28 Stacked Questar images of Specimen F2: (a) after 15 500 cycles, (b) after 16 000 cycles

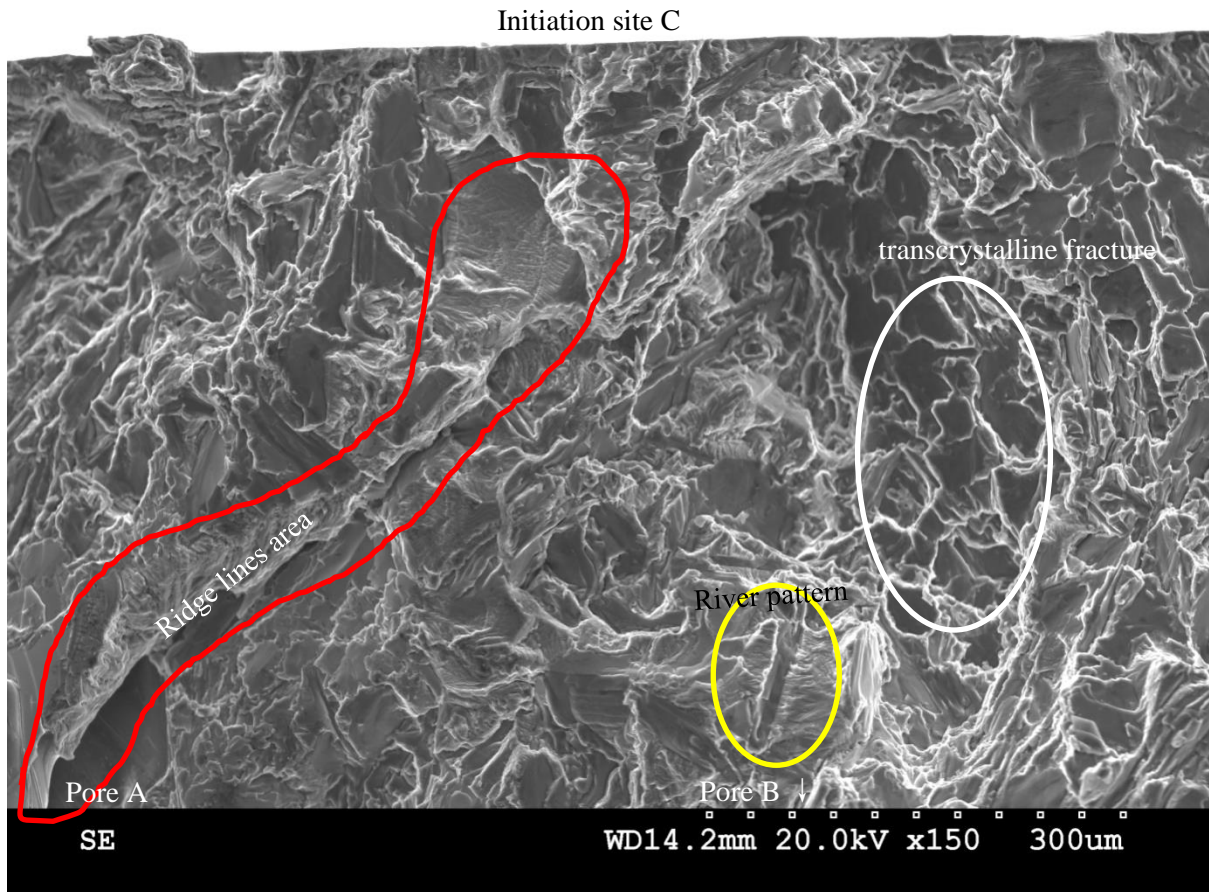


Figure 5-29 Fracture analysis performed on Zone B marked in Figure 5-25(b)

Cracks were observed to initiate simultaneously at site C and at site D at Si phase. Site D is not present on fracture surface as it is covered by the fracture surface caused by another branch crack (Figure 5-30). No subsurface pore was found around initiation site D and no crack was observed to propagate to this area from other pores. Thus hard inclusions may have acted as initiation sites at or around site D although we have no direct evidence.

Crack 2, which is marked in Figure 5-30, initiated from site E (Figure 5-25) near Pore C after 19 350 cycles. The influence of surface Pore C on crack initiation on site E is obvious.



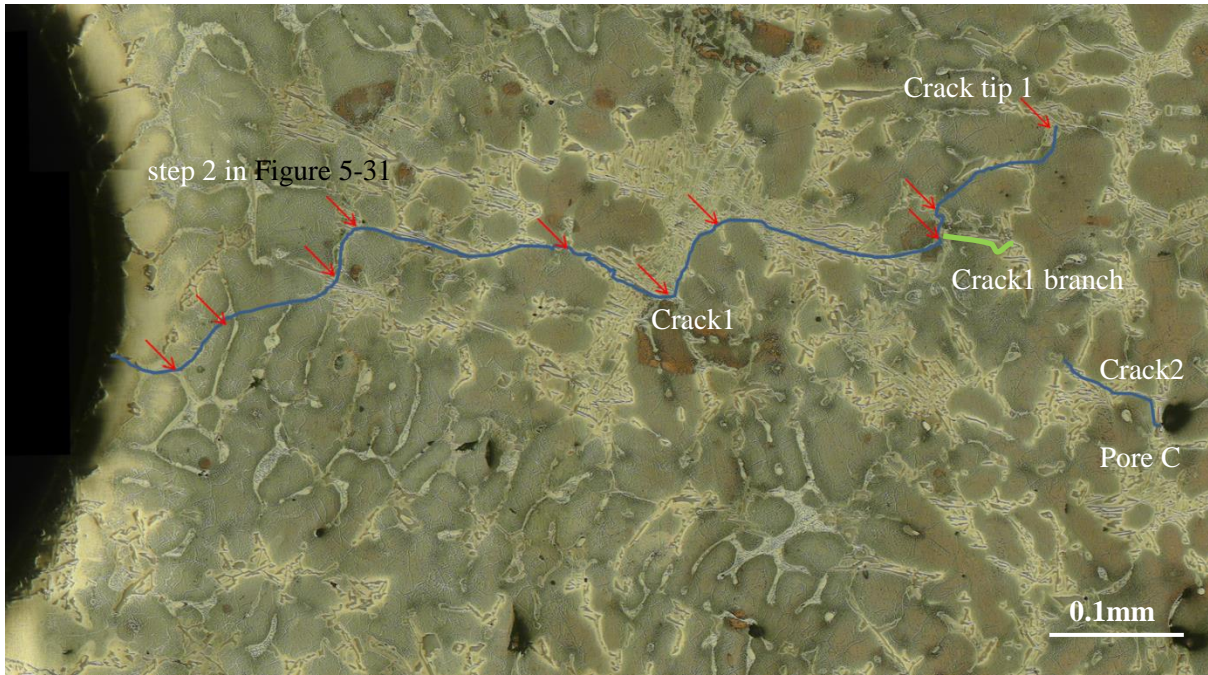


Figure 5-30 OM image in ROI of Specimen F2: the observed crack is marked with lines and arrows indicate locations of crack arrest

### ✓ Crack propagation

The measurements of cracks length in Specimens F1 and F2 are reported in Figure 5-31 in order to analyze cracks propagation. Crack observed on surface of Specimen F2 is much longer than that of Specimen F1 due to numerous large near surface pores in Specimen F2.

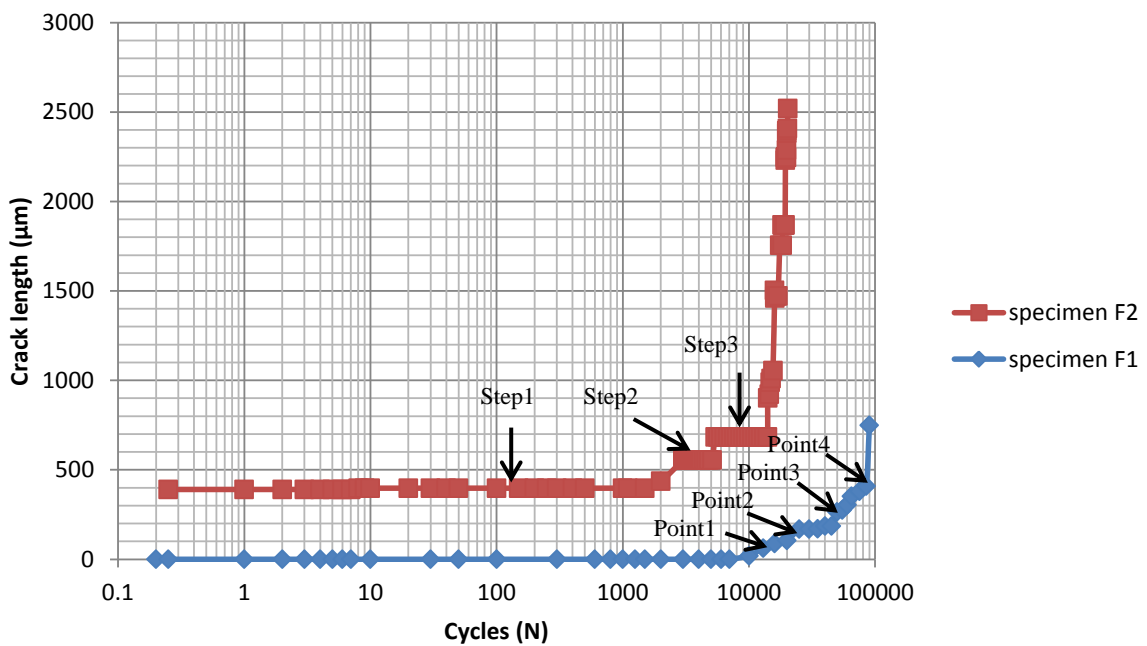


Figure 5-31 Cracks length evolution with number of cycles in Specimens F1 and F2

## Chapter 5 Damage mechanisms in Al-Si alloys

Cracks propagations in Specimen F1 were only observed in Zone 0, thus the following analysis was focused in this zone (Figure 5-32 and Figure 5-33). Crack initiating at Si particle after 7 000 cycles is marked by an arrow in Figure 5-32 (b). It propagated along hard inclusions, including Si phase, iron intermetallics (both  $\alpha$  and  $\beta$  phases),  $\text{Al}_2\text{Cu}$  and  $\text{AlCuMgSi}$  phases, until point 4 where the crack tip was arrested by hard inclusions (shown in Figure 5-32). While the principal crack was arrested at point 4, another crack initiated at hard inclusions at a 2<sup>nd</sup> initiation site below point 4 (Figure 5-32(c)) after 85 000 cycles. Inside the specimen, this secondary crack may be a branch of the main crack as it is close to point 4 or it may also be an individual nucleation site. However, one cannot confirm it using fracture analysis as the 2<sup>nd</sup> initiation site is covered in the final fracture surface.

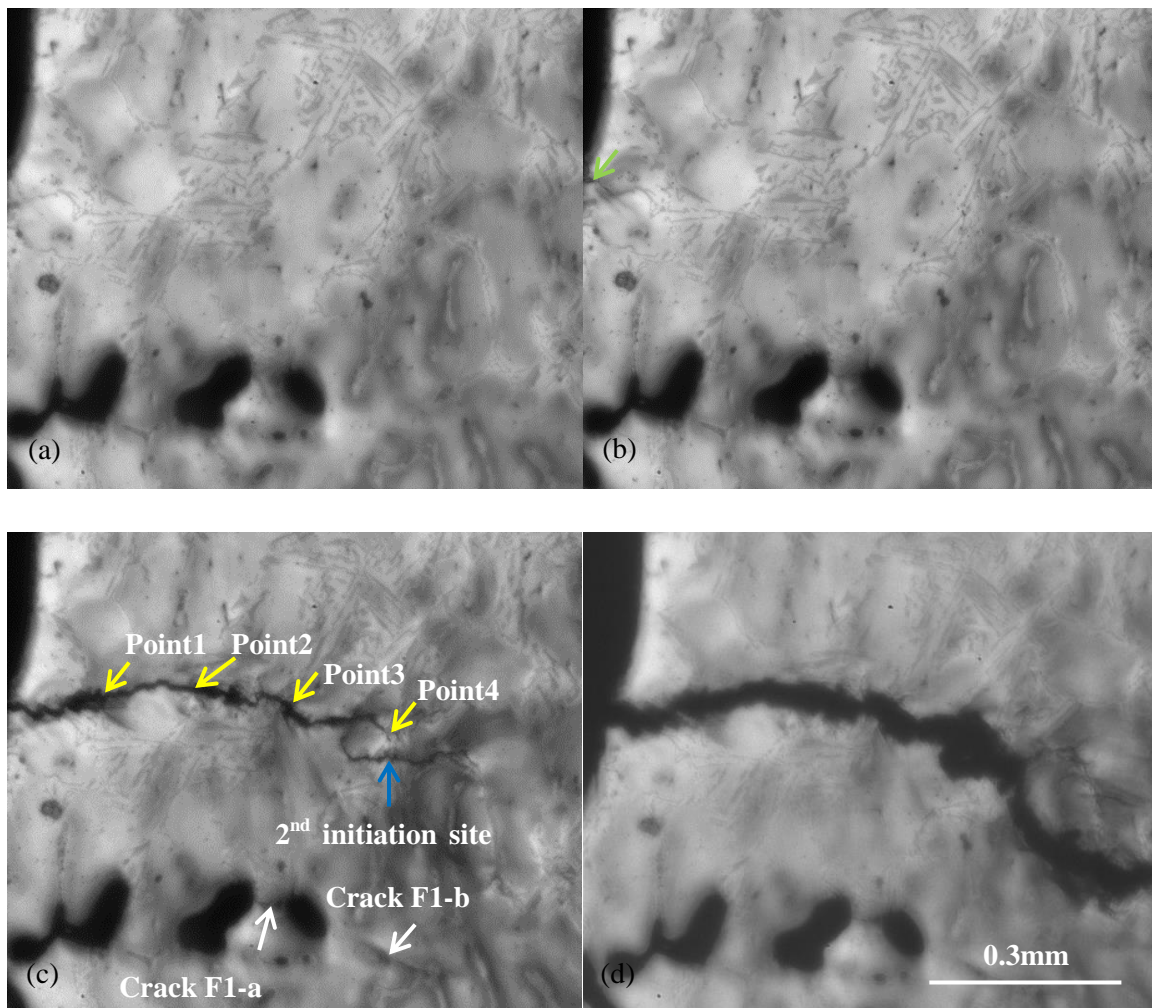


Figure 5-32 Questar images in Zone 0 of Specimen F1: (a) after 7 000 cycles; (b) after 13 000 cycles; (c) after 90 000 cycles; (d) after failure at about 100 000 cycles.

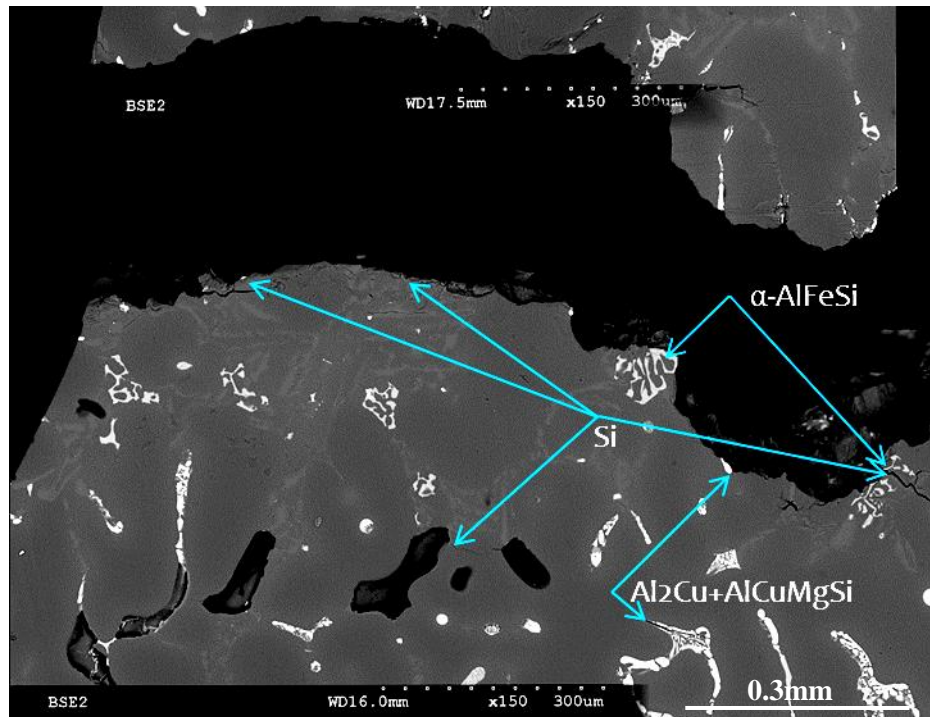


Figure 5-33 BSE image in Zone 0 of specimen F1

After nucleation at sites A and B in Specimen F2 at 1<sup>st</sup> cycle, cracks were arrested for more than 2 000 cycles (step 1 in Figure 5-31) by hard inclusions perpendicular to each crack tips. Once the hard inclusions had failed, the two cracks grew again and connected on surface. These two cracks coalesced due to crack propagation below the surface; river patterns were observed between Pore A and these two initiation sites (marked by an arrow Figure 5-27). Then, this coalesced crack was observed to propagate along hard inclusions. After 15 860 cycles, one crack, which has nucleated from Pore A, propagated towards site C on surface, and another crack initiated at site D on surface. They joined with the cracks that nucleated from site A/B through cracks growth along hard inclusions (step 3 in Figure 5-31). This large coalesced crack propagated until crack tip 1, marked in Figure 5-30, where the crack was arrested by hard inclusions. Transcrystalline fracture (Warmuzek, 2004) was observed in the fracture surface below site D (marked with a white circle in Figure 5-29). It may be caused by monotonic loading when cracks coalesced between sites C and D. However, one cannot confirm it just from fracture analysis.

Influence of the direction of hard inclusions on cracks propagation was observed for both specimens. When the direction of the crack propagation was along the direction of the longest axis of hard inclusions at the surface, the crack grew quickly. However, when the direction of crack propagation was perpendicular to the direction of hard inclusions, the crack may be arrested. For Specimen F1, cracks arrest at hard inclusions was observed at points 1 to 4 in Figure 5-32(c); the corresponding points were also marked in the cracks propagation curve in Figure 5-31. More crack arrests were observed for Specimen F2 as shown in Figure 5-30. The crack grew slowly when its tip encountered



## Chapter 5 Damage mechanisms in Al-Si alloys

hard inclusions having their long axis perpendicular to the crack propagation direction. The crack tip needed many cycles to pass these barriers by two means (Figure 5-30 and Figure 5-32):

(a) **Change of its propagation direction, i.e. growth along these barriers. Once these barriers have been bypassed, the cracks propagated along a new route perpendicular the loading direction.**

(b) **Break these barriers.**

Once the arrested crack has passed these barriers, it grew very fast.

When cracks were arrested by the barriers, some similar phenomena were observed in the area (Figure 5-34) around the crack tip and along the loading direction:

✓ For Specimen F1:

- When crack tip was arrested at Point 3 in Figure 5-32(c), **Crack F1-a**, which is just below Point 3, initiated at Si particle between two surface pores, which are actually one pore that is connected in subsurface as shown in the X-ray tomography observation (Appendix III).
- When crack tip was arrested at Point 4, **Crack F1-b**, which is just below Point 4, initiated at  $\text{Al}_2\text{Cu}$  and  $\text{AlCuMgSi}$  phases. In the same time, crack initiated at hard inclusions (iron intermetallics,  $\text{Al}_2\text{Cu}$  phase and  $\text{AlCuMgSi}$  phase) at **2<sup>nd</sup> initiation site**, which is also below Point 4.

✓ For Specimen F2:

- When the main crack was arrested by hard inclusions at crack tip 1 (Figure 5-30), **Crack 2**, marked in Figure 5-30, initiated on surface around Pore C after 19 350 cycles. Although strain localizations are easily generated around such large pores, no crack was observed before the crack was arrested at crack tip 1.

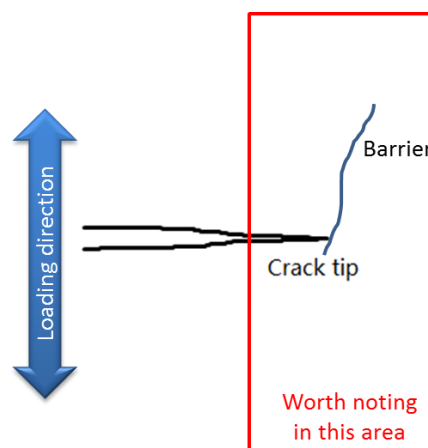


Figure 5-34 Schematic drawing of the area where crack tip is arrested by barrier

## Chapter 5 Damage mechanisms in Al-Si alloys

The above four secondary cracks, i.e. Crack F1-a, Crack F1-b, 2<sup>nd</sup> initiation site for Specimen F1 and Crack 2 for Specimen F2, have a common feature: when the principal crack was arrested, they initiated from hard inclusions that are located in the same vertical direction as the main crack tip (Figure 5-34), i.e. the line through the principal crack tip and along a direction perpendicular to the crack propagation.

The breaking of hard inclusions needs enough applied stress (Starink, 2005). Thus the above observations imply that stress concentrations may occur in the same vertical direction as the crack tip, i.e. the area marked in Figure 5-34, when the crack was arrested. It should be noted that initiation site E for Specimen F2 is a little away from the vertical direction of Crack tip 1. This may be ascribed to the combined effect of the stress concentrations caused by Crack tip 1 and Pore C.

When a secondary crack initiated near the crack tip after the first crack has been arrested by hard inclusions, an additional branch crack was formed that presented a ‘Y’ like shape in Figure 5-35. This shape is similar with the shape of plastic zone from theoretical calculations (Botsis and Humbert, 2006) and experimental observations (Hutchinson, 1968) shown in Figure 5-36. Thus the plastic zone was expected to be observed in the following field measurements.

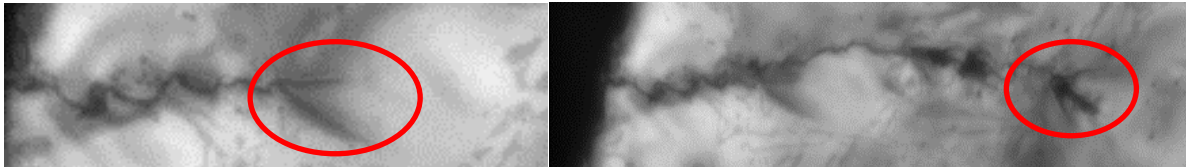


Figure 5-35 Examples of crack tip having the shape of ‘Y’

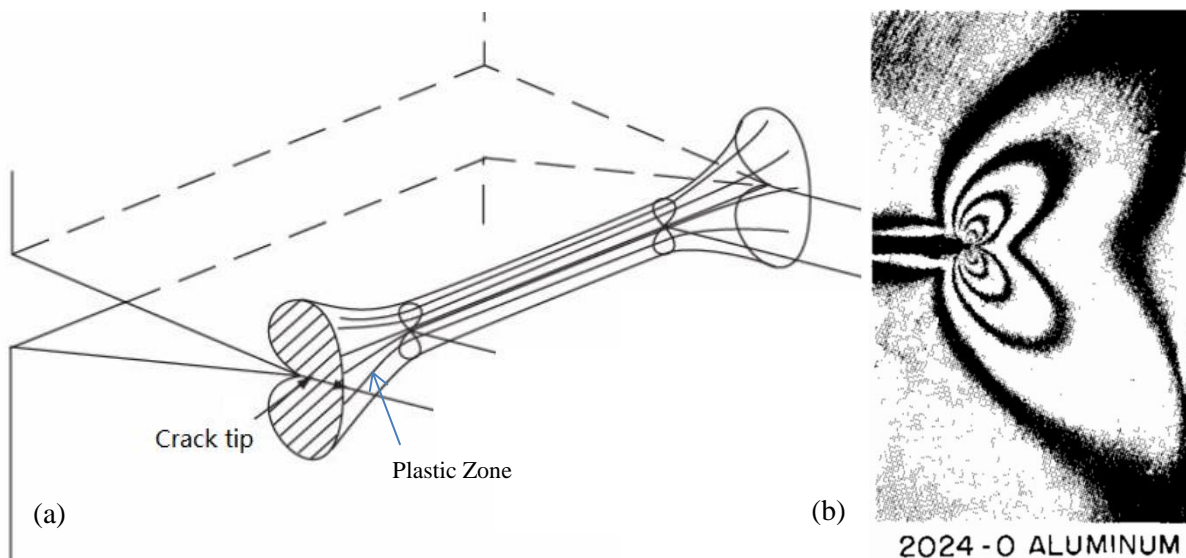


Figure 5-36 (a) Plastic zone shapes through specimen thickness obtained by using the theoretical calculations (Botsis and Humbert, 2006); (b) plastic zone in an aluminum sheet (Hutchinson, 1968)

## Chapter 5 Damage mechanisms in Al-Si alloys

---

### ✓ Final fracture

The principal crack of Specimen F1 was arrested at Point 4 until the final failure (Figure 5-32 (d)). When the crack initiating from the 2<sup>nd</sup> initiation site connected with the principal crack after 90 000 cycles, this large connected crack led to failure quickly.

Crack 2 in Specimen F2 propagated along hard inclusion towards Crack 1. In the same time, a branch crack (marked by a green line in Figure 5-30) propagated in the direction perpendicular to the loading direction and along hard inclusions. When Crack 2 coalesced with the branch of crack 1 after 20 400 cycles, fracture occurred in the following 30 cycles.

Microcracks were observed in ROI in Specimens T1 and T2 with 2D in-situ observation during the tensile tests. However, in fatigue test specimens, the area where many microcracks at hard inclusions were observed, i.e. the area marked with a yellow rectangle for Specimens F1 and F2 (Figure 5-37 and Figure 5-38), is out of the ROI with in-situ observation. In the ROI, there are only a few cracks besides the principal cracks, which led to final fracture. These cracks observed using SEM were also visible in the Questar images; they are marked with white arrows in Figure 5-32(c). The above observations could be easily explained. In the cracks propagation region (marked with red rectangle in Figure 5-37 and Figure 5-38), once the main crack has initiated and propagated on surface, less stress concentration was present behind the crack tip. Thus the stress was not enough to lead to fracture of hard inclusions and no microcracks were observed below and above the cracks propagation region. However, in the fast fracture region, i.e. the zone marked with yellow rectangle, with the propagation of the principal crack, the effective bearing cross-sectional area decreased. Thus the actual loading on the unbroken ligament increased. Once the stress was large enough, the hard inclusions fractured probably under monotonic loading.

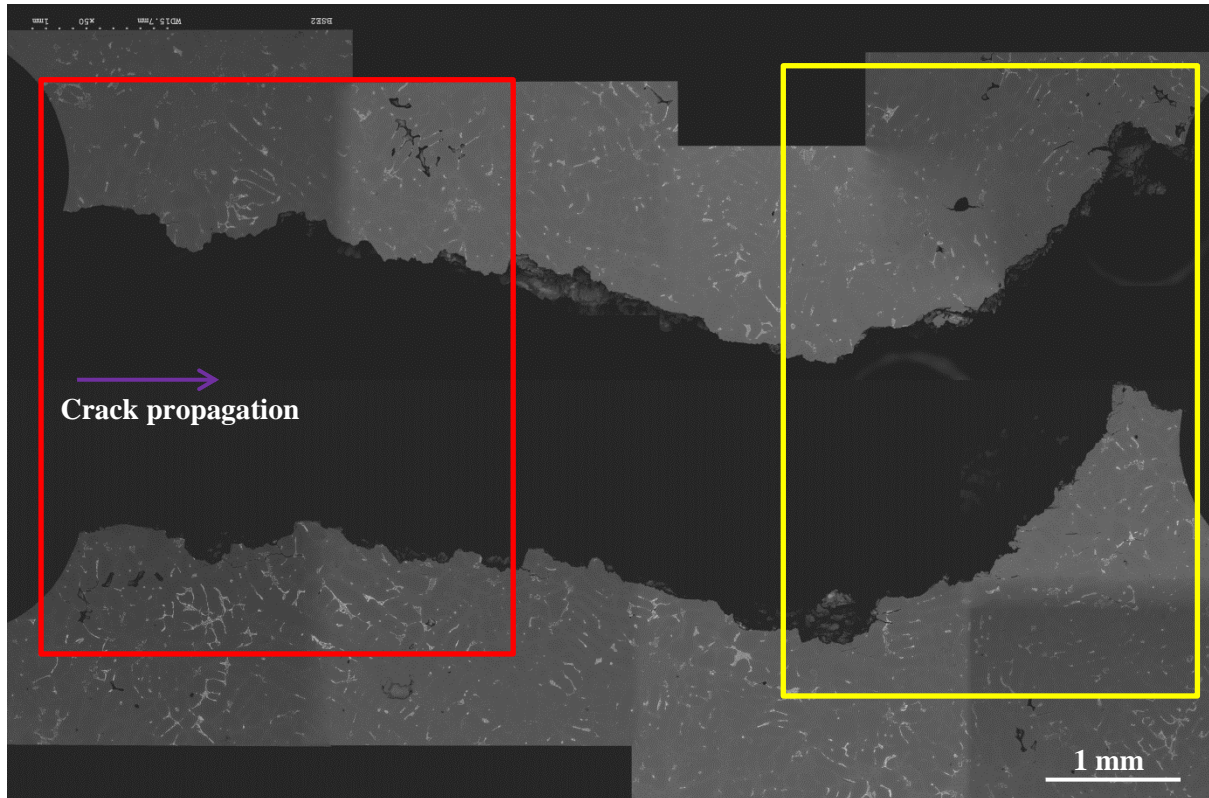


Figure 5-37 BSE images of the surface of Specimen F1 where in-situ observations were done. The selected ROI for in-situ observation is marked with a red rectangle (in left). The area where many microcracks are observed is marked with a yellow rectangle (in right).

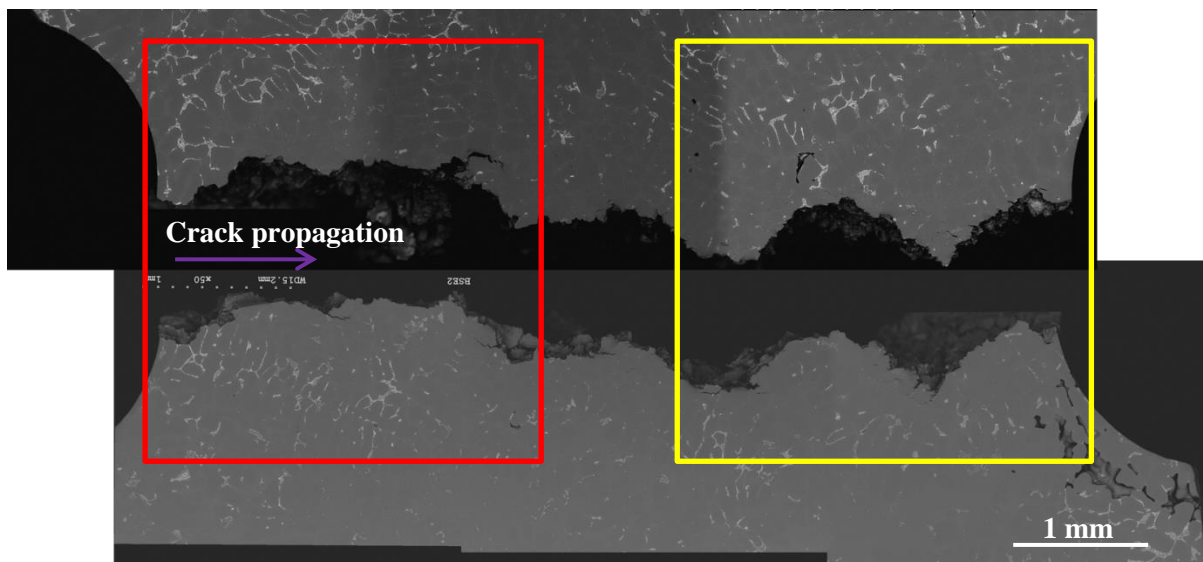


Figure 5-38 BSE images of the surface of Specimen F2 where in-situ observations were done. The selected ROI for in-situ observation is marked with a red rectangle (in left). The area where many microcracks were observed is marked with a yellow rectangle (in right).

## Chapter 5 Damage mechanisms in Al-Si alloys

---

Fracture analysis using SEM-EDS were performed in different regions of the fracture surfaces, i.e. crack propagation area and final fast fracture area (c.f. Appendix VI) in order to identify the chemical composition of hard inclusions in the crack path and to study their failure mode, i.e. either failure or debonding.

### ✓ DIC measurements

DIC measurements were performed between the reference image at the minimum load of the 1<sup>st</sup> cycle and the images at the maximum load of different cycles. The average longitudinal strain at the maximum loading of different cycles deduced from DIC in Zones 0 and 2 of Specimen F1 and that in the whole ROI of Specimen F2 are shown in Figure 5-39. The macroscopic average strain measured by extensometer is also shown for comparison. These measurement zones are recalled in Figure 5-40.

For both Specimens 1 and 2, the average longitudinal strain deduced from DIC in notched area zones was a little larger than the macroscopic average strain measured by the extensometer due to the strain localization in this area. This localization is more significant around the notch root; indeed, the average strain measured by DIC in Zone 0 is generally higher than that in Zone 2.

For Specimen F1, DIC measurements are focused on two zones: Zone 0 where cracks initiation and propagation were observed and Zone 2 where no crack was observed.

Cracks were observed to initiate in Zone 0 due to the pores below the surface in an area where a larger deformation was indeed measured by DIC. During the fatigue test, the gap between these global and local deformation grew larger. Actually, after the cracks initiated in this zone, the opening of the cracks increases with cracks growth as shown in Figure 5-32. These large black cracks in the images had great differences with the original morphologies in the same locations in the reference image. The DIC could not be performed accurately due to the errors introduced by opening of these large cracks. The large deformations measured by DIC in Figure 5-39 were thus mainly caused by crack opening and discontinuities in the displacement field instead of by a real deformation. This situation was also observed for Specimen F2. On the contrary, the average strain in Zone 2, where there is no crack, keeps constant during the test.



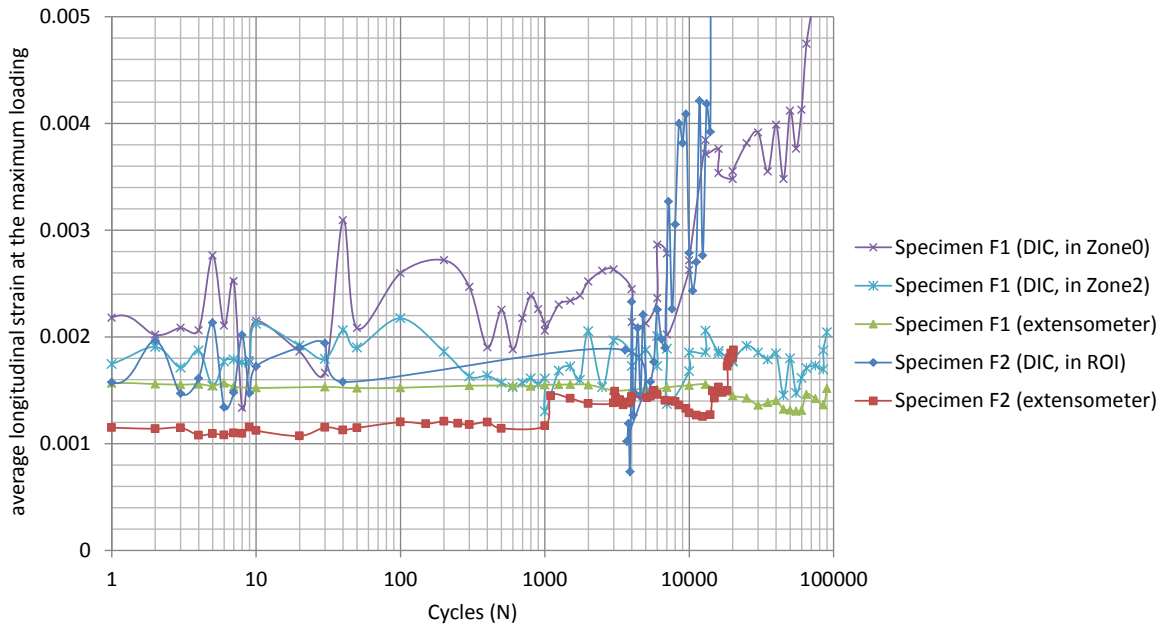


Figure 5-39 Evolution of average longitudinal strain in Specimens F1 and F2, as measured by extensometer and DIC at the maximum load, with the number of cycles

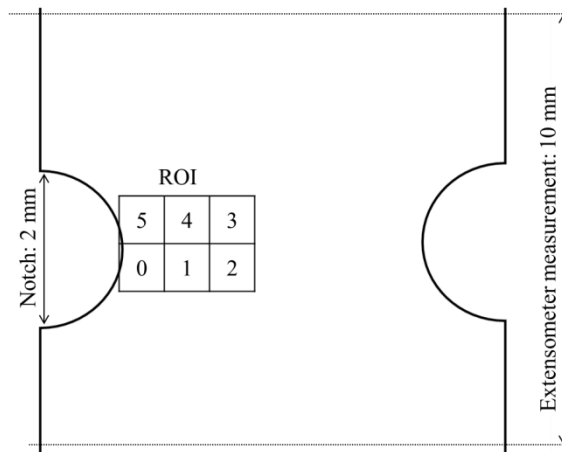


Figure 5-40 Schema of DIC measurement and extensometer measurement

The most important fields measurements in this study are the displacement and the longitudinal strain in the loading direction. Several examples of displacement fields and strain fields for both Specimens F1 and F2 are shown in Figure 5-41 ~ Figure 5-43. It should be noted that, the deformed image, i.e. the image taken at the corresponding cycle, was put behind the measured field to allow its comparison with surface microstructure. In fact, as the measured fields are related to the reference image instead of the deformed images, a little difference may exist between the translucent field and the microstructure behind.

In Figure 5-41, displacement discontinuities in Specimen F1 are located at the crack, and strain localization was observed on the crack path and tip. Again, the large deformations at the cracks (see

## Chapter 5 Damage mechanisms in Al-Si alloys

red areas in Figure 5-41 (b) and (d)) are caused by opening of cracks rather than by real deformation. In the areas marked with circles in (b) and (d), strain localizations ( $>3\%$  for (b), while  $>6\%$  for (d)) occurred while there was still no crack. Crack propagated in the area marked in (b) in the following cycles, and a 2<sup>nd</sup> crack (Figure 5-32 (c)) initiated in the area marked in (d). Strain localizations occurred in these areas prior to the observed crack initiation or propagation. Thus the influence of strain localization on crack initiation and propagation was observed. Besides, the strain measured by DIC in the areas marked with circles in (b) and (d) may also be larger than the real deformation as out-of-plane deformation may have occurred in the areas where cracks nucleated and/or propagated in the following cycles. These out-of-plane deformations induce errors for DIC measurements.

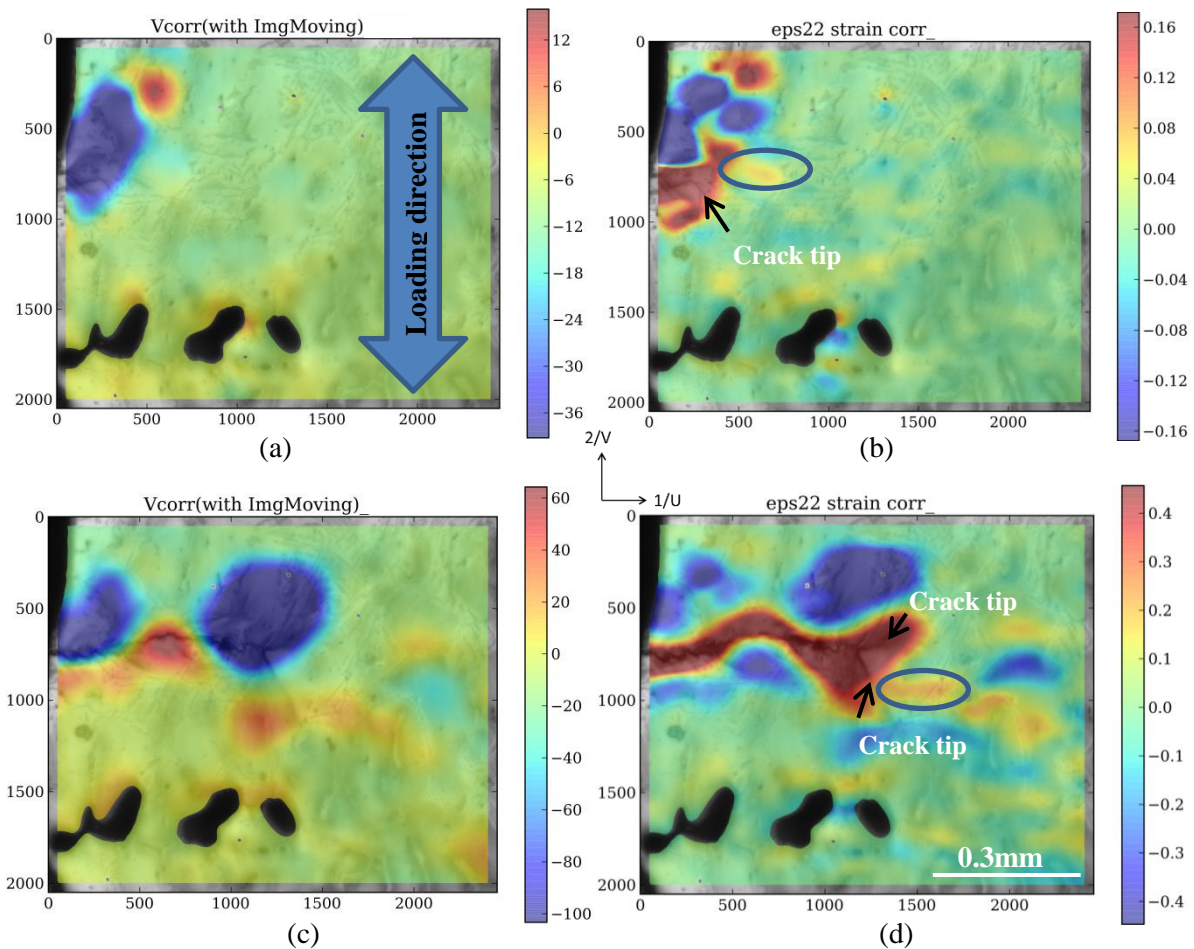


Figure 5-41 Field measurement in zone 0 of Specimen F1: (a) displacement (in pixels, 1 pixel = 0.38  $\mu\text{m}$ ) and (b) strain field after 13 000 cycles; (c) displacement and (d) strain field after 85 000 cycles

One example of the displacement and strain fields in the whole ROI of Specimen F1 is shown in Figure 5-42. Besides the zone 0 (the lower left corner area in the stitched image), the displacement field was uniform and no obvious strain localization was observed until the last step before failure (after 90 000 cycles). The DIC performed in the other five zones gave little useful information. Besides, as in Figure 5-41 (b) and (d), the strain localization (marked by a circle in Figure 5-41) prior to crack propagation occurred where the final fracture took place.

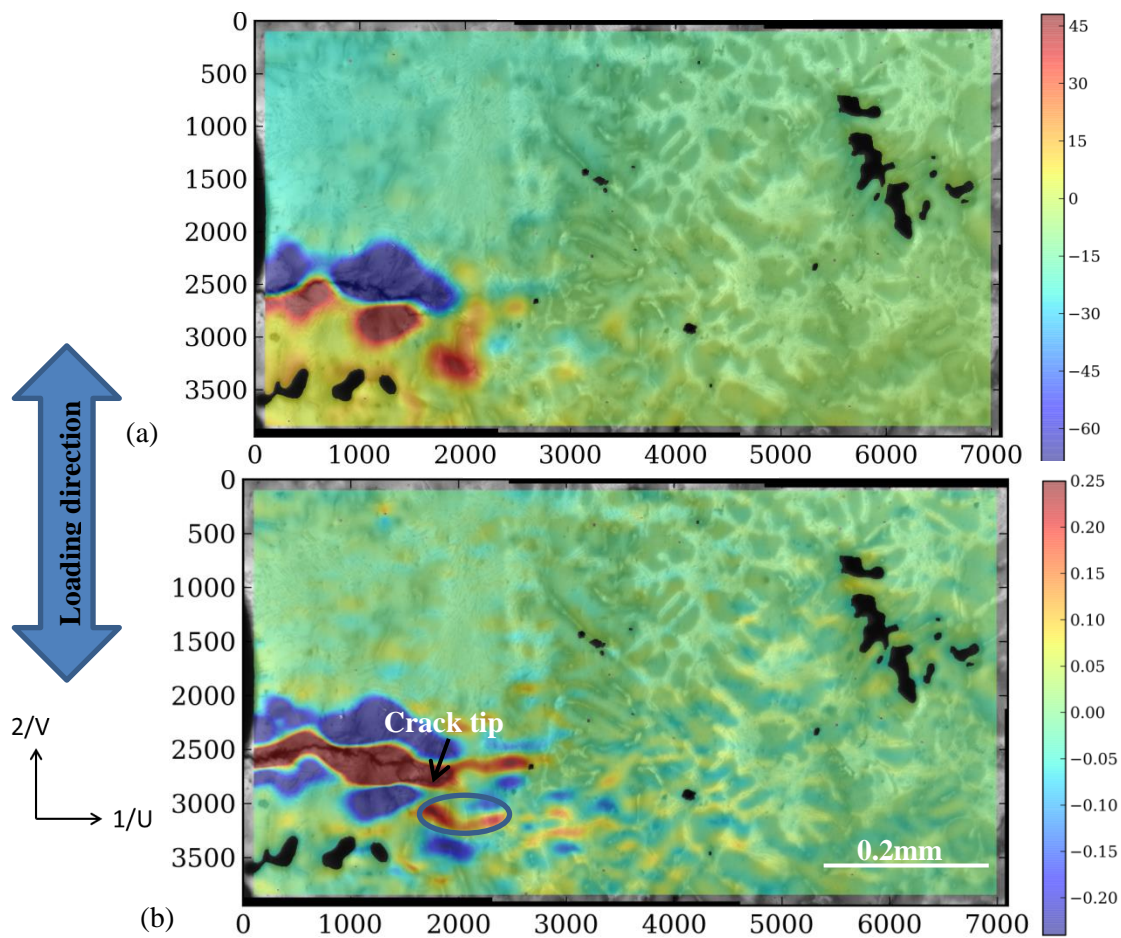


Figure 5-42 Field measurement in the ROI of Specimen F1: (a) displacement ( $V$ , in pixels, 1 pixel =  $0.38 \mu\text{m}$ ) and (b) strain ( $\epsilon_{22}$ ) field after 90 000 cycles (last step before final failure)

The influence of strain localization on crack initiation and propagation was also observed for Specimen F2 in Figure 5-43. The crack tip after 18 410 cycles is marked by arrows, and the cracks initiated from sites C and D (Figure 5-28) have not connected yet. In Figure 5-43(b), strain localizations are observed in the area (marked with a yellow circle) where a secondary crack initiated around the surface pore after 19 350 cycles, when the main crack was arrested by hard inclusions around crack tip (marked by a red arrow). They are also observed in the area (marked with a white circle) where two separate cracks connected on surface in the following cycles.

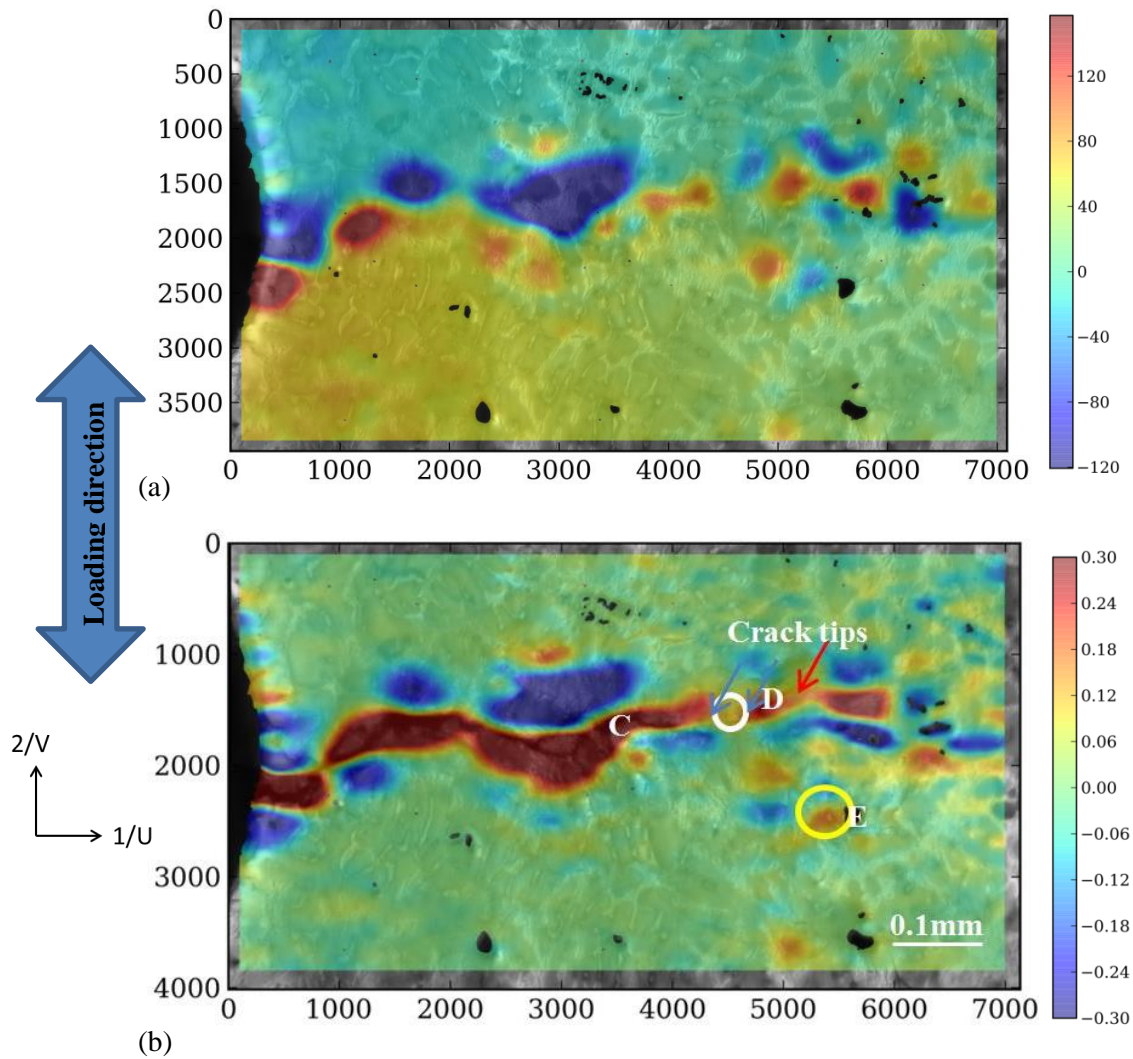


Figure 5-43 Field measurement in the ROI of Specimen F2: (a) displacement ( $V$ , in pixels, 1 pixel = 0.38  $\mu\text{m}$ ) and (b) strain field ( $\epsilon_{22}$ ) after 18 410 cycles

### 5.3.2 Fatigue tests with 3D in-situ observations

#### ✓ Results of 3D fatigue tests

The main parameters of the fatigue tests performed on Specimens F3 and F4 are listed in Table 5-3. The maximum longitudinal strain deduced from DVC (Figure 5-44) shows fluctuations that are due to stress relaxation, cyclic softening, crack growth and reloading. In the case of a lower applied stress, F3 has a larger deformation and a much shorter life than F4 maybe because of a larger volume fraction of pores (0.79%) than F4 (0.42%).



## Chapter 5 Damage mechanisms in Al-Si alloys

Table 5-3 Results of 3D fatigue tests

Specimen	F3	F4
Maximum stress	111MPa	130MPa
R (Stress Ratio)	≈ 0.1	≈ 0.1
Average max. longitudinal strain	0.26 ~ 0.28 %	0.11 ~ 0.17 %
Last scan before failure	10 <sup>th</sup> cycle	10 500 <sup>th</sup> cycle
Final failure	<15 cycles	≈ 10 500 cycles

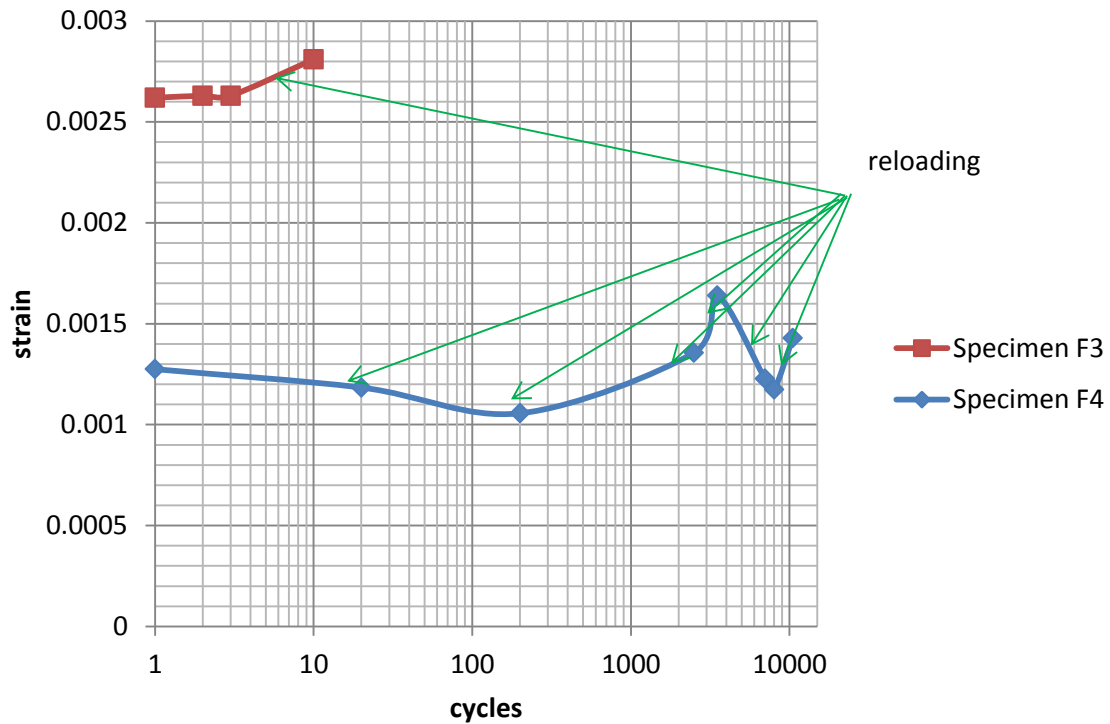


Figure 5-44 Evolution of average maximum longitudinal strain in Specimens F3 and F4, as measured by DVC, with the number of cycles

### ✓ Cracks initiation

The final failure of Specimen F3 occurred through a cluster of pores (Figure 5-45(a)). The slice by slice analysis of the SR tomographic images of Specimen F3 at different cycles (Figure 5-46) reveals that cracks are located at hard inclusions around pores, including eutectic Si, iron intermetallics (both  $\alpha$  and  $\beta$  phases) and copper containing phases. However, no cracks propagation was observed from the 1<sup>st</sup> cycle to the 10<sup>th</sup> cycle, which was the last scan taken before failure. Although the relations between displacement discontinuities and strain localizations in measured fields and cracks and final fracture were well observed (example in Figure 5-45(b) and (c)), the displacement discontinuities and strain localizations did not change very much from the 1<sup>st</sup> cycle to the 10<sup>th</sup> cycle. In addition, as no crack propagation region can be identified, the fracture surface of Specimen F3 was divided into cracks



## Chapter 5 Damage mechanisms in Al-Si alloys

initiation area due to tensile loading, i.e. where cracks were observed in tomographic image, and final fracture area. Fracture analysis using SEM-EDS was performed in both areas (c.f. Appendix VI).

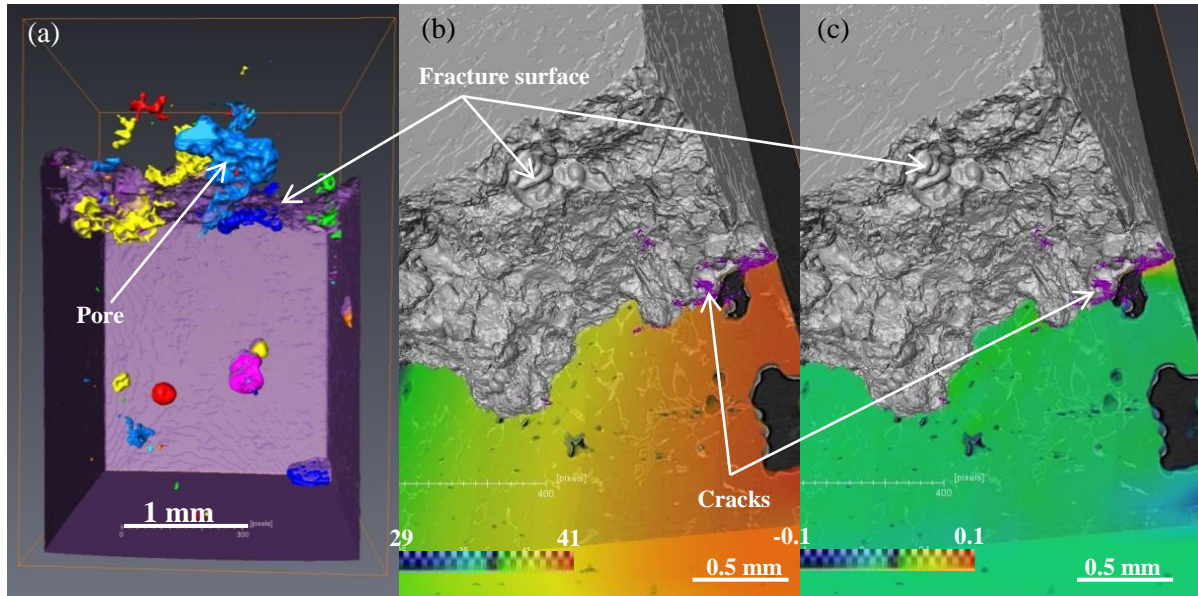


Figure 5-45 (a) 3D rendering of pores and fracture surface of Specimen F3. (b) Displacement field (in pixels, 1 pixel = 1.625  $\mu\text{m}$ ) and (c) strain field at 10<sup>th</sup> cycle shown in translucent with the tomographic image in below. DVC was performed between the minimum loading of the 1<sup>st</sup> cycle and the maximum loading of the 10<sup>th</sup> cycle.

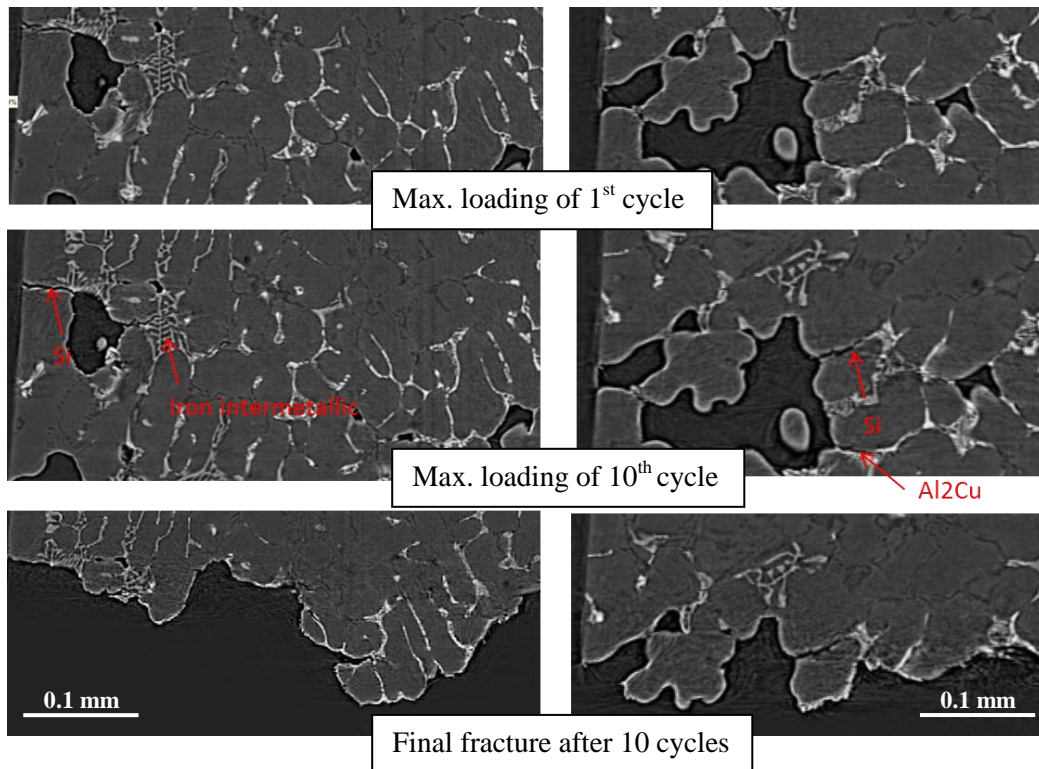


Figure 5-46 Two examples showing cracks in Specimen F3 in the same slice at the maximum loading of 1<sup>st</sup> cycle and 10<sup>th</sup> cycle, and the final fracture after 10 cycles.

## Chapter 5 Damage mechanisms in Al-Si alloys

---

DVC measurements allowed extracting 3D cracks using residual errors in 3D tensile tests. However it does not work in 3D fatigue tests although the relation between cracks or final fracture and displacement discontinuities was also observed (see Figure 5-45(b) for an example). The values of residual errors in some areas along the ‘white colour hard inclusions’ (copper containing phases and some iron intermetallics) in the tomographic image are the same as in the cracks. Thus it was impossible to extract 3D cracks from the maximum residual errors. This problem was mainly caused by the too strong phase contrast provided by SR-CT. For example, one copper containing phase might present different grey level in the different scans. Such a local brightness variation at this phase yielded large residual error around this phase. Fortunately, the phase contrast variation was not observed on displacement or strain field. Besides, the smaller opening of cracks in fatigue tests than in tensile tests is also one reason. In view of the above, the 3D cracks could only be extracted from the tomographic images directly, although this is a tedious work.

In Figure 5-47, Pores A, B, C and D are the four largest pores in Specimen F3, while other pores are much smaller, i.e. less than 0.51mm; their main parameters are given in Table 5-4. The influence of pores on damage can be summarized as follows:

- The final fracture went through the largest three pores, i.e. Pore A, B and C, emphasizing the influence of the size of pores on damage (Wang et al., 2001a).
- Main cracks nucleated around surface Pore B, while only some small cracks nucleated around subsurface Pore A although it is the largest pore. Therefore the location is also important for cracks initiation as surface pore is more dangerous than subsurface pore (Ammar et al., 2008). Besides, a large iron intermetallic was observed in the area around Pore B where cracks nucleated in the tensile stage of 1<sup>st</sup> cycle (marked by arrows in Figure IV-10). It is located in the plane perpendicular to the loading direction and thus is easy to fracture during the tensile loading. Hence this may also be one possible reason why more cracks initiated around Pore B.
- Shape of pores could have been considered important if the morphology of Pore B was sharper than Pore A. The sphericity (F) value in Table 5-4 shows that Pore A has actually a sharper morphology than Pore B. Thus the surface location should be considered as the main reason why more cracks initiated from Pore B than from Pore A.
- Although only few cracks nucleated around other large pores, they are likely to have an influence on fracture damage. Other large pores, such as Pores C and D, might increase the stress concentration around Pores A and B. In other words, the interaction of large pores might increase the stress concentration in this area. The three largest pores located in the same plane perpendicular to the loading direction decreased the effective bearing area seriously. It results in large stress concentration and local deformation that explain why large cracks

## Chapter 5 Damage mechanisms in Al-Si alloys

initiated early in the tensile stage of 1<sup>st</sup> cycle, why the fatigue life is less than 15 cycles and why there is a larger deformation than for Specimen F4 for a lower applied load (Figure 5-44).

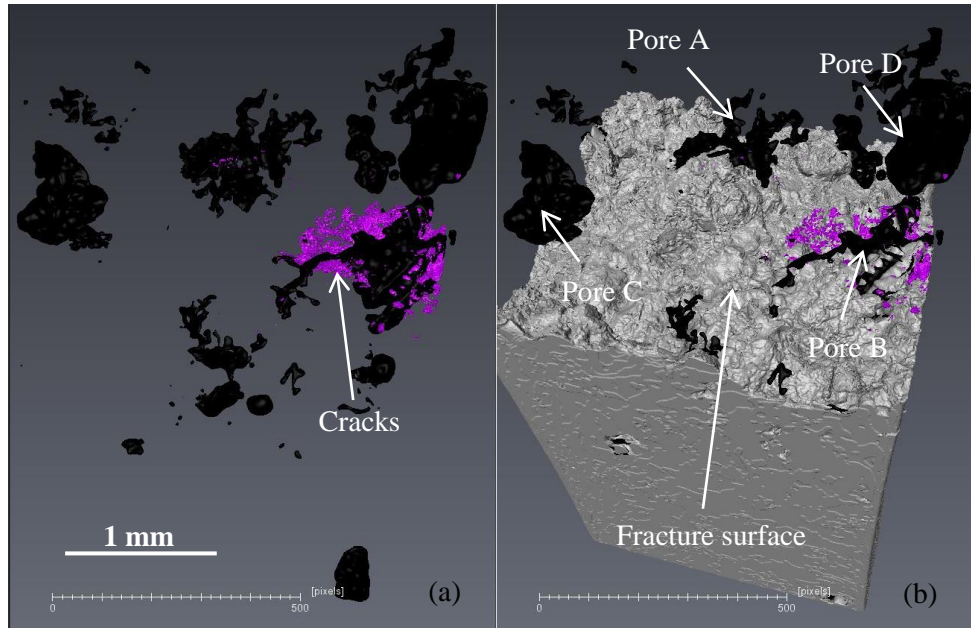


Figure 5-47 (a) 3D cracks and 3D rendering of pores in black; (b) figure (a) shown with fracture surface.

Table 5-4 Parameters of large pores in Figure 5-47

Pore	Feret diameter (mm)	Sphericity(F)	Type	On fracture surface
A	1.55	0.09	Subsurface pore Minimum distance to surface: 0.3 mm	yes
B	0.81	0.19	Surface pore	yes
C	0.76	0.28	Surface pore	yes
D	0.71	0.33	Surface pore	no
others	<0.51	-	-	-

Figure 5-48 shows that the final fracture of Specimen F4 was caused by two main cracks initiating at 1<sup>st</sup> cycle:

- Crack 1: initiated at eutectic Si on surface (shown in the right image).
- Crack 2: initiated at eutectic Si around a large subsurface shrinkage pore (shown in the left image).

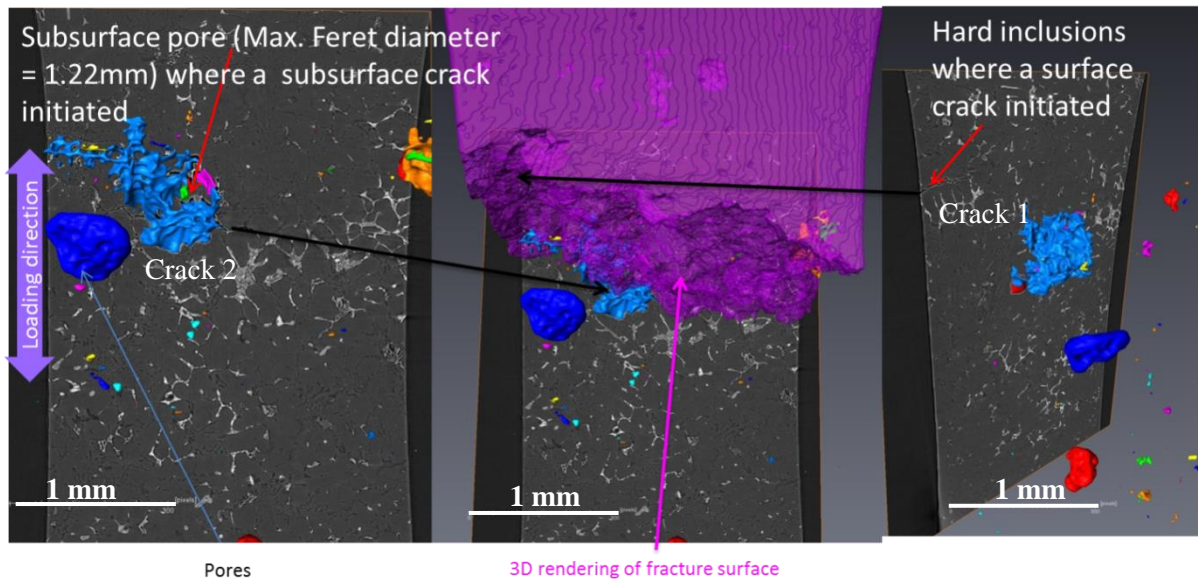


Figure 5-48 Comparison of 3D rendering of pores and fracture surface and tomographic image slice revealed the two main cracks initiated around a large pore (in the left image) and at hard inclusions (in the right image) in Specimen F4

The shrinkage pore, around which Crack 2 initiated, is the largest pore in Specimen F4 where large strain localization occurred in FE simulation results for ROI selection; the pore is marked by an arrow in Figure III-8(b). Its Feret diameter is about 1.22 mm, while the size of other pores is smaller than 0.6 mm. Its volume fraction is close to 40% of all pores in F4. Although this is a subsurface pore, its minimum distance to the surface is only about 0.02 mm. Thus it is not surprising that large cracks initiated around such a large shrinkage pore, which is very close to surface, in the absence of other large surface pores. Then the cracks were observed to propagate along hard inclusions, including eutectic Si, iron intermetallics and copper containing phases, towards the surface.

Crack 1 was found to initiate from eutectic Si in the corner of flat surface and notched surface where stress concentration is prone to occur. Eutectic Si is reported (Fan et al., 2003) (Stolarz et al., 2001) as potential crack nucleation site in the absence of large defects, i.e. above a critical size (Wang et al., 2001a) (Zhang et al., 2007) (Mu et al., 2014). Even though there are large pores in Specimen F4, no pores whose size is larger than 0.02 mm are less than 0.5mm far away from Crack 2 nucleation site. Thus it can be considered that eutectic Si on surface can act as crack nucleation site when there is no large pores in the neighbourhood.

### ✓ Crack propagation

Figure 5-49 shows Cracks 1 and 2 of Specimen F4 in 3D at different cycles viewed along loading direction. Cracks propagated along eutectic Si, iron intermetallics and copper containing phases. Crack 2 propagated around the largest pore, while Crack 1 propagated from surface towards the



## Chapter 5 Damage mechanisms in Al-Si alloys

largest pore inside the specimen. When Crack 2 and Crack 1 coalesced after 10 500 cycles, the final fracture occurred in a few cycles.

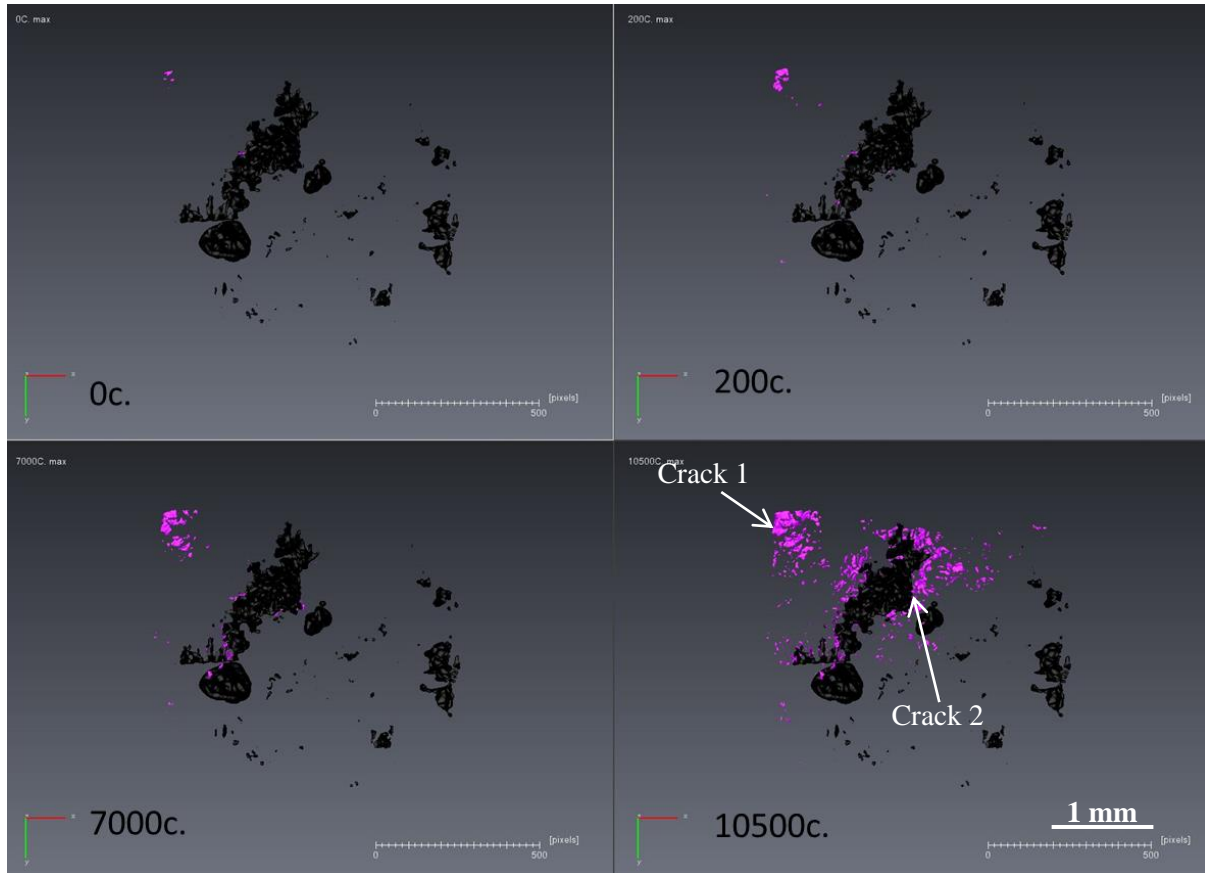


Figure 5-49 3D cracks in Specimen F4 around the 3D rendered pores at different cycles. View along the loading direction.

Unlike Specimen F3, cracks propagation was indeed observed in Specimen F4. Thus its fracture surface was divided into cracks propagation region and final fast fracture region. Fracture analysis using SEM-EDS performed in these two regions are shown in Appendix VI.

In order to study the propagation of these two cracks quantitatively, each crack was projected on a plane perpendicular to the loading direction as shown in Figure 5-50(a). The measured cracks lengths, i.e. the root square of the projection area, in Figure 5-50(b) show that the propagation rate of Crack 1 is a little higher than that of Crack 2 before the final stage. This may be due to a higher stress concentration at the surface corner than inside the specimen.



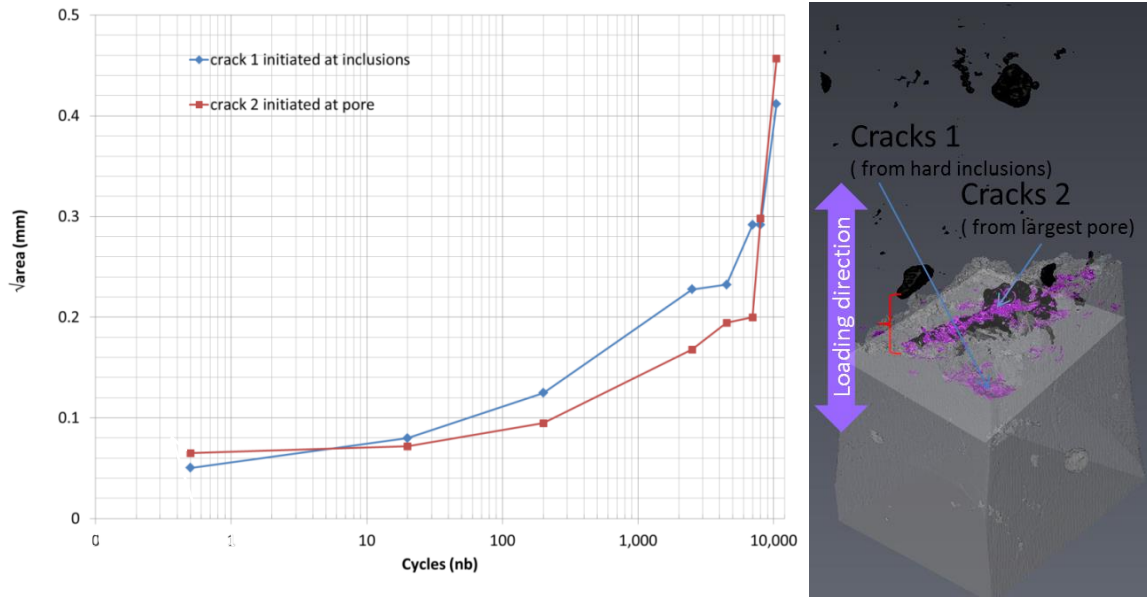


Figure 5-50 (a) Cracks length evolution with the number of cycles in Specimen F4 with (b) the projection plane used for the cracks measurements

DVC measurements were performed between the minimum and maximum loading of each cycle for Specimen F4. The results were analysed slice by slice by comparing with cracks and microstructure in the tomographic images. One example is shown in Figure 5-51 ~ Figure 5-53. One slice of tomographic image, which is about 65  $\mu\text{m}$  below flat surface, is considered and shown with 3D rendering of pores and fracture surface in Figure 5-51. The displacement field (Figure 5-52) and strain field (Figure 5-53) of the same slice at different cycles are shown in translucent with the tomographic image slice in behind.

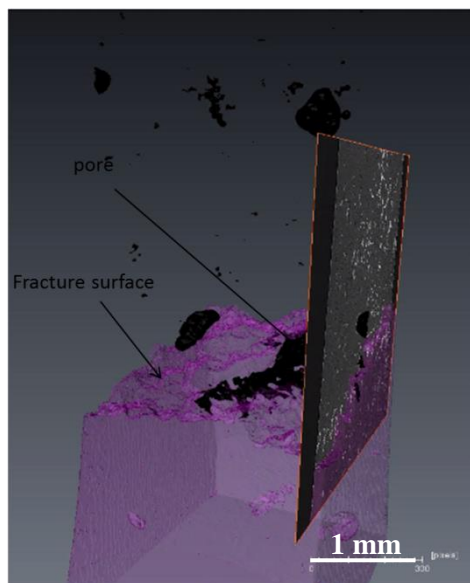


Figure 5-51 One slice (about 65  $\mu\text{m}$  below the flat surface) shown with a 3D rendering of pores and fracture surface of Specimen F4

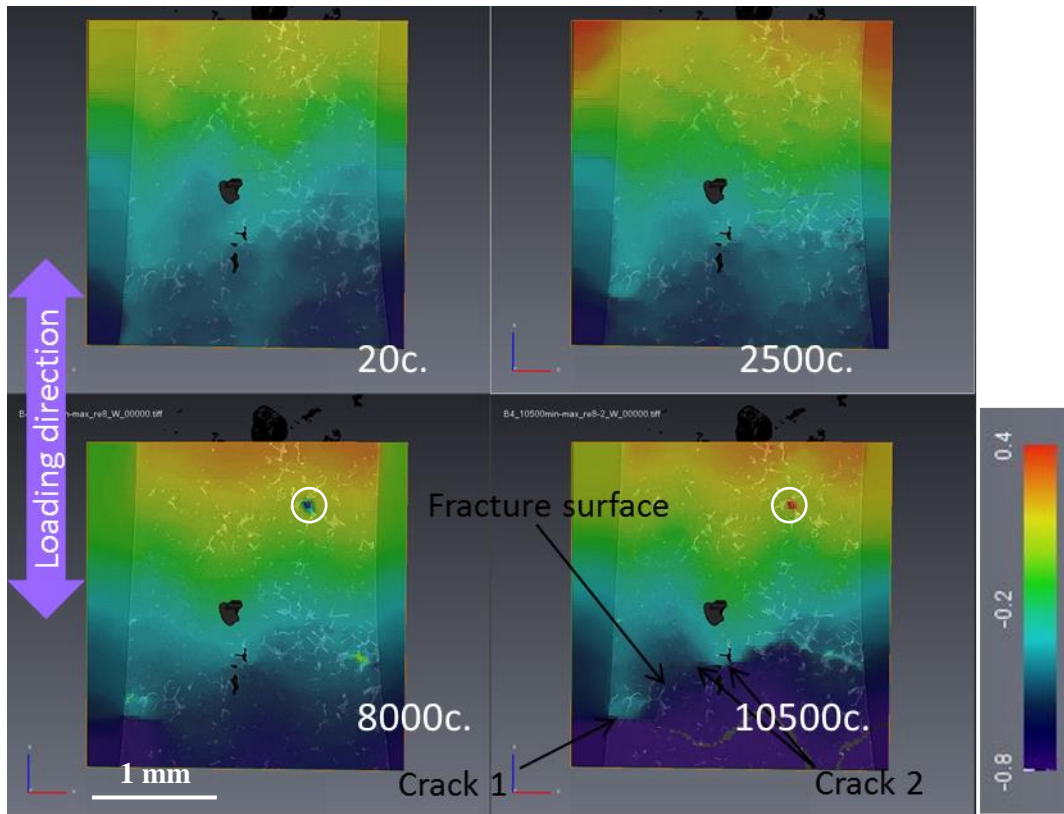


Figure 5-52 DVC displacement fields (in pixels, 1 pixel = 1.625  $\mu\text{m}$ ) of one slice (about 65  $\mu\text{m}$  below the flat surface) of Specimen F4 at different cycles.

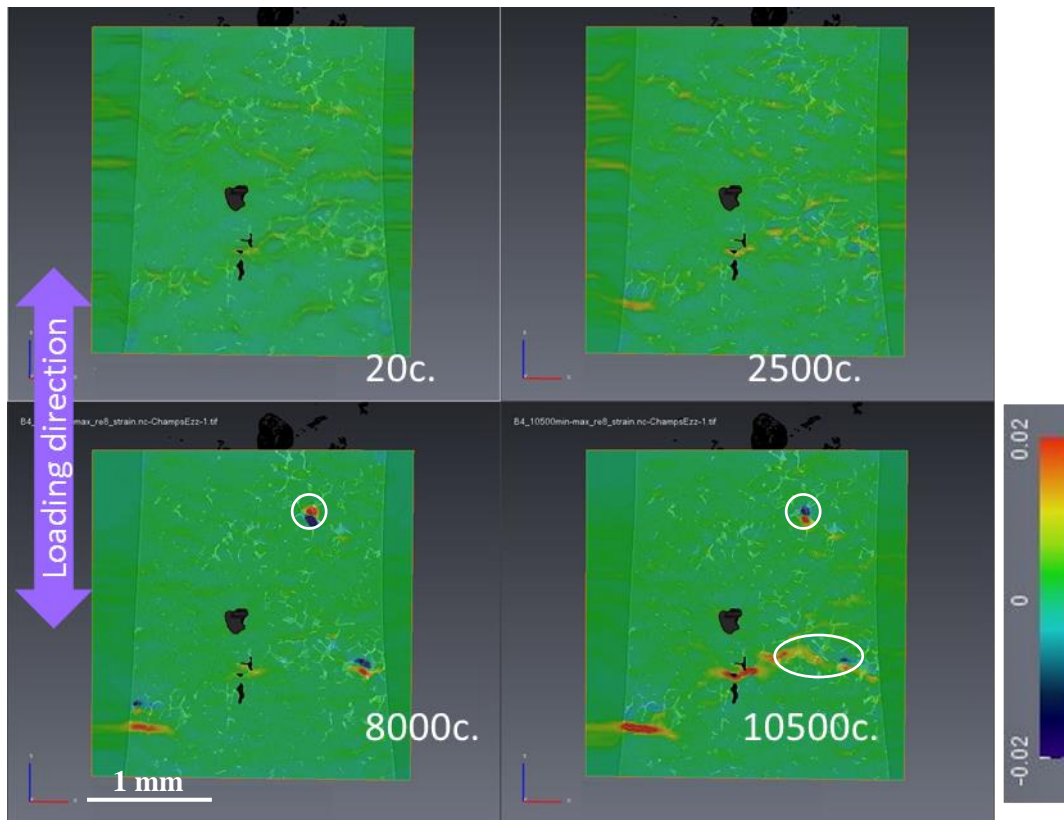


Figure 5-53 DVC strain fields of the same slice (about 65  $\mu\text{m}$  below the flat surface) of Specimen F4 in Figure 5-52 at different cycles.

## Chapter 5 Damage mechanisms in Al-Si alloys

---

The relation between the displacement discontinuities and cracks and final fracture are well observed in Figure 5-52. The relation between displacement discontinuities and Crack 1 was observed when the length of Crack 1 reached 0.25 mm in the slice shown at 2 500 cycles. The relation between displacement discontinuities and Crack 2 was slightly observed at 8 000 cycles while Crack 2 was not observed in this slice until 10 500 cycles. At 10 500 cycles, displacement discontinuities were observed at the areas where final fracture occurred.

In Figure 5-53, relations between strain localizations at hard inclusions and cracks are well observed. Strain localizations were observed at Crack 1 from 2 500 cycles, and were then observed to grow with crack propagation. However, a slight strain localization has been observed from 2 500 cycles in the area where Crack 2 was observed at 10 500 cycles. Besides, strain localizations were also observed at 10 500 cycles in the areas where final fracture occurred. These relations emphasized the influence of strain localizations on cracks propagation. It should be noted that, as in DIC measurements in 2D in-situ fatigue tests, the large deformations in Figure 5-53 around large cracks are caused by crack opening instead of by real deformation. Such an influence is less observed in the averaged strain measured by DVC shown in Figure 5-44 than that measured by DIC shown in Figure 5-39 as the former has fewer fluctuations. This is because (1) the fraction of cracks, hence the fraction of “false strain”, in all the measured volume by DVC is much smaller than that in measured surface by DIC; (2) DVC measurements were performed between the minimum and the maximum loading of each cycle while DIC measurements were performed between the minimum loading of 1<sup>st</sup> cycle and maximum loading of different cycles.

It also should be noted that in some areas, where displacement discontinuities and strain localizations were observed (such as the areas marked with circles in Figure 5-52 and Figure 5-53), sometimes the cracks or final fracture are indeed observed in the tomographic images. However sometimes cracks are hardly identified in the tomographic images even at the last scan before failure (at the 10 500<sup>th</sup> cycle). This is due to the limit of resolution and image quality of X-ray CT. In 2D in-situ tensile and fatigue tests, microcracks can only be observed by using high resolution SEM. Besides, even with the same spatial resolution, the contrast in SEM images was higher than in tomographic images as more details could be identified using SEM. If the scans were performed with a higher resolution, a smaller specimen will be required. The size of such a small specimen will be below the size of large pores in this material so that its distribution of pores will not be similar with that in a large volume of material anymore. Thus such a small specimen could not be representative. At the present resolution, the relations between microcracks outside the final fracture areas and displacement discontinuities and strain localizations could not always be identified inside the specimen s.

Strain localizations were often found along the hard inclusions sometimes out of the final fracture area. The two following reasons can be proposed:

## Chapter 5 Damage mechanisms in Al-Si alloys

- (1) Strain localizations are errors caused by the too strong phase contrast that results in a strong brightness change for hard inclusions.
- (2) Hard inclusions generate stress concentrations easily but they do not always result in crack initiation. The relations between strain localizations and microcracks were indeed observed in such area sometimes.

DVC measurements performed between the minimum loading of 1<sup>st</sup> cycle and the minimum loading of other cycles give cumulated residual strain field due to cumulated plastic deformation (Figure 5-54 and Figure 5-55). As shown in Figure 5-35, plastic zones had a shape of ‘Y’ near the tip of cracks in 2D. The strain localizations with the shape of ‘Y’ are also observed near the cracks tips in Figure 5-54. The red colour strain localizations were probably caused by residual crack opening instead of by real deformation only. However, as crack openings at the minimum loading are small, they results in lower ‘strain value’ in Figure 5-53 than in Figure 5-35.

The propagations of plastic strain localizations were observed with cyclic loading (Figure 5-55). The plastic strain localizations marked with circles were found in the area where cracks or final fracture were found in the following cycles or at final failure. Thus the plastic zones caused by cracks propagations are observed. This is an important result.

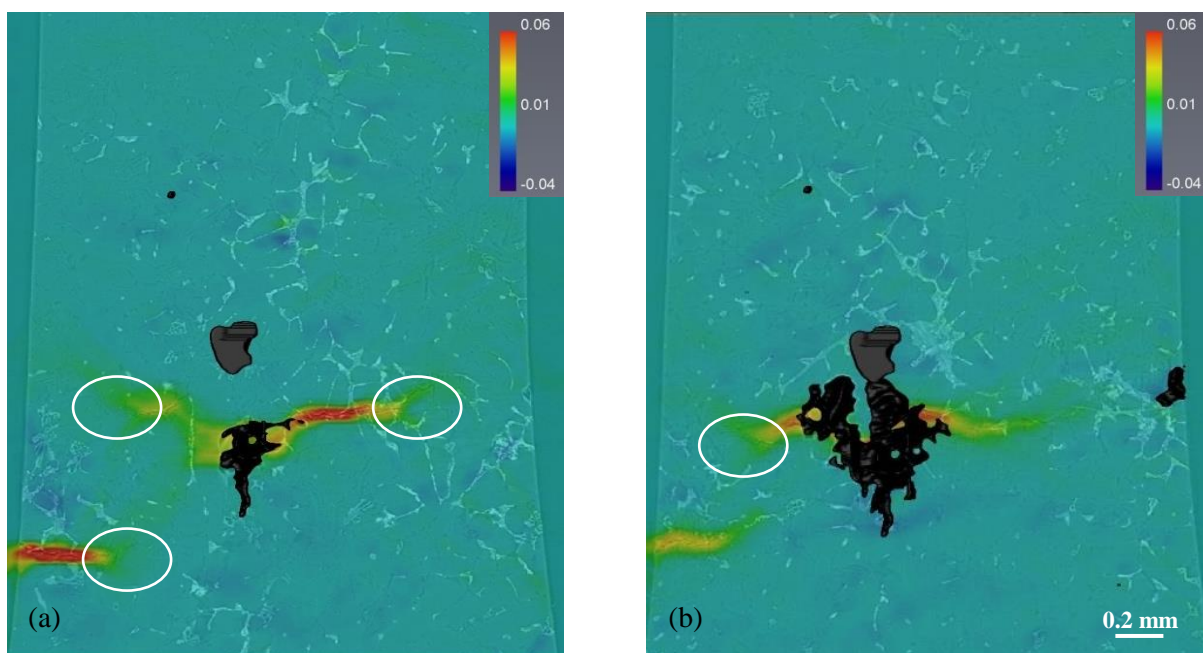


Figure 5-54 Examples showing residual plastic zones with a shape of ‘Y’ near cracks tips: (a) about 80  $\mu\text{m}$  and (b) about 200  $\mu\text{m}$  below flat surface of Specimen F4. DVC was performed between the minimum loads of the 1<sup>st</sup> cycle and of the 10 500<sup>th</sup> cycle



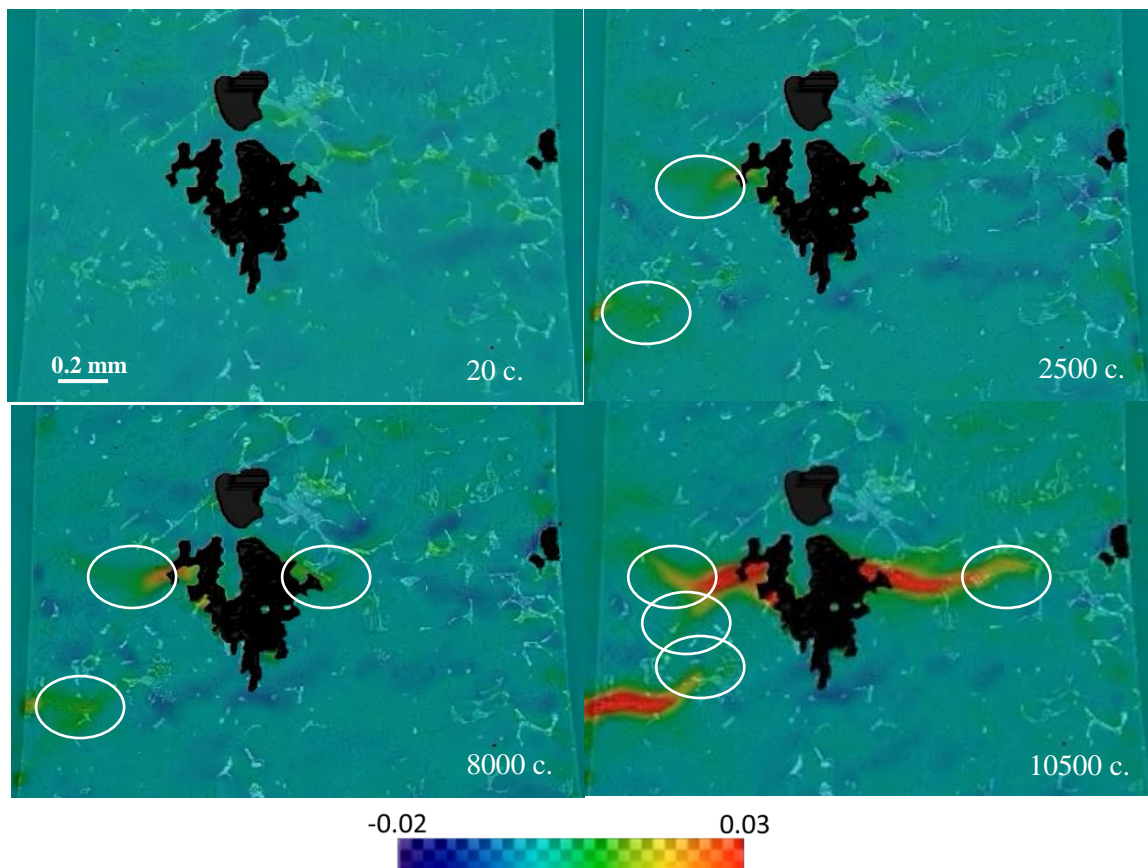


Figure 5-55 Residual plastic strain localizations in the same slice at different cycles (Specimen F4)

### ✓ Crack opening

Crack opening in tomographic images was observed to increase with cyclic loading. As explained previously, crack opening results in larger deformation than real deformation in strain fields. Non-real deformation induced by crack opening was also observed to increase with cyclic loading. In order to measure crack opening, Cracks Opening Displacement (COD) maps (Limodin et al., 2009) (Limodin et al., 2010) are obtained from DVC performed between the minimum and maximum loading of each cycles (Figure 5-56 for Specimen F3 and Figure 5-57 for Specimen F4). The outside areas are shown in black and the projections of pores located between the two selected slices are also shown in black in order to cover the deformation of pores. Unfortunately some small cracks located in the vertical direction to the projection of pores are also covered.

The COD measurements are more difficult to perform and are less accurate than that in (Limodin et al., 2009) (Limodin et al., 2010). Actually, Limodin et al. studied the propagation of a pre-crack that grows in a plane perpendicular to the loading direction in a specimen without large pores. Thus the used COD measurement approach is effective. In our study, large shrinkage pores with complex 3D shapes are everywhere, and multiple cracks initiated around these large pores and spread in 3D instead of in a plane.



## Chapter 5 Damage mechanisms in Al-Si alloys

Despite this, by observing the limited information in the COD maps in Figure 5-56, the opening of cracks around Pore B in Specimen F3 is found to increase with the cyclic loading although crack propagation was not observed. Figure 5-57 shows that the COD of both Crack 1 and Crack 2 in Specimen F4 increase with the cyclic loading.

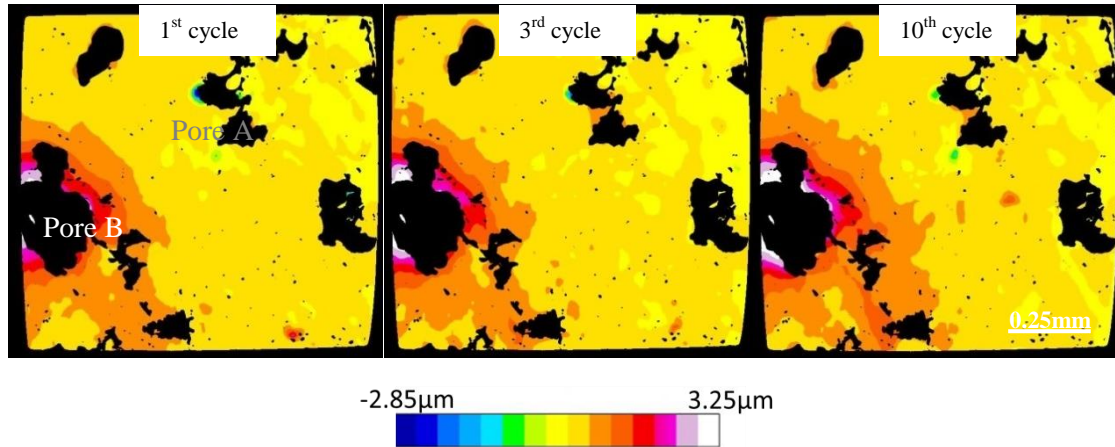


Figure 5-56 Cracks opening displacement map of Specimens F3.

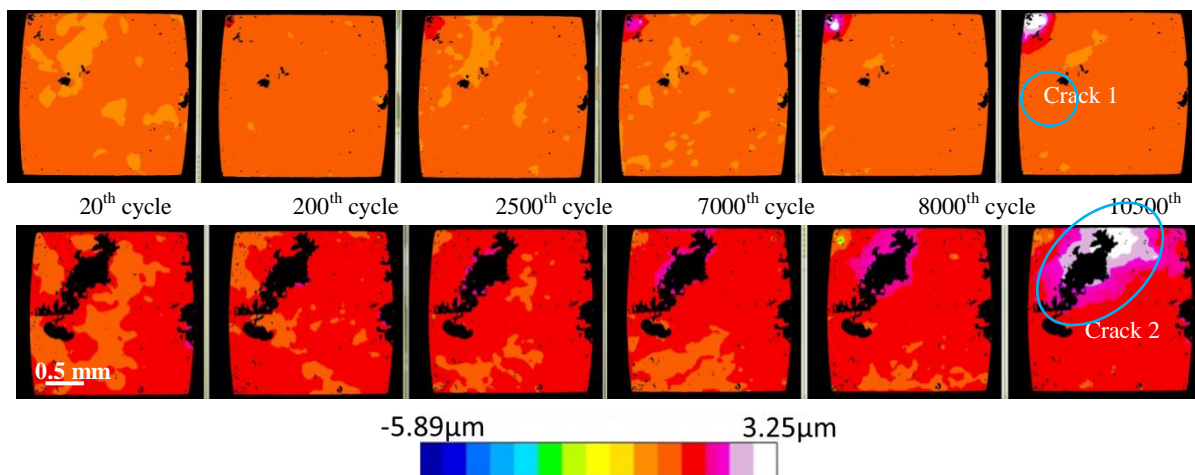


Figure 5-57 Cracks opening displacement map of Crack 1 and Crack 2 in Specimen F4. The location of each crack was shown by a circle in the last cycle.

### 5.3.3 Discussion

The initiation and propagation of cracks in fatigue tests are summarized in Table 5-5. Cracks initiated around large pores and at eutectic Si on surface and then propagated along hard inclusions, including Si phase, iron intermetallics and copper containing phases.

## Chapter 5 Damage mechanisms in Al-Si alloys

Table 5-5 Basic information on fatigue tests

Specimen	F1	F2	F3	F4
Max. loading (MPa)	110	80~110	111	130
Average max. strain	0.15%	0.10%	0.26 ~ 0.28 %	0.11 ~ 0.17 %
Initiation	<b>Pore</b>	<b>Pore + Si (Possible)</b>	<b>Pore</b>	<b>Pore + Si</b>
Propagation	<b>Hard inclusions (Si, iron intermetallics, copper containing phases)</b>			
Final failure (cycles)	≈ 100 000	20 430	< 15	≈ 10 500

### ✓ Crack initiation

Cracks initiated around large pores for all test specimens, thus **pore is undoubtedly the most important microstructural feature for cracks initiation** in the studied material. This is firstly due to the large size of pores in LFC alloy, which is much larger than the critical sizes in the literature (Wang et al., 2001a) (Zhang et al., 2007) (Mu et al., 2014). The minimum size of pores around which cracks initiated is 0.8 mm except for Specimen F1 where a crack initiated at a smaller surface pore, i.e. 0.4 mm, because of the absence of larger pores in the near surface. Cracks initiating from these large pores instead of from the numerous small pores proves that the **size of pore** is an important factor on cracks initiations.

Besides, one can also note that:

- Cracks initiated around a surface pore at the notch root in Specimen F1 instead of other larger pores far from surface.
- In Specimen F2, more cracks initiated from the near surface Pore A (size: 1.31 mm, minimum distance to surface / distance to the notch root: 0.02 mm) and the surface Pore C (size: 0.90 mm, distance to the notch root: 1.70 mm) than from the larger subsurface Pore B (size: 1.37 mm, minimum distance to surface: 0.80 mm, distance to the notch root: 0.90 mm).
- In Specimen F3, more cracks initiated from the surface Pore B (size: 0.81 mm) rather than from the larger subsurface Pore A (size: 1.51 mm, minimum distance to surface: 0.3 mm).

These imply that the **location of pore** is also an important factor on cracks initiations.

In addition, the influence of the **number of large pores** on cracks initiation and fatigue life could be proved through the following analysis:

- In Specimen F2, which has more large pores near surface than Specimen F1, cracks initiated on surface in the tensile stage of 1<sup>st</sup> cycle while cracks initiated on surface of Specimen F1

## Chapter 5 Damage mechanisms in Al-Si alloys

---

after 7 000 cycles. Specimen F1 has a longer fatigue life than Specimen F2 while the former has a larger loading.

- In Specimen F3, which has more large pores than Specimen F4, lots of cracks initiated in the tensile stage of the 1<sup>st</sup> cycle while only a few cracks initiated in Specimen F4 in the tensile stage of the 1<sup>st</sup> cycle. Specimen F3 failed in less than 15 cycles while Specimen F4 failed after 10 500 cycles.

Thus a large number of pores accelerates cracks initiation and also reduces fatigue life (Buffière et al., 2001).

**Shape of pores** ('Sphericity') in Specimen F3 has been discussed previously; it does not seem an important factor. However, all the four pores studied in Specimen F3, i.e. the largest four pores in the specimen, have a Sphericity value less than 0.4. Thus they are all likely to be shrinkage pores as regards their morphologies in Figure 5-47. If there exist two large pores with similar characteristics (size, location etc.), but one has a value of Sphericity close to 0 (shrinkage pore), and another one has a value close to 1 (gas pore), the influence of shape of pores may be more evident as more stress concentration will be caused by the sharp shape of shrinkage pore. But this supposition was not verified in the present studies.

However, the value of Sphericity reflects the global shape of a pore rather than a local shape of large pore which may introduce a local stress concentration. In order to check the influence of the local shape of large pore on crack initiation, FE simulation was performed based on the porous model of Specimens F3 and F4 in tensile condition (for details see Appendix II). One example in Figure 5-58 shows that the strain localizations from FE simulations arise around large pores where cracks are observed in the tomographic image. This implies that the shape of large pore, especially a locally strong curvature, has an important influence on the cracks initiation site.

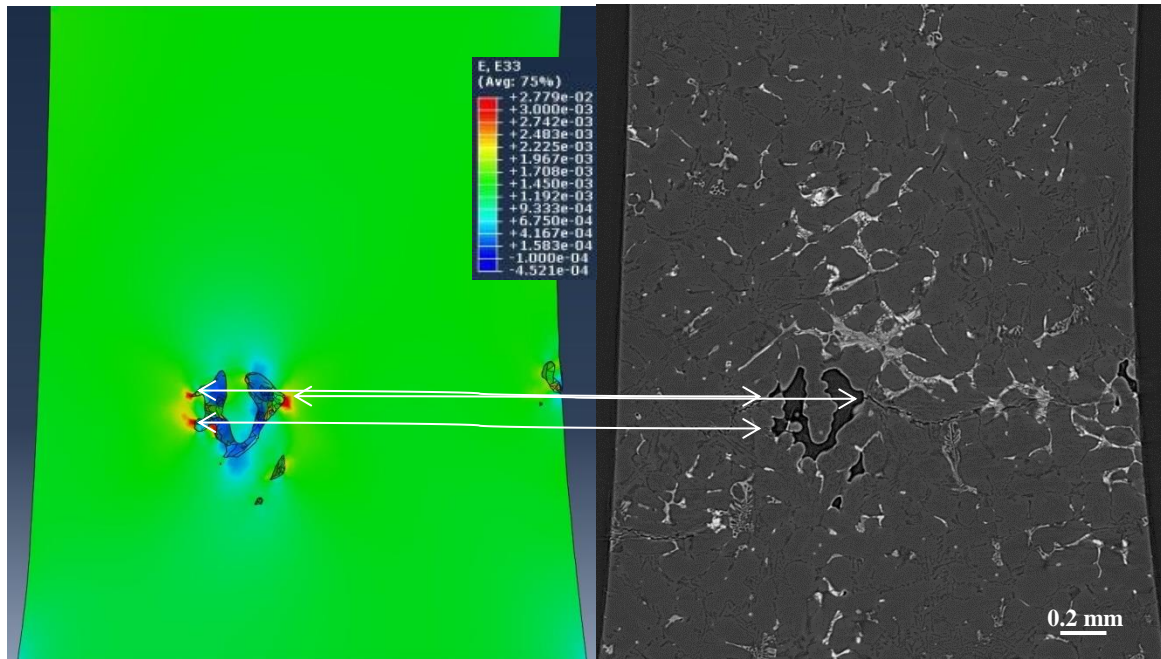


Figure 5-58 Comparison of same slice (390  $\mu\text{m}$  below the flat surface) between FEM simulation results and the tomographic image at 10 500 cycle (Specimen F4)

It should be noted that, **the strain localization areas around large pore include Al matrix and hard inclusions (Si phase, iron intermetallics and copper containing phases)**. However, in 3D observation, cracks always initiate at the hard inclusions around large pores instead of at Al matrix. This emphasizes the role of hard inclusions on cracks initiations when crack nucleated around large pores.

Even if large pores exist, cracks were also observed to initiate at eutectic Si on the surface away from pores:

- In Specimen F4, eutectic Si in the corner of two surfaces, where stress concentration is easy to generate, acted as crack nucleation site (Crack 1) in a region without large pores.
- In Specimen F2, crack may have initiated at Si phase at initiation site D (Figure 5-25). However, initiation at eutectic Si is not the first crack initiation site during the fatigue test. In other words, crack nucleated at site D due to the propagation of the main crack rather than as an initial and independent nucleation site. It is expected that as the tip of the main crack grew closer to initiation site D, the stress field around site D increased and led to crack nucleation.

Herein, we can consider both cases, i.e. cracks initiation at hard inclusions around pores and at eutectic Si on surface. In summary, **cracks are prone to initiate at hard inclusions in the areas where there is an enough high stress concentration; this stress concentration may be induced by large pores (majority case in the present study) or by specimen geometry such as the edge of the specimen.**

## Chapter 5 Damage mechanisms in Al-Si alloys

---

Stress concentration can also explain why a large size pore, a small distance between pore and surface, a large number of pores can promote crack initiation: (1) a large size pore and large number of pores can more easily generate a large stress concentration; (2) a small distance between pore and surface results in a large stress concentration due to the coupled influence of pore and surface on stress field.

Besides, stress concentration effects can also explain initiation of secondary cracks and microcracks at hard inclusions:

- Microcracks (Figure 5-37 and Figure 5-38) at hard inclusions initiated in final fast fracture stage when an enough stress level was reached due to crack propagation.
- Secondary cracks, i.e. Crack F1-a, Crack F1-b and 2<sup>nd</sup> initiation site for Specimen F1 (Figure 5-32) and Crack 2 for Specimen F2 (Figure 5-30), initiated at hard inclusions due to the growth of the main crack tip which increased local stress level.
- In Specimen F2, as analyzed formerly, a secondary crack initiated at Si phase at site D (Figure 5-25). As the main crack tip grew closer to initiation site D, the stress field around site D was increased and led to the nucleation of this secondary crack at Si phase.

The most probable reason why cracks ‘select’ hard inclusions as the initiation sites instead of Al matrix is that **a larger stress concentration is generated at hard inclusions than in Al matrix** because:

- (1) Hard inclusions have a higher elastic modulus and are more fragile than Al matrix (Chen et al., 2010) (Chen et al., 2009).
- (2) Hard inclusions have local sharp morphologies as characterized in Chapter 3.

This assumption can be supported by theory analysis using continuum mechanics and FE simulations in literature (Gall et al., 2000) (McDowell et al., 2003) (Prasannavenkatesan et al., 2009) (Wang et al., 2002). Strain localizations were indeed observed at hard inclusions such as in Figure 5-53. In the present study, FE simulation was only based on a mesh model representing pores and solid matrix, i.e. Al matrix and hard inclusions altogether. A more complex mesh model representing Al matrix, pores and hard inclusions is expected to validate the above hypothesis in future work.

Among all the inclusions in the studied A319 alloy, the influence of Pb particles on crack nucleation was not observed. As discussed in Chapter 3, Pb particles have a very low content and rather act as ‘small pores’ due to their small size, their individual object morphology, and their lower hardness as compared to Al matrix. Thus they can be considered to have no influence on crack initiation.

In Specimen F4, cracks initiated at eutectic Si rather than at iron intermetallics and copper containing phases, as there is lots of eutectic Si but few other hard inclusions around the largest pore where cracks nucleated. In Specimen F3, cracks around large pores were observed at eutectic Si as well as



## Chapter 5 Damage mechanisms in Al-Si alloys

---

iron intermetallics and copper containing phases. Thus eutectic Si, iron intermetallics and copper containing phases are all possible crack initiation sites.

One can assume that eutectic Si is more prone to crack nucleation than other hard inclusions as, on surface, eutectic Si is the only hard inclusion identified at a crack nucleation site. If such an assumption is true, several reasons may be proposed:

- (1) Volume fraction of eutectic Si is larger than that of other hard inclusions.
- (2) In unmodified alloy, the morphology of Si phase is coarse (Barrirero et al., 2013) (Gruzleski et al., 1990). The studied material is not strongly Sr modified, and the thickness of eutectic Si is smaller than other hard inclusions according to 2D characterization in Chapter 3. Thus eutectic Si is more likely to generate stress concentration.
- (3) Eutectic Si is more fragile than other hard inclusions.
- (4) Thanks to high Mn content in the studied material, the content of the more harmful  $\beta$  phase is reduced and the morphology of  $\alpha$  phase is refined (Dinnis et al., 2006) (Taylor, 2004).

However, one cannot confirm this assumption as only two specimens, i.e. Specimen F3 and F4, were studied using 3D in-situ fatigue tests. If more specimens were tested, other hard inclusions on surface might have been observed to be crack nucleation site.

No cracks initiate at slip bands or grain boundaries. The studied material is manufactured at slow cooling rate (LFC) and is not strongly Sr modified. Thus:

- 1) Hard inclusions have coarse microstructures that are apt to induce stress concentration.
- 2) In coarse microstructure, the image stress is dominated by the interaction between dislocations and cell (a cell consisting of an  $\alpha$ -Al secondary dendrite arm, eutectic Si-particles and Fe-rich intermetallic particles) boundaries rather than by the interaction between dislocations and grain boundaries (Wang et al., 2001b).
- 3) Large pores, which are present in the studied material, give enough stress concentration for cracks initiation at hard inclusions.

For the above reasons, **cracks initiation at hard inclusions in the areas where there is a high enough stress concentration, rather than at slip bands and grain boundaries, is the mechanism for cracks initiation in the LFC 319 alloy.**

The mechanisms of crack initiation in LCF discussed above also provide more convincing evidences for tensile damage mechanisms of A319 LFC alloy, which were discussed in §5.2.3.2, because:

- Mechanisms of cracks initiation in tensile stage of the 1<sup>st</sup> fatigue cycle is just tensile damage mechanisms (Specimens F2, F3 and F4).

## Chapter 5 Damage mechanisms in Al-Si alloys

---

- Si phase that was not revealed in 3D tensile tests using lab-CT was revealed in 3D fatigue test using SR-CT.

Cracks initiations were observed in tensile stage at hard inclusions close to pores in Specimens F3 and F4, and at Si phase at specimen edge in Specimen F4. Thus cracks initiation in tensile loading can also be ascribed to hard inclusions including eutectic Si, iron intermetallics and copper containing phases in the areas where there is enough stress concentration.

### ✓ Crack propagation

**Once cracks have initiated, they propagate along hard inclusions including Si phase, iron intermetallics, copper containing phases,** on surface (Specimens F1 and F2) and in volume (Specimens F3 and F4). Cracks propagations along hard inclusions can be ascribed to strain localizations at hard inclusions (e.g. in Figure 5-53). Strain localizations were indeed observed in areas where cracks propagations were observed in following cycles (e.g. in Figure 5-41 ~ Figure 5-43 for 2D fatigue tests, and in Figure 5-54 and Figure 5-55 for 3D fatigue tests).

Figure 5-59 compares equivalent Von Mises strain field<sup>2</sup> from DVC and PEEQ (equivalent cumulative plastic strain, c.f. Appendix II) field from FE simulation. In strain field from DVC, strain localizations are observed at hard inclusions at the 2<sup>nd</sup> cycle. Then they extend with cyclic loading (from (a) to (b)). Due to the limited resolution of tomographic images, it is impossible to know if there are microcracks at these strain localizations areas. However, the propagation of large cracks and final failure went through the areas where strain localizations are marked by circles. Thus the relation between strain localizations at hard inclusions and cracks propagation and final failure are observed. In equivalent cumulative plastic strain field from FE simulation, strain localizations are only observed in the areas around pores where strain localizations are also observed in strain field from DVC. They cannot be observed at hard inclusions from FE simulation based on a porous model. This indicates that hard inclusions have an important influence on strain distribution.

---

<sup>2</sup> The equivalent von Mises strain in 3D is defined as  $\varepsilon^e = \frac{\sqrt{2}}{3} \sqrt{(\varepsilon_1 - \varepsilon_2)^2 + (\varepsilon_2 - \varepsilon_3)^2 + (\varepsilon_1 - \varepsilon_3)^2}$ , where  $\varepsilon_1$ ,  $\varepsilon_2$  and  $\varepsilon_3$  are the principal strains.

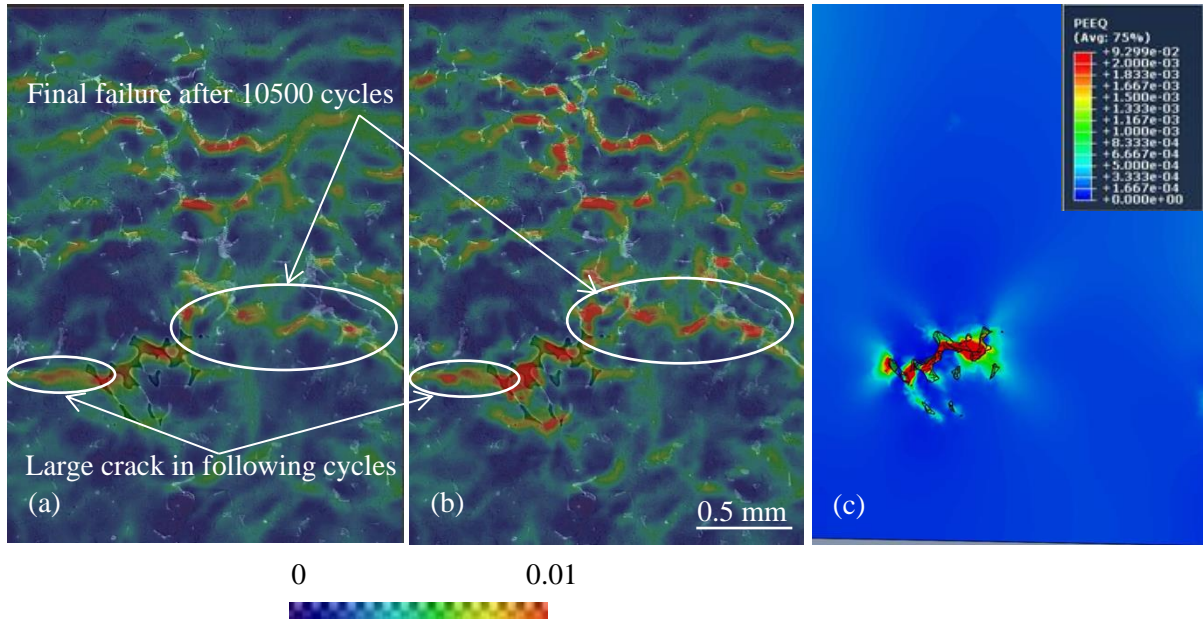


Figure 5-59 Equivalent Von Mises strain field from DVC: correlation between the minimum loading of 1st cycle and the maximum loading of (a) 2<sup>nd</sup> cycle and (b) 20<sup>th</sup> cycle. (c) PEEQ field (after 3 cycles) from FE simulation. (Slice shown is about 680  $\mu\text{m}$  below the flat surface of Specimen F4)

More eutectic Si than iron intermetallics or copper containing phases was observed in crack propagation path. Besides the four possible reasons previously discussed for the assumption that eutectic Si is more prone to crack nucleation than other hard inclusions, there is a fifth possible reason: eutectic Si is extended to the whole volume while copper containing phases form less extended networks.

The influence of Pb particles on crack propagation was never observed. Thus it can be concluded satisfactorily that: Pb particles being an impurity in the studied material has no influence on fatigue damage in LCF.

### ✓ Final fracture

Although in-situ observations cannot follow cracks in final fast fracture areas, postmortem analysis using SEM on flat surfaces shows that final fracture is also more likely to be along hard inclusions. Displacement discontinuities and strain localizations in the last step before failure are indeed observed along hard inclusions in the final fast fracture area (Figure 5-7, Figure 5-45, Figure 5-52 and Figure 5-55). Thus final fracture is easier to occur at hard inclusions due to larger strain localization.

The fact that hard inclusions provide an easy path for crack propagation and final fast fracture was verified by chemical composition analysis using EDS in three different types of regions for each fractured half specimen: (1) the region where cracks initiate and propagate on fracture surface (c.f. Appendix VI), (2) the whole fracture surface, (3) arbitrary regions on flat surfaces. Each element can be correlated to specific constituents of the alloy. The main elements that we are concerned with are:

## Chapter 5 Damage mechanisms in Al-Si alloys

---

- Al- the matrix of material;
- Si- associated to Si phase;
- Fe / Mn- associated to iron intermetallics;
- Cu- associated to Al<sub>2</sub>Cu and AlCuMgSi phases;
- Mg- associated to AlCuMgSi phase.

Comparison of chemical compositions between fracture surfaces and flat surfaces (Table 5-6) shows that the content of Mg, Si, Fe, and Cu is higher in the fracture surfaces than elsewhere in the specimen. It implies that cracks and final fracture are more prone to occur at Si phase, iron intermetallics, Al<sub>2</sub>Cu and AlCuMgSi phases than in Al dendrites. Thus it is consistent with previous observations. However, the different areas on the fracture surface have similar chemical compositions (c.f. Appendix VI). This indicates that hard inclusions play the same important roles whether in cracks initiation during tensile stage, cracks propagation and final fast fracture.

Table 5-6 Ratios of elements mass fraction on fracture surface and on flat surface

Elements	Mg	Si	Fe	Cu
Ratios ( $\frac{\text{mass fraction on fracture surface}}{\text{mass fraction on flat surface}}$ )	2~7	2~3	3~5	2~7

### ✓ **Damage mechanisms of hard inclusions**

Comparisons of X-ray mapping performed on each fracture surface of the same specimen (c.f. Appendix VI) allow identifying whether the damage mechanisms of hard inclusions is decohesion or fracture:

- (1) More fracture than decohesion is found in all fracture surfaces whether in cracks initiation region during tensile stage, cracks propagation regions and final fast fracture regions.
- (2) More decohesion is found in cracks propagations regions than in final fast fracture regions or in cracks initiation regions during tensile stage.
- (3) The above two points are observed for Si phase, iron intermetallics and copper containing phases.

In the literature (Gall et al., 1999) (Mbuya, 2011), hard inclusions are reported to be more likely to debond than fracture during cracks propagation. However, their morphology is also important to consider. Large and elongated particles whose major axis is parallel to the loading direction are said to preferentially fail via fracture while particles having round morphology on flat surface are more likely to debond. Besides a high enough matrix stress is required to break these hard particles.

## Chapter 5 Damage mechanisms in Al-Si alloys

---

In this study, the fractures of large and elongated particles whose major axis is parallel to the loading direction were indeed observed. The fact that more fracture than decohesion of hard inclusions was observed may be due to the following reasons:

- Our studied material is not strongly Sr modified, thus the morphology of Si is not fine.
- In LCF, i.e. in our study, a higher stress level is applied while a lower stress level is applied in HCF, i.e. in the above cited literature.
- Moreover, large pores, which are not present in the above cited literature, are present in LFC Al-Si alloy. These large pores yielded stress concentrations which are large enough to break hard particles nearby. This also indicates that large pores also have an important influence on cracks propagation by increasing the overall stress level.
- Even if Crack 1 in Specimen F4 is far from large pores, it is located at a specimen edge that induces enough stress concentration to break particles.

Besides, if more decohesion is found in crack propagation regions this may be due to the average stress level that is lower in crack propagation stage than in final fast fracture stage.

### 5.4 Summary

Damage mechanisms of A356 LFC alloy in tension and A319 LFC alloy in tension and in LCF tests were revealed using the coupling of experimental methods. First, the developed experimental protocol is evaluated according to its application in this study, and then, the damage mechanisms are summarized.

#### 5.4.1 Experimental protocol

Tensile and fatigue tests with in-situ observation on surface were performed using Questar microscope. However, a preliminary 3D characterization of pores using X-ray CT is necessary to select ROI and to analyse the relation between damage mechanisms on surface and pores below surface. 2D in-situ tests allow cracks initiations and propagations being followed on surface in real time with a higher resolution than 3D in-situ observations. They also allow more representative large specimens and standard testing machines being adopted.

Tensile and fatigue tests with in-situ observation in volume were performed using X-ray tomography. They allow cracks initiation and propagation being revealed directly in 3D and thus allow the damage mechanisms being understood thoroughly, although they have a lower resolution than 2D in-situ observations. Compared with Lab-CT, SR-CT has a much shorter scan time and can reveal Si phase



## Chapter 5 Damage mechanisms in Al-Si alloys

---

thanks to phase contrast although segmentation of microstructure constituents and 3D cracks is difficult due to the too strong phase contrast.

Field measurements were performed using DIC/DVC on the obtained 2D/3D images. The relations between microcracks and final fracture and displacement discontinuities and strain localization in the measured fields are indeed observed. The results from DIC/DVC provide convincing evidences to explain the damage mechanisms.

FE simulation based on tomographic images was efficiently used to select ROI and to study the influence of pores on strain distribution. However, a complex FE mesh model representing pores, Al matrix and various hard inclusions is proposed to study the influence of hard inclusions in future work.

Postmortem analyses were performed using optical microscope, SEM and EDS on flat surfaces and fracture surfaces. They helped identifying final failure, microcracks, microstructure constituents, crack initiation site and also damage mechanisms of hard inclusions.

### 5.4.2 Damage mechanisms

#### 5.4.2.1 A356 LFC alloy

- Under tensile loading, cracks initiate from pores when an enough local stress level is reached. A large size, a surface pore or a small distance between pore and free surface are more prone to crack nucleation.
- Cracks may propagate along hard inclusions, i.e. eutectic Si and iron intermetallics, due to the increasing stress concentration at hard inclusions at increasing monotonic loading.

#### 5.4.2.2 A319 LFC alloy

##### ✓ Tensile damage mechanisms

- Cracks initiate at hard inclusions in the areas with sufficient stress concentrations. These stress localizations are mainly provided by large pores. However, in areas without large pores, a specimen edge was also observed to provide enough stress concentration for crack nucleation.
- In the same way as for A356 alloy, a large size, a surface pore or a small distance between pore and surface promote crack nucleation. The shape of pore has also an important influence on strain distribution.

## Chapter 5 Damage mechanisms in Al-Si alloys

---

- Cracks grow along hard inclusions including eutectic Si, iron intermetallics and copper containing phase, at increasing monotonic load
- ✓ **Fatigue damage mechanisms**

The essence of damage mechanisms can be summarized as:

- Cracks initiate at hard inclusions in areas where there are enough stress concentrations. These stress concentrations can be due to large pores, corner of surfaces etc.
- Cracks propagations and final fast fracture are more prone to be at hard inclusions due to strain localizations around them.

The above mentioned hard inclusions consist in Si phase, iron intermetallics (both  $\alpha$  and  $\beta$  phases), and copper containing phases ( $\text{Al}_2\text{Cu}$  and  $\text{AlCuMgSi}$  phases). Cracks ‘select’ hard inclusions rather than Al matrix as they are more likely to generate stress concentrations. Indeed hard inclusions have higher elastic modulus and are more fragile than Al matrix and they have locally sharp morphologies.

Although cracks initiation at hard inclusions needs enough stress concentration, the following three conditions make it possible: (1) In LCF, global stress level is high; (2) Large pores increase local stress level severely; (3) In LFC and in a weekly Sr modified alloy, the coarse microstructure is prone to the generation of stress concentration. Therefore, other features, such as slip bands and grain boundaries, are not observed to be potential crack nucleation sites.

Pb, which is an impurity, has no influence on damage because it has low content and rather acts as ‘small pores’ due to its small size, individual object morphology, and low hardness.

More eutectic Si than iron intermetallics or copper containing phases were observed to act as crack nucleation site or crack propagation path due to the following possible reasons: (1) Higher volume fraction of eutectic Si than other hard inclusions; (2) Smaller thickness of eutectic Si than other hard inclusions is more likely to generate stress concentration; (3) Eutectic Si is more fragile than other hard inclusions; (4) Thanks to a high Mn content, the more harmful  $\beta$  phase is avoided and the morphology of  $\alpha$  phase is refined; (5) Eutectic Si has a network morphology that may extend to the whole studied volume, i.e. 3.7 mm, while copper containing phases are less extended.

Most cracks in the present study initiated at hard inclusions around large pores due to pore-induced stress concentration. Size, location, number and shape of pores are indeed observed to influence cracks initiation. Pores also influence crack propagation in LCF. They increase true stress level and thus affect the damage mechanisms of hard inclusions: more fracture than decohesion is observed.

Crack propagation at hard inclusions is driven by plastic strain localization caused by crack tip. These plastic zones were observed to present a shape of ‘Y’ in plane. The strain level in the area around crack tip, especially in the loading direction, was found to increase with crack propagation. The

## Chapter 5 Damage mechanisms in Al-Si alloys

---

orientation of hard inclusions has an influence on crack propagation along hard inclusions: (1) When it is the same as the direction of crack propagation, the crack is prone to propagate along hard inclusions; (2) When it is perpendicular to the direction of crack propagation, the crack is arrested.

If a crack is arrested by hard inclusions, the strain level in the area around crack tip, especially at some hard inclusions in the loading direction, increased dramatically. In the same time, the arrested crack spends more cycles to continue to propagate by the following two means: (1) Change its direction of propagation to the direction along hard inclusions; (2) Break hard inclusions and pass them. In addition, even if a crack does not propagate due to barriers, COD also increases with the cyclic loading.

In the final fast fracture stage, hard inclusions in the unbroken ligament are under a much higher stress level. Thus: (1) A large number of microcracks initiate at hard inclusions; (2) Less decohesions of hard inclusions are observed in this area than in the previous crack propagation stage.

## Chapter 6 Conclusions and future work

This thesis was proposed to study the influence of casting microstructure on the fatigue behavior in Lost Foam Cast (LFC) Al-Si alloys in Low Cycle Fatigue (LCF). Although the damage mechanisms in some Al-Si alloys have been studied in literature, the damage mechanisms in LFC Al-Si alloys, which have a much coarser microstructure and a shorter fatigue life time, were still unknown. An experimental protocol, that allows following cracks initiation and propagation both on surface and in volume and allows identifying the relation between damage mechanisms, casting microstructure and measured fields, has been developed.

First of all, it is of primary importance to reveal the microstructure of studied alloys. Optical Microscopy and Scanning Electron Microscope with Energy Dispersive X-ray Spectroscopy were used for 2D characterization. Laboratory (lab-CT) and synchrotron (SR-CT) X-ray tomography were used for 3D characterization. Measurements in 3D are usually more reliable than in 2D as objects that appear individual in 2D may be parts of one 3D object and even form large extended networks. A relatively appropriate parameter was selected for each constituent according to its 3D characterization in order to characterize the size of the microstructure. Although no matter which parameter is chosen, it does never allow a thorough characterization of all the parameters that are of known importance in fatigue. The selected parameters are:

- ♦ **Feret diameter:** Maximum Feret diameter better characterizes the size, i.e. longest dimension or “caliper” diameter, of individual objects but it cannot reflect the local shape, orientation and location of the individual objects
- ♦ **Granulometry:** Granulometry distribution better characterizes the size, i.e. local thickness, of interconnected phases but it cannot reveal the extent of interconnected microstructure.

As A319 alloy is the objective of this study, it was characterized thoroughly both in 2D and in 3D. Besides Al matrix, the microstructure revealed in A319 consists in:

- ♦ **Pores:** There are two types of pores, i.e. gas pores and shrinkage pores. They can be distinguished according to their morphologies: gas pores present approximately spherical morphologies in 2D and are rounded individual objects in 3D, while shrinkage pores present coral-like morphologies in 2D and are tortuous individual objects in 3D. Maximum Feret diameter is selected to characterize the size of pores. The majority pores have a Feret

## Chapter 6 Conclusions and future work

---

diameter greater than 400  $\mu\text{m}$  that is more than 10 times that of other constituents. The maximum size of pore is usually more than 1 mm. Thus pores are first assumed to be the most critical defects in the volume. A probabilistic thermal-mechanical fatigue criterion for LFC aluminum alloys, which has been initially developed based on 2D porosity distribution (Charkaluk et al., 2014), has been improved using the 3D characterization of pores performed in this thesis (Szmytka et al., 2014). Lab-CT and SR-CT can both be used to characterize pores but a large scan volume is recommended due to their large sizes.

- ◆ **Si:** Si phase presents a plat-like morphology in 2D but it forms highly interconnected networks in 3D that can extend to the whole scanned volume. Granulometry is recommended to characterize its size while SR-CT with phase contrast and a high resolution is necessary for its 3D characterization.
- ◆ **Iron intermetallics:** There are two types of iron intermetallics. The  $\alpha(\text{AlFeMnSi})$  phase has a higher Mn content than  $\beta(\text{AlFeSi})$  and presents a ‘Chinese script’ morphology. The  $\beta$  phase has less Mn content than  $\alpha$  and present a needle-like in 2D or plate-like in 3D morphology. Iron intermetallics form highly interconnected networks in 3D and may extend in the whole scanned volume due to the high Fe and Mn content in A319 alloy. This results in more ‘Chinese script’  $\alpha$  phase than platelet  $\beta$  phase. Granulometry, which is chosen to characterize the size of this phase, shows that the majority of iron intermetallics have a thickness between 6 and 18  $\mu\text{m}$ . Lab-CT and SR-CT can both be used to characterize iron intermetallics but a high resolution is recommended.
- ◆ **Copper containing phases:**  $\text{Al}_2\text{Cu}$  and  $\text{AlCuMgSi}$  phases were revealed in 2D and the later presents densely punctate morphology and is usually around the former. However,  $\text{AlCuMgSi}$  phase was not revealed in 3D due to its small size (thickness < 1  $\mu\text{m}$  in 2D) and due to the present resolution of 3D characterization (1 pixel = 1.5  $\mu\text{m}$ ).  $\text{Al}_2\text{Cu}$  phase presents complex structures in 3D that are less extended than Si and intermetallics. Granulometry is also selected to characterize the size of Cu rich phases and most of the  $\text{Al}_2\text{Cu}$  phase has a thickness between 6 and 18  $\mu\text{m}$ . Lab-CT and SR-CT can both be used to characterize  $\text{Al}_2\text{Cu}$  and  $\text{AlCuMgSi}$  phases but a high resolution is recommended especially for  $\text{AlCuMgSi}$  phase.
- ◆ **Pb:** Pb presents small points morphology in 2D that correspond to individual objects in 3D. Thus Feret diameter is selected to characterize the size of Pb particles, and the majority of Pb particles have a maximum Feret diameter between 18 and 60  $\mu\text{m}$ . Considering their sizes, morphologies and mechanical properties, Pb particles can be compared to ‘small pores’. Although Lab-CT and SR-CT can both allow characterizing Pb, a high resolution is required due to the small size of particles as well as a large scan volume due to its low volume fraction (< 0.2%).



## Chapter 6 Conclusions and future work

---

A319 alloy has a volume fraction of natural tracers (microstructure constituents) about 10 times higher (in the case of Lab-CT) than A356, in particular it has eutectic Al-Al<sub>2</sub>Cu phase that is not present in A356 alloy.

The developed experimental protocol was first validated in tensile tests and was then applied in fatigue tests. Although some of the experimental methods have been used in literature, this is the first time that they were coupled in one study. The two types of in-situ tests developed have their own characteristics:

- ◆ **2D in-situ tests:** Using Questar long distance microscope allows following cracks initiations and propagations on surface in real time with a higher resolution than with 3D in-situ observations. More representative large macro specimens and large standard testing machines can be adopted. A preliminary 3D characterization of pores using X-ray CT is necessary to select ROI and to analyse the relation between damage mechanisms on surface and pores below surface.
- ◆ **3D in-situ tests:** Using X-ray tomography allows revealing cracks initiations and propagations directly in bulk and thus allows understanding the damage mechanisms thoroughly. Compared with Lab-CT, SR-CT has a much shorter scan time and can reveal Si phase thanks to phase contrast although it is difficult to segment the microstructure constituents and 3D cracks due to the too strong phase contrast.

**Field measurements** were performed using Digital Image Correlation (DIC)/Digital Volume Correlation (DVC). In 2D, a developed etching solution gives a natural texture to the aluminum dendrites by revealing segregation of Si, which is necessary to make DIC feasible to an acceptable resolution without adding a speckle pattern that will also mask the microstructure. In 3D, the dispersed microstructure constituents in the volume of material revealed by Lab/SR-CT are used as natural tracers for DVC. The stress-strain curves deduced from DIC/DVC can be considered reliable by comparing with that from standard tests. The relations between damage evolutions, i.e. microcracks, crack propagation path, and final fracture, and displacement discontinuities conducting/associated to strain localizations in the measured fields from DIC/DVC are indeed observed. These relations provide convincing evidences to explain the damage mechanisms.

**FEM simulations** based on models representing pores and solid matrix were efficiently used to select ROI and to study the influence of pores on strain distributions both in monotonic and cyclic loading.

**Post-mortem analyses** using OM, SEM and EDS on flat surfaces and fracture surfaces are useful for identifying final failure locations, microcracks, microstructure constituents, crack initiation site and for analysing damage mechanisms of hard inclusions.

## Chapter 6 Conclusions and future work

---

The tensile and fatigue damage mechanisms of studied alloys were revealed using the experimental protocol developed in this thesis:

### **Tensile Damage mechanisms of A356 and A319 LFC alloys:**

- ◆ In A356 LFC alloy, cracks nucleate from pores when an enough local stress level is reached. A large size, a surface pore or a small distance between pore and free surface promote crack initiation. In A319 LFC alloy, cracks nucleate at hard inclusions in areas with sufficient stress concentrations, which are mainly provided by large pores but also by a specimen edge in areas without large pores.
- ◆ In both LFC alloys, cracks may propagate along hard inclusions, i.e. eutectic Si and iron intermetallics and also copper containing phases in A319 alloy, due to the increasing stress concentration at hard inclusions with increasing loading.

### **Fatigue Damage mechanisms of A319 LFC alloy:**

- ◆ Cracks nucleate at hard inclusions in areas where there are enough stress concentrations. These stress concentrations can be due to large pores, corner of specimen etc.
- ◆ Cracks propagate through hard inclusions. The strain localizations were observed at hard inclusions even without cracks, thus we may suppose cracks propagations occur at hard inclusions due to strain localizations.

The above mentioned hard inclusions include Si phase, iron intermetallics (both  $\alpha$  and  $\beta$  phases), and copper containing phases ( $Al_2Cu$  and  $AlCuMgSi$  phases). Cracks 'select' hard inclusions rather than Al matrix as stress concentrations are more likely to occur in the Al matrix around them. Indeed hard inclusions have higher elastic modulus and are more brittle than Al matrix and they have locally sharp morphologies.

Three conditions provide enough stress concentration, which is necessary for crack nucleation at hard inclusions: (1) High global stress level in LCF; (2) Large pores increase local stress level severely; (3) Stress concentrations are more prone to be generated due to the coarse microstructure in LFC and in a weakly Sr modified alloy.

In literature, cracks are usually reported to initiate from pores in Al-Si alloys when large pores are present. In this thesis, cracks nucleate at hard inclusions while the influence of pores is to generate enough stress concentration. According to author's knowledge, this is the first time that damage mechanisms of Al-Si alloy in LCF were revealed.

Due to pore-induced stress concentration, most cracks in the present study nucleated at hard inclusions around large pores. Size, location, number and shape of pores have influence on cracks

## Chapter 6 Conclusions and future work

---

initiation. Pores also have influence on crack propagation in LCF through increasing true stress level that results in more fracture than decohesion of hard inclusions. Hence the control of pores in alloy should be paid much attention in the following LFC process.

Thanks to its low content, small size, individual object morphology, and low hardness, Pb has no influence on damage. More eutectic Si than iron intermetallics or copper containing phases were observed to act as crack nucleation site or crack propagation path. Crack propagation at hard inclusions is driven by plastic strain localization caused by crack tip. These plastic zones present a shape of 'Y' in plane. The orientation of hard inclusions has an influence on crack propagation: (1) When it is the same as the direction of crack propagation, the crack is prone to propagate along hard inclusions; (2) When it is perpendicular to the direction of crack propagation, the crack is arrested. For the latter case, strain level in the area around crack tip, especially at some hard inclusions in the loading direction, increased dramatically. In the same time, the arrested crack spends more cycles to continue to propagate by changing the direction of propagation to the direction along hard inclusions or by breaking hard inclusions to pass them. In addition, even if a crack does not propagate due to barriers, Crack Opening Displacement goes on increasing with the cyclic loading.

In the final fast fracture stage, hard inclusions in the unbroken ligament are under a much higher stress level that leads to a large number of microcracks initiations at hard inclusions and less decohesions than in the previous crack propagation stage.

The following possible directions are proposed for **future work**:

- ◆ More specimens should be studied to confirm the damage mechanisms observed as only two fatigue tests specimens with 3D in-situ observation were presented.
- ◆ A FE model representing pores, Al matrix and various hard inclusions could help to verify strain localizations at hard inclusions and to reveal the influence of different hard inclusions on strain localizations, such as the difference between strain localizations at eutectic Si and at other hard inclusions.
- ◆ The studied material in this study is not strongly Sr modified, and more eutectic Si than other hard inclusions is found to act as crack nucleation site and crack propagation path. Thus the damage mechanisms of A319 alloys modified with higher Sr content (Z. Li, PhD thesis (2013-2016) at LML) could be studied using this experimental protocol. In this case eutectic Si may no longer be the most critical hard inclusion for crack initiation and propagation.
- ◆ If the size, location, number of pores could be controlled in a specimen, the influence of the different parameters of pores on damage mechanisms could be studied. This is one of the objectives of ongoing PhD thesis (2013-2016) at LML (Z. Li, N. Dahdah). To achieve this

## Chapter 6 Conclusions and future work

---

goal, the first step is to elaborate specimens with a controlled microstructure by precision casting and then the cast specimen will be tested in fatigue without any machining.

- ◆ Larger size specimens, which are more representative for the material, could be studied under 3D in-situ fatigue tests. This will allow studying damage mechanisms, in particular crack propagation, in specimens where the defect size is more reasonable as regards the specimen size. For this study, the specimen cross section had an area of about 4.5 mm<sup>2</sup>. In the next experiments, the cross-section will be 12 mm<sup>2</sup> for the same voxel size.
- ◆ As the operating temperature of cylinder heads is 150 – 200 °C, it is necessary to study the damage mechanisms at higher temperatures using the experimental protocol developed in this thesis. This is the object of a following PhD thesis (2013-2016) at LML (N. DAHDAH).

# Appendix

## Contents

---

<b>Appendix I Digital image processing and analysis.....</b>	<b>- 185 -</b>
I.1 Digital image processing fundamentals.....	- 185 -
I.1.1 Filters .....	- 185 -
✓ Median filter.....	- 185 -
✓ Anisotropic diffusion filter.....	- 185 -
I.1.2 Binning .....	- 186 -
I.1.3 Image segmentation.....	- 186 -
✓ Segmentation of laboratory tomography images .....	- 186 -
✓ Segmentation of synchrotron tomography images.....	- 187 -
✓ Phase segmentation test .....	- 188 -
I.1.4 Morphological image processing.....	- 191 -
✓ Eroding.....	- 191 -
✓ Dilation .....	- 192 -
✓ Opening.....	- 192 -
✓ Closing .....	- 193 -
I.2 DAS measurements in 3D rendered image.....	- 193 -
<b>Appendix II FEM simulations .....</b>	<b>- 195 -</b>
II.1 Mesh model .....	- 195 -
II.2 FE calculations .....	- 196 -
II.2.1 Application in tensile test .....	- 196 -
II.2.2 Selection of ROI for fatigue tests with 3D observations .....	- 197 -
II.2.3 Comparisons with DVC results of fatigue tests .....	- 197 -
<b>Appendix III Selections of specimen and ROI .....</b>	<b>- 198 -</b>
III.1 Tensile tests with 2D in-situ observations .....	- 198 -
III.1.1 Specimen T1 .....	- 198 -
III.1.2 Specimen T2 .....	- 199 -
III.2 Tensile tests with 3D in-situ observations: Specimen T3 .....	- 199 -
III.3 Fatigue tests with 2D in-situ observations .....	- 200 -



# Appendix

---

III.3.1 Specimen F1.....	- 200 -
III.3.2 Specimen F2.....	- 202 -
III.4 Fatigue tests with 3D in-situ observations .....	- 204 -
III.4.1 Specimen F3.....	- 204 -
III.4.2 Specimen F4.....	- 205 -
<b>Appendix IV Field measurements .....</b>	<b>- 207 -</b>
IV.1 Principles of 2D/3D image correlation platform at LML .....	- 207 -
IV.2 Examples of parameters for Elastix software .....	- 208 -
<b>Appendix V Crack length measurements in 2D .....</b>	<b>- 212 -</b>
<b>Appendix VI Fracture analysis using SEM-EDS.....</b>	<b>- 213 -</b>
VI.1 Specimen F1 .....	- 214 -
VI.2 Specimen F2 .....	- 215 -
VI.3 Specimen F3 .....	- 216 -
VI.4 Specimen F4 .....	- 218 -

---

## Appendix I Digital image processing and analysis

### I.1 Digital image processing fundamentals

#### I.1.1 Filters

##### ✓ Median filter

Median filter is a simple edge-preserving smoothing filter, which works by sorting pixels covered by an  $N \times N$  ( $N=3$  in the present work) mask according to their gray value. The center pixel is then replaced by the median of these pixels, i.e., the middle entry of the sorted list (Gonzalez and Woods, 2007). An example to illustrate the principle of median filter is shown in Figure I-1.

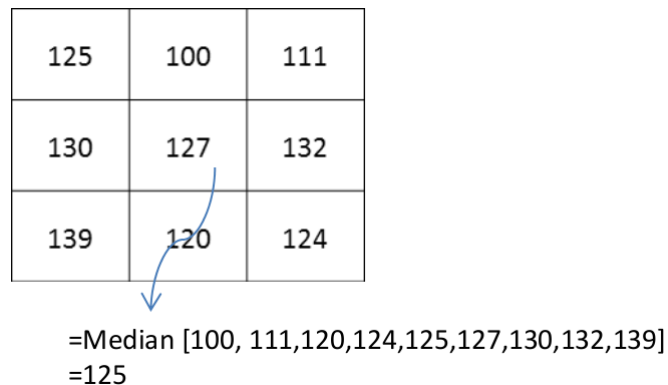


Figure I-1 Principle of median filtering

##### ✓ Anisotropic diffusion filter

Anisotropic diffusion filter works effectively to preserve edges and enhance their contrast. The algorithm compares the value of the current voxel with the value of its 6 neighbors in order to determine the new value for the current voxel. If the difference does not exceed the diffusion stop criterion, there is diffusion (ZIB et al, 2012). An example to illustrate the principle of anisotropic diffusion filter in 2D is shown in Figure I-2. The main parameters of filters selected for Specimen 1 and 2 in chapter 3 are listed in Table I-1.

## Appendix

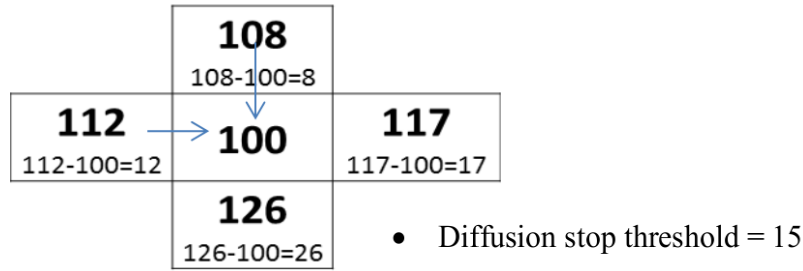


Figure I-2 Principle of anisotropic diffusion filtering

Table I-1 Main parameters of filters selected for Specimen 1 and 2 in chapter 3

Filter	Parameters	Specimen1 (Laboratory tomography image)	Specimen1 (synchrotron tomography image)	Specimen2
Median	Kernel	3	3	3
Anisotropic Diffusion	Diffusion stop threshold	15	5	5

### I.1.2 Binning

The procedure of binning combines a cluster of voxels (herein,  $2 \times 2 \times 2$  voxels) into a single larger voxel, whose gray value is the average of the original cluster. An example to illustrate the procedure of binning in 2D is presented in Figure I-3. The original image size of Specimen 3, i.e.  $800 \times 900 \times 1300$  voxels (1pixel =  $1.7 \mu\text{m}$ ), is reduced to  $400 \times 450 \times 650$  voxels (1pixel =  $3.4 \mu\text{m}$ ) after binning.

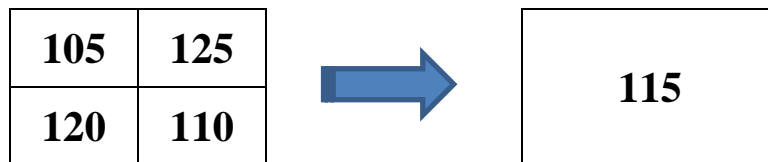


Figure I-3 Procedure of binning

### I.1.3 Image segmentation

#### ✓ Segmentation of laboratory tomography images

The segmentation of the different phases or constituents from laboratory tomography images realized by simple grayscale thresholding directly, and the threshold ranges selected for the different phases in specimens in chapter 3 are listed in Table I-2.

Table I-2 Threshold ranges of the different phases in all the specimens

Specimen	Pore	Intermetallics	$\text{Al}_2\text{Cu}$	Pb
Specimen 1	1-62	104-177	178-252	253-256
Specimen 2	0-20	75-120	121-170	171-256
Specimen 3	0-137	180-255	-	-

# Appendix

---

## ✓ Segmentation of synchrotron tomography images

As presented in § 3.2.4.1, a series of pre-treatment methods for the synchrotron tomography images are necessary to solve the segmentation problems due to the strong phase contrast. At first, it must be noted that these pre-treatment methods are not always consistent in details for all the images, and it depends greatly on the specific image and the operator's experiences. The basic morphological image processing method used here could be found in Appendix I.1.4. This basic process can be summarized as shown in Figure I-4:

- ◆ **Step (a) and (b):** A stronger filter is performed on the original image in order to highlight the morphologies of the pores although this operation makes other areas become blurred and even cover up the other constituents. (see Figure I-4 (a) and (b))
- ◆ **Step (c):** The pores are segmented roughly although some zones in the pores having the same grey values as other constituents are not segmented and/or some zones outside the pores are segmented. (see Figure I-4 (c))
- ◆ **Step (d) and (e):** Then opening\closing operations are performed on the segmented pores until the voids in the pores are added to the segmented pores and the noise segmented outside the pores in the previous step is deleted. (see Figure I-4 (d) and (e))
- ◆ **Step (e):** By comparing with the original tomography image, a slight erosion/dilation operation may be performed on the segmented pores until the morphologies of segmented pores are closest to the real morphologies in the original tomography image. Herein, the segmentation of pores is finished. (see Figure I-4 (e))
- ◆ **Step (f) and (g):** The image of segmented pores with the pore color set to 0 is then used as a mask for the original tomography image, thus the zones inside the pores having the same grey values as Al-Si eutectic and Al matrix are deleted and the segmentation of Al-Si eutectic could be performed as usual. (see Figure I-4 (f) and (g))
- ◆ **Step (h) and (i):** The erosion/dilation operation are again performed on the image of segmented pores until the bright contrast around the pores are just added to the segmented pores. Thus the enlarged zones of pores just cover the bright contrast around the pores and the image obtained is then used as a mask for the original tomography image. The zones with bright contrast around the pores having the same grey values as iron intermetallics and Al<sub>2</sub>Cu phase are deleted and the segmentation of intermetallics and Al<sub>2</sub>Cu phase could be performed as usual. (see Figure I-4 (h) and (i))

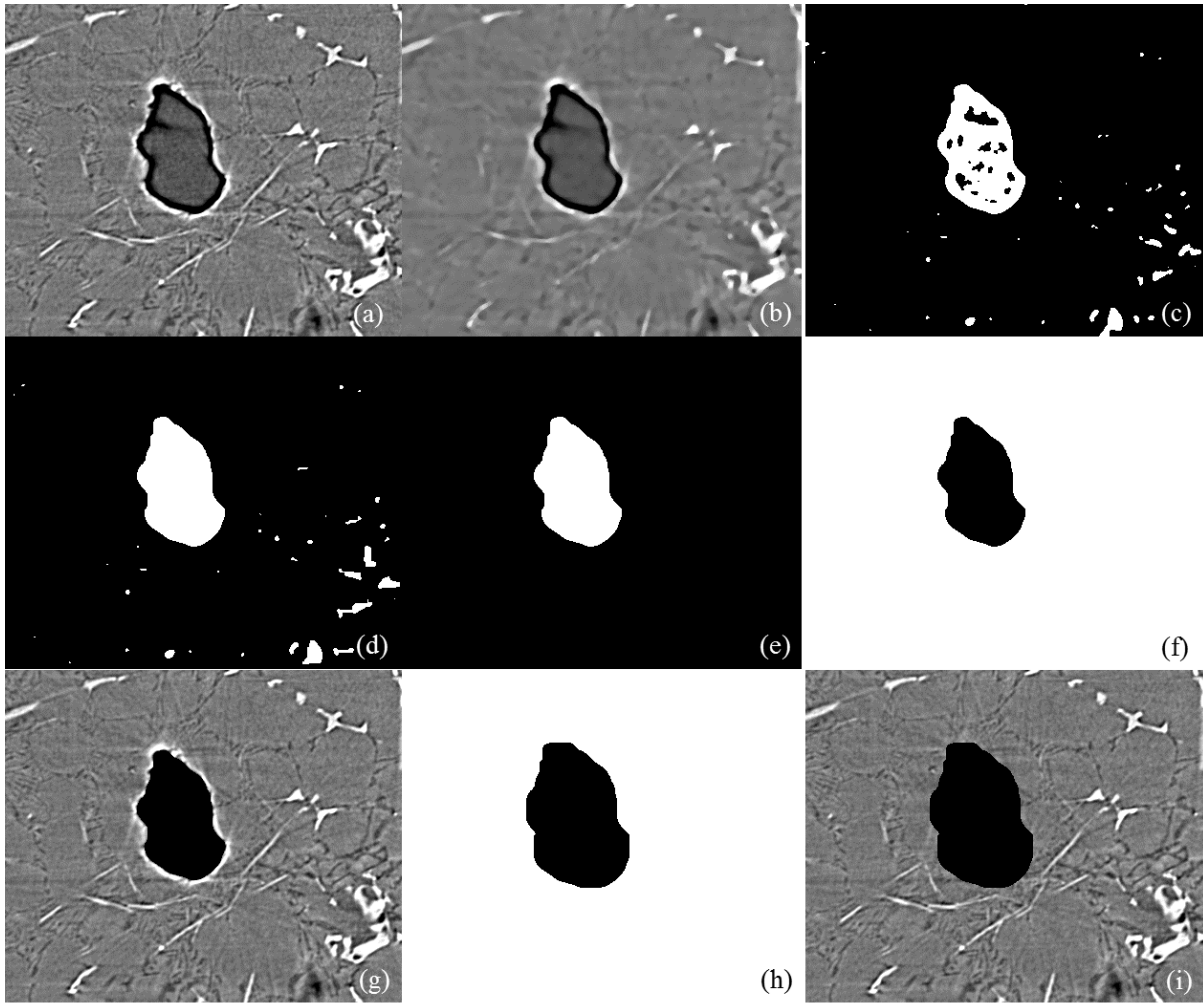


Figure I-4 Pre-treatment methods for SR-CT images: (a) original image; (b) a strong filter is performed on image (a); (c) the roughly segmented image from image (b); (d) a closing operation is performed on image (c); (e) an opening operation is performed on image (d) and the segmentation of porosity is finished; (f) invert color of image (e) to obtain a mask; (g) the original image (a) covered by the mask (f) in order to segment Si; (h) erosion/dilation operation performed on the mask (f) to enlarge the pores and cover the bright contrast around the pores; (i) the original image (a) covered by the mask (h) in order to segment iron intermetallics and Al<sub>2</sub>Cu phases

### ✓ Phase segmentation test

Preliminary segmentation test was performed for the intermetallics in the laboratory tomography image of Specimen 1 in chapter 3 in order to study the influence of the selected threshold interval on the results. 104-177 (Best choice, according to the user) was selected as a threshold interval that slightly under estimates the intermetallics while 102-182 (upper bound in Table I-3) leads to an over estimation, and 106-177 (lower bound in Table I-3) to an under estimation. The analyses were performed for the three threshold intervals separately.

The results of the segmentations tests (see Table I-3 and Figure I-5) show that the threshold interval selected at the segmentation step has a huge influence on the results in particular for the intermetallics



## Appendix

phase. When a larger range of thresholds (102-182) is selected, more objects are detected compared with the standard segmentation (104-177), which is considered as the best, as voxels belonging to other phases are selected. An example is shown in 3D rendering in Figure I-6: the object marked by a red arrow that is not present in the left image (standard segmentation) is present in the right (upper bound segmentation) as a larger range of threshold was selected. Besides, the objects marked by yellow arrows in the left image could be neglected as the volume of each object is less than 8 voxels but they could not be neglected in the right image because the volume of each object has grown to more than 8 voxels with the expansion of the threshold value range. However, the results also show that when a smaller range of thresholds (106-174) is selected, there are still more objects present compared with the standard segmentation as some intermetallics that are completely connected in the standard segmentation were disconnected in the case of lower bound segmentation. Figure I-7 shows an example: the part marked with a red arrow, which is part of a large object in the left image (standard segmentation), is disconnected with the large object and form a small independent object in the right image as a smaller range of threshold was selected. Hence more objects are revealed with the decreasing of the threshold.

Table I-3 Results of the segmentation tests on intermetallics

Range of thresholds	<i>106-174(lower bound)</i>	<b>104-177 (standard)</b>	<i>102-182(upper bound)</i>
Max Eq. diam. ( $\mu\text{m}$ )	883	<b>924</b>	992
Average Eq. diam ( $\mu\text{m}$ )	12	<b>13</b>	11
Max Feret diam. ( $\mu\text{m}$ )	2917	<b>2917</b>	2917
Average Feret diam. ( $\mu\text{m}$ )	23	<b>23</b>	19
Number of objects	18862	<b>18569</b>	24808
Volume fraction (%)	6.52	<b>7.36</b>	8.49

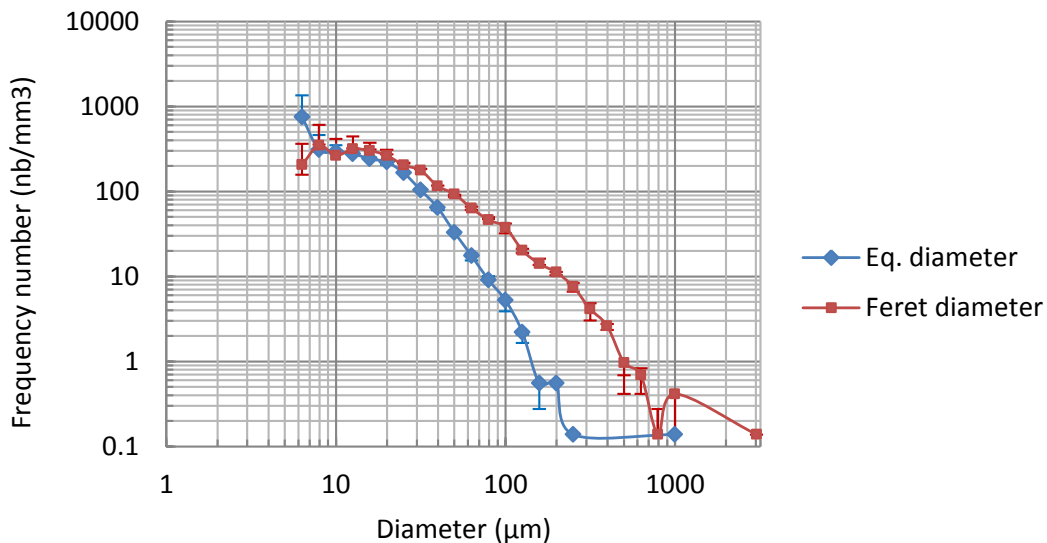


Figure I-5 Distributions of intermetallics as functions of equivalent and Feret diameters

## Appendix

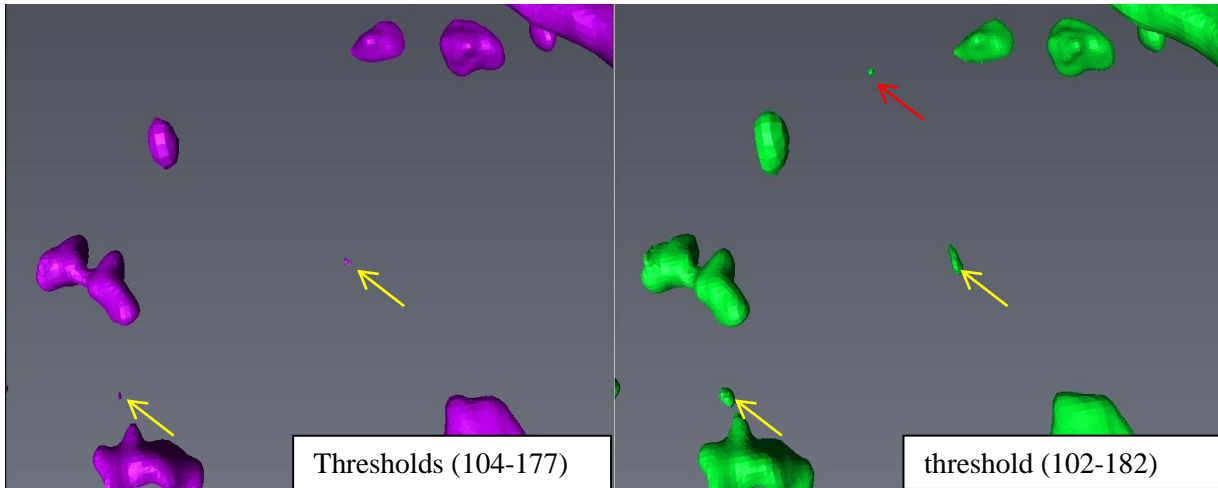


Figure I-6 Comparison of 3D renderings between standard threshold (104-177) (in the left, purple) and upper bound threshold (102-182) (in the right, green)

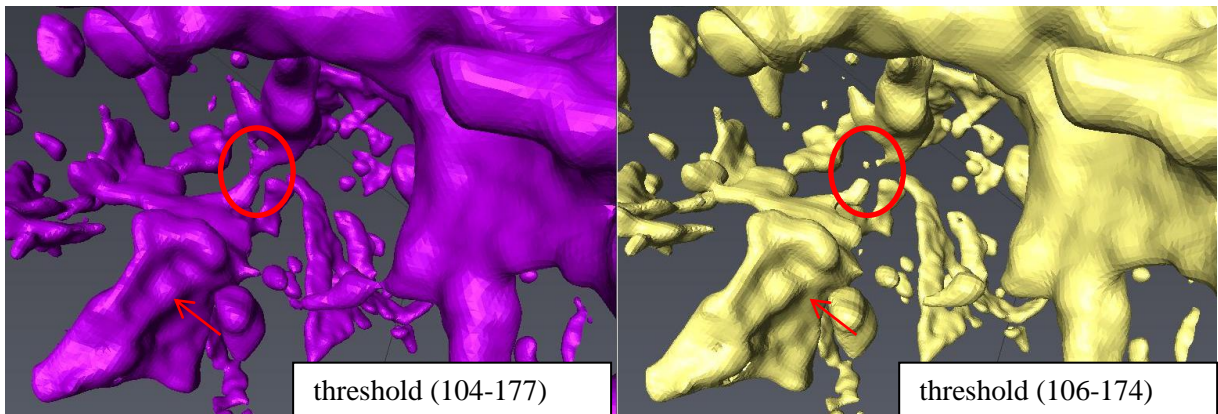


Figure I-7 Comparison of 3D renderings between standard threshold (104 -177) (in the left, purple) and lower bound threshold (106-174) (in the right, yellow)

The segmentation of intermetallics in the lab-CT image is made difficult by the limited contrast and spatial resolution. Figure I-8 illustrates this problem: the range of threshold that allows the intermetallic marked with a red circle in Figure I-8(a) to be completely selected is 99-150, but in this case a lot of other phases are also involved (see Figure I-8(b)). Even in the case of lower bound in Table I-3, some other phases are still involved. Thus, it is impossible to choose an ideal range of thresholds. The choice of the “best” or standard threshold range depends heavily on the operator’s “feeling”. The processing of tomography images is a process that heavily depends on operator’s experiences, such as in (Stein et al., 2006), (Motreff et al., 2010) and (Parra-Denis, 2007).

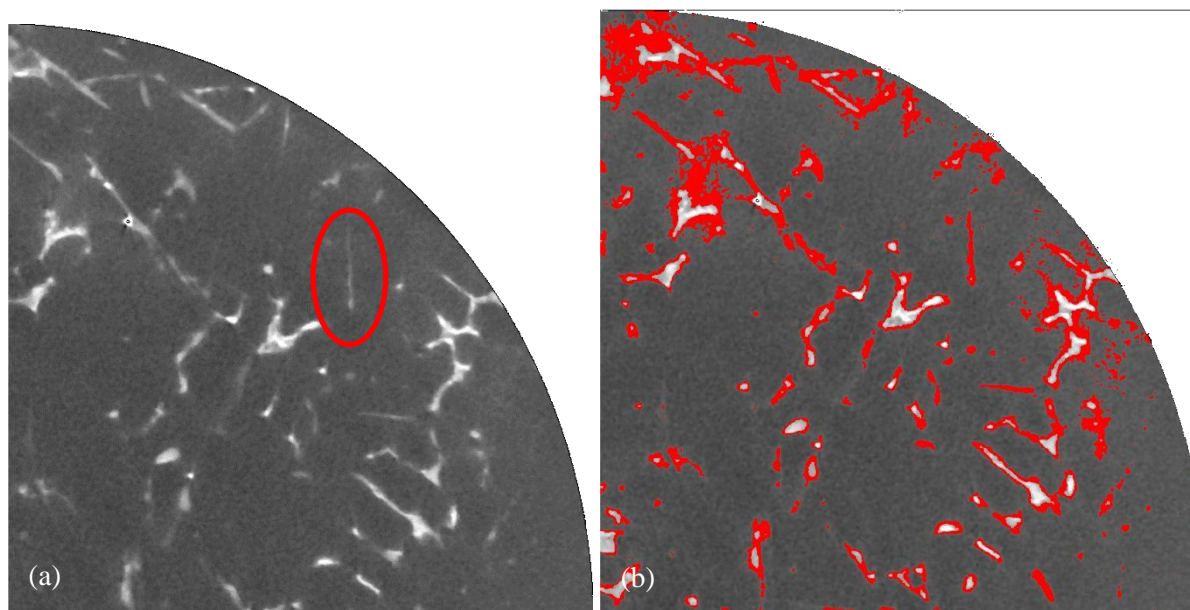


Figure I-8 Illustration of the problem of threshold range selection: the original image (a), the threshold range selected (99-150) are shown by red colour

Even in SR-CT image, this segmentation problem exists more or less, as segmentation boundary between intermetallics and  $\text{Al}_2\text{Cu}$  phases is difficult to determine. Besides, the influence of the bright phase contrast fringe around the porosity having the same grey level as intermetallics and  $\text{Al}_2\text{Cu}$  phases should also be noted. Although pre-treatment methods against this problem were proposed in Appendix I.1.3, some errors are bound to exist during this treatment process that depends on operator. Despite these disadvantages, a qualitative characterization of the 3D morphologies could be performed. Besides, as shown in the segmentation tests above, the error in the quantitative analysis remains limited.

### I.1.4 Morphological image processing

The basic morphological image processing methods used in this thesis, including eroding, dilation, opening operation and closing operation, are presented here in brief. For more details, please refer to (Gonzalez and Woods, 2007).

#### ✓ **Eroding**

When an eroding of  $N$  pixels is applied, it means the region with a width of  $N$  pixels inside the borders of initial objects will be eroded and will be replaced by the value of background. Figure I-9 shows one example of an eroding of 2 pixels: the white region inside the initial object is the object after eroding.

## Appendix

---

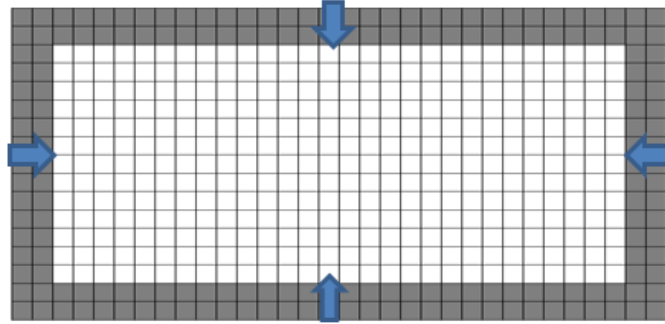


Figure I-9 Eroding of an object.

### ✓ Dilation

A dilation operator is the opposite operation of an eroding operation. When a dilation of  $N$  pixels is applied, the background region with a width of  $N$  pixels outside the borders of initial objects will be replaced by the value of the object. Figure I-10 shows one example of a dilation of 2 pixels : the white region is the initial object and the gray region around it will be added to the object after dilation.

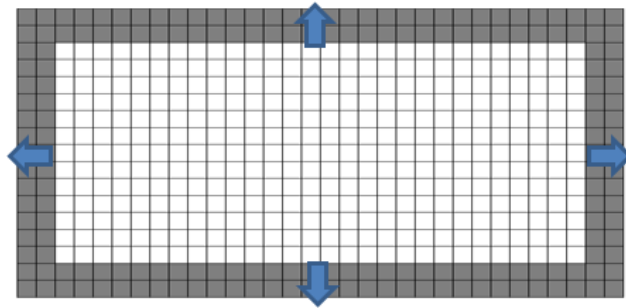


Figure I-10 Dilation of an object.

### ✓ Opening

Opening operation is performed by an eroding operation followed by a dilation operation. Figure I-11 shows an example of an opening operation of 1 pixel. The small objects are removed after opening operation.

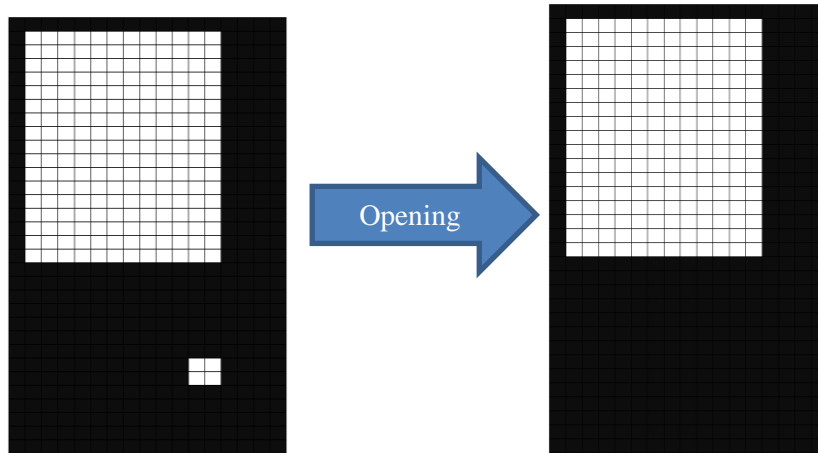


Figure I-11 Example of opening operation.

### ✓ Closing

Closing operation is performed by a dilation operation followed by an eroding operation. Figure I-12 shows an example of a closing operation of 1 pixel. The small holes are removed after closing operation.

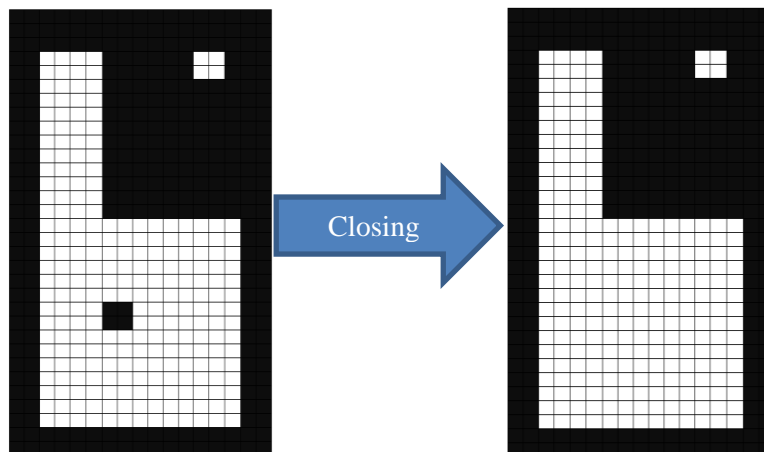


Figure I-12 Example of closing operation.

## I.2 DAS measurements in 3D rendered image

Some measurements of Dendrite Arm Spacing (DAS) (Charbonnier, 1992) were performed in chapter 3 directly in the 3D rendering of pores as shown in Figure I-13. The dendrite arm tips that impinged on the pore surface have left a print so that it is possible to measure the DAS. The distance between several secondary arms was measured, and the DAS in one measurement was obtained by calculating the average distance between two adjacent secondary arms. 6 measurements were performed in Specimen 2 in order to compute an average DAS.



## Appendix

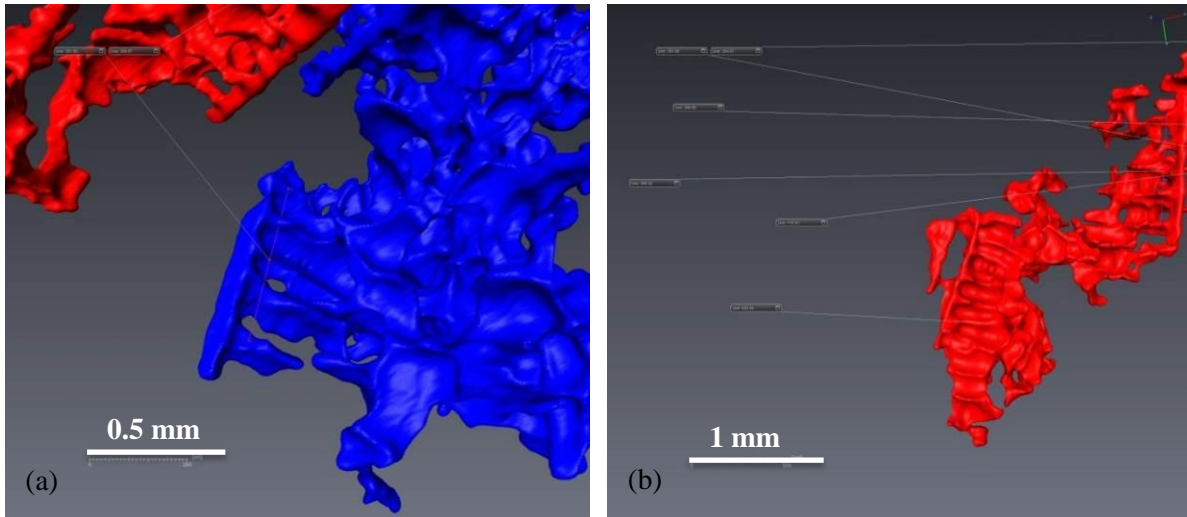


Figure I-13 Examples of Dendrite Arm Spacing (DAS) measurements performed in 3D rendering of pores

## Appendix II FEM simulations

### II.1 Mesh model

The Finite Element mesh representing the solid matrix and the pores could be obtained from the 3D tomographic image. The FEM model including the entire gauge length of the specimen is extracted from the tomographic image. In Avizo software, the basic process (Figure II-1) can be described as (ZIB and VSG, 2012):

- (1) The solid matrix, i.e. the material without pores, of these specimens was segmented from the X-ray tomography 3D image.
- (2) The surface of this solid matrix was extracted from segmentation results: a triangular surface was reconstructed by using “SurfaceGen” module.
- (3) The number of triangles of the reconstructed surface was reduced for the subsequent operations by using the “Surface Simplification” Editor in Avizo. The minimum and maximum sizes for the triangle element were set as 0.2 pixel and 10 pixels, respectively.
- (4) A cumbersome and complex manual surface edition was always necessary before the tetrahedral grid generation. Some important parameters of each element in the surface, such as aspect ratio, dihedral angle, were checked automatically and the elements with improper parameter, e.g. distorted triangles with a high aspect ratio, were repaired manually one by one.
- (5) Once the repair of the elements in the surface was finished, the generation of a volumetric tetrahedral grid was performed using “TetraGen” module. The volume enclosed by the triangular surface was then filled with tetrahedra.

Herein, the FEM model was constructed and meshed. For more details please refer to (ZIB and VSG, 2012). The FEM model so-obtained, which has between 2 and 5 million elements in volume, was then used for FEM simulation.

## Appendix

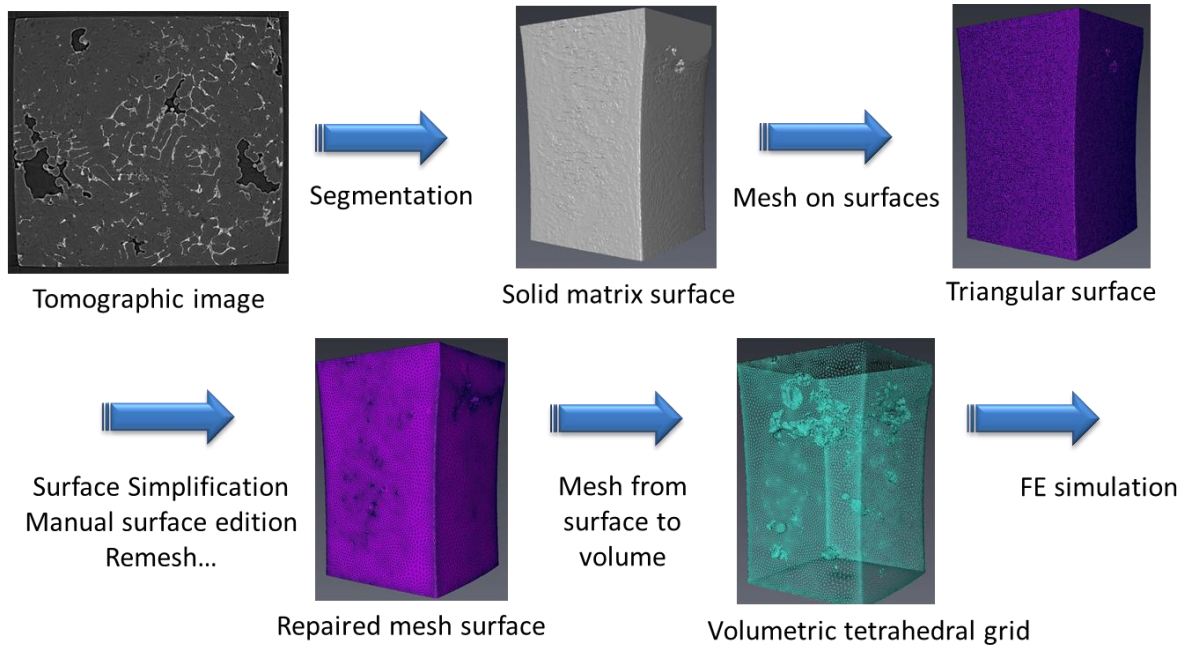


Figure II-1 Schematic of FE mesh process

## II.2 FE calculations

### II.2.1 Application in tensile test

In order to study the influence of pores on strain localizations in tensile test with 3D in-situ observations, FEM model based on the tomographic image with a voxel size of  $4.5 \mu\text{m}$  (used for specimen selection) was used. The average longitudinal strain calculated from DVC was used to draw a stress-strain curve as no extensometer measurement could be done during the in-situ tensile test in lab-CT. This stress-strain curve deduced from DVC (see Chapter 5) was then used for FEM simulation of this porous matrix in order to better study the influence of pores on the strain distribution under monotonic tensile loading. The material property was thus set as elastoplastic and the loading condition for FEM simulation was an imposed uniform displacement  $l/2$  on the upper and lower boundaries of the FEM model. The displacement value was chosen to obtain a macroscopic deformation along the loading direction in the FEM model that is about the same as the average deformation measured in the CT image during the in-situ test at the highest load. Considering that the length of the specimen for FEM simulation is  $L$ , a given displacement  $l$  was imposed at each side of the FEM model, thus a deformation ' $2l/L$ ' was applied. If  $\epsilon$  is the maximum deformation from DVC, then  $2l/L = \epsilon$ . Herein,  $L=1000$  pixels,  $l=5$  pixels for Specimen T3.

### II.2.2 Selection of ROI for fatigue tests with 3D observations

The influence of pores on strain localization has already been highlighted in tensile test through FEM simulation in Chapter 5, thus such a FEM simulation is considered to be used to select ROI for fatigue tests with 3D observations. The FE mesh models were extracted from the tomographic images used for specimen selection (voxel size = 5  $\mu\text{m}$ ). The simulation conditions are the same as that in § II.2.1 except that the average deformation applied at the last iteration  $\epsilon$  was set at about 1%, and that the material property was set as elastic in order to simplify and shorten this time consuming calculation; for the same FE model, an elastoplastic calculation takes 5 to 10 times longer than an elastic one. FEM simulations were performed on 10 specimens for selection of specimens for fatigue tests with 3D observations.

### II.2.3 Comparisons with DVC results of fatigue tests

FE mesh models for Specimens F3 and F4 were extracted from SR-CT references images: thus they represent the real size and shape of specimens after polishing. The same ROI were used for FEM simulation and DVC, i.e. about 2.6 mm along the lengthwise of specimen. The material property is set as elastoplastic using a stress-strain curve from a conventional test on A319 LFC alloy. FEM simulation was performed both in tensile condition and cyclic condition. As in § II.2.1, boundary conditions are an applied displacement on each side of the model. The maximum average deformation deduced from DVC for each specimen was used as the maximum deformation for FE simulation (Dassault Systèmes, 2012). Here  $L=800$  pixels for both Specimens F3 and F4 and  $l=1.12$  pixels for Specimen F3 while  $l=0.56$  pixel for Specimen F4. The equivalent plastic strain at integration points (PEEQ), which measures the amount of permanent strain in material, is used here. It is the total accumulation of plastic strain and is defined as  $\sqrt{\frac{2}{3} d\epsilon^{pl}: d\epsilon^{pl}}$  (Berg, 1972).

## Appendix III Selections of specimen and ROI

### III.1 Tensile tests with 2D in-situ observations

Radiography and optical microscopy were used to select the most suitable specimens for 2D in-situ tensile tests.

#### III.1.1 Specimen T1

In a radiography image, white regions reflect the pores that are present in the direction perpendicular to the flat surface. A cluster of pores (marked by an arrow in Figure III-1) was revealed in the radiography. The region that contains this cluster was selected as the ROI for the following in-situ observation during the tensile test. The corresponding ROI in the OM image taken on the flat surface after polishing is marked by a rectangle in Figure III-1(b). The large surface pores that probably belong to the cluster observed in the radiography are also observed in the OM image.

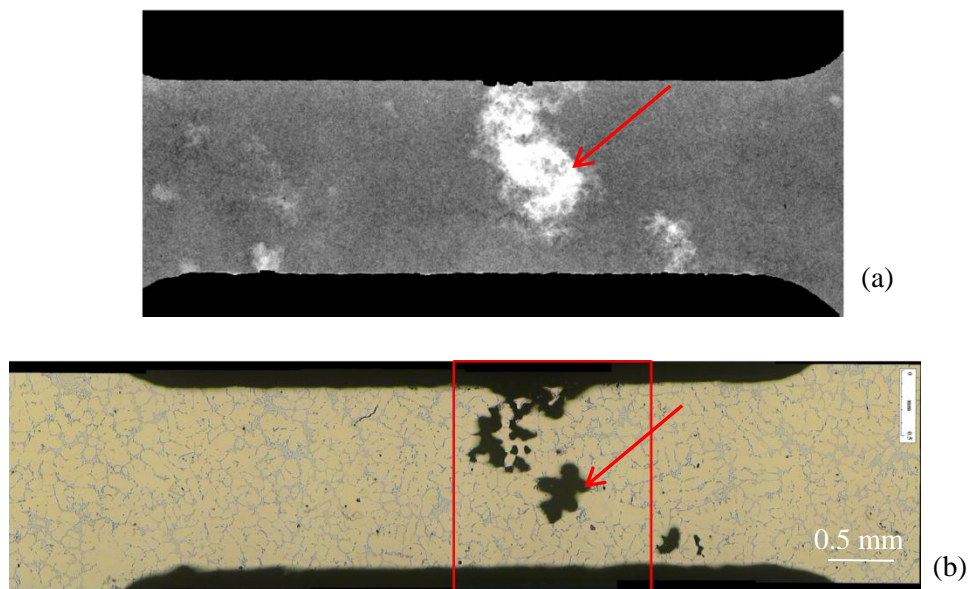


Figure III-1 Specimen T1: (a) radiography and (b) OM image with the ROI marked by a rectangle.



### III.1.2 Specimen T2

The radiography image of Specimen T2 and the corresponding OM image are shown in Figure III-2. Compared with the Specimen T1, no cluster of large pores was found in the radiography image. In order to study the influence of the pore marked with an arrow in Figure III-2(a) on the tensile behavior, notches were added on both sides of this region to generate a stress concentration. This notched region (rectangle in Figure III-2(b)) was then selected as the ROI for in-situ observation during the tensile test.

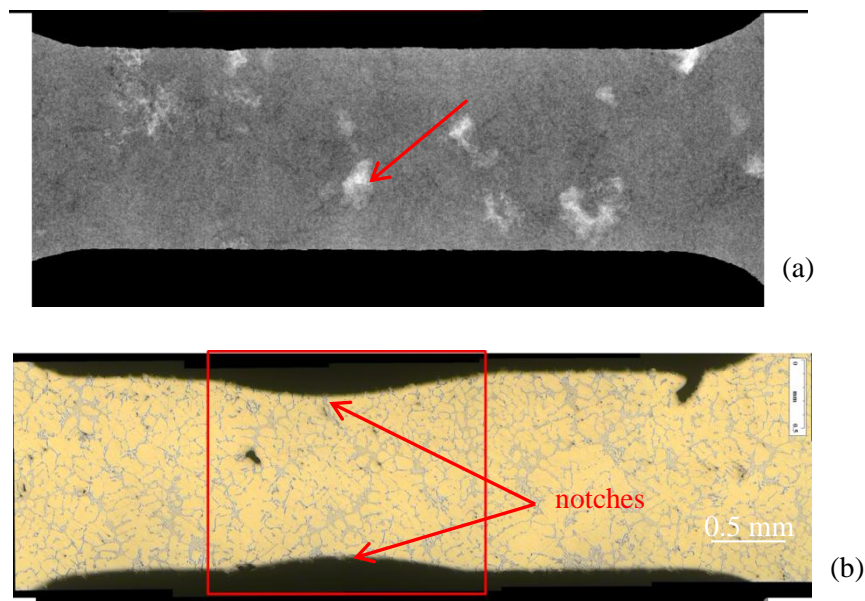


Figure III-2 Specimen T2: (a) radiography and (b) OM image with the ROI marked by a rectangle.

### III.2 Tensile tests with 3D in-situ observations: Specimen T3

The 3D rendering of pores in Specimen T3 (Figure III-3 (a)) shows that no large defects are present near the shoulders in volume while a cluster of pores is located in the gauge length. The area marked by a red rectangle was selected as the ROI for the following in-situ observations as the cracks are more likely to initiate around large pores. A close-up view (Figure III-3(b)) of the largest pore in Specimen T3 shows its complex microstructure and sharp shape.

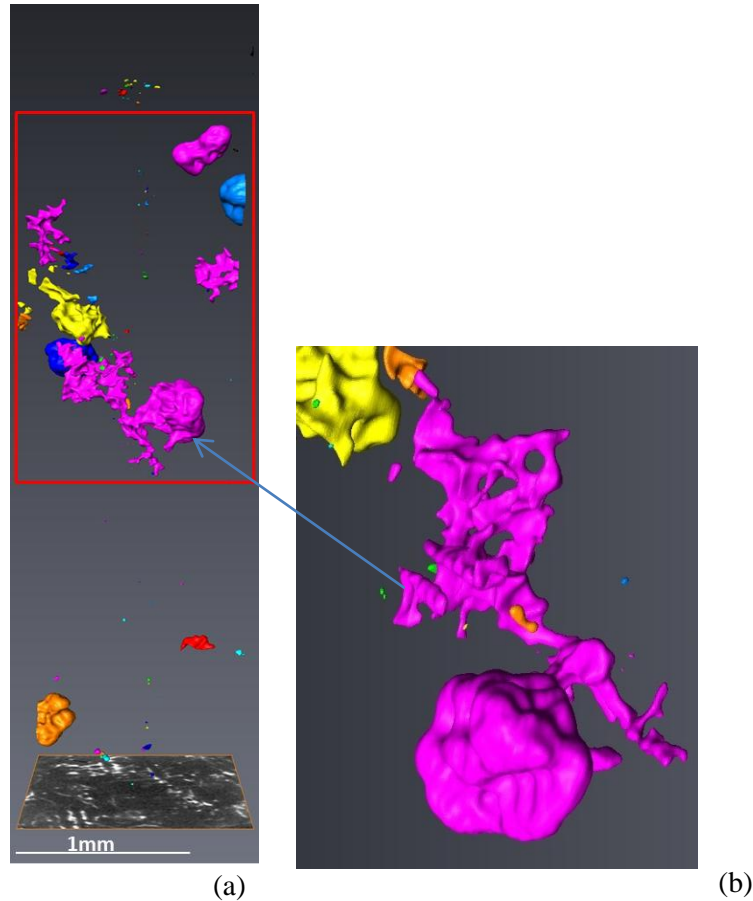


Figure III-3 (a) 3D rendering of pores in Specimen T3; the selected ROI is marked by a red rectangle.  
(b) A close up-view of the largest pore in (a) marked by an arrow.

### III.3 Fatigue tests with 2D in-situ observations

3D characterization of pores with Lab-CT was systematically performed prior to fatigue tests in order to select the most suitable specimens and the ROI for in-situ observation.

#### III.3.1 Specimen F1

3D rendering of pores in bulk of Specimen F1 in Figure III-4(a) shows no obvious cluster of pores near the flat surface in the notched cross-section. However, a surface pore located in the notch is found to be near one of the flat surfaces (less than 0.1 mm). 3D rendering of this pore and of the notched and flat surfaces are shown in Figure III-4 (b). The pore's volume is about  $0.012 \text{ mm}^3$ , and its Feret diameter is about 0.38 mm. Although it is not very large compared with the standard large pores in this material (see Chapter 3), this pore is still supposed to be the most probable crack initiation site on the observed surface through the comprehensive evaluation based on the influence of pores' size and location (summarized in Chapter 2): (a) it is quite near the flat surface and the notch root contrary to the other larger pores in bulk, (b) it is larger than other pores located on the observed surface (Figure III-4 (c)). This pore is projected onto the observed flat surface in Figure III-4 (c). The area

## Appendix

including the pore's projection is selected as the ROI for the following in-situ observation with Questar long distance microscope, and is marked with a red rectangle.

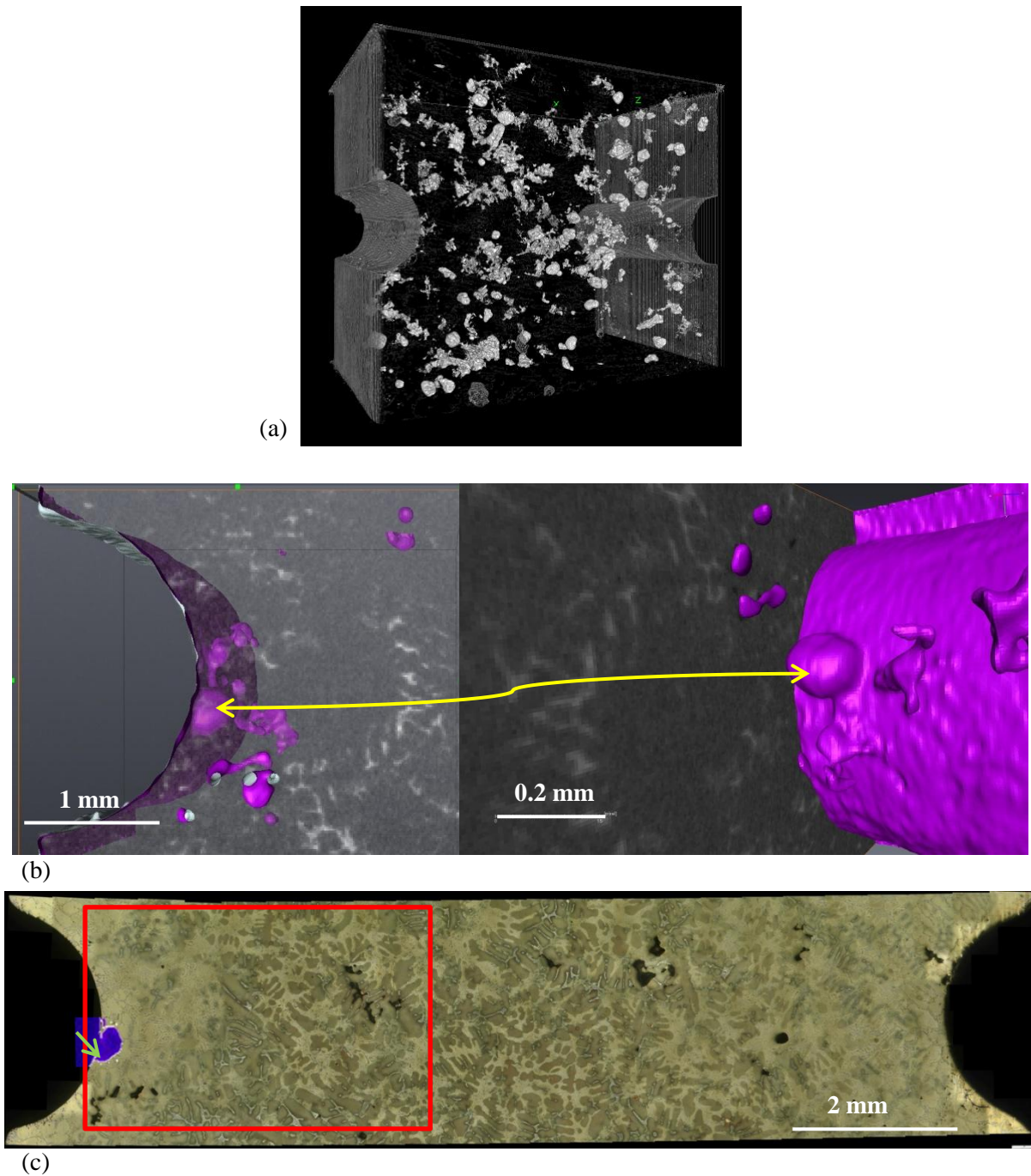


Figure III-4 Specimen F1: 3D rendering of (a) pores in bulk (b) and surface pore in the notched surface marked with a yellow arrow; the specimen surface was set transparent in the left image and opaque in the right image. (c) OM image of the specimen surface after etching: the pore marked with the yellow arrow was projected on the surface and is shown in purple; the selected ROI for the in-situ observation with Questar microscope is marked with a red rectangle; where crack initiated after 7000 cycles on the surface is marked with a green arrow.

### III.3.2 Specimen F2

In Specimen F2, a cluster of pores was found near a notched area and near the flat surface in the lab-CT image whereas large pores were rare found in other areas near the flat surface. The 3D rendering of these pores is shown through different perspectives in Figure III-5 (a) and (b). The sizes and locations of Pore A, B and C are listed in Table III-1. Pore A and Pore B are both large pore with a Feret diameter above 1.3 mm, but Pore A is closer to both flat and notched surfaces. Pore C connected to the flat surface, but it is far from the notch and is smaller than Pores A and B. The pores shown in Figure III-5 (b) are projected onto the flat surface of the specimen in Figure III-5 (c), thus the ROI marked in Figure III-5 (d) is selected. See the OM image of the surface selected for in-situ observation in Figure III-5 (d). No large surface pores were found in the selected ROI, however a cluster of surface pores is found in the right notched area. So, if the selection of ROI is performed through surface observation only, the right side in Figure III-5 (d) will naturally be selected as a ROI for the in-situ observation. The following fatigue test will prove the failure of such a selection and the importance of X-ray tomography in the selection of specimens.



## Appendix

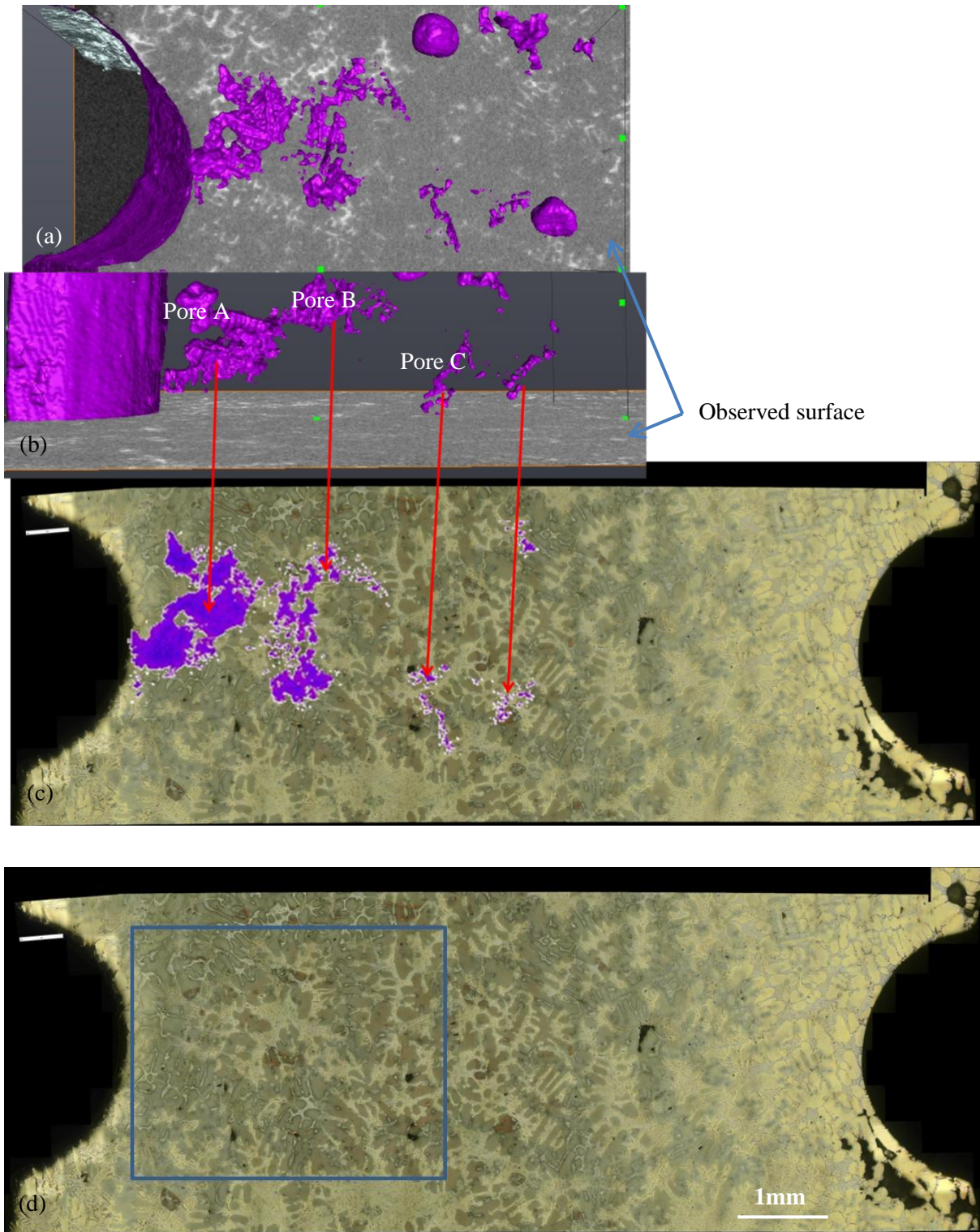


Figure III-5 3D rendering of a cluster of pores near the flat observed surface: in (a) view intercepted perpendicular to the flat surface, (b) view intercepted parallel to the flat surface. (c) OM image taken after etching with the projection of pores shown in (b). (d) OM image taken after etching, the selected ROI was marked with a blue rectangle.



## Appendix

Table III-1 Size and location of Pore A, B and C shown in Figure III-5 (b)

Pore	Ferret diam. (mm)	Connection with the surface	Minimum distance to surface (mm)	
			Flat surface	Notched surface
A	1.31	Subsurface pore	0.18	0.02
B	1.37	Subsurface pore	0.80	0.90
C	0.90	Surface pore	0.00	1.70

### III.4 Fatigue tests with 3D in-situ observations

Prior to the fatigue tests, 3D characterization of pores was performed with Lab-CT at a coarse resolution to select first the most suitable specimens and secondly the ROI for in-situ observation. After the fatigue test under SR-CT, the higher resolution image acquired at the beginning of the test was used to characterize the distributions of hard inclusions.

#### III.4.1 Specimen F3

The volume fraction of pores in Specimen F3 was about 0.76%. The distribution of pores in Figure III-6(a) shows that although there are more small pores than large pores in number, the total volume of small pores is smaller than that of large pores. Compared with the distribution of pores in a larger volume (Specimen 2 in Chapter 3), the pores' distribution in Specimen F3 is representative for this material. The FEM simulation result for Specimen F3 is shown in Figure III-6 (b). Strain localizations occur around a cluster of pores. Thus, the area around these pores, which is marked by a red rectangle in Figure III-6 (b), was selected as the ROI for in-situ observation.

The thickness distribution of hard inclusions (Si phases, iron intermetallics and  $Al_2Cu$  phases) characterized by synchrotron X-ray tomography in Figure III-7 are similar with that in the larger Specimen 1 (presented in Chapter 3). The hard inclusions in Specimen F3 could also be considered as representative for this material.

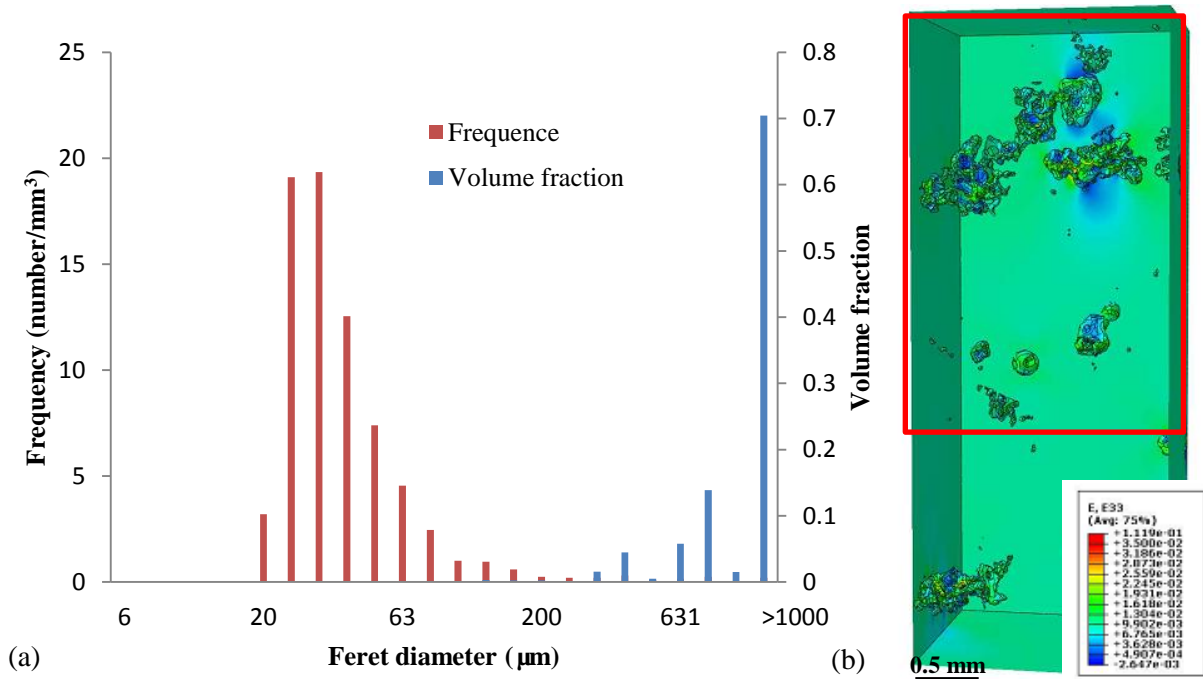


Figure III-6 Specimen F3: (a) distribution of pores and (b) FEM simulation results (E33: longitudinal strain); the selected ROI is marked by a red rectangle.

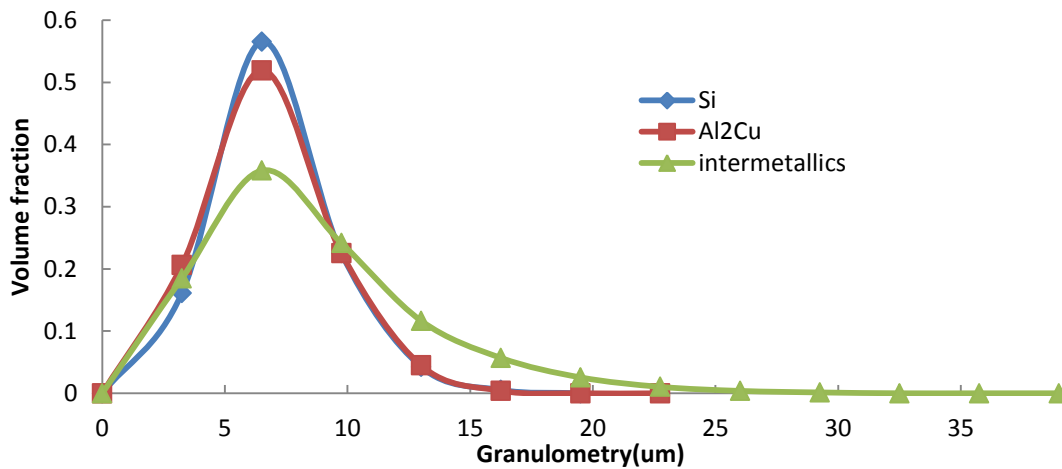


Figure III-7 Thickness distribution of hard inclusions in Specimen F3

### III.4.2 Specimen F4

The volume fraction of pores in Specimen F4 is about 0.42%. The distribution of pores in Figure III-8(a), which is similar with that in Specimen F3, compared well with the pores' distribution in a larger volume (Specimen 2 in Chapter 3). Specimen F4 is thus representative of this material. The FEM simulation result in Figure III-8 (b) shows strain localizations around a large shrinkage pore marked by an arrow. Thus the area around this large shrinkage pore was selected as the ROI, which is

## Appendix

marked by a red rectangle in Figure III-8 (b), for the following in-situ observation. The thickness distribution of hard inclusions (Si phase, iron intermetallics and Al<sub>2</sub>Cu phases) characterized by SR-CT is shown in Figure III-9: their distributions are similar with that in the larger Specimen 1 (presented in Chapter 3). The hard inclusions in Specimen F4 could also be considered as representative for this material.

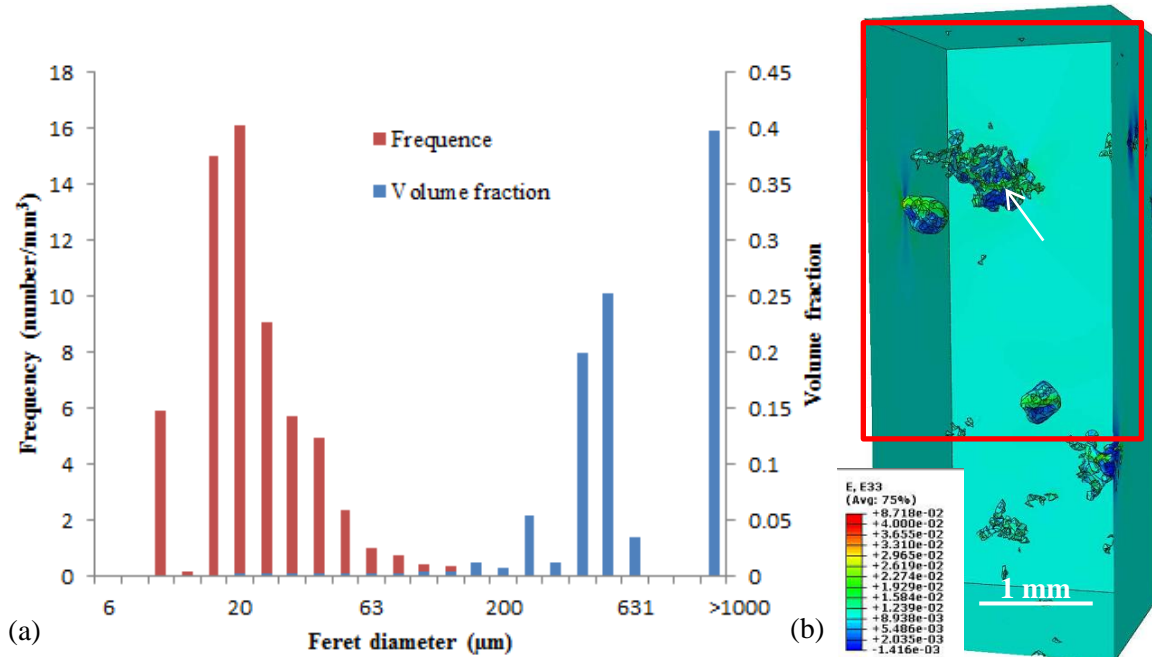


Figure III-8 Specimen F4: (a) distribution of pores and (b) FE simulation results (E33: longitudinal strain) with selected ROI marked by a red rectangle.

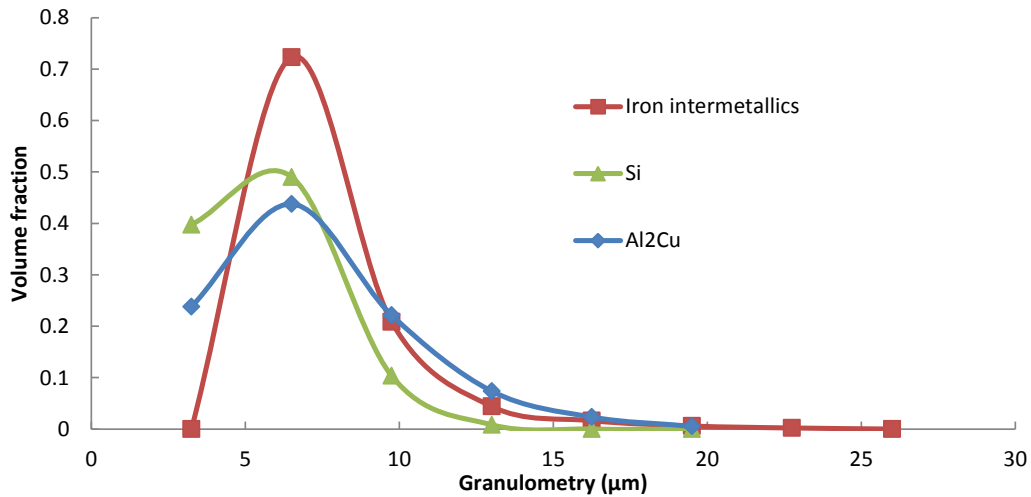


Figure III-9 Thickness distribution of hard inclusions in Specimen F4

## Appendix IV Field measurements

### IV.1 Principles of 2D/3D image correlation platform at LML

This platform is based on C++ programs and is open source libraries. It supports many commonly used image formats, such as jpg, png, tiff, txt, raw, 8bits, 16bits. The results were saved as the format ‘NetCDF’ ([www.unidata.ucar.edu/netcdf/](http://www.unidata.ucar.edu/netcdf/)). Multi-transformation is supported: global deformation, local deformation, and elastic deformation. The parametric registration algorithm, which is similar with Elastix software (Klein et al., 2010), is illustrated in Figure IV-1.

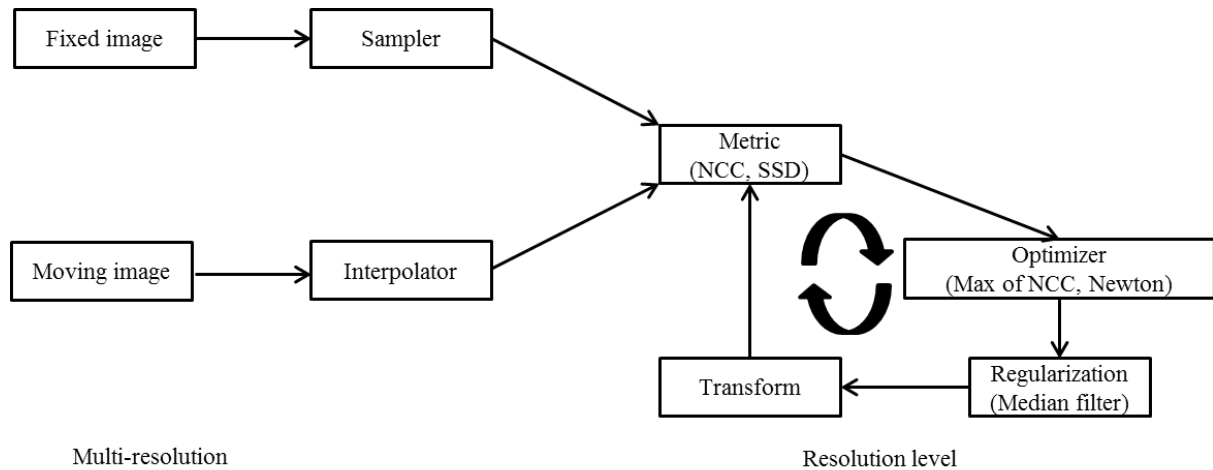


Figure IV-1 The basic registration components of image correlation platform at LML

This platform was only used for DVC measurements in in this thesis. Correlation sequence per image couple was defined as:

- ◆ Analysis sequence: OFI\_H, OFI\_H, OFI\_H, IC, OFFEM16, OFFEM16, OFFEM8
- ◆ Filter sequence = 6, 5, 4, 3, 2, 1, 0 (the number ‘n’, i.e. the associated scale, means that the voxels are averaged over  $2^n \times 2^n \times 2^n$  voxels)

The correlation is based on a multi-resolution scheme. Different strategies, which are described below, were adopted for the different scales. For easy and fast convergence at the coarser scales, only global deformations are searched for, using OFI and IC algorithms while at the finest scales, the more computing intensive OFFEM algorithm was adopted to compute local displacements.

## Appendix

---

‘OFI\_H’ uses Optical-Flow Integrated (OFI) method, and assumes a homogeneous deformation such as rigid body motions, i.e. translations (Tx, Ty, Tz) and rotations (Rx, Ry, Rz), or global strains or shears (Exx, Eyy, Ezz, Exy, Exz, Eyz). It measures the similarity by using Sum of Squared Differences (SSD). OFI was used for global transformation for scales 6 to 4. It can reduce the dimensionality of the problem and it has low sensitivity to noise,

‘IC’ means Inter Correlation method, which contains Fastest Fourier Transform in the West (FFTW), FFTW\_PHASE, Fast Fourier transform (FFT), FFT\_PHASE, and direct method. These methods use Normalized Correlation Coefficient (NCC) for similarity measures and are for local deformation. They were adopted for scale 3.

‘OFFEM’ is Optical Flow elastic transformation based on Finite Element Methods. It uses 8 nodes elements and also relies on Sum of Squared Differences (SSD) for similarity. OFFEM is for elastic deformation. It has a good spatial coherence and is easy to compare with FE calculations (FEMU). ‘OFFEM16’ means the used element size is 16×16×16 voxels while ‘OFFEM8’ means the used element size is 8×8×8 voxels.

By using the above parameters, one DVC measurements performed on one couple of images (725 × 780 × 800 voxels) lasts about 45 to 60 minutes.

This platform was developed by Jean-François WITZ and Rian SEGHIR at LML. To learn more about this platform, please contact the developer: Jean-François WITZ ([jean-francois.witz@ec-lille.fr](mailto:jean-francois.witz@ec-lille.fr)).

## IV.2 Examples of parameters for Elastix software

```
// Example parameter file for B-spline registration
// C-style comments: //

// The internal pixel type, used for internal computations
// Leave to float in general.
// NB: this is not the type of the input images! The pixel
// type of the input images is automatically read from the
// images themselves.
// This setting can be changed to "short" to save some memory
// in case of very large 3D images.
(FixedInternalImagePixelType "float")
(MovingInternalImagePixelType "float")

// The dimensions of the fixed and moving image
// NB: This has to be specified by the user. The dimension of
// the images is currently NOT read from the images.
// Also note that some other settings may have to be specified
// for each dimension separately.
(FixedImageDimension 2)
```



# Appendix

---

(MovingImageDimension 2)

```
// Specify whether you want to take into account the so-called
// direction cosines of the images. Recommended: true.
// In some cases, the direction cosines of the image are corrupt,
// due to image format conversions for example. In that case, you
// may want to set this option to "false".
(UseDirectionCosines "true")
```

```
// ***** Main Components *****
```

```
// The following components should usually be left as they are:
(Registration "MultiMetricMultiResolutionRegistration")
(Interpolator "BSplineInterpolator")
(ResampleInterpolator "FinalBSplineInterpolator")
(Resampler "DefaultResampler")
```

```
// These may be changed to Fixed/MovingSmoothingImagePyramid.
// See the manual.
(FixedImagePyramid "FixedRecursiveImagePyramid")
(MovingImagePyramid "MovingRecursiveImagePyramid")
```

```
// The following components are most important:
// The optimizer AdaptiveStochasticGradientDescent (ASGD) works
// quite ok in general. The Transform and Metric are important
// and need to be chosen careful for each application. See manual.
(Optimizer "AdaptiveStochasticGradientDescent")
(Transform "BSplineTransform")
// (Metric "AdvancedMeanSquares")
(Metric "AdvancedNormalizedCorrelation" "TransformBendingEnergyPenalty")
(Metric0Weight 0.1)
(Metric1Weight 100.0)
```

```
// (Metric "AdvancedMattesMutualInformation")
// (Metric "NormalizedMutualInformation")
```

```
// ***** Transformation *****
```

```
// The control point spacing of the bspline transformation in
// the finest resolution level. Can be specified for each
// dimension differently. Unit: mm.
// The lower this value, the more flexible the deformation.
// Low values may improve the accuracy, but may also cause
// unrealistic deformations. This is a very important setting!
// We recommend tuning it for every specific application. It is
// difficult to come up with a good 'default' value.
(FinalGridSpacingInVoxels 32 32)
```

```
// Alternatively, the grid spacing can be specified in voxel units.
// To do that, uncomment the following line and comment/remove
// the FinalGridSpacingInPhysicalUnits definition.
//(FinalGridSpacingInVoxels 16)
```

```
// By default the grid spacing is halved after every resolution,
// such that the final grid spacing is obtained in the last
```

## Appendix

---

```
// resolution level. You can also specify your own schedule,
// if you uncomment the following line:
//(GridSpacingSchedule 4.0 4.0 2.0 1.0)
// This setting can also be supplied per dimension.

// Whether transforms are combined by composition or by addition.
// In generally, Compose is the best option in most cases.
// It does not influence the results very much.
(HowToCombineTransforms "Compose")

// ***** Similarity measure *****

// Number of grey level bins in each resolution level,
// for the mutual information. 16 or 32 usually works fine.
// You could also employ a hierarchical strategy:
//(NumberOfHistogramBins 16 32 64)
// (NumberOfHistogramBins 32)

// If you use a mask, this option is important.
// If the mask serves as region of interest, set it to false.
// If the mask indicates which pixels are valid, then set it to true.
// If you do not use a mask, the option doesn't matter.
(ErodeMask "true")
// (ErodeMask "false")
// (RequiredRationOfValidSamples 0.05)

// ***** Multiresolution *****

// The number of resolutions. 1 Is only enough if the expected
// deformations are small. 3 or 4 mostly works fine. For large
// images and large deformations, 5 or 6 may even be useful.
(NumberOfResolutions 5)

// The downsampling/blurring factors for the image pyramids.
// By default, the images are downsampled by a factor of 2
// compared to the next resolution.
// So, in 2D, with 4 resolutions, the following schedule is used:
(ImagePyramidSchedule 32 32 16 16 8 8 4 4 2 2)
// And in 3D:
//(ImagePyramidSchedule 8 8 8 4 4 4 2 2 2 1 1 1)
// You can specify any schedule, for example:
//(ImagePyramidSchedule 4 4 4 3 2 1 1 1)
// Make sure that the number of elements equals the number
// of resolutions times the image dimension.

// ***** Optimizer *****

// Maximum number of iterations in each resolution level:
// 200-2000 works usually fine for nonrigid registration.
// The more, the better, but the longer computation time.
// This is an important parameter!
(MaximumNumberOfIterations 4000)
// (MaximumNumberOfIterations 500)

// The step size of the optimizer, in mm. By default the voxel size is used.
```

## Appendix

---

```
// which usually works well. In case of unusual high-resolution images
// (eg histology) it is necessary to increase this value a bit, to the size
// of the "smallest visible structure" in the image:
//(MaximumStepLength 1.0)
```

```
// ***** Image sampling *****
```

```
// Number of spatial samples used to compute the mutual
// information (and its derivative) in each iteration.
// With an AdaptiveStochasticGradientDescent optimizer,
// in combination with the two options below, around 2000
// samples may already suffice.
(NumberOfSpatialSamples 2000)
```

```
// Refresh these spatial samples in every iteration, and select
// them randomly. See the manual for information on other sampling
// strategies.1
(NewSamplesEveryIteration "true")
(ImageSampler "RandomSparseMask")
// (ImageSampler "Random")
```

```
// ***** Interpolation and Resampling *****
```

```
// Order of B-Spline interpolation used during registration/optimisation.
// It may improve accuracy if you set this to 3. Never use 0.
// An order of 1 gives linear interpolation. This is in most
// applications a good choice.
(BSplineInterpolationOrder 3)
```

```
// Order of B-Spline interpolation used for applying the final
// deformation.
// 3 gives good accuracy; recommended in most cases.
// 1 gives worse accuracy (linear interpolation)
// 0 gives worst accuracy, but is appropriate for binary images
// (masks, segmentations); equivalent to nearest neighbor interpolation.
(FinalBSplineInterpolationOrder 3)
```

```
//Default pixel value for pixls that come from outside the picture:
(DefaultPixelValue 0)
```

```
// Choose whether to generate the deformed moving image.
// You can save some time by setting this to false, if you are
// not interested in the final deformed moving image, but only
// want to analyze the deformation field for example.
(WriteResultImage "true")
```

```
// The pixel type and format of the resulting deformed moving image
(ResultImagePixelFormat "float")
(ResultImageFormat "vtk")
```

### Appendix V Crack length measurements in 2D

In order to analyze cracks propagation, the cumulative cracks length of Specimens F1 and F2 was measured using ImageJ software on Questar images taken at each step during cyclic loading. The measured crack length corresponds to the distance between the initiation site at the notch root and the farthest crack tip (see Figure V-1 for an example).

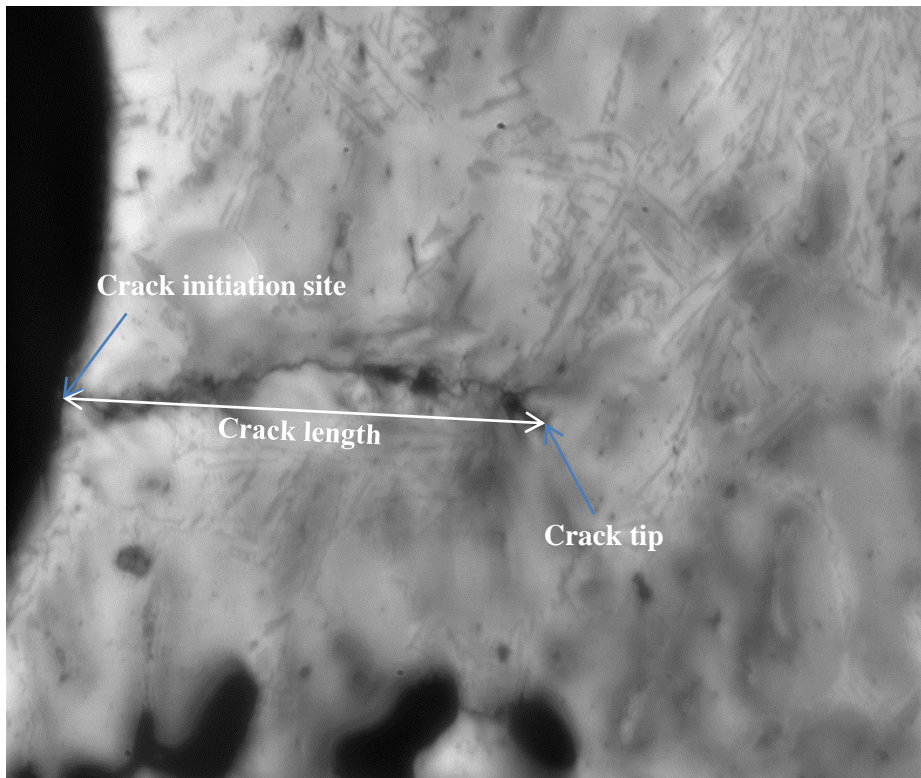


Figure V-1 Crack length measurement method.

### Appendix VI Fracture analysis using SEM-EDS

SEM-EDS performed on Specimens F1, F2, F3 and F4 allow retrieving the chemical compositions analysis (Table 5-6) and X-ray mapping analysis in different regions of the fracture surfaces:

- ◆ In Specimens F1, F2 and F4, analyzed regions are cracks propagation regions and final fast fracture regions which were previously identified by fracture analysis and in-situ observations.
- ◆ In Specimen F3, large cracks were observed during the tensile stage and no cracks propagations was observed before final failure. Thus the fracture surface of Specimen F3 is divided into cracks initiation areas due to tensile loading in 1<sup>st</sup> cycle and final fracture areas.

As characterized in Chapter 3, the size of AlCuMgSi phase is very small compared with other hard inclusions. Thus Mg element, which corresponds to AlCuMgSi phase, is not analyzed using X-ray mapping due to the limit of resolution and contrast. The elements of interest are Si, Fe, Mn, and Cu that corresponds to eutectic Si,  $\rightleftharpoons$  and  $\leftleftharpoons$  iron intermetallics,  $\rightleftharpoons$  iron intermetallics and copper containing phases sequentially.

Due to the roughness of the fracture surface, X-ray mapping was hardly performed accurately as the signals emitted from a lower area may be blocked by a higher area. The comparison by using high resolution BSE images and the chemical elements composition analysis in small areas was also adopted as a supplementary method to identify the compositions.

X-ray mapping images of Si, Fe, Mn, Cu on both fracture surfaces of each specimens are shown in below. Both fracture surfaces images of each specimen are placed side by side. Symmetry and rotation transformations are performed on one of the two images to allow comparison of the constituents in the same position on the two fracture surfaces. If the same constituents are identified in the same location on both fracture surfaces, the failure mechanism is fracture of hard particles. Otherwise, the failure mechanism is decohesion/debonding. The arrow in each image represents crack propagation direction on surface and is put aside the area where cracks propagations were observed in ROI. Cracks propagation region (Specimens F1 and F4) or cracks initiation area due to tensile loading (Specimen F3) is marked by a rectangular box while the other areas are considered as final fast fracture regions.



VI.1 Specimen F1

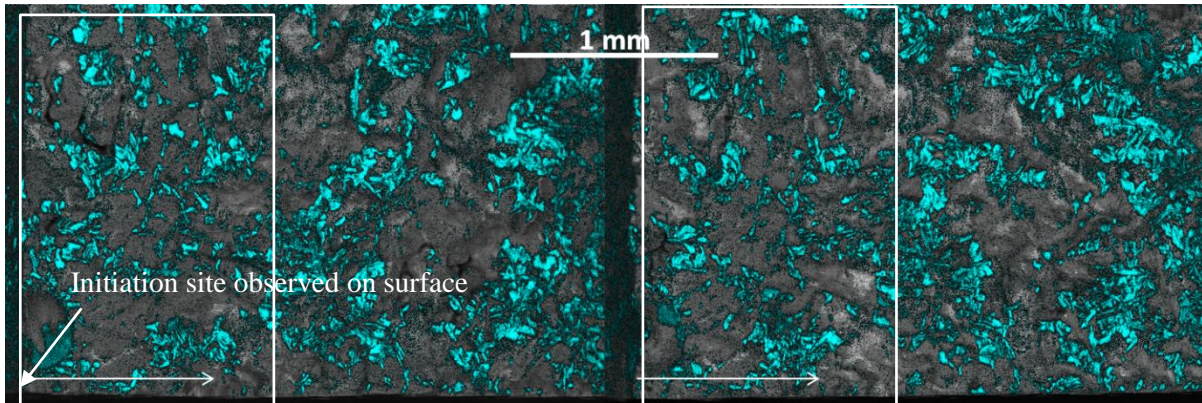


Figure VI-1 X-ray mapping of Si (Specimen F1)

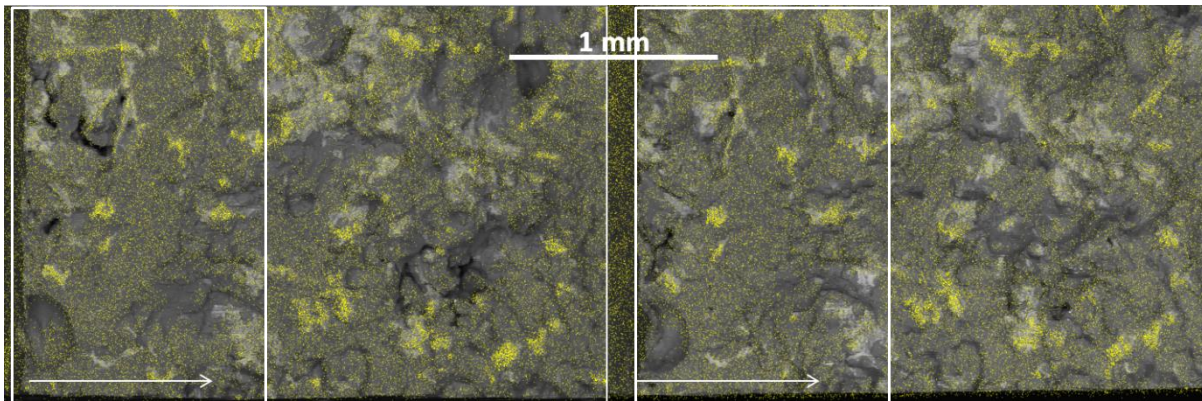


Figure VI-2 X-ray mapping of Fe (Specimen F1)

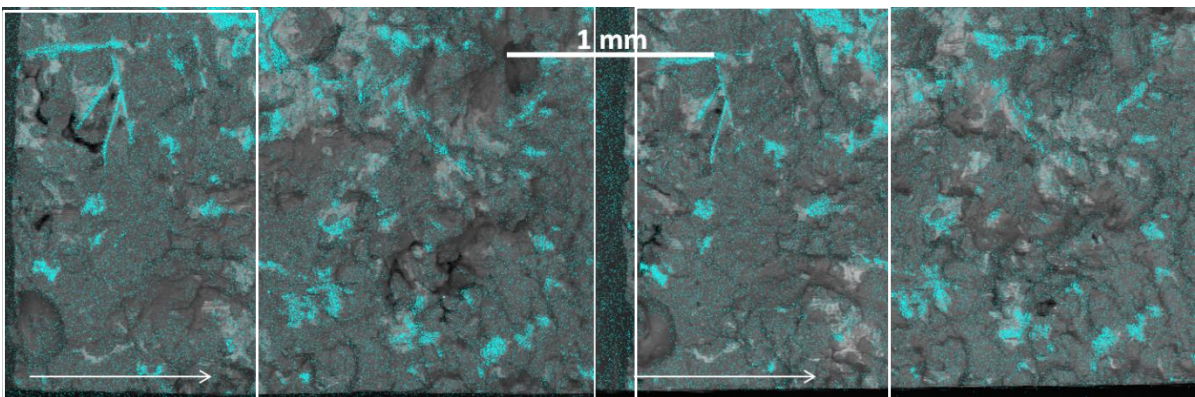


Figure VI-3 X-ray mapping of Mn (Specimen F1)



## Appendix

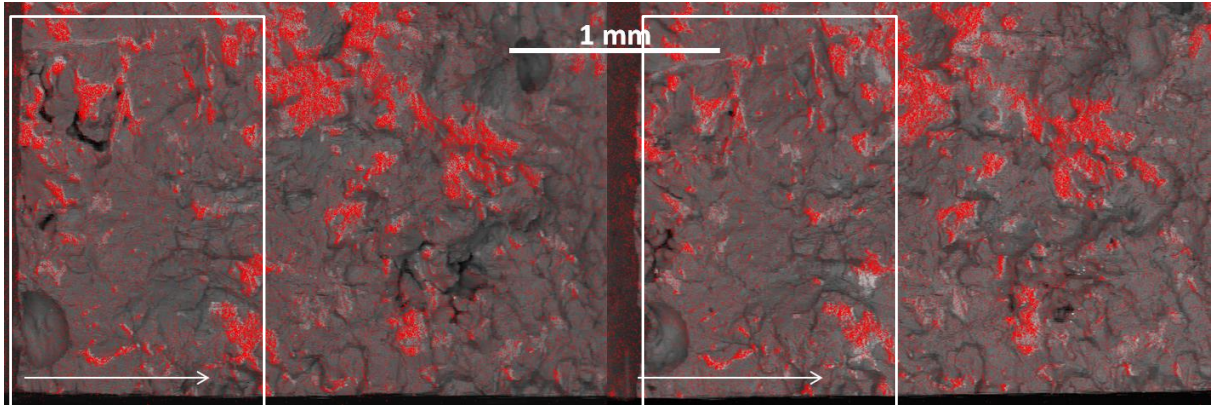


Figure VI-4 X-ray mapping of Cu (Specimen F1)

### VI.2 Specimen F2

The whole area in Figure VI-5 ~ Figure VI-8 is considered as cracks propagation regions.

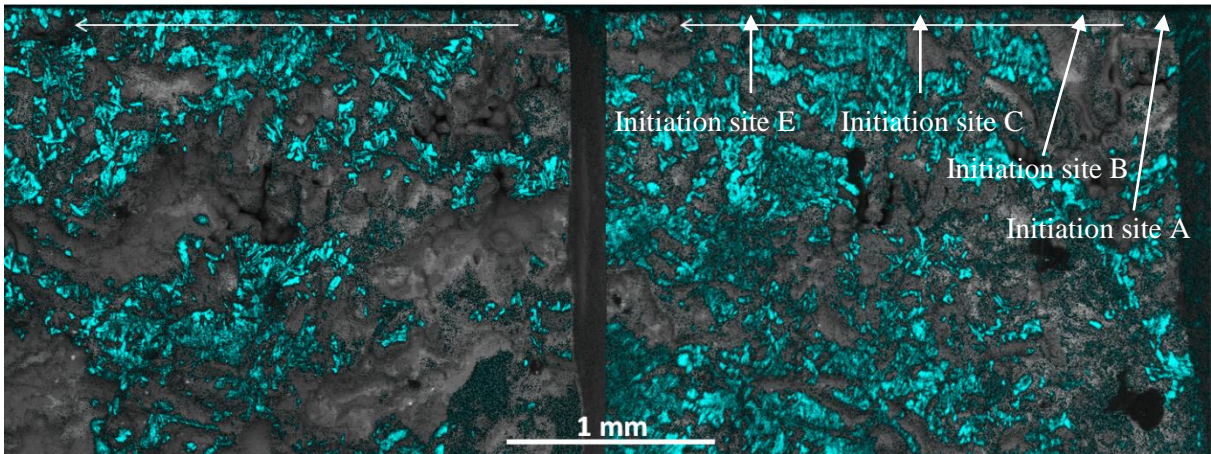


Figure VI-5 X-ray mapping of Si (Specimen F2)

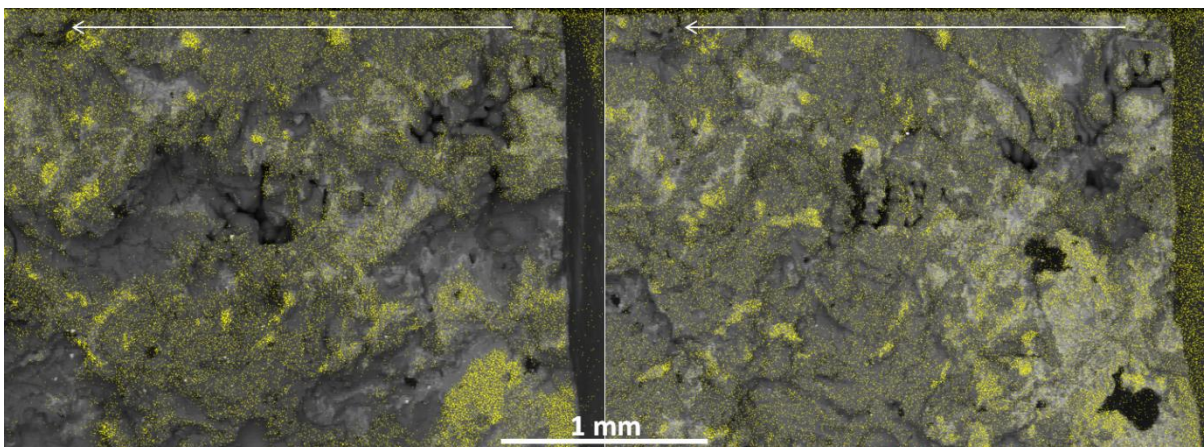


Figure VI-6 X-ray mapping of Fe (Specimen F2)



## Appendix

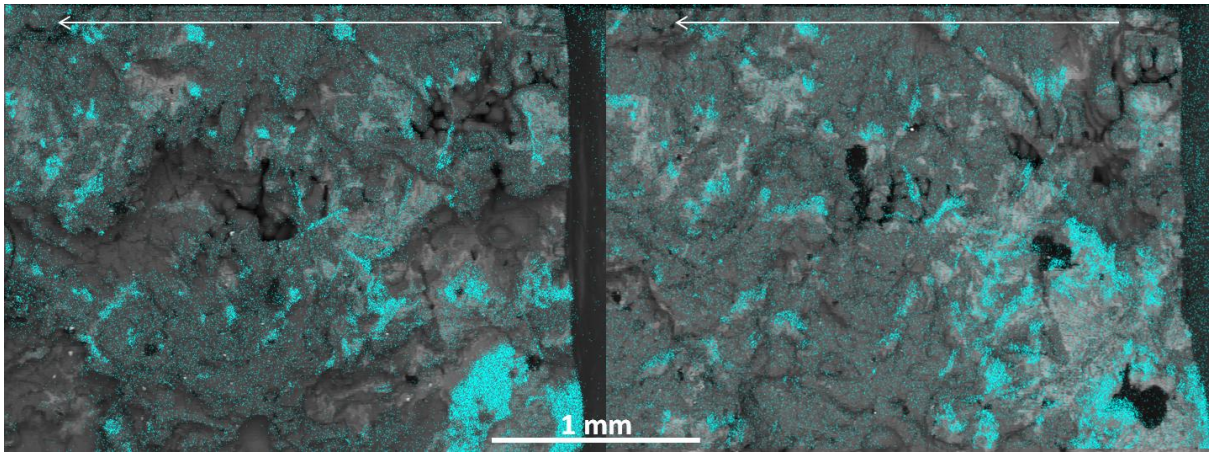


Figure VI-7 X-ray mapping of Mn (Specimen F2)

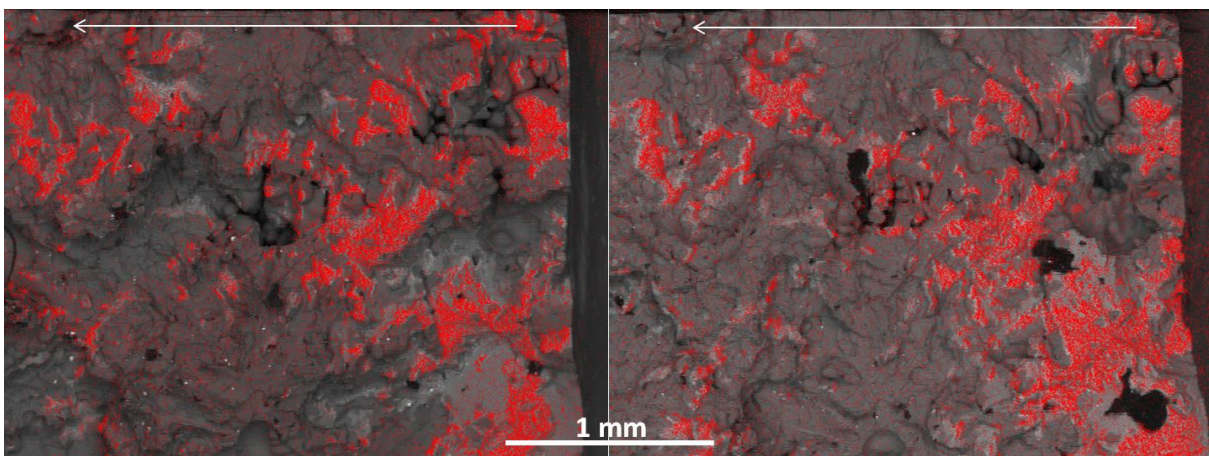


Figure VI-8 X-ray mapping of Cu (Specimen F2)

### VI.3 Specimen F3

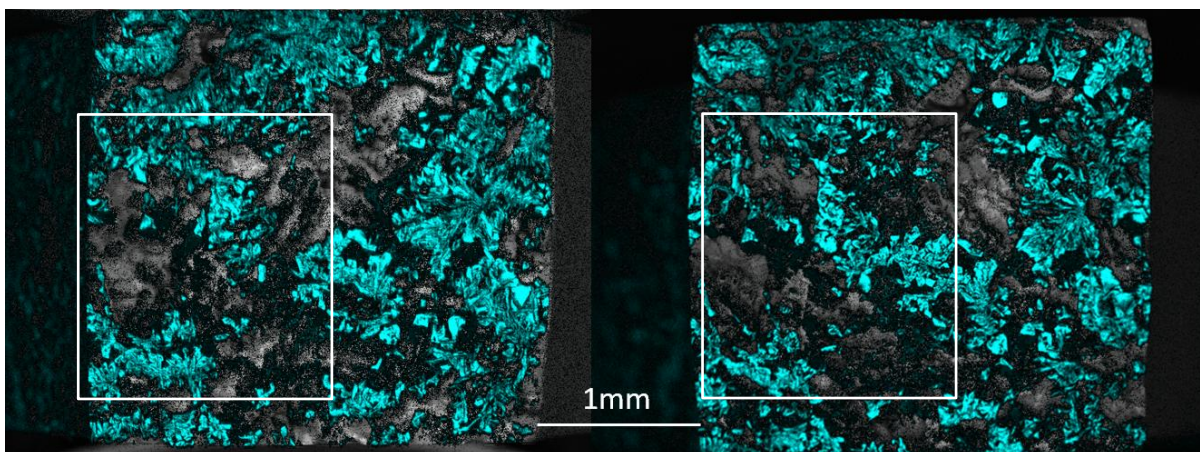


Figure VI-9 X-ray mapping of Si (Specimen F3)



## Appendix

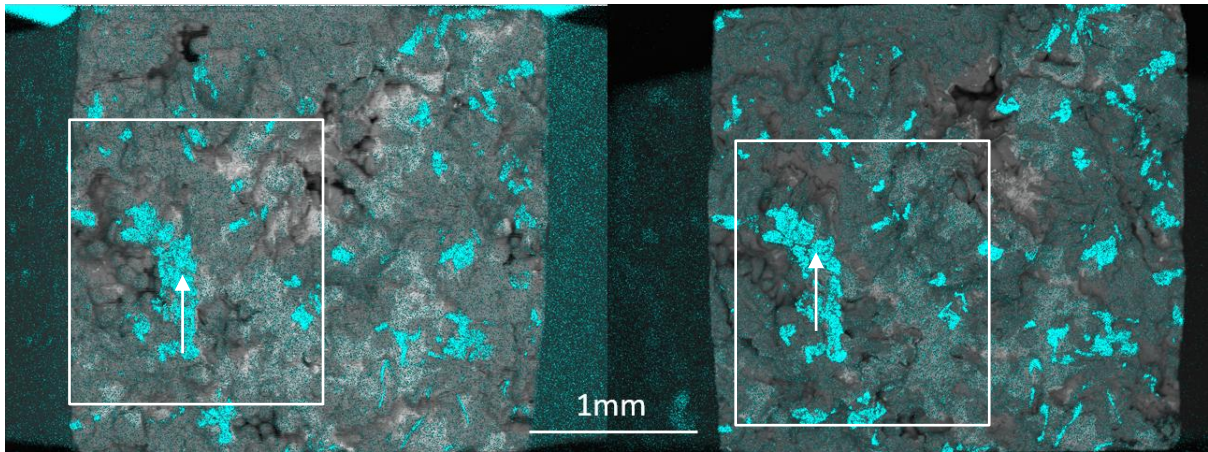


Figure VI-10 X-ray mapping of Fe (Specimen F3)

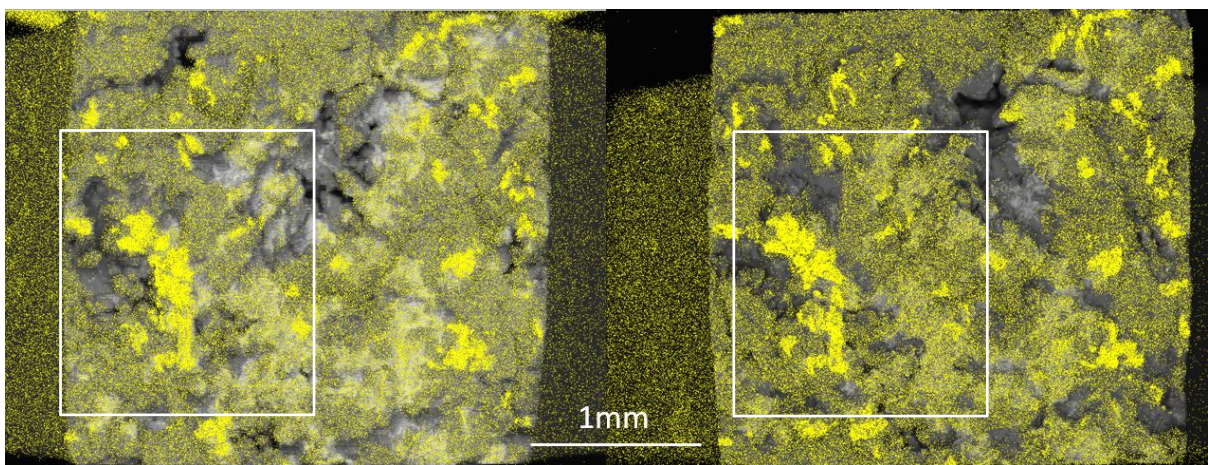


Figure VI-11 X-ray mapping of Mn (Specimen F3)

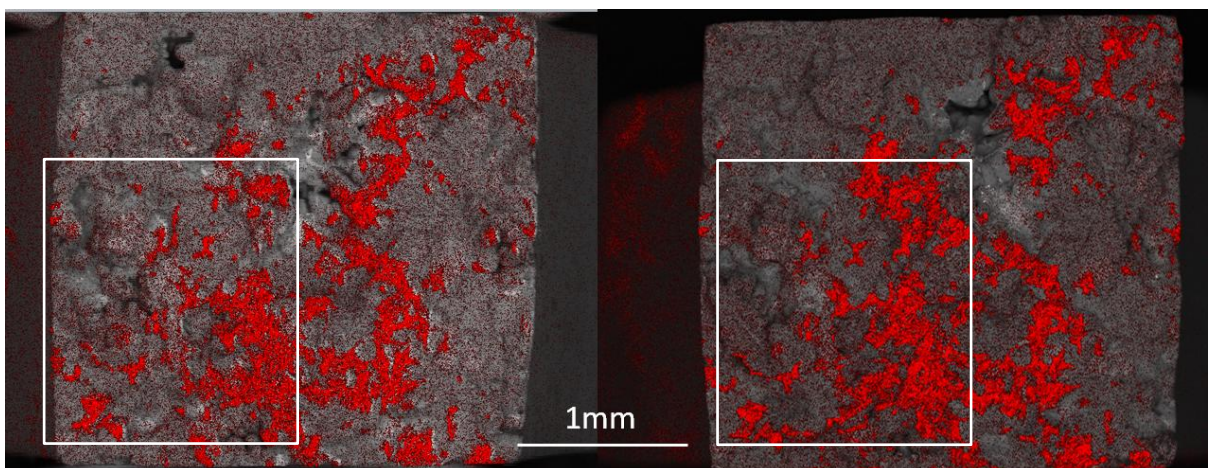


Figure VI-12 X-ray mapping of Cu (Specimen F3)



VI.4 Specimen F4

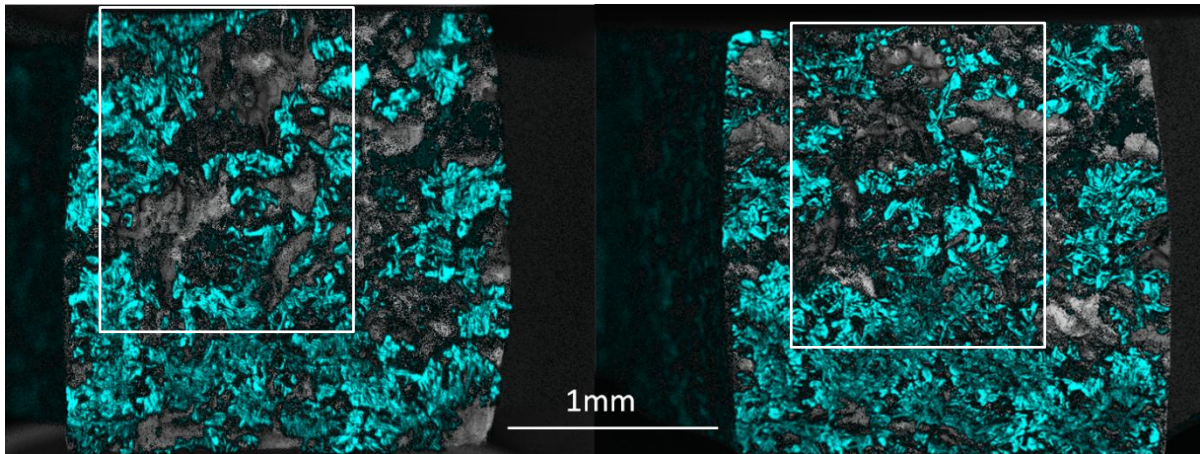


Figure VI-13 X-ray mapping of Si (Specimen F4)

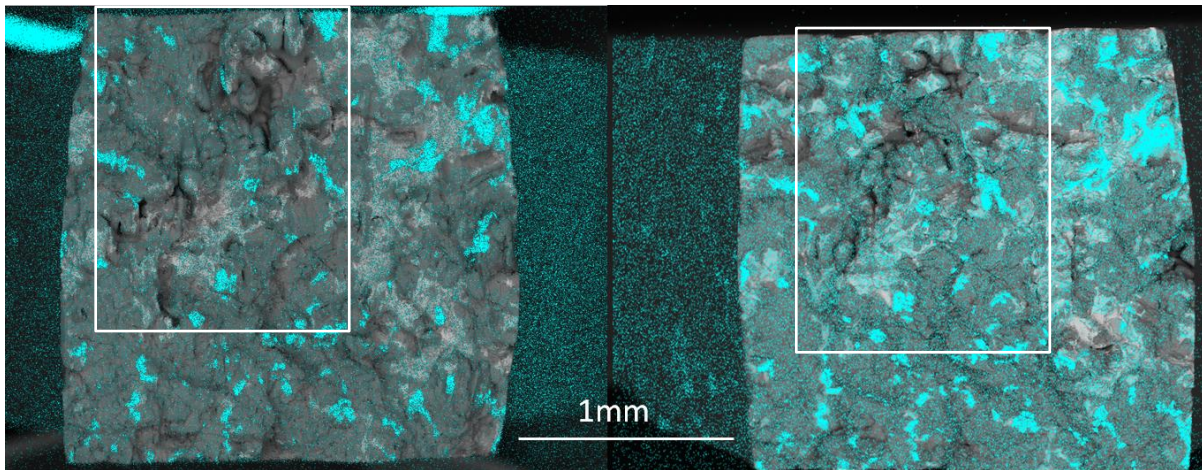


Figure VI-14 X-ray mapping of Fe (Specimen F4)

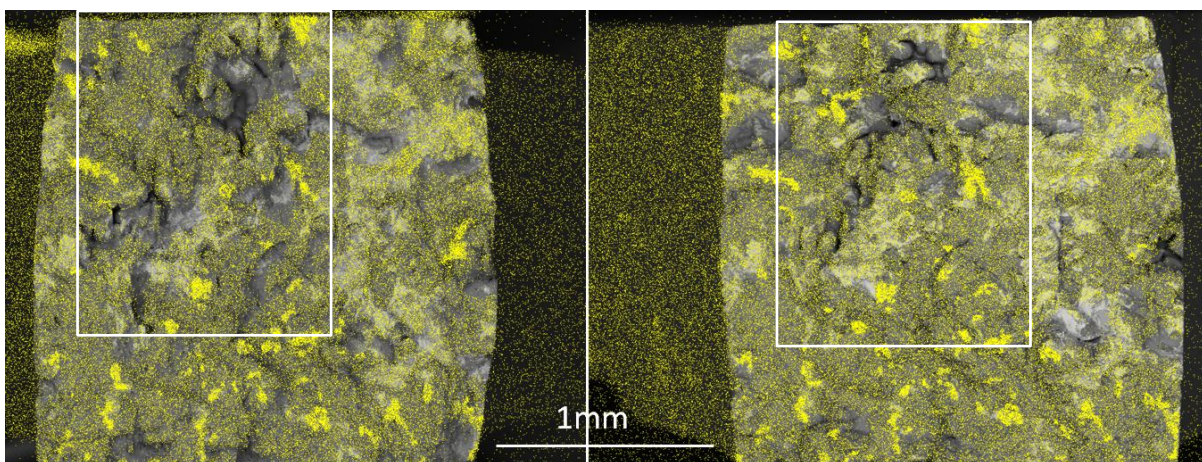


Figure VI-15 X-ray mapping of Mn (Specimen F4)



## Appendix

---

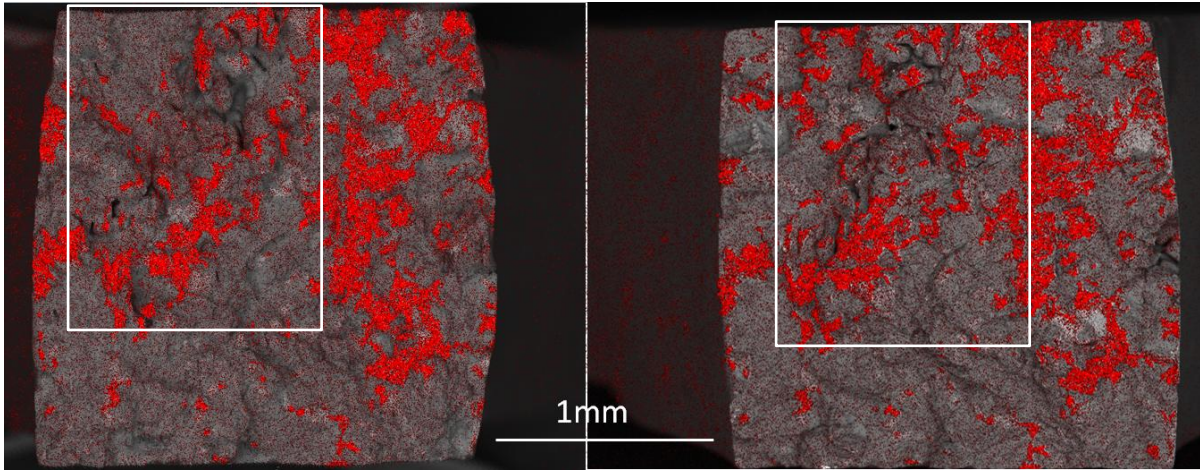


Figure VI-16 X-ray mapping of Cu (Specimen F4)

## References

- Albonetti, R. (2000). Porosity and intermetallic formation in lost foam casting of 356 alloy. M.E.Sc. The University of Western Ontario.
- American Foundry Society (2004). A Design Study in Aluminum Castings - GM Cylinder Block: Lost Foam Casting.
- Amiot, F., Bornert, M., Doumalin, P., Dupré, J.-C., Fazzini, M., Orteu, J.-J., Poilâne, C., Robert, L., Rotinat, R., Toussaint, E., et al. (2013). Assessment of Digital Image Correlation Measurement Accuracy in the Ultimate Error Regime: Main Results of a Collaborative Benchmark. *Strain* 49, 483–496.
- Ammar, H.R., Samuel, A.M., and Samuel, F.H. (2008a). Effect of casting imperfections on the fatigue life of 319-F and A356-T6 Al–Si casting alloys. *Mater. Sci. Eng. A* 473, 65–75.
- Ammar, H.R., Samuel, A.M., and Samuel, F.H. (2008b). Porosity and the fatigue behavior of hypoeutectic and hypereutectic aluminum–silicon casting alloys. *Int. J. Fatigue* 30, 1024–1035.
- Arami, H., Khalifehzadeh, R., Akbari, M., and Khomamizadeh, F. (2008). Microporosity control and thermal-fatigue resistance of A319 aluminum foundry alloy. *Mater. Sci. Eng. A* 472, 107–114.
- Asghar, Z., Requena, G., Degischer, H.P., and Cloetens, P. (2009). Three-dimensional study of Ni aluminides in an AlSi12 alloy by means of light optical and synchrotron microtomography. *Acta Mater.* 57, 4125–4132.
- Bäckerud, L., Chai, G., and Tamminen, J. (1990). Solidification Characteristics of Aluminum Alloys (AFS/Skanaluminium).
- Bangyikhan, K. (2005). Effects of oxide film, Fe-rich phase, porosity and their interactions on tensile properties of cast Al-Si-Mg alloys. PhD thesis. University of Birmingham.
- Barrirero, J., Engstler, M., and Mücklich, F. (2013). Atom Probe Analysis of Sr Distribution in AlSi Foundry Alloys. In *Light Metals 2013*, B.A. Sadler, ed. (John Wiley & Sons, Inc.), pp. 289–296.
- Barrirero, J., Engstler, M., Ghafoor, N., de Jonge, N., Odén, M., and Mücklich, F. (2014). Comparison of segregations formed in unmodified and Sr-modified Al–Si alloys studied by atom probe tomography and transmission electron microscopy. *J. Alloys Compd.* 611, 410–421.
- Baruchel, J., Buffiere, J.-Y., Maire, E., Merle, P., and Peix, G. (2000). *X-ray Tomography in Material Science* (Hermes Science).
- Bay, B.K., Smith, T.S., Fyhrie, D.P., and Saad, M. (1999). Digital volume correlation: Three-dimensional strain mapping using X-ray tomography. *Exp. Mech.* 39, 217–226.
- Belmares-Perales, S., Castro-Román, M., Herrera-Trejo, M., and Ramírez-Vidaurre, L.E. (2008). Effect of cooling rate and Fe/Mn weight ratio on volume fractions of  $\alpha$ -AlFeSi and  $\beta$ -AlFeSi phases in Al–7.3Si–3.5Cu alloy. *Met. Mater. Int.* 14, 307–314.

## References

---

- Boileau, J.M., and Allison, J.E. (2003). The effect of solidification time and heat treatment on the fatigue properties of a cast 319 aluminum alloy. *Metall. Mater. Trans. A* *34*, 1807–1820.
- Borbély, A., Mughrabi, H., Eisenmeier, G., and Höppel, H.W. (2002). A finite element modelling study of strain localization in the vicinity of near-surface cavities as a cause of subsurface fatigue crack initiation. *Int. J. Fract.* *115*, 227–232.
- Bornert, M., Chaix, J.-M., Doumalin, P., Dupré, J.-C., Fournel, T., Jeulin, D., Maire, E., Moreaud, M., and Moulinec, H. (2004). Mesure tridimensionnelle de champs cinématiques par imagerie volumique pour l'analyse des matériaux et des structures. *Instrum. Mes. Métrologie* *4*, 43–88.
- Botsis, J., and Humbert, L. (2006). *Elements of Fracture Mechanics* (Lausannem Swiss: Swiss Federal Institute of Technology, Lausanne).
- Boulos, V., Fristot, V., Houzet, D., Salvo, L., and Lhuissier, P. (2012). Investigating performance variations of an optimized GPU-ported granulometry algorithm. In *2012 Conference on Design and Architectures for Signal and Image Processing (DASIP)*, pp. 1–6.
- Buffière, J.-Y. (2004). Experimental study of the three-dimensional character of short fatigue cracks in a cast aluminium alloy. *Metall. Res. Technol.* *101*, 623–635.
- Buffière, J.-Y., Savelli, S., Jouneau, P.H., Maire, E., and Fougères, R. (2001). Experimental study of porosity and its relation to fatigue mechanisms of model Al–Si7–Mg0.3 cast Al alloys. *Mater. Sci. Eng. A* *316*, 115–126.
- Buffiere, J.-Y., Maire, E., Adrien, J., Masse, J.-P., and Boller, E. (2010). In Situ Experiments with X ray Tomography: an Attractive Tool for Experimental Mechanics. *Exp. Mech.* *50*, 289–305.
- Caceres, C.H., Griffiths, J.R., and Reiner, P. (1996). The influence of microstructure on the Bauschinger effect in an Al-Si-Mg casting alloy. *Acta Mater.* *44*, 15–23.
- Cao, X., and Campbell, J. (2003). The nucleation of Fe-Rich phases on oxide films in Al-11.5Si-0.4Mg cast alloys. *Metall. Mater. Trans. A* *34*, 1409–1420.
- Casari, D., Fortini, A., and Merlin, M. (2013). Fracture behaviour of grain refined A356 cast aluminium alloy: tensile and Charpy impact specimens. In *Convegno Nazionale IGF XXII*, (Roma, Italia), pp. 314–321.
- Caty, O., Buffiere, J.-Y., Maire, E., and Adrien, J. (2011). 3D Characterization of the Influence of Porosity on Fatigue Properties of a Cast Al Alloy. *Adv. Eng. Mater.* *13*, 194–198.
- Chan, K.S., Jones, P., and Wang, Q. (2003). Fatigue crack growth and fracture paths in sand cast B319 and A356 aluminum alloys. *Mater. Sci. Eng. A* *341*, 18–34.
- Charbonnier, A. (Alain) (1992). Secondary dendrite ARM spacing determination in Al-Si casting alloys by conductivity measurements. Master thesis. McGill University.
- Charkaluk, E., Constantinescu, A., Szmytka, F., and Tabibian, S. (2014). Probability density functions: From porosities to fatigue lifetime. *Int. J. Fatigue* *63*, 127–136.
- Chen, C.-L., Richter, A., and Thomson, R.C. (2009). Mechanical properties of intermetallic phases in multi-component Al–Si alloys using nanoindentation. *Intermetallics* *17*, 634–641.

## References

---

- Chen, C.-L., Richter, A., and Thomson, R.C. (2010). Investigation of mechanical properties of intermetallic phases in multi-component Al–Si alloys using hot-stage nanoindentation. *Intermetallics* 18, 499–508.
- Chirita, G.M. (2011). Mechanical and Fatigue Properties of Functionally Graded Aluminium Silicon Alloys. PhD Thesis. Universidade do Minho.
- Cloetens, P., Pateyron-Salomé, M., Buffière, J.Y., Peix, G., Baruchel, J., Peyrin, F., and Schlenker, M. (1997). Observation of microstructure and damage in materials by phase sensitive radiography and tomography. *J. Appl. Phys.* 81, 5878–5886.
- Department of defense, U.S.A (1966). Military standardization handbook: aluminum and aluminum alloys.
- Dietrich, L., and Radziejewska, J. (2011). The fatigue damage development in a cast Al–Si–Cu alloy. *Mater. Des.* 32, 322–329.
- Dinnis, C.M., Taylor, J.A., and Dahle, A.K. (2005). As-cast morphology of iron-intermetallics in Al–Si foundry alloys. *Scr. Mater.* 53, 955–958.
- Dinnis, C.M., Taylor, J.A., and Dahle, A.K. (2006). Iron-related porosity in Al–Si–(Cu) foundry alloys. *Mater. Sci. Eng. A* 425, 286–296.
- Dobrzański, L.A., Borek, W., and Maniara, R. (2006). Influence of the crystallization condition on Al–Si–Cu casting alloys structure. *J. Achiev. Mater. Manuf. Eng.* 18, 211–214.
- Dobrzański, L.A., Maniara, R., Krupiński, M., and Sokolowski, J.H. (2007). Microstructure and mechanical properties of AC AlSi9CuX alloys. *J. Achiev. Mater. Manuf. Eng.* Vol. 24, 51–54.
- Edwards, W.M. (2002). Microstructural and mechanical property modelling for the processing of Al–Si alloys. PhD Thesis. Loughborough University.
- El Bartali, A. (2007). Apport des mesures de champs cinématiques à l'étude des micromécanismes d'endommagement en fatigue plastique d'un acier inoxydable duplex. PhD thesis, Ecole Centrale de Lille.
- El-Labban (2013). Characterization of aluminum alloy-based nanocomposites produced by the addition of al-ti5-b1 to the matrix melt. *Am. J. Nanotechnol.* 4, 8–15.
- Emamy, M., Mahta, M., and Rasizadeh, J. (2006). Formation of TiB<sub>2</sub> particles during dissolution of TiAl<sub>3</sub> in Al–TiB<sub>2</sub> metal matrix composite using an in situ technique. *Compos. Sci. Technol.* 66, 1063–1066.
- E. M. Elgallad, F.H.S. (2010). Effects of Additives on the Microstructures and Tensile Properties of a New Al–Cu Based Alloy Intended for Automotive Castings. In 2010 AFS Transactions, (Schaumburg, IL. USA), pp. 39–56.
- Fan, J., McDowell, D.L., Horstemeyer, M.F., and Gall, K. (2001). Computational micromechanics analysis of cyclic crack-tip behavior for microstructurally small cracks in dual-phase Al–Si alloys. *Eng. Fract. Mech.* 68, 1687–1706.
- Fan, J., McDowell, D.L., Horstemeyer, M.F., and Gall, K. (2003). Cyclic plasticity at pores and inclusions in cast Al–Si alloys. *Eng. Fract. Mech.* 70, 1281–1302.

## References

---

- Feng, L. (2013). Effect of Non-metallic Inclusions on the Local Stress Concentration within Materials. *J. Mech. Eng.* 49, 41.
- Ferreira, T., and Rasband, W. (2012). ImageJ User Guide (IJ 1.46r).
- Firouzdor, V., Rajabi, M., Nejati, E., and Khomamizadeh, F. (2007). Effect of microstructural constituents on the thermal fatigue life of A319 aluminum alloy. *Mater. Sci. Eng. A* 454–455, 528–535.
- Gall, Yang, Horstemeyer, McDowell, and Fan (2000a). The influence of modified intermetallics and Si particles on fatigue crack paths in a cast A356 Al alloy. *Fatigue Fract. Eng. Mater. Struct.* 23, 159–172.
- Gall, K., Yang, N., Horstemeyer, M., McDowell, D.L., and Fan, J. (1999). The debonding and fracture of Si particles during the fatigue of a cast Al-Si alloy. *Metall. Mater. Trans. A* 30, 3079–3088.
- Gall, K., Horstemeyer, M., McDowell, D.L., and Fan, J. (2000b). Finite element analysis of the stress distributions near damaged Si particle clusters in cast Al-Si alloys. *Mech. Mater.* 32, 277–301.
- Gall, K., Horstemeyer, M.F., Degner, B.W., McDowell, D.L., and Fan, J. (2001). On the driving force for fatigue crack formation from inclusions and voids in a cast A356 aluminum alloy. *Int. J. Fract.* 108, 207–233.
- Gao, Y.X., Yi, J.Z., Lee, P.D., and Lindley, T.C. (2004). A micro-cell model of the effect of microstructure and defects on fatigue resistance in cast aluminum alloys. *Acta Mater.* 52, 5435–5449.
- Geffroy, P.-M., Lakehal, M., Goñi, J., Beaunon, E., Heintz, J.-M., and Silvain, J.-F. (2006). Thermal and mechanical behavior of Al-Si alloy cast using magnetic molding and lost foam processes. *Metall. Mater. Trans. A* 37, 441–447.
- Gomes Perini, L.A., Passieux, J.-C., and Périé, J.-N. (2014). A Multigrid PGD-based Algorithm for Volumetric Displacement Fields Measurements. *Strain* 50, 355–367.
- González, R., Martínez, D.I., González, J.A., Talamantes, J., Valtierra, S., and Colás, R. (2011). Experimental investigation for fatigue strength of a cast aluminium alloy. *Int. J. Fatigue* 33, 273–278.
- Grediac, M., and Hild, F. (2012). *Full-Field Measurements and Identification in Solid Mechanics* (London: Wiley-Blackwell).
- Gruzleski, J.E., and Closset, B. (1990). *Treatment of Liquid Aluminum-Silicon Alloys* (Des Plaines, IL: Amer Foundrymens Society).
- Gruzleski, J.E., Closset, B.M., and Society, A.F. (1990). *The treatment of liquid aluminum-silicon alloys* (American Foundrymen's Society, Inc.).
- Hart, E.W. (1972). Theory of dispersion hardening in metals. *Acta Metall.* 20, 275–289.
- Heinz, A., Haszler, A., Keidel, C., Moldenhauer, S., Benedictus, R., and Miller, W.S. (2000). Recent development in aluminium alloys for aerospace applications. *Mater. Sci. Eng. A* 280, 102–107.
- Herman, G.T. (2010). *Fundamentals of Computerized Tomography - Image Reconstruction from Projections*.
- Hild, F., and Roux, S. (2006). Digital Image Correlation: from Displacement Measurement to Identification of Elastic Properties – a Review. *Strain* 42, 69–80.



## References

---

- Hirsch, J. (2011). Aluminium in Innovative Light-Weight Car Design. *Mater. Trans.* 52, 818–824.
- Horstemeyer, M.F., Gall, K., Dolan, K.W., Waters, A., Haskins, J.J., Perkins, D.E., Gokhale, A.M., and Dighe, M.D. (2003). Numerical, experimental, nondestructive, and image analyses of damage progression in cast A356 aluminum notch tensile bars. *Theor. Appl. Fract. Mech.* 39, 23–45.
- Hull, D., and Bacon, D.J. (2001). *Introduction to Dislocations* (Butterworth-Heinemann).
- Hutchinson, J.W. (1968). Plastic stress and strain fields at a crack tip. *J. Mech. Phys. Solids* 16, 337–342.
- ImageJ Software (2013). ImageJ <http://imagej.nih.gov/ij/>.
- Ji, S., Yang, W., Gao, F., Watson, D., and Fan, Z. (2013). Effect of iron on the microstructure and mechanical property of Al–Mg–Si–Mn and Al–Mg–Si diecast alloys. *Mater. Sci. Eng. A* 564, 130–139.
- Joy, D.C. (2006). *Scanning Electron Microscopy*. In *Materials Science and Technology*, (Wiley-VCH Verlag GmbH & Co. KGaA),.
- Kastner, J., Harrer, B., and Degischer, H.P. (2011). High resolution cone beam X-ray computed tomography of 3D-microstructures of cast Al-alloys. *Mater. Charact.* 62, 99–107.
- Kaufman, J.G., and Rooy, E.L. (2004). *Aluminum Alloy Castings: Properties, Processes, and Applications* (ASM International).
- Klein, S., and Staring, M. (2012). *Elastix the manual*.
- Klein, S., Staring, M., and Pluim, J.P.W. (2007). Evaluation of Optimization Methods for Nonrigid Medical Image Registration Using Mutual Information and B-Splines. *IEEE Trans. Image Process.* 16, 2879–2890.
- Klein, S., Pluim, J.P.W., Staring, M., and Viergever, M.A. (2009). Adaptive Stochastic Gradient Descent Optimisation for Image Registration. *Int. J. Comput. Vis.* 81, 227–239.
- Klein, S., Staring, M., Murphy, K., Viergever, M.A., and Pluim, J.P.W. (2010). elastix: a toolbox for intensity-based medical image registration. *IEEE Trans. Med. Imaging* 29, 196–205.
- Kosa, A., Gacsi, Z., and Dul, J. (2012). Effects of strontium on the microstructure of Al-Si casting alloys. *Mater. Sci. Eng.* 37, 43–50.
- Krumeich, F. (2011). *Properties of Electrons, their Interactions with Matter and Applications in Electron Microscopy*.
- Kyle, A.C., Jerri, M., and Miloslav, N. (2012). Advances in Aluminum Relative to Ship Survivability. *Nav. Eng. J.* 124, 105–114.
- Lachambre, J. (2014). Développement d'une Méthode de Caractérisation 3D des Fissures de Fatigue à l'aide de la Corrélation d'Images Numériques obtenues par Tomographie X. Ph. D. thesis, Institut National des Sciences Appliquées de Lyon.
- Lachambre, J., Réthoré, J., Weck, A., and Buffiere, J.-Y. (2014). Extraction of stress intensity factors for 3D small fatigue cracks using digital volume correlation and X-ray tomography. *Int. J. Fatigue*.
- Lee, P.D., and Hunt, J.D. (1997). Hydrogen porosity in directional solidified aluminium-copper alloys: in situ observation. *Acta Mater.* 45, 4155–4169.

## References

---

- Lee, S.G., and Gokhale, A.M. (2006). Formation of gas induced shrinkage porosity in Mg-alloy high-pressure die-castings. *Scr. Mater.* 55, 387–390.
- Lee, Y.-B., Siljander, A., and Lawrence, F.V. (1992). The role of casting porosity in fatigue properties of Al–Si 319 lost foam cast alloy. *KSME J.* 6, 81–87.
- Lester, H., and Arridge, S.R. (1999). A survey of hierarchical non-linear medical image registration. *Pattern Recognit.* 32, 129–149.
- Li, P., Lee, P.D., Maijer, D.M., and Lindley, T.C. (2009). Quantification of the interaction within defect populations on fatigue behavior in an aluminum alloy. *Acta Mater.* 57, 3539–3548.
- Li, Z., Samuel, A.M., Samuel, F.H., Ravindran, C., and Valtierra, S. (2003). Effect of alloying elements on the segregation and dissolution of CuAl<sub>2</sub> phase in Al-Si-Cu 319 alloys. *J. Mater. Sci.* 38, 1203–1218.
- Limodin, N., Réthoré, J., Buffière, J.-Y., Gravouil, A., Hild, F., and Roux, S. (2009a). Crack closure and stress intensity factor measurements in nodular graphite cast iron using three-dimensional correlation of laboratory X-ray microtomography images. *Acta Mater.* 57, 4090–4101.
- Limodin, N., Salvo, L., Boller, E., Suéry, M., Felberbaum, M., Gaillière, S., and Madi, K. (2009b). In situ and real-time 3-D microtomography investigation of dendritic solidification in an Al–10 wt.% Cu alloy. *Acta Mater.* 57, 2300–2310.
- Limodin, N., Réthoré, J., Buffière, J.-Y., Hild, F., Roux, S., Ludwig, W., Rannou, J., and Gravouil, A. (2010). Influence of closure on the 3D propagation of fatigue cracks in a nodular cast iron investigated by X-ray tomography and 3D volume correlation. *Acta Mater.* 58, 2957–2967.
- Limodin, N., Réthoré, J., Adrien, J., Buffière, J.-Y., Hild, F., and Roux, S. (2011). Analysis and Artifact Correction for Volume Correlation Measurements Using Tomographic Images from a Laboratory X-ray Source. *Exp. Mech.* 51, 959–970.
- Limodin, N., Tabibian, S., El Bartali, A., Long, W., Dahdah, N., Rethore, J., Seghir, R., Witz, J.-F., Buffiere, J.-Y., and Charkaluk, E. (2014a). Fatigue of a Lost Foam Cast A319 alloy: influence of the microstructure on the damage micromechanisms (Melbourne).
- Limodin, N., El Bartali, A., Wang, L., Lachambre, J., Buffiere, J.-Y., and Charkaluk, E. (2014b). Application of X-ray microtomography to study the influence of the casting microstructure upon the tensile behaviour of an Al–Si alloy. *Nucl. Instrum. Methods Phys. Res. Sect. B Beam Interact. Mater. At.* 324, 57–62.
- Liu, B., Peng, C., Wang, R., Wang, X., and Li, T. (2010). Recent development and prospects for giant plane aluminum alloys. *Chin. J. Nonferrous Met.* 20, 1705–1715.
- Lu, L., and Dahle, A.K. (2005). Iron-rich intermetallic phases and their role in casting defect formation in hypoeutectic Al–Si alloys. *Metall. Mater. Trans. A* 36, 819–835.
- Ma, Z., Samuel, A.M., Doty, H.W., Valtierra, S., and Samuel, F.H. (2014). Effect of Fe content on the fracture behaviour of Al–Si–Cu cast alloys. *Mater. Des.* 57, 366–373.
- Mandal, D. (2008). Near Net Shape Casting through Investment, Die and Centrifugal Casting. (NML, Jamshedpur), pp. 1–19.
- Marone, F., Münch, B., and Stampanoni, M. (2010). Fast reconstruction algorithm dealing with tomography artifacts. p. 7804.

## References

---

- Martínez D., E.J., Cisneros G., M.A., Valtierra, S., and Lacaze, J. (2005). Effect of strontium and cooling rate upon eutectic temperatures of A319 aluminum alloy. *Scr. Mater.* 52, 439–443.
- Mbuya, T.O. (2011). Analysis of microstructure and fatigue micromechanisms in cast aluminium piston alloys. PhD Thesis. University of Southampton.
- Mbuya, T.O., Sinclair, I., Moffat, A.J., and Reed, P.A.S. (2012). Micromechanisms of fatigue crack growth in cast aluminium piston alloys. *Int. J. Fatigue* 42, 227–237.
- McDowell, D.L., Gall, K., Horstemeyer, M.F., and Fan, J. (2003). Microstructure-based fatigue modeling of cast A356-T6 alloy. *Eng. Fract. Mech.* 70, 49–80.
- Miller, W.S., Zhuang, L., Bottema, J., Wittebrood, A.J., De Smet, P., Haszler, A., and Vieregge, A. (2000). Recent development in aluminium alloys for the automotive industry. *Mater. Sci. Eng. A* 280, 37–49.
- Moës, N., Dolbow, J., and Belytschko, T. (1999). A finite element method for crack growth without remeshing. *Int. J. Numer. Methods Eng.* 46, 131–150.
- Moffat, A.J. (2007). Micromechanistic analysis of fatigue in aluminium silicon casting alloys. PhD Thesis. University of Southampton.
- Moffat, A.J., Mellor, B.G., Chen, C.L., Thomson, R.C., and Reed, P.A.S. (2006). Microstructural Analysis of Fatigue Initiation in Al-Si Casting Alloys. *Mater. Sci. Forum* 519-521, 1083–1088.
- Momose, A., Takeda, T., Itai, Y., and Hirano, K. (1996). Phase-contrast X-ray computed tomography for observing biological soft tissues. *Nat. Med.* 2, 473–475.
- Monroe, R. (2005). Porosity in castings. *AFS Trans.* 113, 519–546.
- Mu, P., Nadot, Y., Nadot-Martin, C., Chabod, A., Serrano-Munoz, I., and Verdu, C. (2014). Influence of casting defects on the fatigue behavior of cast aluminum AS7G06-T6. *Int. J. Fatigue* 63, 97–109.
- Nanakasse, S. (2013). Modélisation de l'effet de particularités microstructurales sur la tenue de fatigue thermomécanique d'alliage d'aluminium (École Polytechnique (Rapport de stage de recherche)).
- Newbury, D.E. (1986). *Advanced Scanning Electron Microscopy and X-Ray Microanalysis* (Springer).
- Nguyen, H. (2005). The effects of solidification rates on porosity formation and cast microstructure of aluminum alloy A356 (Grand Valley State University).
- Niane, N.T., and Michalet, J.-P. (2011). Validation of Foundry Process for Aluminum Parts with Flow3D Software. In *Proceedings of the 2011 International Symposium on Liquid Metal Processing and Casting, 2011*, (New York),.
- Nicoletto, G., Anzelotti, G., and Konečná, R. (2010). X-ray computed tomography vs. metallography for pore sizing and fatigue of cast Al-alloys. *Procedia Eng.* 2, 547–554.
- Nicoletto, G., Konečná, R., and Fintova, S. (2012). Characterization of microshrinkage casting defects of Al-Si alloys by X-ray computed tomography and metallography. *Int. J. Fatigue* 41, 39–46.
- Pan, B. (2007). Research on Digital Image Correlation with Its Application in Experimental Mechanics. PhD thesis, Tsinghua University.

## References

---

- Pan, B., Qian, K., Xie, H., and Asundi, A. (2009). Two-dimensional digital image correlation for in-plane displacement and strain measurement: a review. *Meas. Sci. Technol.* 20, 062001.
- Pan, B., Wu, D., and Wang, Z. (2012). Internal displacement and strain measurement using digital volume correlation: a least-squares framework. *Meas. Sci. Technol.* 23, 045002.
- Passieux, J.-C., and Périé, J.-N. (2012). High resolution digital image correlation using proper generalized decomposition: PGD-DIC. *Int. J. Numer. Methods Eng.* 92, 531–550.
- Pavlovic-Krstic, J. (2010). Impact of casting parameters and chemical composition on the solidification behaviour of Al-Si-Cu hypoeutectic alloy. PhD Thesis. Magdeburg, Univ.
- Prasannavenkatesan, R., Zhang, J., McDowell, D.L., Olson, G.B., and Jou, H.-J. (2009). 3D modeling of subsurface fatigue crack nucleation potency of primary inclusions in heat treated and shot peened martensitic gear steels. *Int. J. Fatigue* 31, 1176–1189.
- Preibisch, S., Saalfeld, S., and Tomancak, P. (2009). Globally optimal stitching of tiled 3D microscopic image acquisitions. *Bioinformatics* 25, 1463–1465.
- Puncreobutr, C., Lee, P.D., Kareh, K.M., Connolley, T., Fife, J.L., and Phillion, A.B. (2014). Influence of Fe-rich intermetallics on solidification defects in Al-Si-Cu alloys. *Acta Mater.* 68, 42–51.
- Rabinovich, S.G. (1999). *Measurement Errors and Uncertainties - Theory and Practice*.
- Rana, R.S., Purohit, R., and Das, S. (2012). Reviews on the Influences of Alloying elements on the Microstructure and Mechanical Properties of Aluminum Alloys and Aluminum Alloy Composites. *Int. J. Sci. Res. Publ.* 2, 1–7.
- Réthoré, J., Hild, F., and Roux, S. (2008). Extended digital image correlation with crack shape optimization. *Int. J. Numer. Methods Eng.* 73, 248–272.
- Réthoré, J., Limodin, N., Buffière, J.-Y., Roux, S., and Hild, F. (2012). Three-dimensional Analysis of Fatigue Crack Propagation using X-Ray Tomography, Digital Volume Correlation and Extended Finite Element Simulations. *Procedia IUTAM* 4, 151–158.
- Reu, P.L. (2013). Uncertainty Quantification for 3D Digital Image Correlation. In *Imaging Methods for Novel Materials and Challenging Applications, Volume 3*, H. Jin, C. Sciammarella, C. Furlong, and S. Yoshida, eds. (Springer New York), pp. 311–317.
- Rosefort, M., Matthies, C., Buck, H., and Koch, H. (2011). Using SEM and EDX for a Simple Differentiation of  $\alpha$ - and  $\beta$ -AlFeSi-Phases in Wrought Aluminum Billets. In *Light Metals 2011*, S.J. Lindsay, ed. (John Wiley & Sons, Inc.), pp. 711–716.
- Roux, S., Hild, F., Viot, P., and Bernard, D. (2008). Three-dimensional image correlation from X-ray computed tomography of solid foam. *Compos. Part Appl. Sci. Manuf.* 39, 1253–1265.
- Rueckert, D., Sonoda, L.I., Hayes, C., Hill, D.L., Leach, M.O., and Hawkes, D.J. (1999). Nonrigid registration using free-form deformations: application to breast MR images. *IEEE Trans. Med. Imaging* 18, 712–721.
- Saigal, A., and Fuller Jr., E.R. (2001). Analysis of stresses in aluminum-silicon alloys. *Comput. Mater. Sci.* 21, 149–158.
- Saint Jean Industries (2013). Technical publication: The gravity die casting.

## References

---

- Salvo, L., Suéry, M., Marmottant, A., Limodin, N., and Bernard, D. (2010). 3D imaging in material science: Application of X-ray tomography. *Comptes Rendus Phys.* *11*, 641–649.
- Salvo, L., Lhuissier, P., Scheel, M., Terzi, S., Michiel, M.D., Boller, E., Taylor, J.A., Dahle, A.K., and Suéry, M. (2012). 3D In Situ Imaging of Aluminium Alloys During Solidification. *Trans. Indian Inst. Met.* *65*, 623–626.
- Samuel, E. H., Samuel, A.M., and Doty, H.W. (1996). Factors Controlling the type and Morphology of Cu-Containing Phases in 319 Al Alloy. *Trans.- Am. FOUNDRYMENS Soc.* *104*, 893–902.
- Schijve, J. (2008). *Fatigue of Structures and Materials* (Springer Science & Business Media).
- Sehitoglu, H., Smith, T., Qing, X., Maier, H.J., and Allison, J.A. (2000). Stress-strain response of a cast 319-T6 aluminum under thermomechanical loading. *Metall. Mater. Trans. A* *31*, 139–151.
- Shi, Y., Cheng, M., and Wang, Y. (2005). Application and Study of Aluminum Alloy in Building Structures. *Build. Sci.* *21*, 7–20.
- Shih, T.-S., and Chen, I.-C. (2005). Decomposition and reaction of thermal-formed alumina in aluminum alloy castings. *Mater. Trans.* *46*, 1868–1876.
- Shore, R.J. (1968). Effects of Porosity on High Strength Aluminum Alloy A.A. 7039 (Ohio State University).
- Sjölander, E., and Seifeddine, S. (2010). Optimisation of solution treatment of cast Al–Si–Cu alloys. *Mater. Des.* *31*, *Supplement 1*, S44–S49.
- Skillingberg, M., and Green, J. (2007). Aluminum Applications in the Rail Industry. *Light Met. Age* *65*.
- Smith, T.S., Bay, B.K., and Rashid, M.M. (2002). Digital volume correlation including rotational degrees of freedom during minimization. *Exp. Mech.* *42*, 272–278.
- Sobolev, V.V., and Guilemany, J.M. (1996). The formation of coating shrinkage porosity in the process of thermal spraying. *J. Mater. Process. Technol.* *58*, 227–232.
- Song, M.S., Kong, Y.Y., Ran, M.W., and She, Y.C. (2011). Cyclic stress–strain behavior and low cycle fatigue life of cast A356 alloys. *Int. J. Fatigue* *33*, 1600–1607.
- Sotiras, A., Davatzikos, C., and Paragios, N. (2013). Deformable Medical Image Registration: A Survey. *IEEE Trans. Med. Imaging* *32*, 1153–1190.
- Starink, M.J. (2005). Reduced fracturing of intermetallic particles during crack propagation in age hardening Al-based alloys due to PFZs. *Mater. Sci. Eng. A* *390*, 260–264.
- Stolarz, J., Madelaine-Dupuich, O., and Magnin, T. (2001). Microstructural factors of low cycle fatigue damage in two phase Al–Si alloys. *Mater. Sci. Eng. A* *299*, 275–286.
- Surappa, M.K., Blank, E., and Jaquet, J.C. (1986). Effect of macro-porosity on the strength and ductility of cast Al-7Si-0.3Mg alloy. *Scr. Metall.* *20*, 1281–1286.
- Sutton, M.A., Li, N., Joy, D.C., Reynolds, A.P., and Li, X. (2007a). Scanning Electron Microscopy for Quantitative Small and Large Deformation Measurements Part I: SEM Imaging at Magnifications from 200 to 10,000. *Exp. Mech.* *47*, 775–787.



## References

---

- Sutton, M.A., Li, N., Garcia, D., Cornille, N., Orteu, J.J., McNeill, S.R., Schreier, H.W., Li, X., and Reynolds, A.P. (2007b). Scanning Electron Microscopy for Quantitative Small and Large Deformation Measurements Part II: Experimental Validation for Magnifications from 200 to 10,000. *Exp. Mech.* *47*, 789–804.
- Sutton, M.A., Orteu, J.J., and Schreier, H. (2009). *Image Correlation for Shape, Motion and Deformation Measurements: Basic Concepts, Theory and Applications* (New York: Springer).
- Szmytka, F., Limodin, N., Wang, L., Adrien, J., Charkaluk, E., and Buffiere, J.-Y. (2014). Probabilistic Thermal-mechanical Fatigue Criteria for Lost Foam Casting Aluminium Alloys based on 2D/3D porosities distribution. In *MATEC Web of Conferences*, (Paris, France),.
- Tabibian, S. (2011). *Contributions to Thermomechanical Fatigue Criteria for Lost Foam Casting Aluminum Alloys*. PhD thesis. Ecole Centrale de Lille.
- Tabibian, S., Charkaluk, E., Constantinescu, A., Oudin, A., and Szmytka, F. (2010). Behavior, damage and fatigue life assessment of lost foam casting aluminum alloys under thermo-mechanical fatigue conditions. *Procedia Eng.* *2*, 1145–1154.
- Tabibian, S., Charkaluk, E., Constantinescu, A., Szmytka, F., and Oudin, A. (2013). TMF–LCF life assessment of a Lost Foam Casting A319 aluminum alloy. *Int. J. Fatigue* *53*, 75–81.
- Tahamtan, S., and Fadavi, A. (2010). Microstructural characteristics of thixoforged A356 alloy in mushy state. *Trans. Nonferrous Met. Soc. China* *20*, *Supplement 3*, s781–s787.
- Tanem, B.S., Svenningsen, G., and Mårdalen, J. (2005). Relations between sample preparation and SKPFM Volta potential maps on an EN AW-6005 aluminium alloy. *Corros. Sci.* *47*, 1506–1519.
- Taylor, J.A. (2004). The effect of iron in Al-Si casting alloys. (Australian Foundry Institute (AFI)), pp. 148–157.
- Terzi, S., Taylor, J.A., Cho, Y.H., Salvo, L., Suéry, M., Boller, E., and Dahle, A.K. (2010). In situ study of nucleation and growth of the irregular  $\alpha$ -Al/ $\beta$ -Al<sub>15</sub>FeSi eutectic by 3-D synchrotron X-ray microtomography. *Acta Mater.* *58*, 5370–5380.
- Tolnai, D., Degischer, H.P., and Lendvai, J. (2009). Characterization of phases in an Al casting alloy by synchrotron tomography. *Phys. Status Solidi A* *206*, 1850–1854.
- Unser, M. (1999). Splines: a perfect fit for signal and image processing. *IEEE Signal Process. Mag.* *16*, 22–38.
- Verdu, C., Cercueil, H., Communal, S., Sainfort, P., and Fougères, R. (1996). Microstructural Aspects of the Damage Mechanisms of Cast Al-7Si-Mg Alloys. *Mater. Sci. Forum* *217-222*, 1449–1454.
- Verhulp, E., Rietbergen, B. van, and Huiskes, R. (2004). A three-dimensional digital image correlation technique for strain measurements in microstructures. *J. Biomech.* *37*, 1313–1320.
- Verreman, Y., and Nie, B. (1991). Short Crack Growth and Coalescence Along the Toe of a Manual Fillet Weld. *Fatigue Fract. Eng. Mater. Struct.* *14*, 337–349.
- Voncina, M., MEDVED, J., BONČINA, T., and ZUPANIČ, F. (2014). Effect of Ce on morphology of  $\alpha$ (Al)–Al<sub>2</sub>Cu eutectic in Al–Si–Cu alloy. *Trans. Nonferrous Met. Soc. China* *24*, 36–41.
- Wang, Q. (2013). Latest advances and developments in aluminum shape casting. *China Foundry* *10*, 43–49.

## References

---

- Wang, X. (2014). Study of plastic deformation in oligo- and single crystals based on kinematic-thermal full-field measurements. PhD thesis. Lille 1.
- Wang, Q.G., and Cáceres, C.H. (1997). Mg Effects on the Eutectic Structure and Tensile Properties of Al-Si-Mg Alloys. *Mater. Sci. Forum* 242, 159–164.
- Wang, J., Lee, P.D., Hamilton, R.W., Li, M., and Allison, J. (2009). The kinetics of Fe-rich intermetallic formation in aluminium alloys: In situ observation. *Scr. Mater.* 60, 516–519.
- Wang, Q.G., Apelian, D., and Lados, D.A. (2001a). Fatigue behavior of A356-T6 aluminum cast alloys. Part I. Effect of casting defects. *J. Light Met.* 1, 73–84.
- Wang, Q.G., Apelian, D., and Lados, D.A. (2001b). Fatigue behavior of A356/357 aluminum cast alloys. Part II – Effect of microstructural constituents. *J. Light Met.* 1, 85–97.
- Wang, Q.G., Crepeau, P.N., Davidson, C.J., and Griffiths, J.R. (2006). Oxide films, pores and the fatigue lives of cast aluminum alloys. *Metall. Mater. Trans. B* 37, 887–895.
- Wang, Q.Y., Bathias, C., Kawagoishi, N., and Chen, Q. (2002). Effect of inclusion on subsurface crack initiation and gigacycle fatigue strength. *Int. J. Fatigue* 24, 1269–1274.
- Warmuzek, M. (2004). *Aluminum-silicon Casting Alloys: An Atlas of Microfractographs* (ASM International).
- Wikipedia (2014a). Aluminium <http://en.wikipedia.org/wiki/Aluminium>.
- Wikipedia (2014b). Lead <http://en.wikipedia.org/wiki/Lead>.
- Wu, Y., Xiong, J., Lai, R., Zhang, X., and Guo, Z. (2009). The microstructure evolution of an Al–Mg–Si–Mn–Cu–Ce alloy during homogenization. *J. Alloys Compd.* 475, 332–338.
- Ye, H. (2003). An overview of the development of Al-Si-Alloy based material for engine applications. *J. Mater. Eng. Perform.* 12, 288–297.
- Yi, J.Z., Gao, Y.X., Lee, P.D., Flower, H.M., and Lindley, T.C. (2003). Scatter in fatigue life due to effects of porosity in cast A356-T6 aluminum-silicon alloys. *Metall. Mater. Trans. A* 34, 1879–1890.
- Yi, J.Z., Gao, Y.X., Lee, P.D., and Lindley, T.C. (2004). Effect of Fe-content on fatigue crack initiation and propagation in a cast aluminum–silicon alloy (A356–T6). *Mater. Sci. Eng. A* 386, 396–407.
- Yi, J.Z., Lee, P.D., Lindley, T.C., and Fukui, T. (2006). Statistical modeling of microstructure and defect population effects on the fatigue performance of cast A356-T6 automotive components. *Mater. Sci. Eng. A* 432, 59–68.
- Zeng, L., Sakamoto, J., Fujii, A., and Noguchi, H. (2014). Role of eutectic silicon particles in fatigue crack initiation and propagation and fatigue strength characteristics of cast aluminum alloy A356. *Eng. Fract. Mech.* 115, 1–12.
- Zeren, M., KARAKULAK, E., and GÜMÜŞ, S. (2011). Influence of Cu addition on microstructure and hardness of near-eutectic Al-Si-xCu-alloys. *Trans. Nonferrous Met. Soc. China* 21, 1698–1702.
- Zhang, Chen, and Poirier (2000). Effect of solidification cooling rate on the fatigue life of A356.2-T6 cast aluminium alloy. *Fatigue Fract. Eng. Mater. Struct.* 23, 417–423.

## References

---

- Zhang, G., Zhang, J., Li, B., and Cai, W. (2011). Characterization of tensile fracture in heavily alloyed Al-Si piston alloy. *Prog. Nat. Sci. Mater. Int.* *21*, 380–385.
- Zhang, H., Toda, H., Hara, H., Kobayashi, M., Kobayashi, T., Sugiyama, D., Kuroda, N., and Uesugi, K. (2007). Three-Dimensional Visualization of the Interaction between Fatigue Crack and Micropores in an Aluminum Alloy Using Synchrotron X-Ray Microtomography. *Metall. Mater. Trans. A* *38*, 1774–1785.
- Zhao, L., Liao, H., Pan, Y., Wang, Q., and Sun, G. (2011). In-situ observation of porosity formation during directional solidification of Al-Si casting alloys. *CHINA FOUNDRY* *08*, 14–18.
- ZIB (Konrad-Zuse-Zentrum für Informationstechnik Berlin), and VSG (Visualization Sciences Group). (2012). Avizo Online Help <http://www.fei.com/software/avizo-3d-resources/>.
- Zitová, B., and Flusser, J. (2003). Image registration methods: a survey. *Image Vis. Comput.* *21*, 977–1000.
- Zwieg, T. (2003). Specimen preparation for high edge retention of aluminum alloys. *Ind. Heat.* *70*, 43–45.

## Extended Abstract (French)

Dans l'industrie automobile, le moulage en coquille par gravité est le procédé généralement utilisé pour la fabrication des culasses. Il est progressivement remplacé par le Procédé à Modèle Perdu (PMP) dans un but d'optimisation de la géométrie, de réduction des coûts et de contrôle de la consommation des véhicules. Cependant, les pièces automobiles en alliage d'aluminium fabriquées par PMP ont une microstructure plus grossière et plus de pores que les pièces fabriquées en moulage en coquille par gravité à des vitesses de refroidissement plus rapides (0.8 °C/s pour le moulage en coquille, 30 °C/s pour le PMP). Cette microstructure a une influence majeure sur le comportement en fatigue. Les travaux récents de Tabibian (Tabibian, 2011) ont montré que la durée de vie de l'alliage A319 obtenue par PMP est considérablement réduite par rapport au même alliage obtenu en moulage coquille par gravité bien que la réponse cyclique macroscopique soit pratiquement inchangée.

Au cours des dernières années, des études ont été réalisées afin d'identifier les mécanismes d'endommagement des alliages Al-Si. Au-dessus d'une taille critique (Wang et al., 2001) (Zhang et al., 2007) (Mu et al., 2014), les pores jouent un rôle décisif en offrant des sites préférentiels d'amorçage de fissures (Ammar et al., 2008). Une influence de la phase Si (Buffière et al., 2001) (Stolarz et al., 2001), des intermétalliques au fer et au cuivre (Firouzdor et al., 2007) (Tabibian et al., 2013) est également observée. Cependant, la plupart de ces études ont été réalisées en fatigue à grand nombre de cycles. De plus, même si l'analyse post-mortem permet d'identifier le ou les défauts à l'origine d'une fissure au site d'amorçage, elle ne permet pas d'étudier la relation entre la microstructure et la propagation des fissures à la surface et en volume au cours du temps. Cette analyse est d'autant plus difficile en fatigue oligocyclique que la rupture découle souvent de multifissuration (Stolarz et al., 2001) plutôt que d'une seule fissure. Par conséquent, la fatigue oligocyclique des alliages Al-Si moulés par le procédé PMP nécessite davantage d'études.

L'objectif de cette thèse est donc de développer une méthode expérimentale pour étudier les mécanismes d'endommagement dans les alliages Al-Si en fatigue oligocyclique à température ambiante. Tout d'abord, il est d'une importance primordiale de révéler la microstructure des alliages étudiés. La Microscopie Optique (MO) et la Microscopie Electronique à Balayage (MEB) équipé d'un Spectromètre à Dispersion d'Energie (EDS) ont été utilisées pour la caractérisation 2D. La tomographie aux rayons X, sur source de laboratoire et sur source synchrotron, a été utilisée pour la caractérisation 3D. Les caractérisations en 3D sont généralement plus fiables qu'en 2D parce que des objets qui apparaissent isolés en 2D peuvent faire partie d'un même objet 3D voire former de grands

## Extended Abstract (French)

---

réseaux étendus. Un paramètre approprié a été choisi pour chaque constituant en fonction de sa morphologie 3D afin de caractériser sa taille. Il faut noter cependant que quelque soit le paramètre choisi, il ne permet jamais une caractérisation complète de tous les paramètres qui sont d'une importance notoire pour la fatigue. Les principaux paramètres sélectionnés sont:

- ♦ **Diamètre de F éret** : le diamètre de F éret maximum caractérise mieux la taille, c'est à dire la plus grande dimension des objets individuels, mais il ne peut pas refléter la forme locale, l'orientation et la position des objets.
- ♦ **Granulométrie** : la distribution de granulométrie caractérise mieux la taille (l'épaisseur locale) des phases interconnectées mais elle ne peut pas révéler l'étendue de la microstructure interconnectée.

L'alliage A319, objet de cette étude, a été caractérisé à la fois en 2D et en 3D. Outre la matrice Al, la microstructure de l'A319 consiste en :

- ♦ **Pores** : Les deux types de pores, i.e. la porosité gazeuse et les microretassures, peuvent être distingués par leur morphologie. La porosité gazeuse présente une forme quasi circulaire en 2D qui se révèle être effectivement une sphère en 3D. Une microretassure est un objet individuel 3D de forme tortueuse qui, observé en 2D, peut être séparé en plusieurs objets présentant chacun une morphologie en corail. La majeure partie des pores ont un diamètre de F éret maximum supérieur à 400  $\mu\text{m}$ , soit une taille 10 fois supérieure à celle des autres constituants. Avec une taille maximale généralement supérieure à 1 mm, les pores sont supposés les défauts les plus critiques dans le volume. Un critère probabiliste de fatigue thermomécanique, initialement développé à partir de distributions de pores mesurés en 2D (Charkaluk et al., 2014), a été amélioré en utilisant la caractérisation 3D des pores réalisés dans cette thèse (Szymtka et al., 2014). Si la tomographie est une technique adaptée pour caractériser les pores, un grand volume de scan (quelques dizaines de  $\text{mm}^3$ ) est cependant recommandé en raison de leurs grandes tailles.
- ♦ **Si** : La phase Si présente une morphologie en fibres en 2D mais elle forme des réseaux fortement interconnectés en 3D qui peuvent s'étendre à l'ensemble du volume scanné. Seule la tomographie synchrotron avec contraste de phase permet de caractériser le Si en 3D et une résolution plus haute que celle utilisée dans cette thèse (1 voxel = 1.61  $\mu\text{m}$ ) est nécessaire pour obtenir des données quantitatives fiables.
- ♦ **Intermétalliques au fer** : Il y a deux types d'intermétalliques au fer. La phase  $\alpha$  (AlFeMnSi) a une teneur en Mn supérieure à la phase  $\beta$  (AlFeSi) et présente une morphologie en « écriture chinoise ». La phase  $\beta$  contient moins de Mn que  $\alpha$  et présente une forme en aiguilles en 2D et en plaquettes en 3D. Les intermétalliques au fer forment des réseaux hautement interconnectés en 3D qui peuvent s'étendre à l'ensemble du volume scanné en raison de la



## Extended Abstract (French)

---

haute teneur en Fe (~0,6% m.) et en Mn (~0,5% m.) de l'alliage A319. L'addition de Mn favorise la formation de la phase  $\alpha$  aux dépens de la phase  $\beta$ . La majorité des intermétalliques au fer ont une épaisseur comprise entre 6 et 18  $\mu\text{m}$ . La tomographie en contraste d'absorption peut être utilisée pour caractériser les intermétalliques au fer, mais une haute résolution (voxel < 1.5  $\mu\text{m}$ ) est nécessaire vu la finesse de cette phase.

- ♦ **Les phases au cuivre :** Les phases  $\text{Al}_2\text{Cu}$  et  $\text{AlCuMgSi}$  ont été observées en 2D. La phase  $\text{AlCuMgSi}$  présente un aspect «moucheté» et se localise généralement autour de la phase  $\text{Al}_2\text{Cu}$ . Cependant, la phase  $\text{AlCuMgSi}$  n'a pas été observée en 3D en raison de sa faible taille (épaisseur < 1  $\mu\text{m}$  en 2D) trop faible par rapport à la résolution de la caractérisation 3D (1 pixel = 1.5  $\mu\text{m}$ ). La phase  $\text{Al}_2\text{Cu}$  présente des structures complexes en 3D qui sont moins étendues que pour le Si et les intermétalliques au fer. La majeure partie de la phase  $\text{Al}_2\text{Cu}$  a une épaisseur comprise entre 6 et 18  $\mu\text{m}$ . La tomographie en contraste d'absorption permet de caractériser les phases au Cu mais une haute résolution (voxel < 1.5  $\mu\text{m}$ ) est nécessaire en particulier pour la phase  $\text{AlCuMgSi}$ .
- ♦ **Pb :** Le plomb Pb se présente sous forme de petits points dispersés en 2D qui correspondent à des objets individuels peu étendus en 3D. La majorité des particules de Pb ont un diamètre de Fétet maximal compris entre 18 et 60  $\mu\text{m}$ . Compte tenu de leurs tailles, morphologies et propriétés mécaniques, les particules de Pb peuvent être assimilées à des «petits pores». Bien que la tomographie permette de caractériser le Pb, une haute résolution (voxel < 1.5  $\mu\text{m}$ ) est nécessaire en raison de la petite taille des particules.

Le protocole expérimental développé a été validé sur des essais de traction avant d'être appliqué aux essais de fatigue. Bien que certaines des méthodes expérimentales aient déjà été utilisées dans la littérature, c'est la première fois qu'elles sont couplées dans une même étude. Les deux types d'essais in-situ développés sont :

- ♦ **Essais in-situ 2D :** L'utilisation d'un microscope longue distance (Questar) permet de suivre l'amorçage et la propagation des fissures en surface en temps réel avec une résolution supérieure à celle des observations in-situ en 3D. Des éprouvettes plus larges, et donc potentiellement plus représentatives, peuvent être utilisées. Une caractérisation préliminaire 3D des pores à l'aide de la tomographie aux rayons X est nécessaire pour sélectionner la région d'observation ou région d'intérêt (ROI) pour les essais in-situ et analyser la relation entre les mécanismes d'endommagements observés en surface et les pores sous la surface.
- ♦ **Essais in-situ 3D :** L'utilisation de la tomographie aux rayons X permet de suivre l'amorçage et la propagation des fissures directement en volume et donc de mieux comprendre les mécanismes d'endommagement. Par rapport à la tomographie de laboratoire, la tomographie synchrotron permet des temps d'acquisition beaucoup plus courts et donc plus compatibles avec la durée des essais de fatigue et peut, grâce au contraste de phase, révéler la phase Si.

## Extended Abstract (French)

---

Cependant, ce même contraste de phase rend la segmentation des constituants de la microstructure et des fissures plus difficile.

**Les Mesures de Champs** cinématiques ont été effectuées à l'aide de la Corrélation d'Images Numériques (CIN) et de la Corrélation d'Images Volumiques (CIV). En 2D, une attaque chimique donne un mouchetis naturel aux dendrites d'aluminium en évitant la ségrégation du Si et rend ainsi possible la CIN à une résolution acceptable sans ajouter de mouchetis artificiel qui viendrait masquer la microstructure. En 3D, les constituants de la microstructure révélés par la tomographie sont utilisés comme traceurs naturels pour la CIV. Les relations entre, d'une part, les évolutions d'endommagement, c'est-à-dire les microfissures, le chemin de propagation de la fissure et la rupture finale et d'autre part, les discontinuités de déplacement et les localisations de déformation dans les champs mesurés sont observées et analysées pour conforter l'interprétation des mécanismes d'endommagement.

Les **simulations EF** basées sur un modèle représentant les pores et la matrice solide ont été utilisées pour sélectionner la ROI et étudier l'influence des pores sur les distributions de contrainte tant en chargement monotone que cyclique. **Les analyses** post-mortem utilisant la microscopie, optique et électronique, et l'analyse EDS sur des surfaces planes de l'éprouvette et sur les surfaces de rupture ont permis d'identifier les zones de rupture finale, les microfissures, les constituants impliqués dans la surface de rupture, les sites d'amorçages des fissures et les mécanismes d'endommagement des inclusions dures.

Les mécanismes d'endommagement en traction et en fatigue de l'alliage A319 PMP ont été identifiés :

### **Mécanismes d'endommagement en traction :**

- ◆ Les fissures s'amorcent aux inclusions dures dans les zones où il y a suffisamment de concentrations de contraintes, c'est-à-dire principalement autour des grands pores mais aussi sur les bords de l'éprouvette en l'absence de grands pores.
- ◆ Les fissures peuvent se propager en suivant les inclusions dures, soit le Si eutectique et les intermétalliques au fer et au cuivre, en raison de l'augmentation de la concentration de contraintes aux inclusions dures avec l'augmentation du chargement.

### **Mécanismes d'endommagement en fatigue :**

- ◆ L'amorçage des fissures se produit aux inclusions dures dans les zones où il y a suffisamment de concentrations de contraintes. Ces concentrations de contraintes peuvent être causées par de grands pores, un coin de l'éprouvette, etc.
- ◆ Les fissures se propagent à travers des inclusions dures. Les localisations de déformation ont été observées sur des inclusions dures même sans fissures, donc nous pouvons supposer que

## Extended Abstract (French)

---

la propagation des fissures se produit aux inclusions dures en raison des localisations de déformation.

Les inclusions dures mentionnées ci-dessus comprennent la phase Si, les intermétalliques au fer (à la fois phases  $\alpha$  et  $\beta$ ) et au cuivre (phases  $Al_2Cu$  et  $AlCuMgSi$ ). Les fissures se propagent plutôt à travers les 'inclusions dures' que à travers la matrice Al car les concentrations de contraintes sont plus susceptibles de se produire dans la matrice Al autour des inclusions. En effet les inclusions dures ont un module d'élasticité plus élevé et sont plus fragiles que la matrice Al et elles ont des formes localement pointues.

Trois conditions fournissent une concentration de contraintes suffisante à l'amorçage des fissures aux inclusions dures : (1) Un haut niveau de contrainte nominale en fatigue oligocyclique; (2) Les grands pores qui augmentent fortement le niveau de contrainte locale; (3) la microstructure grossière et la faible modification au Sr de l'alliage PMP étudié qui favorisent les concentrations de contrainte.

L'étude bibliographique sur la fatigue des alliages Al-Si montre que les fissures s'amorcent généralement sur des pores lorsque de grands pores sont présents. Dans cette thèse, les fissures s'amorcent aux inclusions dures tandis que l'influence des pores est de générer suffisamment de concentration de contraintes. A ma connaissance, c'est la première fois que les mécanismes d'endommagement en fatigue oligocyclique de l'alliage Al-Si obtenu par procédé PMP ont été étudiés.

En raison de la concentration de contraintes produite par les pores, la plupart des fissures dans cette étude s'amorce aux inclusions dures autour des grands pores. La taille, l'emplacement, le nombre et la forme des pores ont une influence sur l'amorçage des fissures. Les pores ont également une influence sur la propagation de fissures en fatigue oligocyclique en augmentant le niveau de contrainte effectif, ce qui se traduit par plus de rupture que de décohésion des inclusions dures. Il est donc nécessaire d'accorder plus d'attention au contrôle des pores dans le procédé PMP.

Grace à sa faible teneur, sa petite taille, sa morphologie, et sa faible dureté le Pb n'a aucune influence sur l'endommagement. Par contre, le Si eutectique semble fournir des sites d'amorçage et des chemins de propagation privilégiés pour les fissures devant les intermétalliques au fer ou au cuivre. La propagation des fissures aux inclusions dures est favorisée par la localisation de déformation plastique en avant de la pointe de fissure. Ces zones plastiques présentent une forme en «Y» dans un plan parallèle à la direction de sollicitation et à la direction de propagation.

L'orientation des inclusions dures a une influence sur la propagation des fissures: (1) Lorsque c'est la même que la direction de propagation de la fissure, la fissure a tendance à se propager suivant les inclusions dures; (2) Quand elle est perpendiculaire à la direction de propagation de la fissure, la fissure est arrêtée. Pour ce dernier cas, le niveau de contrainte dans la zone autour de la fissure, en

## Extended Abstract (French)

---

particulier à certaines inclusions dures situées suivant une ligne verticale passant par la pointe de la fissure et orientée dans la direction de chargement, a augmenté de façon spectaculaire. Dans le même temps, la fissure est bloquée pendant plusieurs cycles avant de se propager à nouveau soit en changeant sa direction de propagation pour la direction des inclusions dures, soit en cassant des inclusions dures pour les traverser. En outre, même si une fissure ne se propage pas en raison d'obstacles, l'ouverture de la fissure augmente quand même pendant le chargement cyclique.

Lors de la rupture finale, les inclusions dures dans le ligament non rompu sont sous un niveau de contrainte beaucoup plus élevé qui conduit à un grand nombre d'amorçages de microfissures aux inclusions dures et à moins décohésions que dans l'étape de propagation des fissures.

## Abstract

### **Influence of the casting microstructure on damage mechanisms in Al-Si alloys by using 2D and 3D in-situ analysis**

An experimental protocol was developed in this thesis in order to study the influence of casting microstructure on the fatigue behavior in Lost Foam Casting Al-Si alloys in tension and in Low Cycle Fatigue at room temperature. First of all, the microstructures of studied alloys were thoroughly characterized both in 2D and in 3D. The most suitable and representative specimens and Region of Interest (ROIs) where the in-situ monitoring was performed were selected through a preliminary characterization using X-ray tomography, which is also necessary to understand damage mechanisms after failure. In-situ observations performed on surface using Questar long distance microscope and in volume using X-ray tomography allow following cracks initiations and their propagations and thus allow identifying the relation between damage mechanisms and casting microstructure. 2D/3D displacement and strain fields measured using Digital Image Correlation and Digital Volume Correlation allows analyzing the relation between measured fields and damage mechanisms. Postmortem analysis and FEM simulation gave more information for the damage mechanisms. Large pores favor crack initiation as they strongly increase local stress level. Hard inclusions (Si phase, iron intermetallics and copper containing phases) also play an important role in crack initiation and propagation due to strain localizations at these inclusions.

**Key words :** Al-Si alloy, X-ray tomography, Digital Image/Volume Correlation, Low Cycle Fatigue, damage mechanisms.

## Résumé

### **Etude de l'influence de la microstructure sur les mécanismes d'endommagement dans des alliages Al-Si de fonderie par des analyses in-situ 2D et 3D**

Un protocole expérimental a été développé dans cette thèse pour étudier l'influence de la microstructure héritée du procédé de fonderie dit Procédé à Modèle Perdu sur le comportement en fatigue oligocyclique des alliages Al-Si à température ambiante. Dans un premier temps, la microstructure des alliages étudiés a été caractérisée à la fois en 2D et en 3D. Les éprouvettes les plus appropriées et les plus représentatives et les régions d'intérêt où le suivi in-situ est réalisé (ROIs) ont été sélectionnées par une caractérisation préliminaire en tomographie aux rayons X. Cette caractérisation 3D est également nécessaire pour comprendre les mécanismes d'endommagement après rupture de l'éprouvette. Les observations in-situ réalisées en surface en utilisant un microscope longue distance (Questar) et en volume avec la tomographie aux rayons X permettent de suivre l'amorçage et la propagation des fissures et ainsi d'identifier la relation entre les mécanismes d'endommagement et les microstructures moulées. Les champs de déplacement et de déformation en 2D/3D mesurés à l'aide de la Corrélation d'Images Numériques et la Corrélation d'Images Volumiques permettent d'analyser la relation entre les champs mesurés et les mécanismes d'endommagement. L'analyse post-mortem et la simulation éléments finis ont permis de compléter l'analyse des mécanismes d'endommagement. Les grands pores favorisent l'amorçage de fissures car ils augmentent fortement le niveau de contrainte locale. Les inclusions dures (phase Si, intermétalliques au fer et phases au cuivre) jouent un rôle important dans l'amorçage et la propagation des fissures en raison des localisations de déformation sur ces inclusions.

**Mots-clefs :** alliage Al-Si, tomographie aux rayons X, corrélation d'images 2D/3D numériques, fatigue oligocyclique, mécanismes d'endommagement.